

**A Thesis Submitted for the Degree of PhD at the University of Warwick**

**Permanent WRAP URL:**

<http://wrap.warwick.ac.uk/133256>

**Copyright and reuse:**

This thesis is made available online and is protected by original copyright.

Please scroll down to view the document itself.

Please refer to the repository record for this item for information to help you to cite it.

Our policy information is available from the repository home page.

For more information, please contact the WRAP Team at: [wrap@warwick.ac.uk](mailto:wrap@warwick.ac.uk)

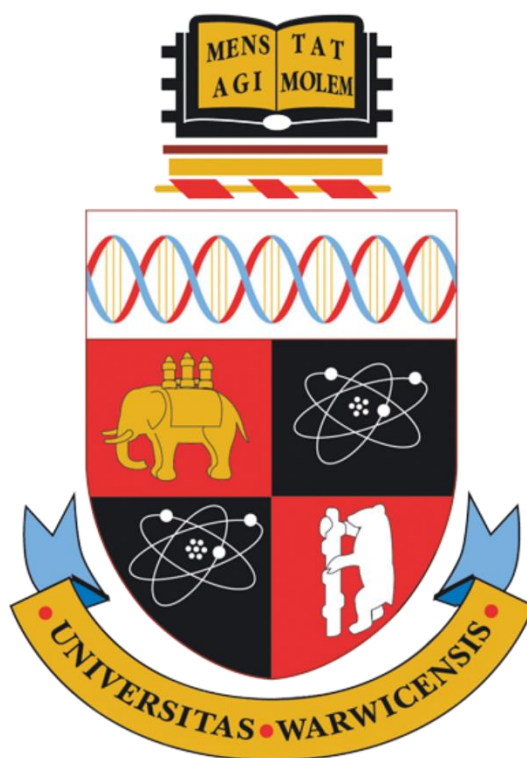
# THE APPLICATION OF MESOPOROUS SILICA NANOPARTICLES TO MEDICAL IMAGING

---

**GEORGE HENRY LEE**

---

A thesis submitted in fulfilment of the requirements for  
the degree of Doctor of Philosophy



Molecular Analytical Science Centre for Doctoral  
Training, University of Warwick.

December 2018

## **Table of Contents**

	<b>Page</b>
<b>Acknowledgements</b>	<b>XIII</b>
<b>Declarations</b>	<b>XIV</b>
<b>Abbreviations</b>	<b>XV</b>
<b>List of Figures, Tables and Equations</b>	<b>XVIII</b>
<b>Abstract</b>	<b>XXVII</b>
<b>Chapter 1</b>	<b>Introduction</b>
<b>1.1</b>	<b>Summary</b>
<b>1.2</b>	<b>Silica Nanoparticles, SiNPs</b>
<b>1.2.1</b>	<b>Mesoporous Silica</b>
<b>1.2.2</b>	<b>Mesoporous Silica Nanoparticle, MSN, Synthesis</b>
<b>1.2.3</b>	<b>Surface Functionalisation of MSNs</b>
<b>1.2.4</b>	<b>Polymer Modification of MSN Surfaces</b>
<b>1.2.5</b>	<b>SiNP Toxicity</b>
<b>1.2.6</b>	<b>Applications in Medicine</b>
<b>1.3</b>	<b>Magnetic Resonance Imaging, MRI</b>
<b>1.3.1</b>	<b>MRI History</b>
<b>1.3.2</b>	<b>MRI Basic Principles</b>
<b>1.3.3</b>	<b>Contrast Agent Theory</b>
<b>1.3.4</b>	<b>Gd<sup>3+</sup> Based Contrast Agent Toxicity</b>
<b>1.3.5</b>	<b>GBCAs based on MSNs</b>

<b>1.4</b>	Aims and Objectives	40
<b>1.5</b>	References	42
<b>Chapter 2</b>	<b>Experimental</b>	<b>59</b>
<b>2.1</b>	Materials and General Procedures	59
<b>2.1.1</b>	Starting Materials	59
<b>2.2</b>	Experimental Procedures	61
<b>2.2.1</b>	Experimental Details for Chapter 3	61
<b>2.2.1.1</b>	Preparation of Mesoporous Silica Nanoparticles with Pore Diameter Variation	61
<b>2.2.1.2</b>	Preparation of Mesoporous Silica Nanoparticles with Amine Location Variation	61
<b>2.2.1.3</b>	Gd <sup>3+</sup> -DOTA Functionalisation	62
<b>2.2.2</b>	Experimental Details for Chapter 4	63
<b>2.2.2.1</b>	Internally Gd <sup>3+</sup> -DOTA Functionalised MSN synthesis	63
<b>2.2.2.2</b>	‘Grafting From’ Method of pNIPAM Addition to MSNs	63
<b>2.2.2.3</b>	Preparation of pNIPAM	64
<b>2.2.3</b>	Experimental Details for Chapter 5	65
<b>2.2.3.1</b>	Preparation of Internally Fluorescein Functionalised MSNs	65
<b>2.2.3.2</b>	‘Grafting From’ Method of NVA/MAA Copolymer Addition to	65

	MSNs using Free Radical Polymerisation	
<b>2.2.3.3</b>	NVA/MAA Copolymer Synthesis using Free Radical Polymerisation	66
<b>2.2.3.4</b>	‘Grafting From’ Method of NVA/MAA Copolymer Addition to MSNs using Atom Transfer Radical Polymerisation	67
<b>2.2.3.5</b>	PNA Functionalisation of NVA/MAA Surface Functionalised Fluorescein MSNs	67
<b>2.2.3.6</b>	NVA/MAA Copolymer Synthesis using Atom Transfer Radical Polymerisation	68
<b>2.2.3.7</b>	Colon Cancer Cell Interaction Assay	68
<b>2.2.3.8</b>	Cell Toxicity Screening	69
<b>2.3</b>	Characterisation Techniques	70
<b>2.3.1</b>	Infrared Spectroscopy	70
<b>2.3.2</b>	Thermogravimetric Analysis	70
<b>2.3.3</b>	Dynamic Light Scattering and Zeta Potential	70
<b>2.3.5</b>	Small Angle X-ray Scattering (SAXS)	70
<b>2.3.6</b>	Porosimetry	70
<b>2.3.7</b>	Transmission Electron Microscopy	70
<b>2.3.8</b>	Gel permeation Chromatography	71
<b>2.3.9</b>	Turbidimetry Analysis	71

2.3.10	UV/vis Spectroscopy and Fluorometry with Cell Cultures	71
2.3.11	Ion Coupled Plasma Mass Spectrometry	72
2.3.12	T <sub>1</sub> Relaxation Spectroscopy	72
2.3.12.1	13.1 MHz Xigo	72
2.3.12.2	9.4 T MRI Scanner	72
2.3.12.3	3 T MRI Scanner	73
2.4	References	74
<b>Chapter 3</b>	<b>Investigating the Impact of Nanoparticle Design on MRI Contrast Behaviour</b>	<b>75</b>
3.1	Chapter Summary	75
3.2	Introduction	77
3.2.1	Aims	79
3.3	Preparation and Characterisation of MSNs with Controlled Variation of Pore Diameter and Gd <sup>3+</sup> -DOTA Functionalisation Location	80
3.3.1	Transmission Electron Microscopy	80
3.3.2	Infrared Spectroscopy	85
3.3.3	Thermogravimetric analysis	87
3.3.4	Dynamic Light Scattering and Zeta Potential	89
3.3.5	Small Angle X-ray Scattering	90
3.3.6	Gas Sorption Porosimetry Analysis	92

<b>3.4</b>	Investigation of MSN Pore Diameter and Gd <sup>3+</sup> -DOTA Location on Relaxivity	95
<b>3.4.1</b>	Analysis at 13.1 MHz	95
<b>3.5</b>	Conclusions	99
<b>3.6</b>	Future Work	101
<b>3.7</b>	References	103
<b>Chapter 4</b>	<b>Thermo-responsive MSNs as Diagnostic MRI Contrast Agents</b>	<b>106</b>
<b>4.1</b>	Chapter Summary	106
<b>4.2</b>	Introduction	108
<b>4.2.1</b>	Aims	111
<b>4.3</b>	Preparation and Characterisation of pNIPAM surface functionalised MSNs synthesised using a ‘Grafting From’ method	112
<b>4.3.1</b>	Zeta Potential	113
<b>4.3.2</b>	Transmission Electron Microscopy	115
<b>4.3.3</b>	Infrared Spectroscopy	116
<b>4.3.4</b>	Dynamic Light Scattering	117
<b>4.3.5</b>	Gel Permeation Chromatography	119
<b>4.3.6</b>	Thermogravimetric analysis	120
<b>4.3.7</b>	Spectroscopic Analysis of Thermoresponsive Behaviour	122
<b>4.4</b>	Investigation into the pNIPAM surface functionalised Gd <sup>3+</sup> -DOTA	126

	MSNs' application as an MRI Contrast Agent	
4.4.1	Relaxometry Analysis	126
4.4.2	3 Tesla Clinical MRI Scanner analysis	130
4.5	Conclusions	133
4.6	Future Work	134
4.7	References	135
<b>Chapter 5</b>	<b>The Application of MSNs as a Fluorescent Marker for Colorectal Cancer Cells</b>	<b>140</b>
5.1	Chapter Summary	140
5.2	Introduction	142
5.2.1	Aims	146
5.3	Free Radical Polymerisation Approach	147
5.3.1	Dynamic Light Scattering and Zeta Potential Analysis of Nanocomposites	148
5.3.2	Transmission Electron Microscopy	151
5.3.3	Gel Permeation Chromatography Analysis of 0.2 mol% and 1 mol% NVA/MAA Copolymer	152
5.3.4	Infrared Spectroscopy	154
5.3.5	Thermogravimetric analysis	155
5.4	Investigation into the Non-Specific binding of the Surface	158



	Functionalised NVA/MAA copolymer MSNs using Free Radical Polymerisation with the Colorectal Cancer Cells	
<b>5.4.1</b>	Colorectal Cancer Cell Binding Assay	158
<b>5.5</b>	Preparation and Characterisation of Fluorescent MSNs with Surface Functionalised NVA/MAA Copolymer Synthesised using Atom Transfer Radical Polymerisation	160
<b>5.5.1</b>	Dynamic Light Scattering and Zeta Potential	162
<b>5.5.2</b>	Transmission Electron Microscopy	165
<b>5.5.3</b>	Infrared Spectroscopy	166
<b>5.5.4</b>	Thermogravimetric analysis	168
<b>5.5.5</b>	Gel Permeation Chromatography	170
<b>5.6</b>	Investigation into the Specific Binding of the PNA Functionalised MSNs with the Colorectal Cancer Cells	172
<b>5.6.1</b>	Colorectal Cancer Cell Binding Assay	172
<b>5.6.2</b>	Cell Viability Test	174
<b>5.7</b>	Conclusions	177
<b>5.8</b>	Future Work	178
<b>5.9</b>	References	179

<b>Chapter 6</b>	<b>Conclusions</b>	<b>185</b>
<b>Appendix</b>	<b>Chapter 3: Investigating the Impact of Nanoparticle Design on MRI Contrast Agent Behaviour</b>	<b>188</b>

## **Acknowledgements**

I would like to thank my supervisors Dr Gemma-Louise Davies and Professor Charles Hutchinson for the extensive help and support throughout my PhD. Dr Sarah Wayte for her MRI expertise. Also, Professor Matthew Gibson for adopting me into his group and providing exceptional knowledge in polymer chemistry that was of great use to me in the latter part of my work.

All the Gibson group have been incredibly supportive and friendly, however there are members that deserve a special mention. Dr Collette Guy for keeping me company in the lab by listening to my ramblings and allowing me to put my ‘eclectic’ music on. Also, Dr Sarah-Jane Richards and Dr Caroline Biggs for nodding politely when I talked at them and for organising my life. I promise one day I will learn how to read emails. I must highlight Trisha Bailey for being a cell wizard and willing to put into layman’s terms the magic she performs in the bat cave. There are other PhD students that I would like to thank specifically as well such as Charlotte Fletcher, Alice Frayter, Ben Graham, Ziedo Solomon, Christopher Stubbs and James Teahan for being helpful and fun simultaneously.

I would like to thank my family for always being supportive. Finally, Sophia Gibbs for being simply perfect in every way.

## **Declarations**

All the work presented in this thesis is entirely my own work, except where it is acknowledged in the text. I confirm that this thesis has not been submitted for a degree at another university.

## **Abbreviations**

ACVA = 4,4'-Azobis (4-Cyanovaleric Acid)  
AIBN = Azobisisobutyronitrile  
APTES = (3-Aminopropyl) triethoxysilane  
ATRP = Atom Transfer radical Polymerisation  
 $B_0$  = Applied Magnetic Field  
 $B_1$  = Radiofrequency Pulse  
BIBB =  $\alpha$ -Bromoisobutyryl Bromide  
CBMA = Carboxybetaine Methacrylate  
CRC = Colorectal Cancer  
CTAB = n-Hexadecyltrimethylammonium Bromide  
CTAB = n-Hexadecyltrimethylammonium Bromide  
DLS = Dynamic Light Scattering  
DNA = Deoxyribonucleic Acid  
DODE = Dodecyltrimethylammonium Bromide  
DOPA = L-3, 4-Dihydroxyphenylalanine  
DOPA-pCBMA = CBMA polymer using DOPA as initiator  
DOTA = 1,4,7,10-Tetraazacyclododecane-1,4,7,10-tetraacetic Acid  
DOTA-NHS-ester = 2,2',2''-(10-(2-((2,5-Dioxopyrrolidin-1-yl)oxy)-2-oxoethyl)-1,4,7,10-tetraazacyclododecane-1,4,7-triyl)triacetic Acid  
DTPA = Diethylenetriaminepentaacetic Acid  
EDC-HCl = N-(3-Dimethylaminopropyl)-N'-Ethylcarbodiimide Hydrochloride  
EPR = Enhanced Permeability and Retention  
FDA = US Food and Drug Administration  
FITC = Fluorescein  
FTIR = Fourier transform Infrared  
Gal- $\beta$ (1-3)GalNac =  $\beta$ -D-Galactosyl-(1-3)-N-Acetyl-D-Galactosamine  
GBCA = Gd<sup>3+</sup> Based Contrast Agent  
Gd<sup>3+</sup>-DOTA = Gd<sup>3+</sup> bound in DOTA complex  
Gd<sup>3+</sup>-Si-DTTA = Gd<sup>3+</sup> bound (Trimethoxysilylpropyl)die-ethylenediaminetetraacetate  
GPC = Gel Permeation Chromatography

GRAS = Generally Recognised As Safe

HAS = Human Serum Albumin

I = Spin Quantum Number

ICP-MS = Inductively Coupled Plasma Mass Spectrometry

LCST = Lower Critical Solution Temperature

MAA = Methacrylic Acid

$M_n$  = Number Averaged Molar Mass

MP = Mannosylated Polyethylenimine

MRI = Magnetic Resonance Imaging

MRI = Magnetic Resonance Imaging

MSN = Mesoporous Silica Nanoparticle

MSNs = Mesoporous Silica Nanoparticles

$M_w$  = Molecular Weight

MYRI = Myristyltrimethylammonium Bromide

NHS = N-Hydroxysuccinimide

NSF = Nephrogenic Systemic Fibrosis

NVA = N-Methyl-N-Vinylacetamide

NVA/MAA MSNs = N-Methyl-N-Vinylacetamide/Methacrylic acid copolymer surface functionalised MSNs

PAMAM = Polyamidoamine

PDI = Polydispersity Index

PEG = Polyethylene Glycol

PEI = Polyethylenimine

PMDETA = N, N, N', N'', N'''-Pentamethyldiethylenetriamine

PMOs = Periodic Mesoporous Organo-Silicas

PNA = *Arachis Hypogaea* Lectin (Peanut Agglutinin)

PNA MSNs = N-Methyl-N-Vinylacetamide/Methacrylic Acid copolymer surface functionalised MSNs with PNA amide bound to the Methacrylic acid

pNIPAM = Poly(N-Isopropylacrylamide)

pNIPAM-MSNs = pNIPAM surface functionalised MSNs

PPs = Peyer's Patches

PS-b-PAA = Polystyrene-b-Poly(acrylic) Acid

PVP = Polyvinyl Pyrrolidone

RGD = Arginylglycylaspartic acid  
RNA = Ribonucleic Acid  
SAXS = Small Angle X-ray Scattering  
SBM = Solomon-Bloembergen-Morgan  
SiNPs = Silica Nanoparticles  
SiRNA = Small Interfering Ribonucleic Acid  
SRDDS = stimuli responsive drug delivery systems  
STEM = Scanning Transmission Electron Microscopy  
 $T_1$  relaxation = Spin-Lattice Relaxation  
 $T_2$  relaxation = Spin-Spin Relaxation  
TE = Echo Time  
TEA = Triethanolamine  
TEM = Transmission Electron Microscopy  
TEM = Transmission Electron Microscopy  
TEOS = Tetraethyl Silicate  
TF = Thomsen-Friedenreich  
TGA = Thermogravimetric Analysis  
TR = Retention Time  
UV = Ultraviolet  
UV/vis = Ultraviolet and Visible  
 $\gamma$  = Gyromagnetic Moment  
 $\tau_m$  = Water Residence Time  
 $\tau_R$  = Tumbling Rate  
 $\omega_0$  = Larmor Frequency

## **List of Figures, Tables and Equations**

<b>Figure 1.1.</b> The hydrolysis of tetra alkyl silicates (tetraethyl silicate, TEOS) and the condensation of the subsequent silicic acid molecules to form silica.	2
<b>Figure 1.2.</b> Possible mechanistic pathways for the formation of MCM-41: 1) liquid crystal phase initiated and 2) silicate anion initiated.	4
<b>Figure 1.3.</b> Transmission electron micrographs of several MCM-41 materials having a pore size of a) 20, b) 40, c) 65 and d) 100 Å.	5
<b>Figure 1.4.</b> The quaternary ammonium surfactant salts utilised to investigate mesoporosity of MCM 41 particles with TEM images by Grün et al.	6
<b>Figure 1.5.</b> The mechanisms for acid and base catalysed hydrolysis/condensation of alkyl silanes.	7
<b>Figure 1.6.</b> Examples of stabilising reagents used in previous publications with TEM images of the resulting nanoparticles obtained underneath.	9
<b>Figure 1.7.</b> Interactions between the inorganic silicate network and the head group of the surfactant with consideration of the possible synthetic pathways in acidic, basic or neutral media.	10
<b>Figure 1.8.</b> Grafting (post-synthetic modification) for organic modification of MSNs with terminal organosilanes of the type $(R'O)_3SiR$ . R = organic functional group and R' = alkyl chain.	11
<b>Figure 1.9.</b> Co-condensation method (direct synthesis for the organic modification of MSNs with terminal organosilanes of the type $(R'O)_3SiR$ . R = organic functional group and R' = alkyl chain.	12
<b>Figure 1.10.</b> General synthetic pathway for PMOs that are constructed from bis-silylated organic bridging units. R = organic bridge, R' = alkyl chain.	14
<b>Figure 1.11.</b> Schematic description of 'Grafting to' and 'Grafting from' approaches for the synthesis of polymer surface functionalisation of nanoparticles.	15



<b>Figure 1.12.</b> Cytochrome c transportation into the cytoplasm using MSNs	21
<b>Figure 1.13.</b> A schematic representation of the conceptual passive targeting (EPR effect) of nanomedicine.	22
<b>Figure 1.14.</b> A schematic representation of the CdS nanoparticle capped MSN-based drug delivery system.	23
<b>Equation 1.1.</b> Calculating the Larmor frequency from the gyromagnetic moment and the magnetic field strength	25
<b>Figure 1.15.</b> A schematic representation of 12 nuclei with $I \geq \frac{1}{2}$ in no magnetic field and with the addition of magnetic field, $B_0$ .	26
<b>Figure 1.16.</b> A schematic showing 6 nuclei with $I \geq \frac{1}{2}$ precessing around $B_0$ with a common origin in either the low energy state, in the direction of $B_0$ or the high energy state, and its simplification representing the net longitudinal direction of the magnetic moment of the nuclei.	26
<b>Figure 1.17.</b> The promotion of nuclei from the low energy state to the high energy state and the synchronisation of precession by the addition of a radiofrequency pulse at Larmor frequency perpendicular to $B_0$ , $B_1$ . Thus, rotating the net magnetisation of the nuclei from a net longitudinal direction to a net transverse direction.	27
<b>Figure 1.18.</b> A schematic representing of the addition of $B_1$ to 6 nuclei in $B_0$ and the subsequent relaxation steps, $T_2$ and $T_1$ relaxation observed after removal of $B_1$ .	28
<b>Figure 1.19.</b> The loss of transverse magnetisation against time for nuclei with fast and slow $T_2$ relaxation and the general theory behind observing the differences in $T_2$ relaxation between nuclei with fast and slow relaxation experimentally.	29
<b>Figure 1.20.</b> The recovery of longitudinal magnetisation against time for nuclei with fast and slow $T_1$ relaxation and the general theory behind observing the differences in $T_1$ relaxation between nuclei with fast and slow relaxation experimentally.	30

<b>Equation 1.2.</b> the Boltzmann distribution of the population difference between $H^1$ nuclei in the low and high energy state.	31
<b>Equation 1.3.</b> Calculating the $T_1$ relaxation of two hydrogen nuclei using <i>Solomon-Bloembergen-Morgan</i> (SBM) theory.	31
<b>Equation 1.4.</b> Calculating the $T_2$ relaxation of two hydrogen nuclei using <i>Solomon-Bloembergen-Morgan</i> (SBM) theory.	31
<b>Figure 1.21.</b> Schematic representation of inner, second and outer sphere water interactions with a $Gd^{3+}$ based contrast agent.	32
<b>Equation 1.5.</b> Calculating $T_1$ relaxation by the sum of the constituent $T_1$ relaxations	33
<b>Figure 1.22.</b> The molecular structure of $Gd^{3+}$ -DTPA and $Gd^{3+}$ -DOTA with a single coordinated water molecule.	33
<b>Figure 1.23.</b> A schematic illustrating how binding a $Gd^{3+}$ -chelate to a macromolecule decreases the tumbling rate, $\tau_R$ , therefore increasing $T_1$ relaxation.	36
<b>Figure 1.24.</b> The molecular structure and the computational molecular optimisation in 3D space of the DOTA variants investigated by Carniato <i>et al.</i>	37
<b>Figure 3.1.</b> General schematic representation of the synthesis of mesoporous silica nanoparticles.	80
<b>Figure 3.2.</b> TEM images of MSNs synthesised using three different surfactants.	81
<b>Figure 3.3.</b> The TEM images and the particle diameter of MSNs synthesised using the surfactants.	82
<b>Figure 3.4.</b> A schematic of an MSN with the cross section of a pore highlighted to show the difference between the three $Gd^{3+}$ -DOTA functionalisation locations used in investigating the effect of changing the pore diameter on relaxivity and therefore MRI contrast applicability.	83

<b>Figure 3.5.</b> TEM images and a Bar chart of the particle diameter analysis by TEM of the 6 MSNs families synthesised with CTAB Plain and MYRI Plain as a comparison between aminated and non-aminated MSNs.	84
<b>Figure 3.6.</b> The FTIR spectra of A) CTAB Internal MSNs, CTAB Edge MSNs and CTAB External MSNs compared to CTAB surfactant and B) MYRI Internal MSNs, MYRI Edge MSNs and MYRI External MSNs compared to MYRI surfactant.	86
<b>Figure 3.7.</b> The TGA analysis between 30 - 600 °C of A) CTAB Internal MSNs, CTAB Edge MSNs and CTAB External MSNs compared to CTAB surfactant and B) MYRI Internal MSNs, MYRI Edge MSNs and MYRI External MSNs compared to MYRI surfactant.	88
<b>Table 3.1.</b> The mean hydrodynamic diameter obtained by DLS and zeta potential on all amine functionalisation locations, Internal, Edge and External, using the CTAB and MYRI surfactants.	89
<b>Figure 3.8.</b> An example of the data acquired by SAXs for CTAB Internal MSNs Repeat 1 with the area representing the particle diameter and the pore diameter of the MSNs being analysed using the EasySAXS modelling software.	91
<b>Table 3.2.</b> The particle diameter and pore diameter analysed by SAXS for each of the MSNs obtained using the all the variations of amine functionalisation location and CTAB and MYRI surfactants.	92
<b>Figure 3.9.</b> Plots of the pore diameters of the MSNs obtained by porosimetry.	93
<b>Equation 3.1.</b> Calculating relaxivity, $R_1$ , using $T_1$ relaxation	95
<b>Equation 3.2.</b> The experimental method of calculating relaxivity, $R_1$ .	95
<b>Figure 3.10.</b> A schematic of the variation in location, Internal, Edge and External, of the $Gd^{3+}$ -DOTA functionalisation on the MSNs and the bar chart of the relaxivity at 13.1 MHz of the 6 families of MSNs synthesised	96
<b>Table 3.3.</b> The mass of $Gd^{3+}$ per mg of MSNs for each repeat of the six families synthesised plus the $Gd^{3+}$ Adsorption Control.	98

<b>Figure 3.11.</b> The relaxivity at 9.4 Tesla of the 3 families of MSNs synthesised using the MYRI surfactant in the three locations, Internal, Edge and External.	101
<b>Figure 4.1.</b> A schematic of the change in intermolecular interactions of pNIPAM above and below its LCST.	109
<b>Figure 4.2.</b> The transition metal catalysed (i.e. copper bromide and PMDETA) ATRP of NIPAM to obtain pNIPAM.	110
<b>Figure 4.3.</b> A Schematic of the functionalisation method to obtain thermoresponsive MRI contrast agents.	113
<b>Table 4.1.</b> The Zeta potential obtained after key steps in the synthesis of thermoresponsive MSNs.	114
<b>Figure 4.4.</b> The TEM images obtained for the 0.2 mol%, 1 mol%, 2.5 mol% pNIPAM surface functionalised Gd <sup>3+</sup> -DOTA MSNs and Adsorption Control Gd-DOTA MSNs.	115
<b>Figure 4.5.</b> The infrared spectra of the three varying surface densities of pNIPAM, 0.2 mol%, 1 mol% and 2.5 mol%, the parent MSNs and the Adsorption Control compared to pNIPAM polymerised using ATRP.	116
<b>Table 4.2.</b> the hydrodynamic diameters and PDIs obtained by DLS of the pNIPAM external surface functionalised Gd <sup>3+</sup> -DOTA MSNs with theoretical surface densities of 0.2 mol%, 1 mol% and 2.5 mol%.	117
<b>Figure 4.6.</b> Schematic representation of different surface grafting densities of pNIPAM grafted from parent Gd <sup>3+</sup> -DOTA-MSNs (grey spheres, a): b) 0.2 mol%; c) 1 mol%; d) 2.5 mol%, e) Adsorption Control MSNs. Mol% as determined by the grafting density of the initiator, described in Figure 4.3	118
<b>Equation 4.1.</b> Calculating the theoretical molecular weight, $M_w$ .	119
<b>Equation 4.2.</b> Calculating the number average molecular weight.	
<b>Table 4.3.</b> A table providing the calculated theoretical molecular weight, $M_w$ , and the number averaged molar mass, $M_n$ , with the polydispersity obtained	119

by GPC of the calculated 0.2 mol%, 1 mol% and 2.5 mol% equivalent concentrations of BIBB.

**Figure 4.7.** The plot of log of the molecular weight, logM, against normalised  $\text{dwdlogM}$  for the ATRP reactions involving the theoretical BIBB concentrations calculated for the 0.2 mol%, 1 mol% and 2.5 mol% surface functionalised MSNs. 120

**Figure 4.8.** The percentage mass loss obtained by TGA of the three grafting densities, 0.2 mol%, 1 mol% and 2.5 mol%, Adsorption Control, the parent MSNs and pNIPAM versus temperature. 121

**Table 4.4.** The percentage by overall mass of PNIPAM on the 0.2 mol%, 1 mol%, 2.5 mol% pNIPAM surface density functionalised MSNs and Adsorption Control. 122

**Figure 4.9.** The Background normalised  $1/\text{transmittance}$  at 700 nm between 25 °C and 50 °C of 0.2 mol%, 1 mol% and 2.5 mol% MSN surface coverage of pNIPAM against the Adsorption Control and the  $\text{Gd}^{3+}$ -DOTA MSNs. 123

**Figure 4.10.** Photographs of 2.5 mol%, 1 mol%, 0.2 mol%, water and parent Gd-DOTA MSNs at 35 °C and 40 °C. 124

**Figure 4.11.** The plots of  $\text{Gd}^{3+}$  concentration versus water normalised  $R_1$  for A) 0.2 mol%, B) 1 mol% and C) 2.5 mol%. Each sample has three repeats of that sample concentration and  $R_1$  analysis was performed at room temperature. slope is relaxivity according to Equations 3.1 and 3.2 Section 3.5.1 Chapter 3. 126

**Figure 4.12.** A bar chart showing the comparison in relaxivity between  $\text{Gd}^{3+}$ -DOTA MSNs, 0.2 mol%, 1 mol% and 2.5 mol% polymer functionalised  $\text{Gd}^{3+}$ -DOTA MSNs samples at room temperature. 128

**Table 4.5.** The ICP-MS analysis of copper and gadolinium in the samples 0.2 mol%, 1 mol% and 2.5 mol% pNIPAM surface functionalised MSNs, mol% of amine functionalisation with respect to TEOS. 129

**Figure 4.13.** The plots of Cu concentration versus water normalised  $R_1$  for the Cu Control. The three repeats correspond to three separate aliquots of the 129

same batch of MSNs and  $R_1$  analysis was performed at room temperature. slope is relaxivity according to Equations 3.1 and 3.2 Section 3.5.1 Chapter 3.

**Figure 4.14.** Phantom  $T_1$  weighted images obtained by a 3 Tesla MRI scanner of the pNIPAM surface density functionalised MSNs, 2.5 mol%, 1 mol% and 0.2 mol% compared to water and  $Gd^{3+}$ -DOTA MSNs at 35 °C and 40 °C. 131

**Figure 5.1** the chemical structure of the Gal- $\beta$ (1-3)GalNac terminal sugar on the TF antigen. 143

**Figure 5.2.** The reaction mechanism for free radical polymerisation of styrene using AIBN as initiator. 145

**Figure 5.3.** The general reaction mechanism for amide bond formation using EDC-HCl and NHS coupling agents. 146

**Figure 5.4.** A Schematic of the functionalisation method to obtain fluorescent MSNs with NVA/MAA copolymer surface functionalisation using free radical polymerisation. 148

**Table 5.1.** The Hydrodynamic diameter, polydispersity index, PDI, and zeta potential obtained after the key steps in the synthesis of NVA/MAA copolymer surface functionalised MSNs. 149

**Figure 5.5.** The proposed schematic for the variation in zeta potential whilst still having equivalent hydrodynamic diameters obtained by DLS for 0.2 mol% surface functionalised NVA/MAA copolymer and 1 mol% surface functionalised NVA/MAA copolymer. 151

**Figure 5.6.** The TEM images obtained for 0.2 mol% and 1 mol% NVA/MAA copolymer surface functionalised MSNs compared to the Parent MSNs. The diameters of the MSNs were calculated by the mean and standard deviation of 100 MSN diameters. 152

**Table 5.2.** The number average molecular weight,  $M_n$ , obtained by GPC with the polydispersity of the calculated 0.2 % and 1 % concentrations of ACVA. 153

<b>Figure 5.7.</b> The plot of logM against normalised dwdlogM for the free radical polymerisation reactions involving the theoretical ACVA concentrations calculated for the 0.2 % and 1 % surface functionalised MSNs.	153
<b>Figure 5.8.</b> The IR Spectra of the NVA/MAA copolymers obtained using 0.2 % and 1 % concentrations of ACVA initiator.	154
<b>Figure 5.9.</b> The comparison between the IR spectra obtained for 0.2 % and 1 % NVA/MAA copolymer surface functionalised MSN to their respective copolymers and parent MSNs.	155
<b>Figure 5.10.</b> The percentage mass loss against temperature for the NVA/MAA copolymers obtained using 0.2 % and 1 % theoretical concentrations of ACVA compared to the Parent MSNs between 30 °C and 600 °C.	156
<b>Figure 5.11.</b> The percentage mass loss versus temperature of 0.2 % NVA/MAA MSNs and 1 % NVA/MAA MSNs compared to their respective copolymers synthesised in the absence of MSNs and the Parent MSNs.	157
<b>Figure 5.12.</b> The background normalised fluorescence obtained at 528 nm after excitation at 485 nm from serial dilutions from 1.25 mg/mL to 1.22 µg/mL described as a percentage of the fluorescence obtained for the respective MSNs at 1.25 mg/mL after incubation with SW480 cells for 24 hrs and subsequent washes. The results shown are of the Parent Fluorescent MSNs, 0.2 % NVA/MAA MSNs and 1 % NVA/MAA MSNs.	159
<b>Figure 5.13.</b> A schematic of the synthetic steps performed to obtain fluorescent MSNs with NVA/MAA copolymer surface functionalisation using ATRP.	162
<b>Table 5.3.</b> the hydrodynamic diameters and PDIs obtained by DLS with the zeta potentials found for each of the key steps required to synthesise NVA/MAA copolymer surface functionalised MSNs using ATRP with PNA amide bound to the methacrylic acid carboxyl functional group.	163
<b>Figure 5.14.</b> The TEM images of The Parent MSNs compared to the ATRP MSNs and the PNA MSNs.	165

**Figure 5.15.** the IR spectra of the NVA/MAA copolymer using 0.2 % 166  
concentration of initiator by free radical polymerisation and ATRP.

**Figure 5.16.** The IR spectra of NVA/MAA copolymer using 0.2 mol% 167  
equivalent BIBB in the absence of MSNs, 0.2 mol% ATRP NVA/MAA  
surface functionalised MSNs and PNA bound 0.2 mol% NVA/MAA surface  
functionalised MSNs compared to Parent MSNs.

**Figure 5.17.** The percentage mass loss versus temperature for the 0.2 % 168  
NVA/MAA copolymer obtained using ATRP in the absence of MSNs  
compared to the 0.2 % and 1 % NVA/MAA copolymer obtained by free  
radical polymerisation.

**Figure 5.18.** The percentage mass loss versus temperature for PNA MSNs 169  
compared to PNVA/MAA MSNs, PNVA/MAA synthesised in the absence  
of MSNs and the PNA Adsorption Control.



## **Abstract**

The survival rate of previously incurable diseases in the modern era is staggering due to the rapid advancement of pharmaceutical chemistry and our understanding of the human body. However, one limitation which is still prevalent is the ability to correctly diagnose the disease in its early stages. The clear correlation between successful medical treatments and early disease diagnosis has led to numerous analytical methods being developed. Magnetic resonance imaging, MRI, has come to the fore in this field due to it being a versatile high-resolution non-invasive technique with no radiation exposure to the patient required. Considerable focus is now being applied to the development of contrast agents that can be administered to further aid diagnosis. This research has led to gadolinium-based contrast agents, GBCAs. However, the indiscriminate interactions of previous clinically used GBCAs and the emergence of gadolinium deposits in the tissues of patients after multiple scans has resulted in increased demand for MRI contrast agents with higher specificity and lower dosages. Mesoporous silica nanoparticles, MSNs, have been shown to excel in this field due to its high surface area, facile functionalisation, and low toxicity. The application of MSNs as an MRI contrast agent could therefore result in earlier diagnosis of patients and consequently less global deaths from treatable diseases (**Chapter 1**). So, the optimisation of the MSN structure to be utilised as a GBCA is performed by variation of the pore diameter and gadolinium ion chelate location to obtain the highest amount of contrast with the minimum dosage of gadolinium (**Chapter 3**). Following this investigation, the possibilities of stimuli interactive GBCAs are pursued by the formation of a polymer/MSN hybrid system which can change its properties depending on the temperature of the surrounding environment. This response is explored further by observing the tuneability of the interaction by varying the grafting density and length of the MSN bound polymer (**Chapter 4**). Finally, polymer/MSNs hybrid systems are investigated to allow for specific binding interactions to occur between the system and colorectal cancer cells. This begins with research into how to remove indiscriminate interactions between GBCAs and neighbouring cells. Then, having achieved this, a lectin able to differentiate between healthy and cancerous rectal cells was chemically attached to the MSN bound polymer and shown to highlight colorectal cancer cells by retention of their specific intermolecular interactions. The non-toxicity of the polymer/MSN system was confirmed *in-vitro* (**Chapter 5**).

# Chapter 1

## 1. Introduction

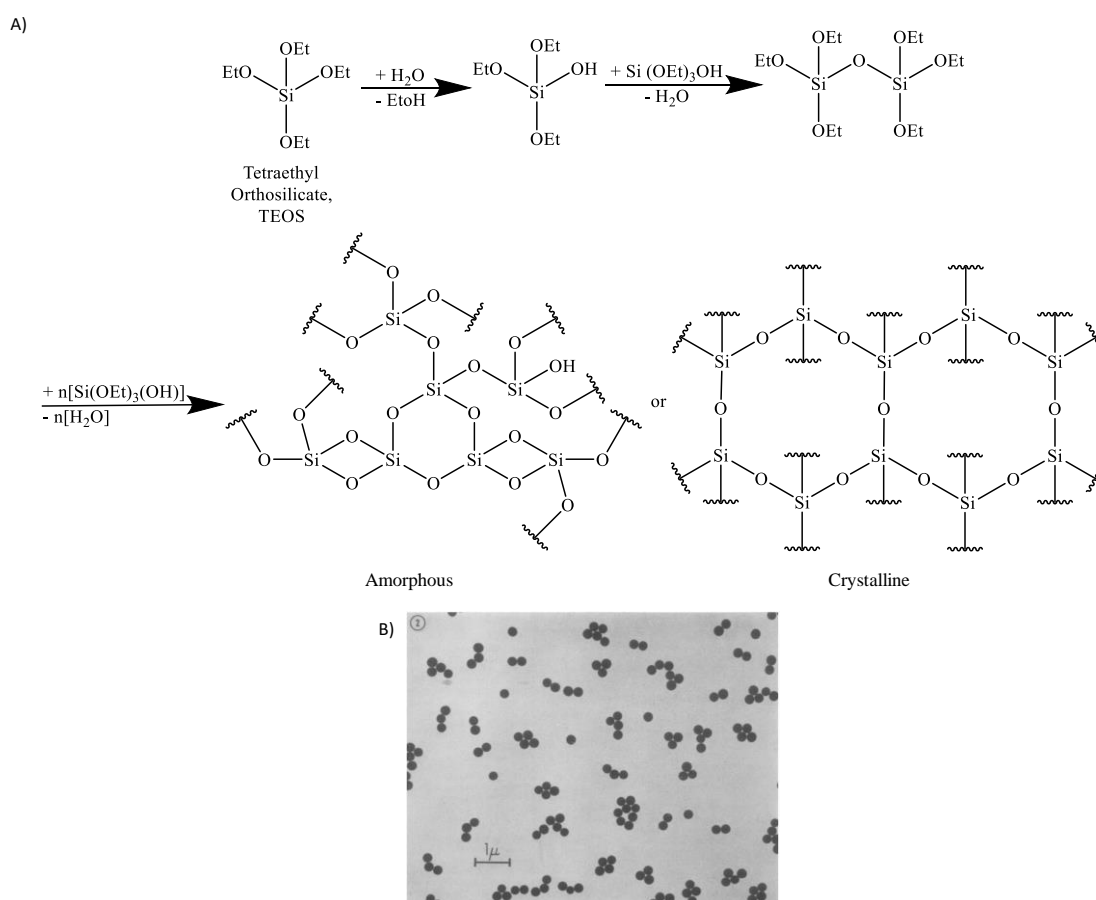
---

### 1.1 Summary

Nanomaterials have seen a burst of research in recent years, thanks to their unique size dependent properties such as high surface area, high loading capacities and strength density.<sup>1</sup> These have made nanomaterials ideal candidates to a wide range of applications of electronics,<sup>2</sup> civil engineering,<sup>3</sup> agriculture,<sup>4</sup> cosmetic<sup>5</sup> and catalysis.<sup>6</sup> An application where nanomaterials have really progressed is in medicine where there has been extensive research of nanomaterials in long life medical implants and drug delivery.<sup>7</sup> Silica nanomaterials have come to the fore in the medical field due to its biocompatibility, ease of synthesis and functionalisation.<sup>8</sup> Silica has a lattice structure based on a tetrahedron where silicon is in the centre surrounded by four oxygen atoms.<sup>9</sup> An advantage of silica lattice structure is the high adaptability to its overall structure allowing multiple bespoke morphologies to be synthesised.<sup>10</sup>

## 1.2 Silica Nanoparticles, SiNPs

Silica nanostructures were described by Stöber *et al.* in the seminal 1968 paper, which described a robust method of synthesising silica spheres in the nano-micron size regime.<sup>11</sup> In this silica spheres were prepared by adding tetra alkyl silicates to basic solution of ammonia and an alcohol/aqueous solvent system. The reaction proceeded through the hydrolysis of the tetra alkyl silicate and condensation of the subsequent silicic acids (*Figure 1.1*).



*Figure 1.1. A) The hydrolysis of tetra alkyl silicates (tetraethyl silicate, TEOS) and the condensation of the subsequent silicic acid molecules to form silica. B) Electron micrograph of a sample of silica spheres obtained by Stöber *et al.*<sup>11</sup>*

The reaction conditions were basic pH with only agitation required. The reaction completed with most variants within an hour, with some only taking 15 minutes. The progress of the reaction being easily observed by the solution becoming increasingly opalescent. It was also proven how scalable the reaction was by performing the

reaction with 2 litres of solution and obtaining the same silica spheres obtained with the 80 mL reaction.

The adaptability of this procedure has been investigated by changing the solvent system and alkyl silicate.<sup>11-13</sup> These were found to change the rate of reaction and the particle diameters of the silica spheres obtained, the particle diameter increasing from 0.05  $\mu\text{m}$  to 2  $\mu\text{m}$ . The robustness of this procedure has been investigated by even performing the reaction in space.<sup>14</sup> Thus proving the ease of formation and control of silica nanoparticle structure that can be obtained.

### 1.2.1 Mesoporous Silica

Porosity in nanostructures is an incredibly desirable property due to the large increase surface area that porosity provides.<sup>15</sup> This results in porous nanomaterials having greater surface interactions between the surrounding molecules and the nanomaterial. There are numerous sizes of pore diameter that can be utilised. Nanomaterials with pores  $< 100$  nm are defined as nanopores, mesopores are between 2 nm and 50 nm and micropores are  $< 2$  nm.<sup>16</sup> As the approximate size calculated using mean bond lengths and bond angles of a water molecule, the standard biological solvent, is around 2.75 Å micropores significantly restricts the flow of water into the nanoparticle. This restriction inhibits interaction between molecules and the core of the pores. The opposite is the case with nanopores where there is no inhibition of molecules flowing through the nanoparticle. However, the size of the pores has inherently reduced the amount of surface area that molecules can interact with. Mesoporosity sits in a goldilocks zone where the pores are large enough that they allow facile flow of molecules through the nanoparticle whilst minimising the amount of surface area lost to allow this to occur.

In 1992, Kresge *et al.* published a paper on a new family of ordered mesoporous silica molecular sieves.<sup>17, 18</sup> The desirability of these structures comes from the increased surface area ( $\geq 1000$  m<sup>2</sup>/g) obtained which allows for greater interaction between molecules and the structure enhancing properties like catalytic activity and adsorptive capacity. In this paper the synthesis of this new family, named M41S, is described with emphasis on one member, MCM-41. In the synthetic protocol quaternary ammonium surfactant salts were utilised to provide the porosity. The proposed theory is the liquid crystal templating mechanism, whereby the surfactant forms a liquid

crystal structure in the water solvent, which the inorganic silicate present can form around to produce the observed porous inorganic structure (*Pathway 1 of Figure 1.2*). This mechanism conforms with the aggregation of quaternary ammonium surfactant salts in water, as hexagonal arrangements are observed in both.<sup>19, 20</sup> Another possible mechanistic pathway involves the silicate influencing the formation of the liquid-crystal phase (*Pathway 2 of Figure 1.2*). The subsequent growth of the mesoporous silica structure may be due to nucleation by the initial structure<sup>21</sup> or assembly of several substructures.<sup>22</sup> The surfactant can be removed from the mesoporous silica structure by calcination.

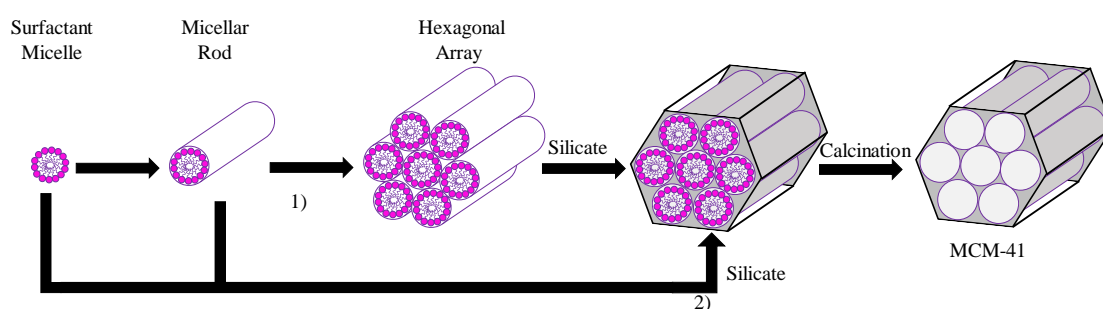


Figure 1.2. Possible mechanistic pathways for the formation of MCM-41: 1) liquid crystal phase initiated and 2) silicate anion initiated.<sup>17, 18</sup>

Kresge *et al.* pursued this investigation further by utilising surfactants with varying carbon chain lengths.<sup>17, 18</sup> It was observed that lowering the carbon chain length of the surfactant obtained smaller pore diameters (pore diameter of 18 Å for 8 Cs compared to 37 Å for 16 Cs). Also, the addition of an organic solvent, in this case 1,3,5-trimethylbenzene, was found to increase pore diameter if added at the start of the synthesis. This is due to the swelling of the hydrophobic interiors of the micelles increasing the micelle diameter (*Figure 1.3*).<sup>23</sup> Both these findings strongly suggesting the validity of the liquid crystal template mechanism proposed and the versatility of the synthetic protocol described.

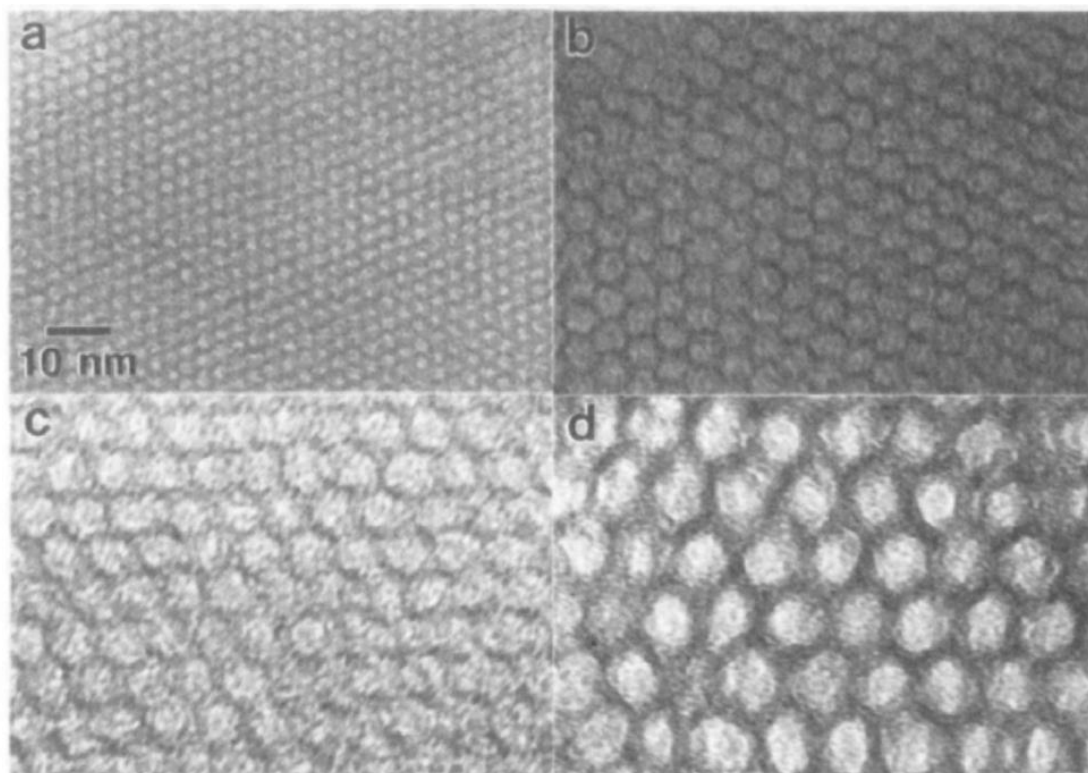


Figure 1.3. Transmission electron micrographs of several MCM-41 materials having a pore size of a) 20, b) 40, c) 65 and d) 100 Å.<sup>17</sup>

The acquisition of a porous structure using surfactants is defined as an endotemplate method or soft matter templating. In exotemplating methods or hard templating a porous solid is used as the template instead of the surfactant which is subsequently cured. This provides a negative image porous structure compared to the template.<sup>24</sup> Exotemplating was used by Zhao *et al.* to extend the family of highly ordered mesoporous structures by synthesising Santa Barbara Amorphous (SBA) materials.<sup>25</sup> In particular, SBA-15 which was synthesised using the triblock copolymer of poly (ethylene oxide)-poly(propylene oxide)-poly(ethylene oxide). The advantage of exotemplating is that reproducibility between nanoparticles can be more easily obtained due to the rigid nature of the template allowing for more precise dimensions. However, the separation of the template from the nanoparticles is more likely to cause damage to the nanoparticle structure due to the harsher conditions required. Endotemplates require softer methods of template removal, but the template is formed in the reaction allowing for less control over the resulting nanoparticle structure.<sup>26</sup>

### 1.2.2 Mesoporous Silica Nanoparticle, MSN, Synthesis

The simple process to obtain mesoporous silica described by Kresge *et al.* was pursued in many directions, especially in the field of catalysis.<sup>27-32</sup> In 1997, Grün *et al.* published a paper that combined the Stöber synthesis with the synthesis of MCM-41 to make the first spherical MSNs.<sup>33</sup> This combining of protocols was performed simply by adding a quaternary ammonium surfactant salt, in this case *n*-hexadecyltrimethylammonium bromide, CTAB, or *n*-hexadecylpyridinium bromide (Figure 1.4), to an otherwise identical solution described previously by Stöber of TEOS and ammonia in ethanol.

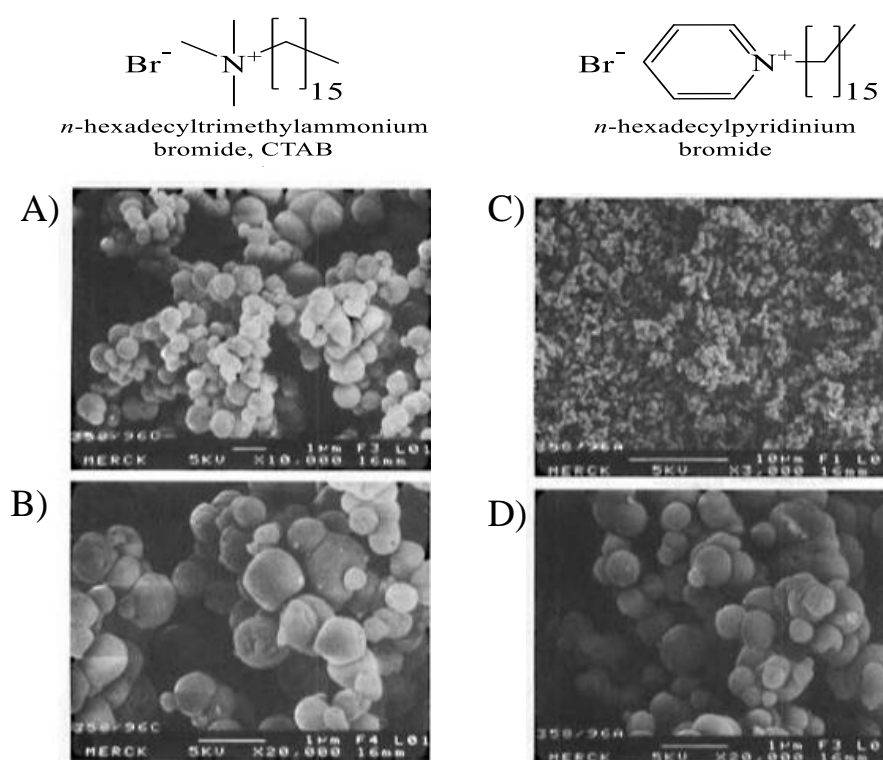


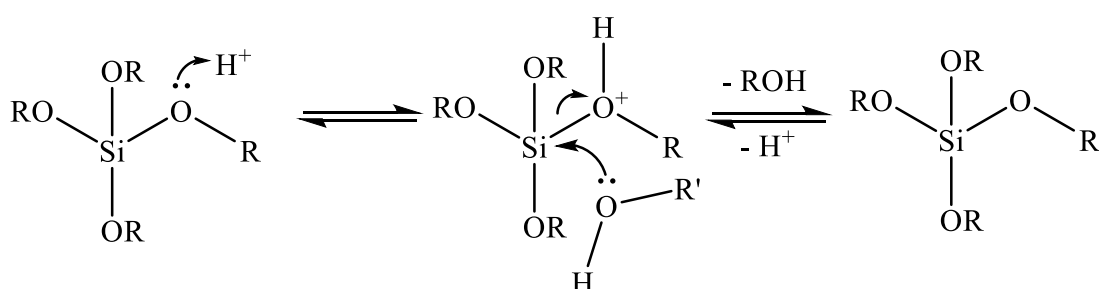
Figure 1.4. The quaternary ammonium surfactant salts utilised to investigate mesoporosity of MCM 41 particles with scanning electron microscopy, SEM, images of A, B) MSNs obtained using CTAB and C, D) MSNs obtained using *n*-hexadecylpyridinium bromide by Grün *et al.*<sup>33</sup>

Then the surfactant was removed from the pores by calcination in the work up. This yielded spherical MCM-41 particles which were essentially the same as silica spheres synthesised previously by Stöber *et al.*, but with the additional property of having pores of diameter 3.14 nm using CTAB as a template and 3.05 nm using *n*-hexadecylpyridinium bromide. The only other property affected by the variation in

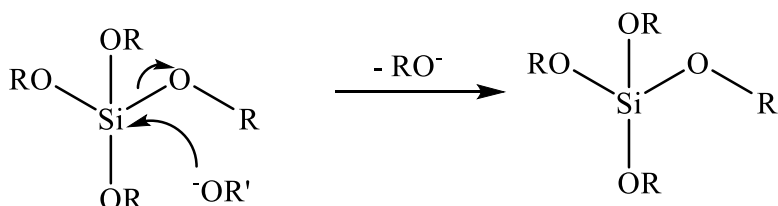
surfactant in this investigation was the *n*-hexadecylpyridinium bromide promoted greater long-range order and homogeneity of pores.

Since the first published synthesis of MSNs there has been a tremendous amount of research in adaptations to this protocol to obtain MSNs with tailored properties to suit their application.<sup>34</sup> For example changing the pH of the reaction affects particle formation time, structural order and particle size by changing rates of hydrolysis and condensation of silane. This is due to the hydrolysis and condensation of the Si-OR bond in silanes being catalysed by acidic or basic conditions (*Figure 1.5*).

#### Acid Catalysed Hydrolysis/Condensation



#### Base Catalysed Hydrolysis/Condensation



R= alkyl chain and R' = H [Hydrolysis] or  $\text{Si(OR)}_3$  [Condensation]

*Figure 1.5. The mechanisms for acid and base catalysed hydrolysis/condensation of alkyl silanes.*


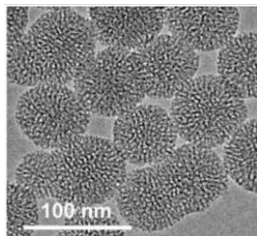
The basic catalysed hydrolysis/condensation reaction has a rate of reaction which is parallel to the charge density. The rate of hydrolysis/condensation plateaus at pH 7.5 and then decreases due to the gradual instability of silica at high pH. However, the addition of a cationic surfactant allows for the rate of hydrolysis/condensation to continue increasing up to pH 10.5. This is because of the strong interaction between the silicate and the surfactant having a stabilisation effect up to a pH 12. This pH dependence has allowed for fast pH-changing methods of MSN synthesis to be developed.<sup>35</sup> Fowler *et al.* started the synthesis of MSNs using an alkaline solution, followed by neutralisation to significantly decrease the reaction rate.<sup>36</sup> This introduced



mesoscopic order and control of the nanoparticle diameter. Mesoporous silica nanorods as well as hexagonal MSNs are also able to be synthesised by varying the pH.<sup>37, 38</sup>

The variation of the base used has been investigated, for example Möller *et al.* substituted ammonia for triethanolamine, TEA.<sup>39</sup> The use of TEA resulted in colloidally stable MSNs with worm-like pores due to TEA acting as a complexing agent for the silicate. Variation in TEA concentration also facilitated the synthesis of MSNs between 50 – 100 nm with high yield because of TEA encapsulating the MSNs, limiting growth as well as aggregate formation. In addition, Möller *et al.* describe a different extraction method of the ammonium surfactant salt from calcination. This method simply uses an acidified ethanol solution and sonification. Application of this method resulted in successful removal of the surfactant template without the use of high temperatures. Other methods have been investigated also to remove the surfactant from the pores of the nanoparticles such as dialysis.<sup>40</sup>

Before the use of TEA the principal method for obtaining MSNs in the 50 – 100 nm size range involved very high dilutions. Rathosky *et al.* obtained MSNs of 100 nm using 1:5300 dilution of sodium metasilicate/ water.<sup>41</sup> Ostafin *et al.* obtained MSNs of 70 nm using a molar ratio of TEOS/solvent of 1:4000 and 60 nm with molar ratio of 1:1500 respectively.<sup>42</sup> 30 nm MSNs were obtained using a molar ratio of 1:2600<sup>35</sup> and 60- 140 nm MSNs using 1:1200 by Cai *et al.*<sup>38</sup> Finally Mann *et al.* created a highly versatile MSN synthetic protocol using an approximate molar ratio of 1:900.<sup>36</sup> The main drawback of these previous very dilute protocols is the scalability, the low yields and/or the difficult isolation procedures to obtain the MSNs. Whereas Möller *et al.* using TEA was able to lower the molar ratio of TEOS/water to 1:120, minimising the amount of solvent required. Other stabilising reagents have been researched to obtain colloidally stable 50 - 100 nanometre MSNs such as polyvinyl pyrrolidone (average Mw = 10,000 g/mol), PVP<sup>43</sup>, L-lysine<sup>44</sup> and Pluronic F127, EO<sub>106</sub>PO<sub>60</sub>EO<sub>106</sub><sup>45, 46</sup> (Figure 1.6).



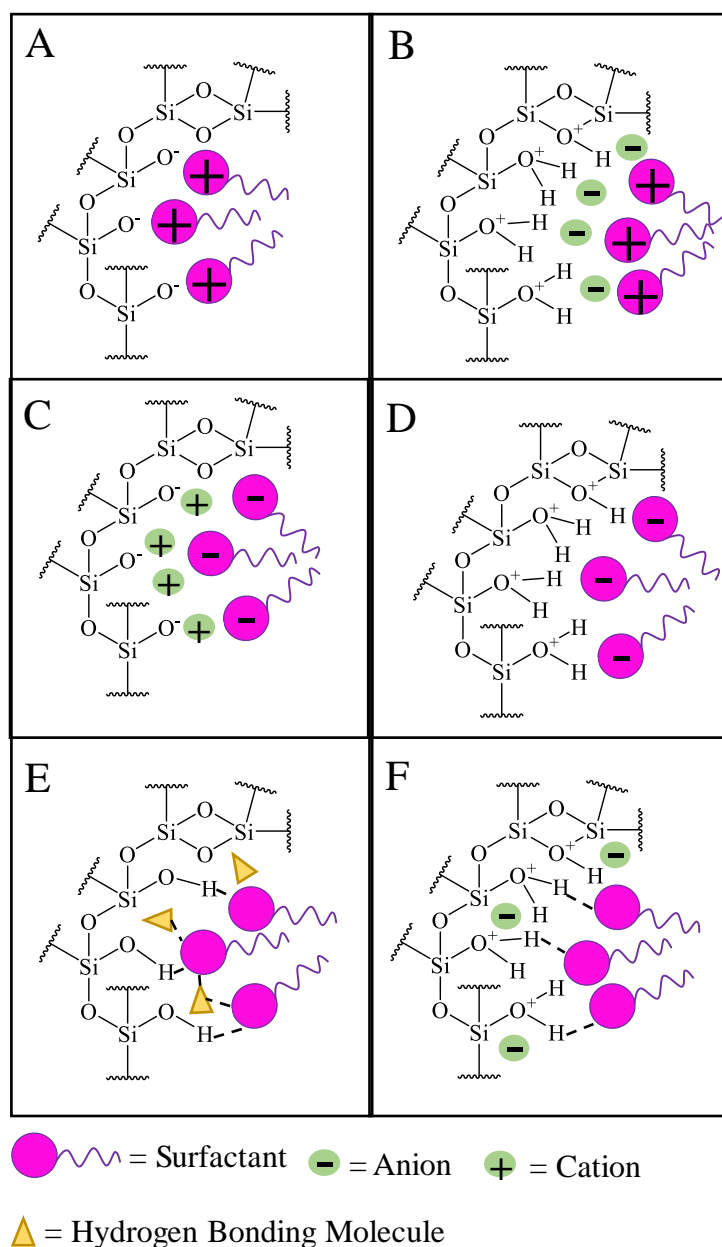


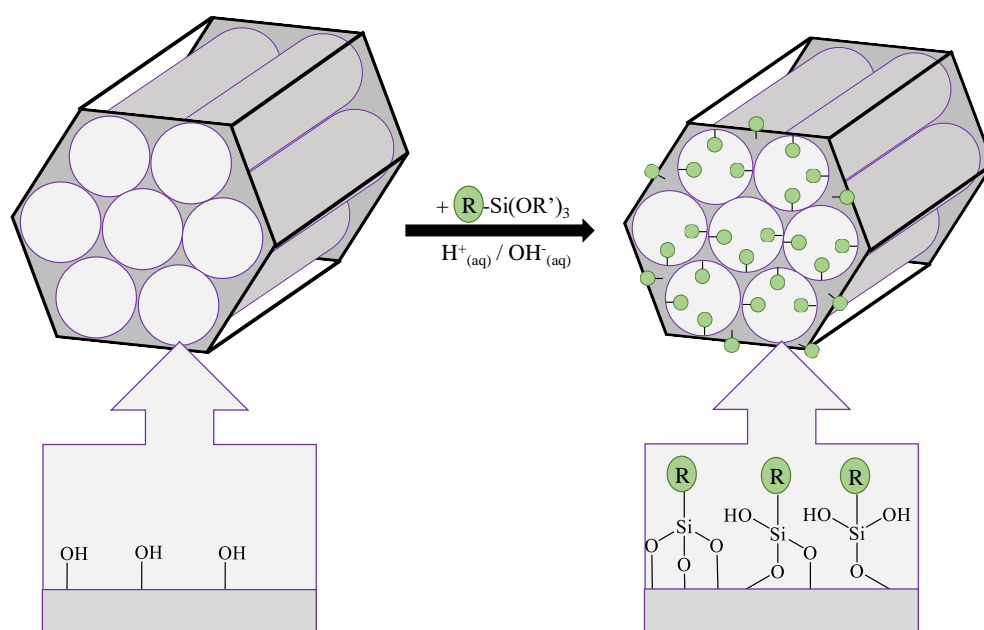
Figure 1.7. Interactions between the inorganic silicate network and the head group of the surfactant with consideration of the possible synthetic pathways in acidic, basic or neutral media. A) Cationic surfactant in basic media, B) cationic surfactant in acidic media, C) anionic surfactant in basic media, D) anionic surfactant in acidic media, E) neutral surfactant in neutral media and F) neutral surfactant in acidic media.<sup>31</sup>

MSNs with dual pore diameters have been investigated by Niu *et al.*<sup>51</sup> This was achieved by the utilisation of an amphiphilic block copolymer, polystyrene-*b*-poly(acrylic) acid, PS-*b*-PAA, and CTAB as co-templates. In aqueous ammonia conditions the PS-*b*-PAA forms rod-like aggregates that coupled with the CTAB

micelles due to the electrostatic interaction between the  $\text{PAA}^-$  and the  $\text{CTA}^+$  molecules.

### 1.2.3 Surface Functionalisation of MSNs

In addition to the ease of MSNs synthesis, another advantage is facile and versatile methods of functionalisation. These methods fall into three pathways, 1) post-synthetic modification or grafting, 2) co-condensation and 3) periodic mesoporous organo-silicas, (PMOs), production.<sup>52, 53</sup> Grafting involves the modification of the MSN after its synthesis with silica phases with organic functional groups. This method in general uses an organosilane in the form of  $(\text{R}'\text{O})_3\text{SiR}$ , chlorosilanes  $\text{Cl}_3\text{SiR}$  or silazanes  $\text{HN}(\text{SiR}_3)_2$ . These react with the free silanol groups on the pore surfaces (*Figure 1.8*).

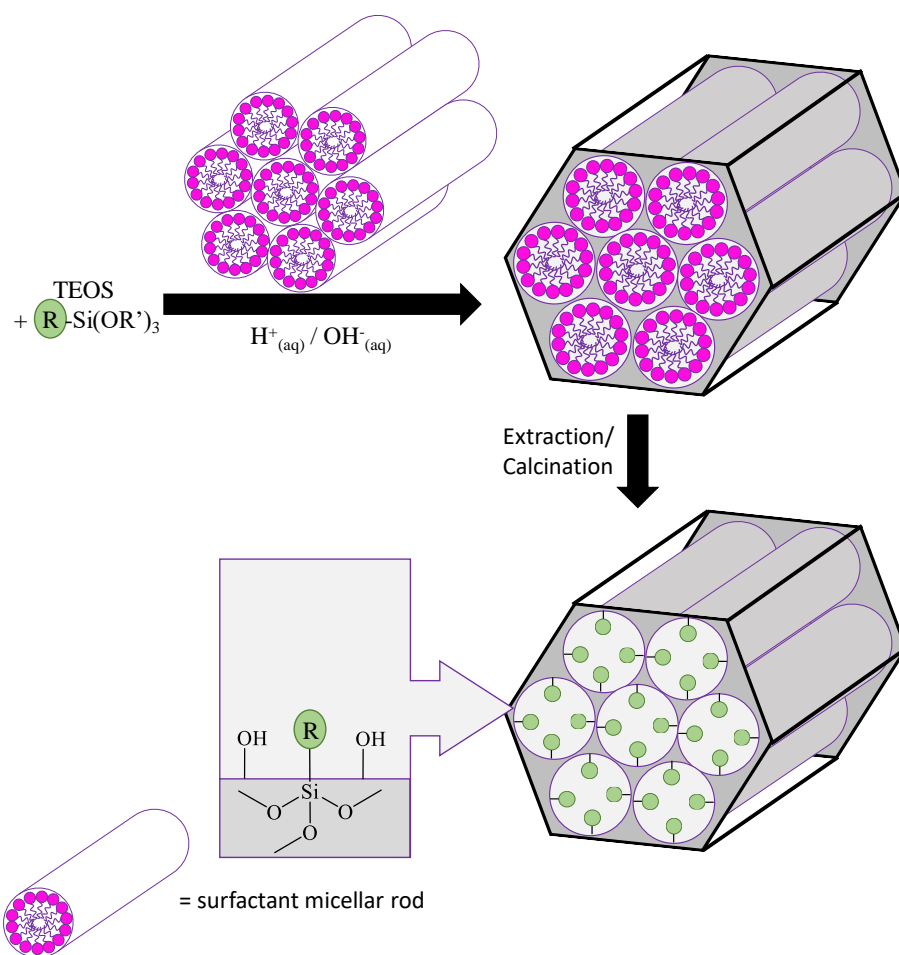


*Figure 1.8. Grafting (post-synthetic modification) for organic modification of MSNs with terminal organosilanes of the type  $(\text{R}'\text{O})_3\text{SiR}$ .  $\text{R}$  = organic functional group and  $\text{R}'$  = alkyl chain.<sup>54</sup>*

Using the grafting method, a wide variety of organic groups can be added to the MSNs such as amino or aminopropyl groups,<sup>55-61</sup> diamino,<sup>62, 63</sup> triamino,<sup>63</sup> ethylenediamine,<sup>64</sup> malonamide,<sup>65</sup> carboxy,<sup>57, 60</sup> thiol,<sup>55, 59, 66</sup> 1-allyl,<sup>67</sup>  $\alpha$ -benzoyl-3-propylthiourea,<sup>68, 69</sup> dithiocarbamate,<sup>70</sup> imidazole groups<sup>71-73</sup> as well as saccharides.<sup>74</sup> Another advantage

of the grafting method is that the mesostructure of the MSN is usually retained. However, depending on the mol% of organic residue added to the MSN, there is a possibility of reduction in the porosity of the subsequent hybrid material, leading to pore closure at high mol%.<sup>54</sup> Also, organosilanes react preferentially to the surface or inside channels near the channel openings of the nanoparticle, resulting in a heterogenous distribution of the organic functional groups and can be detrimental to the diffusion of further molecules, lowering occupation.<sup>75</sup>

Co-condensation is a one pot synthetic method where organosilane is reacted with the tetralkyl silicate forming the MSNs before completion of the reaction. This results in organic residues anchored covalently inside the pore walls (*Figure 1.9*).



*Figure 1.9. Co-condensation method (direct synthesis for the organic modification of MSNs with terminal organosilanes of the type  $(R'O)_3SiR$ . R = organic functional group and  $R'$  = alkyl chain.<sup>54</sup>*

The advantage of co-condensation is that pore blocking is less likely to occur than with grafting because the organic functionalities are incorporated directly into the

silica matrix in the presence of the template. However, a degree of structural integrity is lost with increasing concentration of the organosilane, resulting in high mol% with complete structural disorder.<sup>76</sup> Therefore, organic functionalisation generally does not exceed 40 mol%.<sup>54</sup> Also, the amount of organic functionalisation incorporated into the MSNs is lower than for grafting compared to the amount of added.<sup>54</sup> This is due to uncontrolled homo-condensation of the organosilanes occurring at the cost of cross-linking co-condensation reactions with the silica precursors. Finally, for more complex organic functionalisation, the extraction method for the removal of the surfactant template needs to be carefully considered as calcination may not be appropriate. The versatility of the functional groups able to be bound to MSNs using co-condensation is vast. Using the respective organosilanes, alkyl,<sup>77, 78</sup> thiol,<sup>78-82</sup> amino,<sup>76, 79, 82-87</sup> cyano/isocyano,<sup>76, 83, 88</sup> vinyl/allyl,<sup>75, 76, 78, 79, 82, 89-91</sup> organophosphines,<sup>88, 92</sup> alkoxy<sup>79</sup> and aromatic groups<sup>77, 79, 82, 88, 93, 94</sup> have all been successfully bound to MSNs. This method as well as post-synthetic modification makes the functional groups accessible not just limited to the organic functional groups present in organosilanes. Once these functional groups have been bound to MSNs the functional groups can be chemically altered as they would following standard chemical techniques. For example, Asefa *et al.* have successfully transformed silica bound vinyl groups in to alcohols *via* hydroboration, the corresponding diols by epoxidation and bromide addition *via* bromination.<sup>95</sup> Silica thiols have been transformed to sulfonic acid,<sup>96-99</sup> in particular Stucky *et al.* who performed the oxidation of the thiol *in situ* to the co-condensation reaction with addition of H<sub>2</sub>O<sub>2</sub>.<sup>100</sup> Also 2-cyanoethyl-functionalised MSNs can be converted to their respective carboxylic acid by careful hydrolysis with H<sub>2</sub>SO<sub>4</sub><sup>101</sup> and phosphoric acids functionalisation by ester hydrolysis of diethyl phosphonate.<sup>102</sup>

PMOs were first synthesised in 1999.<sup>103-105</sup> PMOs are organic-inorganic hybrid materials which are synthesised by hydrolysis and condensation reactions of organosilica precursors of the type (R'O)<sub>3</sub>Si-R-Si(R'O)<sub>3</sub>. R groups that have been successfully converted into PMOs are alkyl chains where C = 1 and 2<sup>103-107</sup> and aromatic groups<sup>106, 108-115</sup> and R' is an alkyl chain, in the presence of a surfactant. Unlike post-synthetic modification and co-condensation, the organic unit is incorporated via covalent bonds into the three-dimensional framework of the MSN. This leads to complete homogeneity of the MSN functionality (*Figure 1.10*).

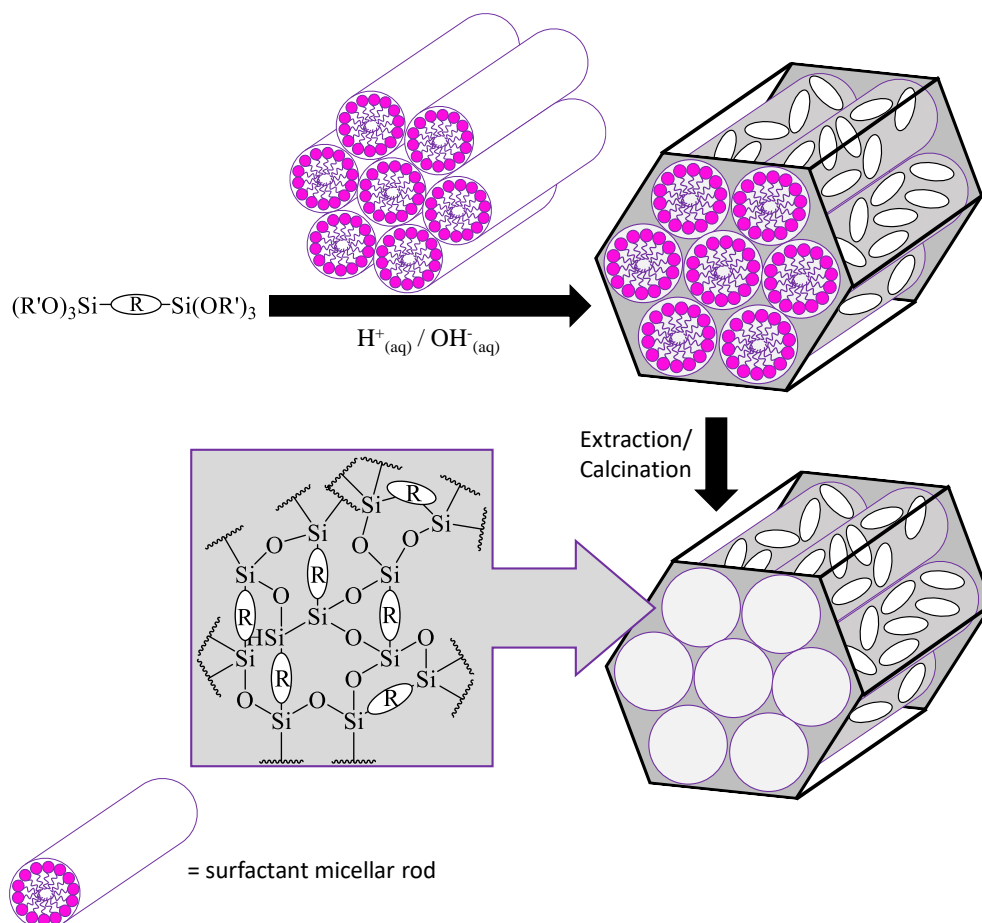


Figure 1.10. General synthetic pathway for PMOs that are constructed from bis-silylated organic bridging units.  $R$  = organic bridge,  $R'$  = alkyl chain.<sup>54</sup>

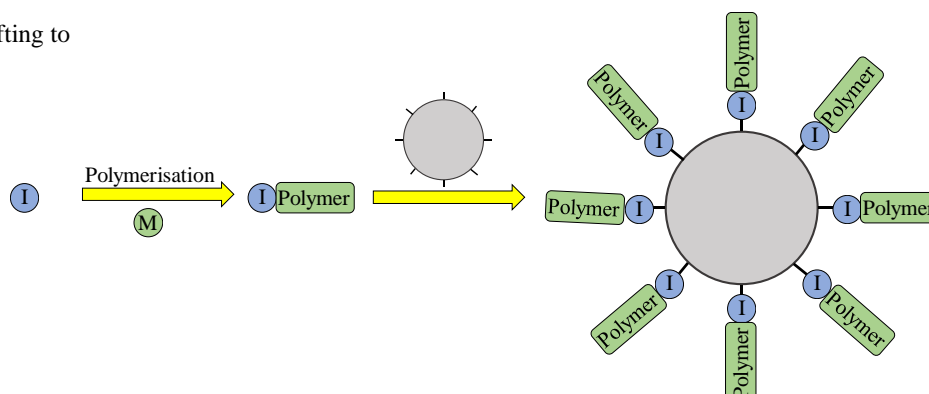
The advantages of PMOs is there large inner surface areas of up to  $1800 \text{ m}^2 \text{ g}^{-1}$ , high thermal stability, periodically organised pore systems and very narrow pore radius distributions.<sup>54</sup> The key disadvantage being that grafting has to be performed after PMO synthesis in order to perform further surface modification.

### 1.2.4 Polymer Modification of MSN Surfaces

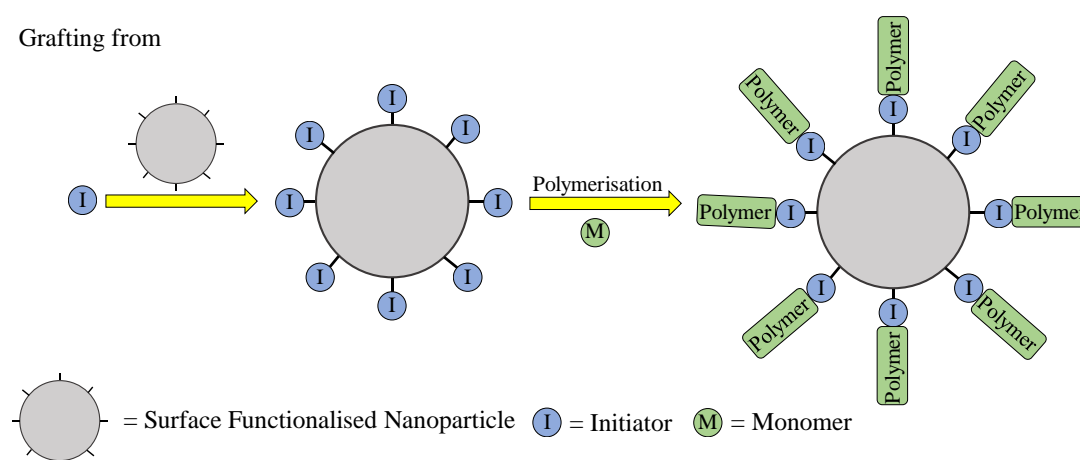
The functionalisation of MSNs with polymers has become a popular method to change or add desirable physical properties.<sup>116</sup> These properties can range from biological inertness by pegylation<sup>117</sup>, to allowing the MSN to react to external stimuli.<sup>118-120</sup> There are two methods to nanoparticle surface polymer functionalisation, ‘grafting to’ and ‘grafting from’. The ‘grafting to’ method requires an end-functionalised polymer reacting to or adsorbing onto the nanoparticle surface. Due to being able to fully characterise each component prior nanoparticle assembly this method allows for increased polymerisation reaction control resulting in more uniform polymer chain

lengths being obtained.<sup>121</sup> In the ‘grafting from’ method the polymer chains are grown from a nanoparticle that has an initiator bound to the surface (*Figure 1.11*).<sup>122-125</sup>

Grafting to



Grafting from



*Figure 1.11. Schematic description of ‘Grafting to’ and ‘Grafting from’ approaches for the synthesis of polymer surface functionalisation of nanoparticles.*

The ‘grafting from’ method obtains a higher percentage of grafting density onto the surfaces of the nanoparticle.<sup>116, 121</sup> However, control of polymer chain length is more challenging as observing the amount of initiator successfully bound to the nanoparticle is non-trivial and the amount of initiator in the polymerisation directly effects polymer chain length. There is no limitation in the mechanism of polymerisation which can be used for ‘grafting from’, with radical, anionic, cationic and living polymerisation having previously been utilised to immobilise polymers onto a range of different surfaces.<sup>126, 127</sup>

Hsin-Lien *et al.* successfully applied the ‘grafting to’ method of polymer functionalisation to obtain thermosensitive silica coated iron oxide nanoparticles.<sup>128</sup> This was achieved by polymerising N-isopropylacrylamide (NIPAM) with azobisisobutyronitrile, as the initiator. The resulting poly(N-isopropylacrylamide),



pNIPAM, was then incubated with silica-coated iron oxide nanoparticles, to allow the pNIPAM to adsorb to the silica surface. The thermosensitive nature was confirmed, and further investigation involved the analysis of different silica coating thickness on the iron oxide nanoparticles. The thermoresponsive nature of the pNIPAM functionalised nanoparticles varied with the thickest silica coating aggregating at the highest temperature observed 36 °C, and the lowest weight ratio obtaining the lowest at 34 °C. Zhu *et al.* also used the adsorption of polymer chains in a ‘grafting to’ methodology to obtain zwitterionic polymer-coated MSNs to promote stability in complex media and reduce protein fouling.<sup>129</sup> The polymerisation was performed using L-3, 4-dihydroxyphenylalanine, DOPA, bromide as the initiator and carboxybetaine methacrylate, CBMA, monomer, to obtain the polymer DOPA-pCBMA. This was then incubated with MSNs causing adsorption of the DOPA-pCBMA via the surface adhesive catechol residue group. The DOPA-pCBMA MSNs were analysed for their fouling resistance capabilities and then, due to the free carboxyl groups in pCBMA, were Arginylglycylaspartic acid, RGD, protein functionalised and analysed for their uptake by cells. Whereas Yang *et al.* used a ‘grafting from’ to obtain pNIPAM functionalised MSNs.<sup>118</sup> These were obtained by post synthetic amine modification of fluorescent MSNs. These amine groups were then reacted with 2-bromoisobutyryl bromide, BIBB to form amide bonds. The polymerisation of NIPAM occurred using the MSN bound BIBB as the initiator. The subsequent pNIPAM-MSNs exhibited an aggregation response at 35 °C. Further investigations analysed the uptake and cytotoxicity of these nanoparticles with MCF-7 cancer cells. It was observed at 37 °C the nanoparticles were uptaken by the cancer cells and that the nanoparticles had a negligible effect on cell growth.

### 1.2.5 SiNP Toxicity

There have been numerous investigations into the toxicity and biocompatibility of MSNs. Yu *et al.* investigated silica toxicity on a cellular level with macrophages, lung carcinoma cells and human erythrocytes.<sup>130</sup> Eight sets of silica nanoparticles, SiNPs, were synthesised, non-porous SiNPs (115 nm), MSNs (120 nm), mesoporous silica nanorods with aspect ratio 2, mesoporous silica nanorods with aspect ratio 4, mesoporous silica nanorods aspect ratio 8 and finally the aminated counterparts of each variant. The quantitative association of SiO<sub>2</sub> to the cells under investigation was obtained using inductively couple plasma mass spectrometry (ICP-MS). Association

was found to increase in the order: MSNs (aspect ratio 1, 2, 4, 8) < aminated MSNs (aspect ratio 1, 2, 4, 8) < aminated non-porous SiNPs < non-porous SiNPs. The amount of association was directly linked to plasma membrane damage. This trend agreed with previous research which found the addition of porosity reducing toxicity.<sup>131-134</sup> This was due to the high silanol groups on the external surface of non-porous SiNPs being accessible to the cell membrane, causing higher cellular impact. The addition of cationic functional groups like amine groups to MSNs increasing cellular uptake was also confirmed using cervical cancer cells.<sup>135</sup> In addition, it was confirmed that below 100 µg/mL there was no haemolytic toxicity observed for any of the MSNs or mesoporous silica nanorod variants. The effect of surface charge was pursued further, the results confirming an increased immune response and cytotoxicity with cationic surface charge compared to anionic and neutral, but were advantageous for trans vascular transport in tumours, neutral having the longest circulation times and interstitial transports in tumours.<sup>136, 137</sup>

Nabeshi *et al.* have investigated the relationship between SiNP diameter and toxicity both *in vivo* and *in vitro*.<sup>138</sup> SiNPs with particle diameters ranging from 70 to 1000 nm were investigated to observe their skin and nuclear penetration. It was found that the SiNPs with a diameter of 70 nm penetrated the skin barrier and exerted various negative biological effects in both the regional and systemic level, such as DNA fragmentation. Rancan *et al.* also investigated MSNs skin penetration properties.<sup>139</sup> the size dependent manner was confirmed with amorphous silica nanoparticles ranging from  $42 \pm 3$  nm to  $291 \pm 9$  nm. SiNPs of diameter >75 nm were found to be blocked from penetrating by the skin. Making the SiNP surface positively charged was also found to increase cellular uptake.

This cellular uptake below 100 nm is however a desirable property for drug delivery. Awaad *et al.* investigated the uptake of fluorescent organosilica particles of varying particle diameters by the small intestine.<sup>140</sup> The Peyer's Patches ,PPs, small masses of lymphatic tissue in the small intestine, were focussed on.<sup>141</sup> The diameters investigated were 95 nm, 110 nm, 130 nm, 200 nm, 340 nm, 695 nm and 1050 nm. Quantitative analysis showed that within this range of diameters investigated the optimal was 95 nm, which had 124.0 % fluorescent areas of the PPs with respect to 110 nm. With 130 nm, 200 nm, 340 nm, 695 nm and 1050 nm having 110 nm respective fluorescent areas of 89.1 %, 73.8 %, 20.2 %, 9.2 % and 0.5 % respectively.

Additionally, two novel pathways through the PPs were observed, transcellular, through the cells, and paracellular, between cells. Mou *et al.* investigated cellular uptake further with MSN and Hela cells.<sup>142</sup> The trend between size dependence and cellular uptake was found to be 50 nm > 30 nm > 110 nm > 280 nm > 170 nm. The optimal particle diameter of ~50 nm observed was consistent with other previous research using different nanoparticles on the size dependence of cellular uptake.<sup>143, 144</sup>

Despite Yu *et al.* finding no toxicity difference between MSNs and mesoporous silica nanorods of various aspect ratios, their organ distribution after administration *in vivo* differ.<sup>130</sup> Huang *et al.* investigated the distribution of intravenously administered fluorescent mesoporous silica nanorods with aspect ratios of 1.5 and 5 as well as pegylated mesoporous silica nanorods into mice after 2 hrs.<sup>145</sup> >80 % of all types of silica nanorods were found in the liver, spleen and lung of various ratios depending on nanorod aspect ratio and pegylation. The 1.5-aspect ratio mesoporous silica nanorods were primarily observed in the liver whereas the 5-aspect ratio nanorods were found in the spleen. Pegylation of either the 1.5 or the 5-aspect ratio nanorods resulted in increased accumulation in the lungs. No significant toxicity was found in any of the MSNs investigated and the MSNs were mainly excreted in the urine and faeces. Xie *et al.* also investigated organ distribution of intravenous administered fluorescent and <sup>125</sup>I labelled SiNPs with varying particle diameters 20 nm and 80 nms.<sup>146</sup> It was found that nanoparticles of these diameters were evenly located in the liver, but were concentrated in the white pulp of the spleen. Also, it was observed that both the 20 nm and 80 nm SiNPs were able to be excreted using the renal pathway.

The surface functionalisation of the SiNPs affects circulation organ distribution. He *et al.* investigated SiNPs with particle diameters ~45nm and their surface either unfunctionalized, carboxylic acid functionalised or pegylated.<sup>147</sup> The SiNPs were intravenously administered and it was found that the pegylated SiNPs had significantly longer circulation times and liver uptake. All SiNPs investigated were able to be cleared from circulation and excreted through the renal pathway.

Intravenous administration is the most popular method of exposure for investigating SiNPs toxicity. Liu *et al.* investigated both the lethal dose and the effect of continuous administration for 14 days of 110 nm mesoporous hollow silica

nanoparticles in mice.<sup>148</sup> The lethal dose was found to be > 1000 mg/kg of the mouse's body mass and no death was observed for continuous intravenous injection of nanoparticles with doses ranging from 20, 40 and 80 mg/kg for 14 days. In addition, complete clearance of the nanoparticles from the body could be achieved and the entire clearance completed after four weeks. Fu *et al.* expanded this investigation into different exposure routes using the same 110 nm silica nanoparticles.<sup>149</sup> This included intravenous, hypodermic, intramuscular injection and oral administration. Hypodermic and intramuscular injection obtained the lowest absorption rates as the nanoparticles were unable to cross different biological barriers effectively. It was also found that these methods caused inflammatory responses around the injection sites due to muscle and hypodermic tissue damage. Oral administration of nanoparticles was more successful however with the SiNPs being absorbed into the intestinal tract and observed in the liver. It was also further confirmed that silica nanoparticles were excreted in the urine and faeces.

There have been multiple studies on the transplacental transport of nanomaterials in pregnant animals and the nanomaterial induced neurotoxicity in their offspring.<sup>150-155</sup> These investigations have mainly focussed on titanium dioxide, polystyrene and quantum dots. Yamashita *et al.* investigated the resorption of intravenously administered 70 nm silica nanoparticles and foetal growth restriction.<sup>156</sup> The SiNPs were observed in the placenta, foetal liver and foetal brain. Also, the presence of the SiNPs caused pregnancy complications, smaller uteri and smaller foetuses than the controls. However, these detrimental effects were abolished with surface functionalisation of the SiNPs to carboxyl and amine groups.

The toxicity research performed on silica has led the US Food and Drug Administration (FDA) to approve silica as a “generally recognised as safe” (GRAS) and has resulted in silica being widely used in cosmetic and food additives.<sup>10, 157</sup>

### **1.2.6 Applications in Medicine**

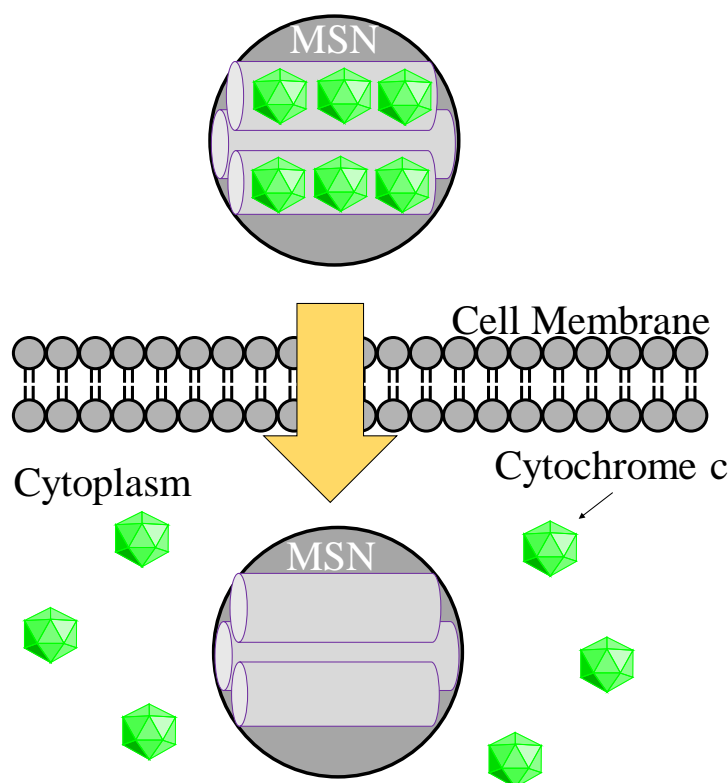
Due to the robust, simple and scalable method of synthesis, ease of functionalisation and low toxicity, SiNPs have had large amount of research in the applied field of nanomedicine,<sup>158, 159</sup> in particular as biosensors.<sup>160</sup> Azioune *et al.* bound human serum albumin (HSA) to ester functionalised polypyrrole SiNPs and observed the activity of the bound HSA to anti-HSA after incubation.<sup>161</sup> Kim *et al.*<sup>162</sup> and Kang *et al.*<sup>163</sup>

independently synthesised fluorescent SiNPs with surface  $\text{Ni}^{2+}$  modification for specific interaction with histidine-tagged proteins. This allowed for protein isolation and purification as well as site specific labelling, essential techniques in the field of proteomics. Shiomi *et al.* covalently bound haemoglobin to a SiNP and then grew the SiNPS around the haemoglobin with a second layer of silica. Which, after the removal of the haemoglobin templates were now able to obtain haemoglobin recognition.<sup>164</sup> SiNPs have been utilised for other forms of biological recognition. Wang *et al.* synthesised aptamer functionalised SiNPs that were able to detect lysozymes in the range 0-22.5  $\mu\text{M}$ .<sup>165</sup> Hilliard *et al.* immobilised oligonucleotides to fluorescent SiNPs by disulphide bridges.<sup>166</sup> These were then incubated with deoxyribonucleic acid, DNA, to cause hybridisation which could be observed by fluorometry. SiNPs have also been utilised for pharmaceutical applications. Gore *et al.* used colloidal silica to stabilise aspirin tablets,<sup>167</sup> whilst colloidal silica has also been used to strengthen magnesium stearate tablets.<sup>168</sup> SiNPs have been investigated for the possible application as a glidant.<sup>169</sup>

An application where MSN research dominates is in drug delivery.<sup>159</sup> Vallet-Regi *et al.* first applied MCM-41 silica to drug delivery.<sup>170</sup> The charge and pore diameter were investigated to observe their effects on ibuprofen release. Using MCM-41 silica nanoparticles high drug capacity was obtained with constant drug release. It was concluded that the charge of the material had more effect on drug release than pore diameter. The ability to change the surface charge of MSNs allows for a wide range of pharmaceutical drugs, with varying hydrophobicity and molecular weight, to be incorporated into MSNs such as doxorubicin,<sup>171</sup> camptothecin,<sup>172</sup> cisplatin<sup>173</sup> and itaconazole.<sup>174</sup> There has been an explosion of research of MSNs as drug delivery systems with a vast range of possible drugs and targets including bone/tendon tissue engineering,<sup>175-178</sup> diabetes,<sup>179, 180</sup> inflammation<sup>181</sup> and cancer<sup>172</sup> being investigated.

Another interesting feature of MSNs as therapeutic delivery agents are their ability to transport membrane impermeable native proteins into the cytosol of cells, of vital importance to ensure that the drug can reach the target on which it is designed to act, rather than being digested or expelled from the typical cellular endocytic pathway of nanoparticles.<sup>182-184</sup> Slowing *et al.* highlighted the MSNs efficacy as a carrier system through membranes by successfully storing cytochrome c, a membrane

impermeable protein that triggers apoptosis in cells,<sup>185</sup> in the pores and transporting it through a cell membrane whilst retaining its activity (*Figure 1.12*).<sup>186</sup>

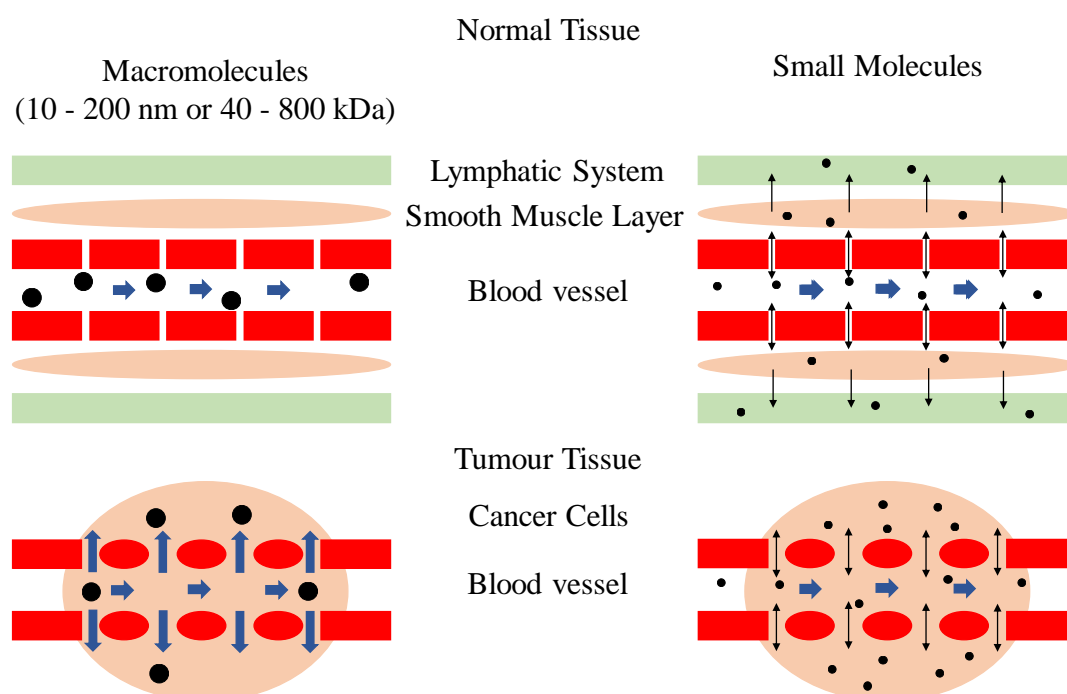


*Figure 1.12. Cytochrome c transportation into the cytoplasm using MSNs.*<sup>186</sup>

MSNs have been also applied to gene delivery, a process in which DNA is transported to the nucleus of the host cell allowing for genetic research or gene therapy.<sup>187</sup> Here polycation polymers, for example polyamidoamine (PAMAM),<sup>188</sup> polyethylenimine (PEI)<sup>189</sup> and mannosylated polyethylenimine (MP),<sup>190</sup> have been utilised for the non-covalent attachment of DNA/RNA. The attachment of PEI additionally being found to increase cellular uptake due to the proton sponge effect whereby the cationic nature of PEI in physiological conditions causes  $H^+$  and  $Cl^-$  ions to enter the endosome containing the PEI functionalised nanoparticle causing osmotic swelling and resulting in endosome rupture.<sup>191, 192</sup> Polymer functionalisation is not a necessity however for DNA or RNA MSN uptake. Gu et al adsorbed DNA/RNA using MSNs without surface modification.<sup>193, 194</sup> In this application MSN pore size is of paramount importance.<sup>195, 196</sup> Large pore sizes being able to transport plasmids in the supercoiled formed, providing protection from nucleases.<sup>196</sup>

A particularly useful feature of MSNs is its non-discriminatory ability to uptake and host different molecule, allowing for co-drug delivery.<sup>171, 180, 197-199</sup> This attribute has been utilised against multi-drug resistant cancer cells. He *et al.* used MSNs loaded with doxorubicin and Bcl-2 small interfering RNA, SiRNA, to reverse drug resistance in cancer cells.<sup>171</sup> Brinker *et al.* were able to have a kill effect on cancer cells  $10^6$  greater than comparable liposomes by delivering a cocktail of doxorubicin, 5-fluorouracil and cis-platin using surface lipid bilayer functionalised MSNs.<sup>197</sup>

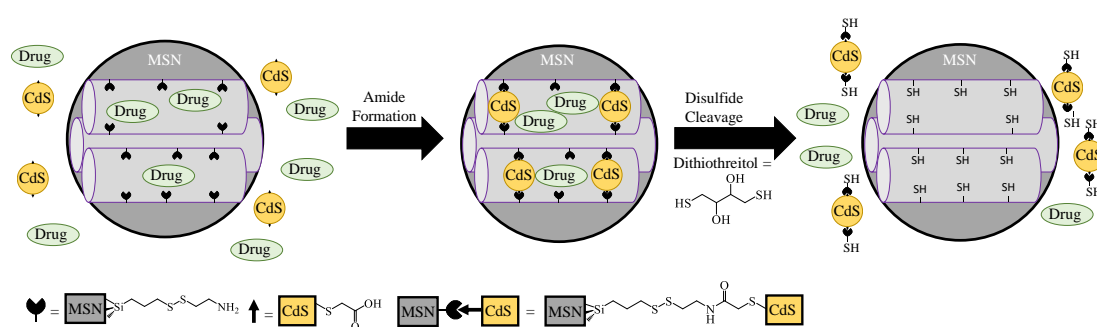
Despite the overwhelming amount of research into MSNs as drug delivery systems, especially in the field of tumour targeting, there are only two major examples of clinically used nanoparticles, Abraxane<sup>®</sup> and Doxil<sup>®</sup>. The reason for this is previous nanoparticle research reliance on the enhanced permeability and retention, EPR, effect.<sup>200</sup> The EPR effect states that due to the hyperpermeable nature of tumour vasculature, the permeability of large particles, such as proteins, macromolecules, liposomes, micelles and other soluble particles, is enhanced. These large particles can avoid renal clearance, which when combined with an impaired lymphatic drainage system limiting the removal of tumour particles, causes enhanced retention of the nanoparticles at tumour sites (*Figure 1.13*).



*Figure 1.13. A schematic representation of the conceptual passive targeting (EPR effect) of nanomedicine.<sup>201</sup>*

The EPR effect however has a severely muted effect in humans carcinoma tissue compared to in mice.<sup>202</sup> this is due to murine models being drastically different to human cancer tissue in rate of development, the size relative to the host, metabolic rates and host lifespan. Specifically, human tumours have different microenvironments compared to murine tumours simply because rodent tumours grow faster. A subcutaneous tumour grows roughly 1 cm (~0.5 g) in 2-4 weeks. In humans this would represent a growth of 20 cm (1-2 kg).<sup>203</sup> Due to this rapid murine tumour growth, blood vessels in mouse tumour do not develop properly, resulting in a leaky nature. This is not necessarily the case in humans, resulting in a heterogenous distribution of pore sizes and therefore heterogenous extravasation and delivery.<sup>204</sup> Also the large tumour to host's body ratio significantly alters the pharmacokinetics of the drug carriers. Murine tumours are usually observed to be 10 % of the mouse's body weight. This in a 70 kg human would be a 7 kg tumour, which would be roughly the volume of a basketball.<sup>205</sup> This has forced researchers to use more relevant *in vivo* tumour models, such as patient derived tumour explant, PDX, models, which more faithfully reflect the morphology, complexity and heterogeneity of clinical tumours.<sup>206</sup>

The failure of the EPR effect in clinical trials has led to greater research into stimuli responsive drug delivery systems, SRDDS, in a bid to ensure that therapeutics are released at the appropriate place for maximum impact. Lin *et al.* bound cadmium sulphide (CdS) into the pores of MSNs using disulphide bridges.<sup>207</sup> The disulphide bridges can be cleaved by disulphide bond reducing molecules to release the encapsulated drug molecules from within the pores allowing for controlled drug release (*Figure 1.14*).



*Figure 1.14. A schematic representation of the CdS nanoparticle capped MSN-based drug delivery system.*<sup>207</sup>



This has been developed further by the group to incorporate gold<sup>208</sup> and magnetic nanoparticle capping, allowing the gating mechanism to react to different external stimuli.<sup>209</sup> SRDDs have been developed to respond to a wide range of stimuli such as UV,<sup>208, 210-214</sup> pH,<sup>215-219</sup> ultrasound,<sup>179</sup> redox,<sup>220-222</sup> magnetic field,<sup>223</sup> electric field,<sup>224</sup> enzymes<sup>225-229</sup>, temperature<sup>118</sup> and even multi-responsive DDSs.<sup>230-232</sup> However very few of these have progressed into *in vivo* studies.<sup>233</sup> This is due to the challenge of remotely manipulating them *in vivo* using the correct stimuli.

Another avenue of research explored is the bioconjugation of targeting ligands to the surface of MSNs that specifically bind to cancer cells.<sup>234</sup> The range of targeting ligands previously bound to MSNs for cancer cell targeting consists of folate to target folate receptors,<sup>235-237</sup> transferring to target transferrin receptors,<sup>238</sup> aptamer to target PTK7 (human protein kinase-7) overexpressed in colon carcinomas<sup>239</sup> and antibodies that target Her-2 receptors overexpressed in breast or lung cancer.<sup>240</sup> Li *et al.* has bound silica nanoparticles to mesenchymal stem cells, MSCs, which has a tumour-tropic property towards malignant cells.<sup>241</sup> Up to 1500 Doxorubicin loaded nanoparticles were anchored to MSCs by specific antibody-antigen recognition. These silica burdened cells delivered doxorubicin with a wider distribution and longer retention time than both free doxorubicin and silica encapsulated doxorubicin, resulting in greater apoptosis.

## 1.3 Magnetic Resonance Imaging, MRI

### 1.3.1 MRI History

The history of MRI begins with the fundamental studies performed by Rabi *et al.* measuring the magnetic moment of a molecular beam of LiCl, LiF, NaF and Li<sub>2</sub> to obtain the magnetic moments of <sup>3</sup>Li<sup>6</sup>, <sup>3</sup>Li<sup>7</sup> and <sup>9</sup>F<sup>19</sup>.<sup>242</sup> This was developed further to be able to acquire the magnetic moment of H<sub>2</sub>.<sup>243</sup> This is an essential step in the development of clinical MRI as this technique only measures the magnetic moment of <sup>1</sup>H predominantly in the form of H<sub>2</sub>O. For this work he was awarded a Nobel prize in 1944. Bloch *et al.*<sup>244</sup> and Purcell *et al.*<sup>245</sup> extended this work to solids and liquids which resulted in them jointly receiving the Nobel prize in 1952. Damadian *et al.* performed the first research into using MR relation times as a medical diagnostic tool to decipher between healthy and cancer cells in 1971.<sup>246</sup> Lauterbur *et al.* published an image using MR in 1973 of two capillaries of H<sub>2</sub>O, submersed in a glass tube of D<sub>2</sub>O by rotating the specimen.<sup>247</sup> Mansfield *et al.* simultaneously producing an image utilising magnetic gradients.<sup>248</sup> This culminated in the imaging of a human finger in 1977<sup>249</sup> and an image of the human body in 1978 using variable magnetic gradients called the line-scan technique.<sup>250</sup> For this work Paul Lauterbur and Sir Peter Mansfield were awarded the Nobel prize in 2003.

### 1.3.2 MRI Basic Principles

Atomic nuclei have a spin quantum number, I. If  $I \geq \frac{1}{2}$  then the nuclei have an intrinsic magnetic moment and spin angular momentum. When not in a magnetic field the magnetic moments of the nuclei are randomly orientated leading to no net magnetic field. However, if a magnetic field is applied, B<sub>0</sub>, then the nuclei start precessing at the Larmor frequency,  $\omega_0$ , which is proportional to B<sub>0</sub> and the gyromagnetic moment of the nucleus,  $\gamma$  (Equation 1.1).

$$\omega_0 = \gamma B_0 \text{ (Equation 1.1)}$$

The nuclei either precess around B<sub>0</sub> in the low energy state or against B<sub>0</sub> in the high energy state exclusively (Figure 1.15).

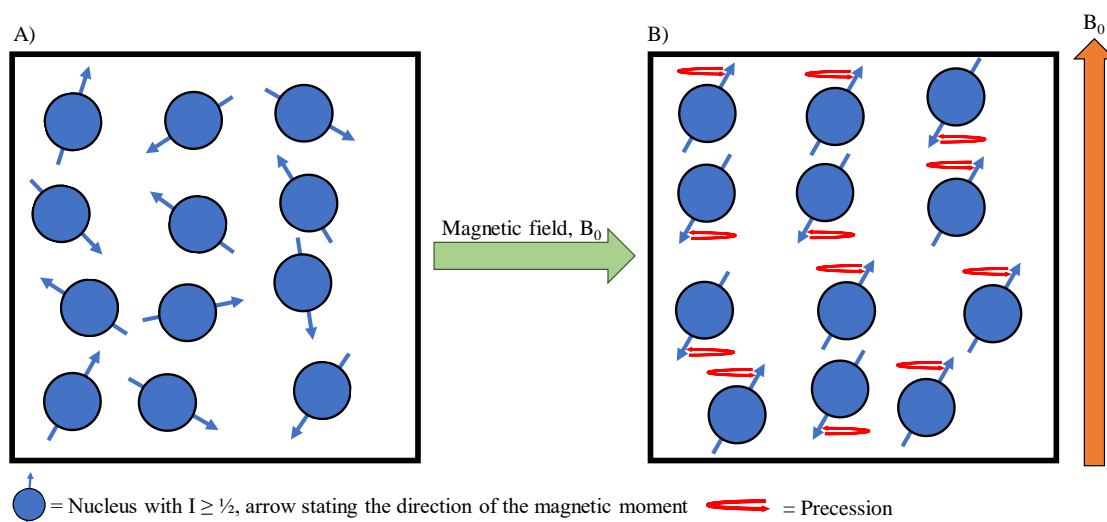


Figure 1.15. A schematic representation of 12 nuclei with  $I \geq \frac{1}{2}$  in A) no magnetic field and B) addition of magnetic field,  $B_0$ .

As more nuclei are present precessing in the direction of  $B_0$  than against, there is a net longitudinal magnetic moment in the direction of  $B_0$  (Figure 1.16).

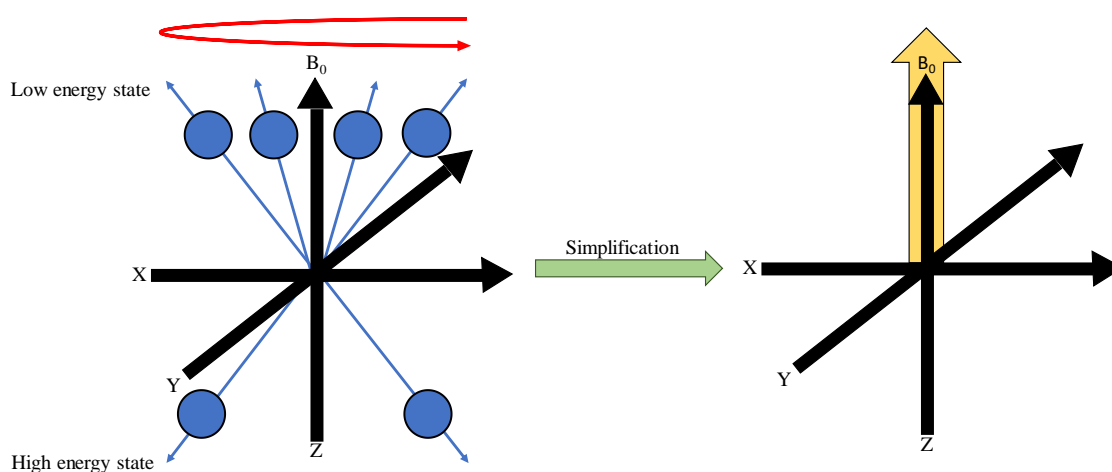
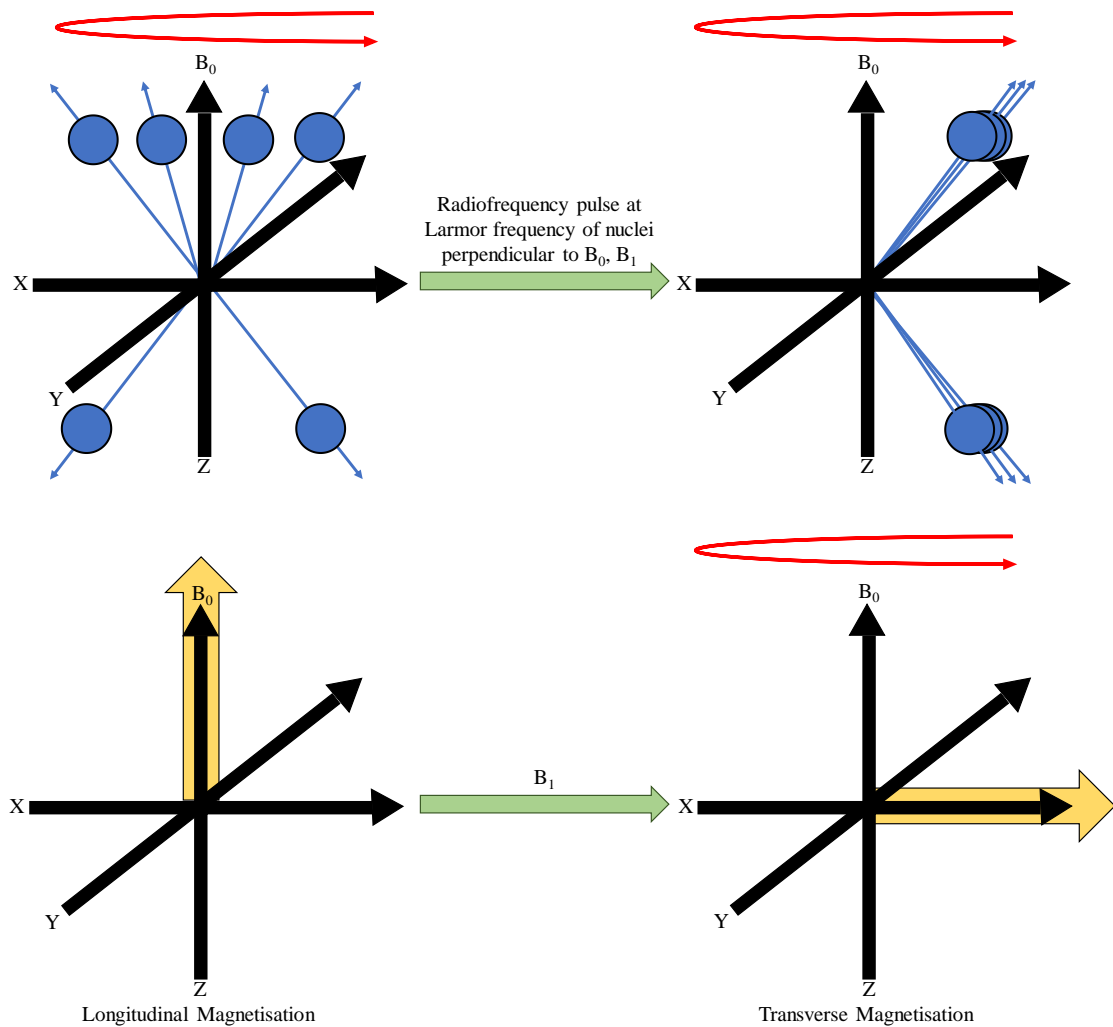


Figure 1.16. A schematic showing 6 nuclei with  $I \geq \frac{1}{2}$  precessing around  $B_0$  with a common origin in either the low energy state, in the direction of  $B_0$  or the high energy state, and its simplification representing the net longitudinal direction of the magnetic moment of the nuclei.

When a radiofrequency pulse is applied to the system at the Larmor frequency of the nuclei (42.58 MHz for  $^1\text{H}$  at 1 Tesla) perpendicular to  $B_0$ , known as  $B_1$ , energy is

provided to the nuclei in the low energy state such that nuclei are promoted to the high energy state, neutralising the longitudinal magnetic moment. The precession of the nuclei is also synchronised by  $B_1$ , causing a net transverse magnetic moment perpendicular to  $B_0$ , which can be observed by electromagnetic induction (*Figure 1.17*).



*Figure 1.17. The promotion of nuclei from the low energy state to the high energy state and the synchronisation of precession by the addition of a radiofrequency pulse at Larmor frequency perpendicular to  $B_0$ ,  $B_1$ . Thus, rotating the net magnetisation of the nuclei from a net longitudinal direction to a net transverse direction.*

Upon removal of  $B_1$ , the nuclei return to their original state aligned with  $B_0$  in a process known as relaxation. This occurs in two different mechanisms. Firstly, the precession of the nuclei desynchronises, leading to loss of the transverse magnetisation, with the relaxation referred to as  $T_2$  relaxation or spin-spin relaxation and the time it takes to

relax as  $T_2$ . The return of the magnetic moment from the xy plane to the z axis, leads to a regaining of the longitudinal magnetisation, with the relaxation referred to as  $T_1$  relaxation or spin-lattice relaxation, with a relaxation time of  $T_1$  (Figure 1.18).

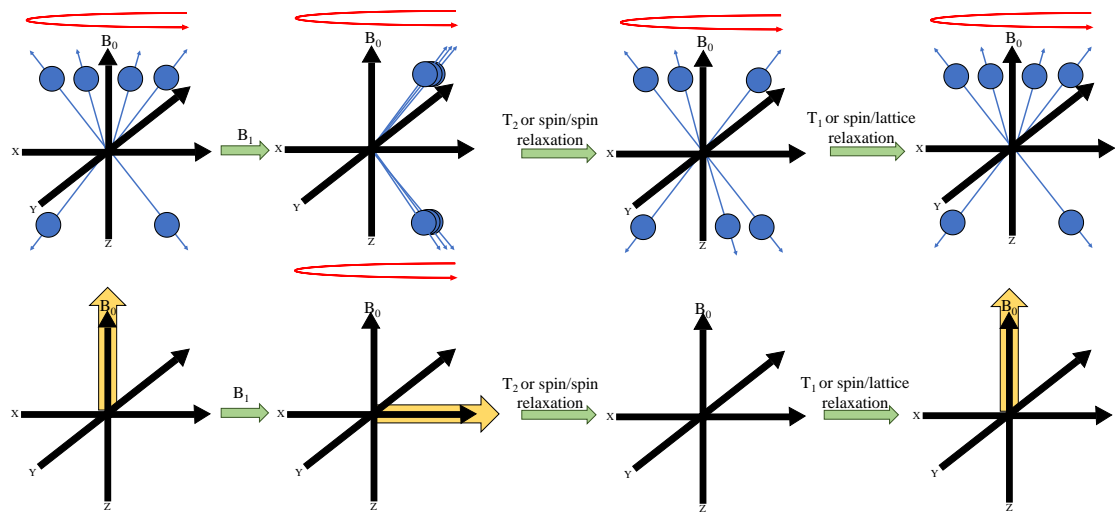


Figure 1.18. A schematic representing of the addition of  $B_1$  to 6 nuclei in  $B_0$  and the subsequent relaxation steps,  $T_2$  and  $T_1$  relaxation observed after removal of  $B_1$ .

$T_2$  and  $T_1$  relaxation of a nucleus is affected by the local magnetic fields of neighbouring nuclei via dipole/dipole interactions. Therefore, analysing  $T_2$  and  $T_1$  relaxation allows for the observation of deviations in the nuclei's local environment, for instance between different healthy tissues and cancerous tissue.  $T_2$  relaxation is observed by applying  $B_1$ , removing  $B_1$ , pausing such that there is maximum variation between nuclei with slow relaxation and fast relaxation, which is known as Echo Time or  $T_E$ , and then recording the transverse magnetisation. Nuclei with fast  $T_2$  relaxation would have desynchronised more than the nuclei with slower  $T_2$  relaxation resulting in nuclei with fast relaxation having less transverse magnetisation observed (Figure 1.19). On application of a grey-scale, this would result in slow  $T_2$  relaxation nuclei appearing lighter whereas fast  $T_2$  relaxation nuclei appearing darker.

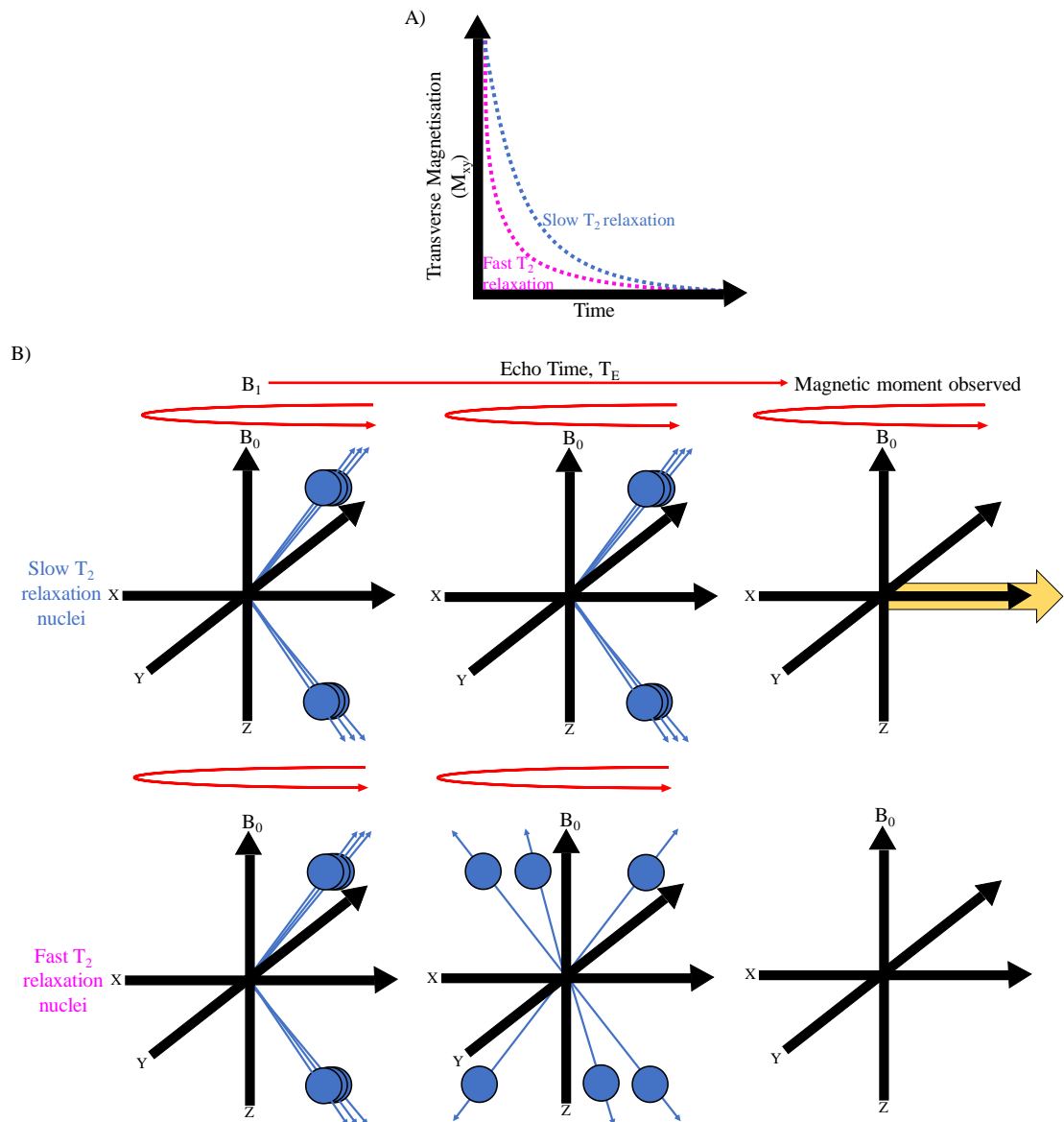
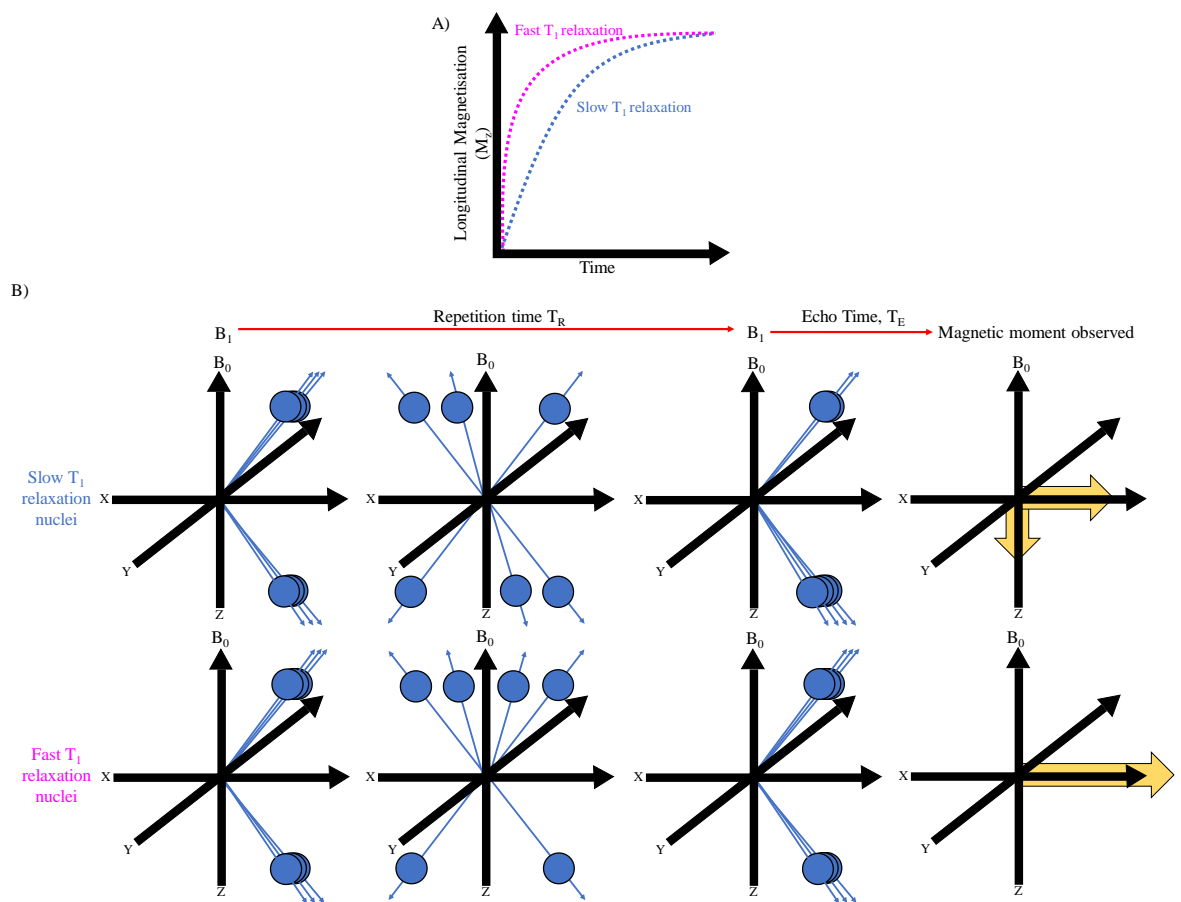


Figure 1.19. A) The loss of transverse magnetisation against time for nuclei with fast and slow  $T_2$  relaxation and B) the general theory behind observing the differences in  $T_2$  relaxation between nuclei with fast and slow relaxation experimentally.

Analysing  $T_1$  is more complicated due to only transverse magnetisation being able to be analysed effectively, due to all variation in longitudinal magnetisation being overwhelmed by  $B_0$ . First  $B_1$  is applied, then time is allowed for  $T_2$  and  $T_1$  relaxation to occur, the time gap between  $B_1$  pulses being known as the Repetition Time or  $T_R$ .  $T_R$  should enable nuclei with fast  $T_1$  relaxation to have completely relaxed whereas nuclei with slow  $T_1$  relaxation to be still in the process. Then a second  $B_1$  pulse is administered. The purpose of the secondary pulse is to promote the nuclei in the fully relaxed state. For a nucleus with fast  $T_1$  the nuclei promoted should be proportionately

the same as for the initial  $B_1$  pulse as the nuclei have returned to their relaxed state. However, for nuclei with slow  $T_1$  relaxation, the nuclei have not returned to their completely relaxed state. So, this second  $B_1$  will result in more nuclei being promoted to the high energy state from the low energy state despite the low energy state not having been completely repopulated from the first  $B_1$ , leading to more nuclei being in the high energy state than the low. This imbalance causes the direction of the net magnetisation of the nuclei to have an antiparallel characteristic with  $B_0$ . Reducing transverse magnetisation and therefore causing a detectable difference between nuclei with fast and slow  $T_1$  relaxation (*Figure 1.20*).



*Figure 1.20. A) The recovery of longitudinal magnetisation against time for nuclei with fast and slow  $T_1$  relaxation and B) the general theory behind observing the differences in  $T_1$  relaxation between nuclei with fast and slow relaxation experimentally.*

As multiple analyses are performed for one image,  $T_1$  and  $T_2$  weighted images are described by their pulse sequence.  $T_2$  weighted images have a long  $T_R$  to allow for complete relaxation between  $B_1$  pulses and a long  $T_E$  to allow for the deviation

between  $T_2$  relaxation to be maximised. Whereas  $T_1$  weighted images have a short  $T_R$  time to minimise complete relaxation to only the nuclei with fast  $T_1$  relaxation and a short  $T_E$  to minimise  $T_2$  relaxation between the pulse and data acquisition.

### 1.3.3 Contrast Agent Theory

The sensitivity of MRI is based on the population difference between the number of nuclei in the low energy state compared to the high energy state when  $B_0$  is applied. The population difference is based on a Boltzmann distribution (*Equation 1.2*), where  $P_{Low}/P_{High}$  is the population difference between the low ( $P_{Low}$ ) and the high ( $P_{High}$ ) energy states,  $\Delta E$  is the energy difference between the high and the low energy state (Joules),  $k_b$  is the Boltzmann constant ( $1.38 \times 10^{-23}$  J/K) and  $T$  is temperature in Kelvin.

$$\frac{P_{Low}}{P_{High}} = e^{\frac{\Delta E}{k_b T}} \text{ (Equation 1.2)}$$

$\Delta E$  for  $^1H$  at 20 Tesla =  $5.6 \times 10^{-25}$  J, so at 298 K  $P_{Low}/P_{High} = 1.0001$ . This means for every 10,001  $^1H$  atoms precessing aligned to  $B_0$ , 10,000 are aligned against. This makes MRI have a very low signal to noise ratio.

This can be improved by the addition of an MRI contrast agent. As previously stated the  $T_1$  and  $T_2$  relaxation of a nucleus is affected by local magnetic fields *via* dipole/dipole interactions. The dipole/dipole interaction between a nucleus is proportional to the  $\gamma$  of the nucleus squared and the external  $\gamma$  squared as stated in the Solomon-Bloembergen-Morgan (SBM) Theory for two hydrogen nuclei (*Equation 1.3 and 1.4*).<sup>251</sup> In these equations for  $T_1$  and  $T_2$   $\tau_c$  is the correlation time or the time a nuclei takes to rotate 1 radian ( $\sim 57^\circ$ ),  $\omega$  is angular velocity,  $\hbar$  is  $h/2\pi$  ( $1.055 \times 10^{-34}$  J.s),  $r$  is distance between spins and  $\gamma$  is the gyromagnetic constant.

$$\frac{1}{T_1} = \frac{6}{20} \times \frac{\hbar^2 \gamma^4}{r^6} \left[ \frac{\tau_c}{1 + \omega^2 \tau_c^2} + \frac{4\tau_c}{1 + 4\omega^2 \tau_c^2} \right] \text{ (Equation 1.3)}$$

$$\frac{1}{T_2} = \frac{3}{20} \times \frac{\hbar^2 \gamma^4}{r^6} \left[ 3\tau_c + \frac{5\tau_c}{1 + \omega^2 \tau_c^2} + \frac{2\tau_c}{1 + 4\omega^2 \tau_c^2} \right] \text{ (Equation 1.4)}$$

As a lone electron has a gyromagnetic moment 660 times greater than that of a hydrogen proton, the dipole/dipole interaction between an electron and a proton is 435,600 greater than between two protons.<sup>252</sup> Therefore to obtain the greatest effect as a contrast agent the element or ion with a high number of unpaired electrons would



have the greatest effect on neighbouring  $^1\text{H}$  nuclei and by consequence relaxation. Gadolinium, Gd, has an electron configuration  $[\text{Xe}] 4f^7 5d^1 6s^2$ , which when in its ionised (3+) form,  $\text{Gd}^{3+}$ , is  $[\text{Xe}] 4f^7$ , with each electron unpaired in the f suborbitals. This is the largest number of unpaired electrons in any stable element or ion, making  $\text{Gd}^{3+}$  an excellent candidate for application as an MRI contrast agent.  $\text{Gd}^{3+}$  is administered to patients in a chelated form to minimise  $\text{Gd}^{3+}$  deposition in tissues by providing a physical barrier between  $\text{Gd}^{3+}$  and cells. However the  $\text{Gd}^{3+}$  requires a site for water coordination in which to interact with the water in the inner sphere of the complex as dipole interaction deteriorates with distance,  $r$ , between dipoles by  $r^6$  (Figure 1.21).<sup>253</sup>

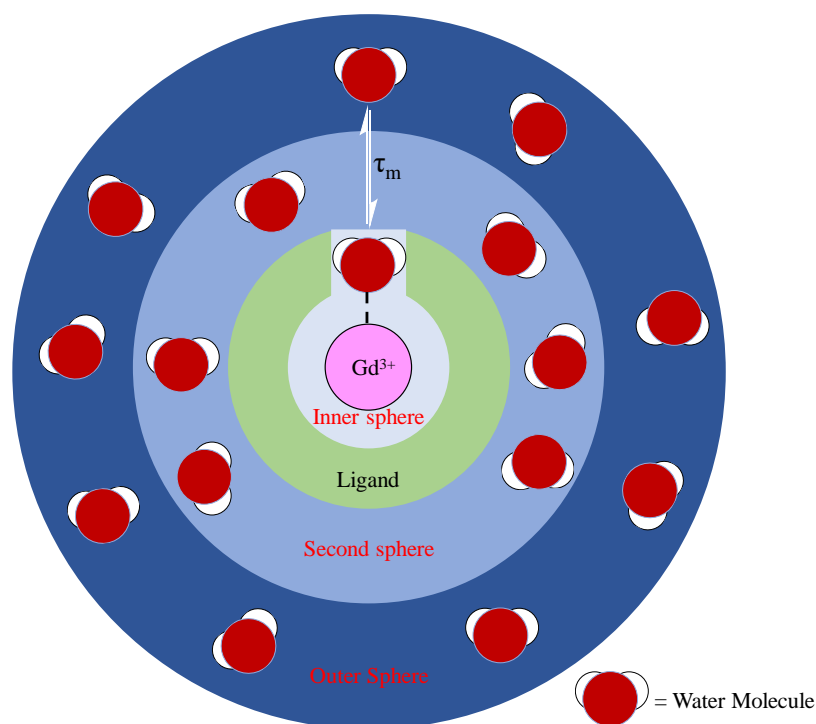
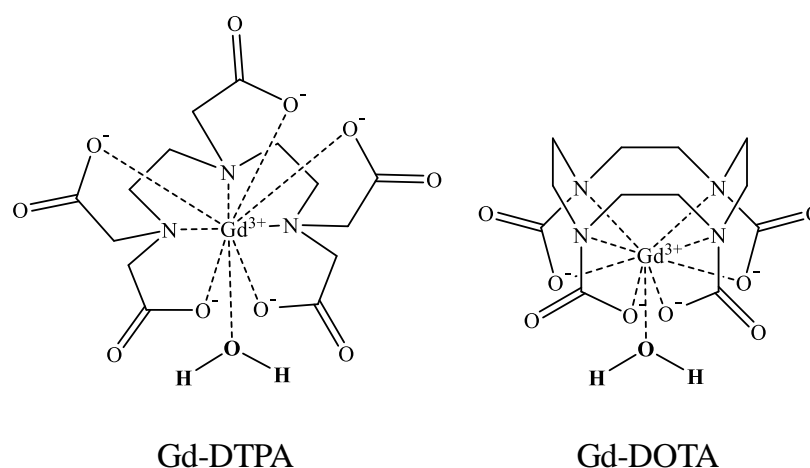


Figure 1.21. Schematic representation of inner, second and outer sphere water interactions with a  $\text{Gd}^{3+}$  contrast agent where  $\tau_m$  = water residence time.

The overall  $T_1$  observed by the addition of a contrast being the sum of the  $T_1$  relaxation provided by the inner sphere (water molecules directly coordinated to the  $\text{Gd}^{3+}$  centre),  $T_{IS}$ , second sphere (water molecules hydrating the complex),  $T_{SS}$ , and outer sphere (those diffusing near the chelate),  $T_{OS}$ , (Equation 1.5). However  $T_{IS}$  is thought to be the largest contributor.<sup>254</sup>

$$\frac{1}{T_1} = \frac{1}{T_{IS}} + \frac{1}{T_{SS}} + \frac{1}{T_{OS}} \text{ (Equation 1.5)}$$

In 1988 the first  $Gd^{3+}$  based contrast agent, GBCA, known as Gadopentetate dimeglumine<sup>®</sup>, was approved by the U.S Drug and Food Administration, FDA. Gadopentetate dimeglumine<sup>®</sup> used diethylenetriaminepentaacetic acid, DTPA, a linear ionic ligand to chelate the  $Gd^{3+}$ ,  $Gd^{3+}$ -DTPA. The latest approved GBCA, Dotarem<sup>®</sup>, uses the macrocyclic ionic ligand 1,4,7,10-Tetraazacyclododecane-1,4,7,10-tetraacetic acid, DOTA, as the ligand,  $Gd^{3+}$ -DOTA (*Figure 1.22*).



*Figure 1.22. The molecular structure of  $Gd^{3+}$ -DTPA and  $Gd^{3+}$ -DOTA with a single coordinated water molecule.*

All MRI contrast agents lower both  $T_1$  and  $T_2$  relaxation. However,  $Gd^{3+}$  lowers  $T_1$  significantly more than  $Gd^{3+}$  lowers  $T_2$ . This is due to  $T_1$  primarily being stimulated by fluctuating magnetic fields near the Larmor frequency sourced by nearby protons and electrons whereas  $T_2$  is primarily stimulated by local static magnetic fields such as ferromagnetism, represented by the  $3\tau_c$  in *Equation 1.6*.<sup>244</sup> Therefore,  $Gd^{3+}$ -DOTA is described as a positive contrast agent as it makes the area of its location brighter in a  $T_1$  weighted image. An MRI contrast agent which lowers  $T_2$  more than  $T_1$  is called a negative contrast agents as it makes the area of its location darker in a  $T_2$  weighted image.<sup>255</sup> Negative contrast agents are based predominantly on iron oxide nanoparticles.<sup>256</sup>

### 1.3.4 Gd<sup>3+</sup> Based Contrast Agent, GBCA, Toxicity

GBCAs are now administered in 35 % of all MRI examinations.<sup>257</sup> The possibility of having a true allergic reaction is exceptionally rare and most commonly concern mild anaphylactoid reactions.<sup>258</sup> Immediate adverse reactions, defined as unintended side effects occurring within 1 hour of GBCA exposure, are also exceptionally rare.<sup>259</sup> Despite >200 million GBCA administrations, there have been only 614 reports of severe adverse reactions (for example hypertensive urgency or refractory vasovagal reactions). Of these at least a subset of these physiological reactions may be attributed to the Weber and Lalli effects, in which a new pharmaceutical agent to the market or to an individual patient results in increased perception and reporting of potential adverse effects.<sup>260, 261</sup> These results did not vary significantly depending on GBCA administered.<sup>259, 262-264</sup>

Kanda *et al.* reported the increased accumulation of Gd<sup>3+</sup> in the brain after multiple GBCA administrations.<sup>265</sup> The observation of Gd<sup>3+</sup> deposits in the brain was subsequently confirmed by cadaver studies.<sup>266</sup> This finding was GBCA specific however with no T<sub>1</sub> hypersensitivity found in rat brain using repeated doses of the GBCAs that are based on macrocyclic ligands, such as Dotarem<sup>®</sup>.<sup>267</sup> This variation between Gd<sup>3+</sup> deposits and GBCAs is due to the linear ligands allowing transmetalation, where endogenous cations such as Cu<sup>2+</sup>, Zn<sup>2+</sup> and Ca<sup>2+</sup> displace Gd<sup>3+</sup>.<sup>268</sup> Linear ligands are flexible open chains which do not offer strong kinetic stability. In contrast macrocyclic ligands are rigid preorganised rings which have been specifically designed to be of optimal size to cage Gd<sup>3+</sup>. This results in the Gd<sup>3+</sup> complexation within a macrocyclic ligand to be 10<sup>5</sup> more kinetically stable than linear ligand complexation.<sup>269, 270</sup> Macrocyclic complexes being more stable than linear complexes results in macrocyclic ligand based GBCAs, Like Dotarem<sup>®</sup>, performing less transmetalation as Gd<sup>3+</sup> is bound more strongly to the ligand.<sup>271</sup> Despite the occurrence of these deposits in the brain there have been no histopathological effects observed and the identity of the speciation within which Gd is retained in tissues is still an ongoing challenge.<sup>272, 273</sup> Gd<sup>3+</sup> deposits have also been found in the bone<sup>274</sup>, skin<sup>275</sup> and liver.<sup>276</sup> However Gd<sup>3+</sup> was able to be partially removed from the liver tissue by subsequent administration of a chelating agent, deferoxamine<sup>®</sup>.<sup>276</sup>

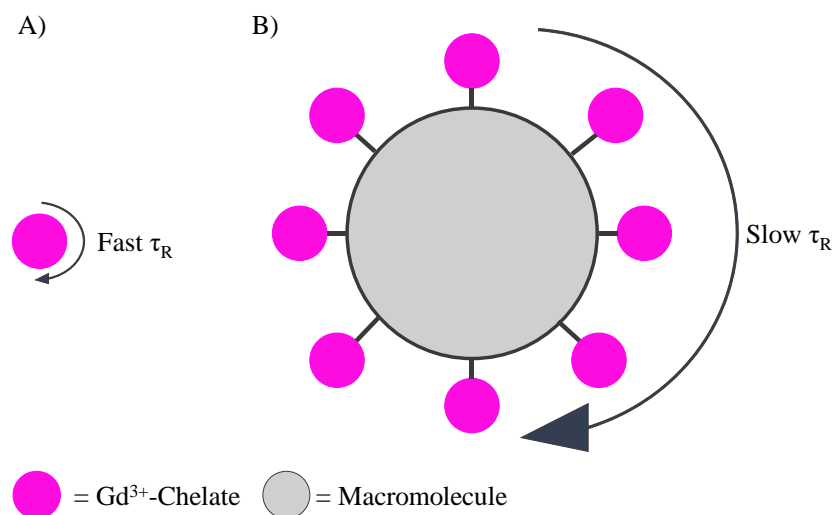
In 2006 the connection between GBCA administration in patient with advanced renal disease and the development of nephrogenic systemic fibrosis, NSF, was observed.<sup>277, 278</sup> NSF is usually a fatal disease that occurs due to the excessive production of fibrous connective tissue in the skin, joints, eyes, and internal organs because of a reparative response to injury or damage. NSF symptoms most commonly appear within 6 months of GBCA exposure, with the clear majority of patients with NSF developing the symptoms within 2 years of GBCA exposure.<sup>279, 280</sup> However, some cases have appeared after 10 years of GBCA exposure.<sup>281-283</sup> NSF is exceedingly rare with only 1,000 recorded after >200 million GBCA administrations.<sup>257</sup> No cases have been described in patients without significant renal disease.<sup>257</sup> Chronic liver disease does not predispose patients to NSF like previously thought.<sup>284, 285</sup> Patients with chronic kidney disease have decreased incidence of NSF with subsequent dialysis after GBCA administration.<sup>286</sup> Also, the vast majority of NSF cases occurred after receiving a GBCA dose far greater than the currently advised dosages.<sup>279, 284</sup> This lowering of administered GBCAs and the development towards macrocyclic ligands has resulted in few if any cases of NSF resulted from GBCA administration after 2010.<sup>257</sup> There have also been cases of GBCA-induced recurrent pancreatitis and renal failure from acute tubular necrosis.<sup>287</sup>

Regarding prenatal and neonatal GBCA administration, there has been no statistically increased risk of stillbirth/death, NSF-like outcomes, or congenital anomalies after GBCA administration in the first trimester. However, there is an increased adjusted relative risk in rheumatological/ inflammatory conditions and stillbirth/neonatal death after administration in the second and third trimester.<sup>288</sup> Less than 1% of the GBCA dose appears in the patient's breast milk and of that less than 1 % reaches the infant bloodstream.<sup>289</sup>

### **1.3.5 GBCAs based on MSNs**

The limitation of current clinically used GBCAs is that they are based on small molecules that lack the sensitivity to provide satisfactory image enhancement in the early stages of disease. A method of increasing positive contrast is to further enhance  $T_1$  relaxation. For GBCAs,  $T_1$  relaxation can be enhanced by increasing the number of directly coordinated water molecules around  $Gd^{3+}$ . However, this leads to less sites filled by the ligand, leading to weaker kinetic stability between the  $Gd^{3+}$  and the ligand

resulting in greater likelihood of transmetalation and potential  $\text{Gd}^{3+}$  deposition in tissues. Another method described by Solomon *et al.* involves the variation of the tumbling rate,  $\tau_R$ , of the  $\text{Gd}^{3+}$  chelate around the Larmor frequency of  $^1\text{H}$ .<sup>290</sup> Solomon *et al.* observed an increase in  $T_1$  relaxation when the tumbling rate became closer to the Larmor frequency. This observation can be applied to GBCAs by binding the  $\text{Gd}^{3+}$  complex to a macromolecule, protein or nanoparticle (*Figure 1.23*).<sup>291</sup>



*Figure 1.23. A schematic illustrating how binding a  $\text{Gd}^{3+}$ -chelate to a macromolecule decreases the tumbling rate,  $\tau_R$ , therefore increasing  $T_1$  relaxation. A) The  $\tau_R$  of the lone  $\text{Gd}^{3+}$ -Chelate, B) The  $\tau_R$   $\text{Gd}^{3+}$ -chelate chemically bound to a macromolecule.*

Lin *et al.* in 2004 incorporated  $\text{Gd}^{3+}$  into MSNs.<sup>292</sup> 4 different weight percentages, wt%, of  $\text{Gd}^{3+}$  with respect to MSN were investigated, 1.6 wt%, 2.3 wt%, 3.1 wt% and 6.8 wt%. A proportional relationship was observed with wt% of  $\text{Gd}^{3+}$  and  $T_1$  relaxation time at 400 MHz changing  $T_1$  in the order 1.6 wt% < 2.3 wt% < 3.1 wt% < 6.8 wt%. However, all  $\text{Gd}^{3+}$  incorporated MSNs shortened  $T_1$  relaxation more than  $\text{Gd}^{3+}$ -DTPA. Taylor-Pashow *et al.* and Hsiao *et al.* both independently investigated  $\text{Gd}^{3+}$ -chelate bound to MSNs.<sup>293, 294</sup> Taylor-Pashow *et al.* performed a post synthetic modification method on 75 nm MCM-41 nanoparticles with pore diameter  $\sim 2.4$  nm, using Gd bound (trimethoxysilylpropyl)die-ethylenediaminetetraacetate,  $\text{Gd}^{3+}$ -Si-DTTA. These MSNs were analysed *in-vitro* using 3.0 T and 9.4 T MR scanners. Very short  $T_1$  relaxation rates were observed compared to non-porous silica nanoparticles synthesised by the same group.<sup>295</sup> This is due to the mesopores of the MSNs providing easier access into the magnetic centre, which significantly reduces  $T_1$  and  $T_2$  relaxation.<sup>296</sup> However, it should be noted that the solid silica nanoparticles used as a

comparison in this investigation used DTPA as the chelating ligand for  $\text{Gd}^{3+}$ , which has one coordination site for  $\text{Gd}^{3+}$ /water interactions to occur compared to DTTA's two. *In-vivo* studies were performed using the 9.4 T scanner and it was found that the same amount of  $T_1$  relaxation could be observed administering into mice significantly lower dosages than clinically administered using the MSN bound  $\text{Gd}^{3+}$ -DTTA (2.1  $\mu\text{mol/kg}$  compared to 0.1-0.3 mmol/kg). Hsiao *et al.* synthesised 120 nm MSNs with mean pore diameter 2.31 nm, that were dual functionalised with fluorescein and  $\text{Gd}^{3+}$ -DTPA. These MSNs were successfully applied to the tracking of stem cells *in-vivo* using a 1.5 T clinical MRI scanner. The application of MSNs to the function as a GBCA was investigated further by Carniato *et al.* by substituting the weak chelating agents of DTTA and DTPA utilised previously with DOTA.<sup>297</sup> Carniato *et al.* pursued the importance of the MSN bound chelate species by modifying the 1,4,7,10-tetraazacyclododecane structure and the MSN surface functional groups (Figure 1.24).<sup>297, 298</sup>

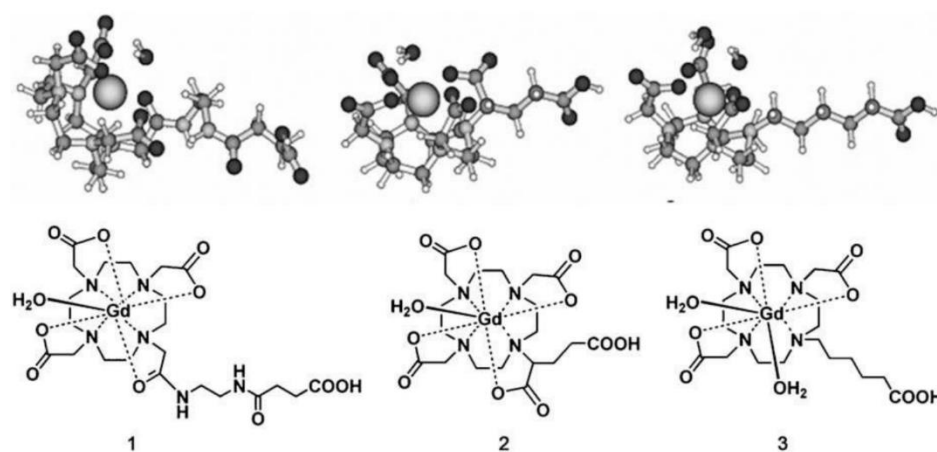


Figure 1.24. The molecular structure and the computational molecular optimisation in 3D space (above) of the DOTA variants investigated by Carniato *et al.*<sup>298</sup>

Carniato *et al.* concluded from this work that DOTA derivative 1 and the surface acetylation of the MSNs provided the largest  $T_1$  relaxation.

The observed enhancement of binding  $\text{Gd}^{3+}$ -DOTA to MSNs was optimised by Davis *et al.* by manipulating the location of  $\text{Gd}^{3+}$ -DOTA location.<sup>299</sup> In this research  $66.3 \pm 6.6$  nm MCM-41 MSNs with pore diameter  $3.2 \pm 1.3$  nm were synthesised and  $\text{Gd}^{3+}$ -DOTA functionalised using post-synthetic modification and two variants of co-condensation depending on DOTA-silane addition time. A significant increase of  $T_1$

relaxation was observed for the co-condensation functionalised MSNs with a long delay between the start of MSN synthesis and  $\text{Gd}^{3+}$ -DOTA addition at 7 T. Also, the percentage loading of  $\text{Gd}^{3+}$ -DOTA on the MSN was investigated with the lowest loading analysed (1.37 wt% of  $\text{Gd}^{3+}$  with respect to MSN) providing the shortest  $T_1$  relaxation. This agreed with the trend described previously by Lin *et al.* with  $\text{Gd}^{3+}$  incorporated MSNs.<sup>292</sup> Interestingly 1.37 wt% provided the shortest  $T_1$  relaxation times compared to the other wt%s even after biomodification with PEG5000. This shows that the steric hindrance of water to the  $\text{Gd}^{3+}$  complexes from the surface modification of MSNs with long polymer chains and proteins doesn't inhibit the use of MSNs as an MRI contrast agent. Karaman *et al.* pursued the optimisation of MSN's physical properties investigation further.<sup>300</sup>  $\text{Gd}^{3+}$  was non-covalently incorporated into ~500 nm MSNs or hollow MSNs using two different ionic compounds ( $\text{GdCl}_3$  and  $\text{Gd}(\text{acetylacetonate})_3$ ) either post graft or *in situ*. The effect of whether surfactant removal by solvent extraction or calcination was also observed. The conclusion of this investigation being that hollow MSNs with post-synthetic  $\text{Gd}(\text{acetylacetonate})_3$  incorporation with calcination removal of the surfactant provided the optimised MSN based GBCA.

The principal advantage of using MSNs as the macromolecule in which to bind the  $\text{Gd}^{3+}$ -chelate to is their high porosity and high surface area allowing for multiple functionality. This allows the GBCA MSNs to have multi modal imaging capabilities.<sup>301</sup> The most popular combination of imaging techniques are MRI and optical due to the application of optical imaging being beneficial in surgery and MRI for post operation investigations.<sup>294, 302-305</sup> The possibility of multiple functionality has also been utilised to vary the  $T_1$  relaxation enhancement by the response to an external stimulus. Huang *et al.* synthesised  $\text{Gd}^{3+}$ -DOTA bound biotinylated MSNs ( $66.3 \pm 6.6$  nm diameter) that pores ( $3.2 \pm 1.3$  nm diameter) were capped with streptavidin (~5 nm), blocking water/ $\text{Gd}^{3+}$  interactions and therefore increasing water  $T_1$  relaxation times. The streptavidin was able to be removed by biotinylated bovine serum albumin, BSA, to recover water/ $\text{Gd}^{3+}$  interactions and therefore regain shorter water  $T_1$  relaxation times.<sup>306</sup> In addition cell targeting GBCA MSNs have been explored with Taylor *et al.* synthesising  $\text{Gd}^{3+}$  doped MSNs that surface functionalised with RGD peptides to target colorectal cancer cells.<sup>307</sup> It should be noted that considerable non-specific

binding between MSNs with no RGD peptide functionalisation and colorectal cancer cells was observed.



## 1.4 Aims and Objectives of the PhD

We initially aimed to probe the impact of pore size on the relaxation behaviour of  $\text{Gd}^{3+}$ -chelate loaded MSNs. It is well known that the diffusional behaviour of water changes when confined in different sized spaces. The versatility of MSNs enables ease of variation of the pore diameter and coupled with variation of the location of  $\text{Gd}^{3+}$ -chelate contrast agents, will facilitate the production of new families of contrast agents with relaxation properties which are tuneable according to the nanostructure itself. We further aimed to produce stimuli responsive MRI contrast agents based on MSNs through the production of hybrid organic-inorganic nanomaterials that would vary their physical properties with temperature variation. The ability of MSNs to be used for this function is facilitated by their facile functionalisation and high thermal stability. Finally, we investigated targeting cells using MSNs that have minimal binding affinity to colorectal cancer cells, CRCs, provided again by organic surface modification. MSNs utilisation being advantageous to this application again due to the ease of MSNs functionalisation and their inherent inertness. Then to induce specific binding to the MSNs using lectins to allow for observation of the target cells. MSN being able to be dual functionalised being a necessity in this application.

The specific objectives are:

- Production of MSNs with varying pore size and similar particle diameters.
- Immobilisation of  $\text{Gd}^{3+}$ -chelates onto MSNs with varying pore diameters and analysis of their relaxation behaviour.
- Investigation of polymer functionalisation of MSNs by covalent binding of a thermoresponsive polymer
- Analysis of the polymer's response to temperature with change in polymer density on MSN surface.
- Immobilisation of  $\text{Gd}^{3+}$ -chelates onto thermoresponsive polymer surface functionalised MSNs and analysis of their relaxation behaviour.
- Polymer surface functionalisation of MSNs with a biocompatible low cell affinity polymer.
- Varying low cell affinity polymer surface density on MSNs and observe the effect on non-specific binding with cells.

- Optimisation of polymer surface functionalisation with low cell binding affinity polymer to remove reactant impurities.
- Binding of a lectin to the low affinity polymer MSN surface and investigation into specific affinity to colorectal cancer cells, CRC.
- Investigate toxicity of lectin bound to MSNs with surface modification of low cell binding affinity to CRCs.

## 1.5 References

1. B. Bhushan, D. Luo, S. R. Schricker, W. Sigmund and S. Zauscher, *Handbook of nanomaterials properties*, Springer Science & Business Media, 2014.
2. D. Jariwala, V. K. Sangwan, L. J. Lauhon, T. J. Marks and M. C. Hersam, *Chemical Society Reviews*, 2013, **42**, 2824-2860.
3. K. Gajanan and S. Tijare, *Materials Today: Proceedings*, 2018, **5**, 1093-1096.
4. L. R. Khot, S. Sankaran, J. M. Maja, R. Ehsani and E. W. Schuster, *Crop protection*, 2012, **35**, 64-70.
5. S. Raj, S. Jose, U. Sumod and M. Sabitha, *Journal of Pharmacy & Bioallied sciences*, 2012, **4**, 186.
6. Z.-Y. Zhou, N. Tian, J.-T. Li, I. Broadwell and S.-G. Sun, *Chemical Society Reviews*, 2011, **40**, 4167-4185.
7. M. O. Guler and A. B. Tekinay, *Therapeutic Nanomaterials*, 2016, 1.
8. V. Mamaeva, C. Sahlgren and M. Lindén, *Advanced drug delivery reviews*, 2013, **65**, 689-702.
9. T. Gerber and B. Himmel, *Journal of non-crystalline solids*, 1986, **83**, 324-334.
10. N. J. Halas, *ACS nano*, 2008, **2**, 179-183.
11. W. Stöber, A. Fink and E. Bohn, *Journal of colloid and interface science*, 1968, **26**, 62-69.
12. D. Green, J. Lin, Y.-F. Lam, M.-C. Hu, D. W. Schaefer and M. Harris, *Journal of colloid and interface science*, 2003, **266**, 346-358.
13. D. Green, S. Jayasundara, Y.-F. Lam and M. Harris, *Journal of non-crystalline solids*, 2003, **315**, 166-179.
14. D. D. Smith, L. Sibille, R. J. Cronise, A. J. Hunt, S. J. Oldenburg, D. Wolfe and N. J. Halas, *Langmuir*, 2000, **16**, 10055-10060.
15. S. Lowell and J. E. Shields, *Powder surface area and porosity*, Springer Science & Business Media, 2013.
16. M. Thommes, *Chemie Ingenieur Technik*, 2010, **82**, 1059-1073.

17. J. S. Beck, J. Vartuli, W. J. Roth, M. Leonowicz, C. Kresge, K. Schmitt, C. Chu, D. H. Olson, E. Sheppard and S. McCullen, *Journal of the American Chemical Society*, 1992, **114**, 10834-10843.
18. C. Kresge, M. Leonowicz, W. J. Roth, J. Vartuli and J. Beck, *nature*, 1992, **359**, 710.
19. G. J. Tiddy, *Physics reports*, 1980, **57**, 1-46.
20. H. Fabre, N. Kamenka, A. Khan, G. Lindblom, B. Lindman and G. J. Tiddy, *The Journal of Physical Chemistry*, 1980, **84**, 3428-3433.
21. H. Yang, A. Kuperman, N. Coombs, S. Mamiche-Afara and G. A. Ozin, *Nature*, 1996, **379**, 703.
22. E. Groenen, A. Kortbeek, M. Mackay and O. Sudmeijer, *Zeolites*, 1986, **6**, 403-411.
23. P. Spegt, A. Skoulois and e. V. Luzzati, *Acta Crystallographica*, 1961, **14**, 866-872.
24. F. Schüth, *Angewandte Chemie International Edition*, 2003, **42**, 3604-3622.
25. D. Zhao, J. Feng, Q. Huo, N. Melosh, G. H. Fredrickson, B. F. Chmelka and G. D. Stucky, *science*, 1998, **279**, 548-552.
26. Y. Xie, D. Kocaefe, C. Chen and Y. Kocaefe, *Journal of Nanomaterials*, 2016, **2016**, 11.
27. N. K. Raman, M. T. Anderson and C. J. Brinker, *Chemistry of Materials*, 1996, **8**, 1682-1701.
28. X. S. Zhao, G. Lu and G. J. Millar, *Industrial & Engineering Chemistry Research*, 1996, **35**, 2075-2090.
29. A. Sayari, *Chemistry of Materials*, 1996, **8**, 1840-1852.
30. J. Y. Ying, C. P. Mehnert and M. S. Wong, *Angewandte Chemie International Edition*, 1999, **38**, 56-77.
31. G. J. d. A. Soler-Illia, C. Sanchez, B. Lebeau and J. Patarin, *Chemical reviews*, 2002, **102**, 4093-4138.
32. A. Stein, *Advanced Materials*, 2003, **15**, 763-775.
33. M. Grün, I. Lauer and K. K. Unger, *Advanced Materials*, 1997, **9**, 254-257.
34. S.-H. Wu, C.-Y. Mou and H.-P. Lin, *Chemical Society Reviews*, 2013, **42**, 3862-3875.
35. H.-P. Lin and C.-P. Tsai, *Chemistry letters*, 2003, **32**, 1092-1093.

36. C. Fowler, D. Khushalani, B. Lebeau and S. Mann, *Advanced Materials*, 2001, **13**, 649-652.
37. M.-C. Chao, H.-P. Lin, C.-Y. Mou, B.-W. Cheng and C.-F. Cheng, *Catalysis today*, 2004, **97**, 81-87.
38. Q. Cai, Z.-S. Luo, W.-Q. Pang, Y.-W. Fan, X.-H. Chen and F.-Z. Cui, *Chemistry of materials*, 2001, **13**, 258-263.
39. K. Moller, J. Kobler and T. Bein, *Advanced Functional Materials*, 2007, **17**, 605-612.
40. C. Urata, Y. Aoyama, A. Tonegawa, Y. Yamauchi and K. Kuroda, *Chemical Communications*, 2009, 5094-5096.
41. J. Rathousky, M. Zukalova, P. J. Kooyman and A. Zukal, *Colloids and Surfaces A: Physicochemical and Engineering Aspects*, 2004, **241**, 81-86.
42. R. I. Nooney, D. Thirunavukkarasu, Y. Chen, R. Josephs and A. E. Ostafin, *Chemistry of materials*, 2002, **14**, 4721-4728.
43. Y.-S. Lin and C. L. Haynes, *Chemistry of Materials*, 2009, **21**, 3979-3986.
44. T. Yokoi, Y. Sakamoto, O. Terasaki, Y. Kubota, T. Okubo and T. Tatsumi, *Journal of the American Chemical Society*, 2006, **128**, 13664-13665.
45. K. Suzuki, K. Ikari and H. Imai, *Journal of the American Chemical Society*, 2004, **126**, 462-463.
46. K. Ikari, K. Suzuki and H. Imai, *Langmuir*, 2006, **22**, 802-806.
47. G. A. Parks, *Chemical Reviews*, 1965, **65**, 177-198.
48. H.-P. Lin and C.-Y. Mou, *Accounts of chemical research*, 2002, **35**, 927-935.
49. Q. Huo, D. I. Margolese, U. Ciesla, P. Feng, T. E. Gier, P. Sieger, R. Leon, P. M. Petroff, F. Schüth and G. D. Stucky, *Nature*, 1994, **368**, 317.
50. Q. Huo, D. I. Margolese, U. Ciesla, D. G. Demuth, P. Feng, T. E. Gier, P. Sieger, A. Firouzi and B. F. Chmelka, *Chemistry of Materials*, 1994, **6**, 1176-1191.
51. D. Niu, Z. Ma, Y. Li and J. Shi, *Journal of the American Chemical Society*, 2010, **132**, 15144-15147.
52. U. Schubert, *Synthesis of inorganic materials*, John Wiley & Sons, 2012.
53. P. Gómez-Romero and C. Sanchez, *Functional hybrid materials*, 2004, 1-14.
54. F. Hoffmann, M. Cornelius, J. Morell and M. Fröba, *Angewandte Chemie International Edition*, 2006, **45**, 3216-3251.

55. A. Walcarius, M. Etienne and B. Lebeau, *Chemistry of materials*, 2003, **15**, 2161-2173.
56. A. Matsumoto, K. Tsutsumi, K. Schumacher and K. K. Unger, *Langmuir*, 2002, **18**, 4014-4019.
57. K. Y. Ho, G. McKay and K. L. Yeung, *Langmuir*, 2003, **19**, 3019-3024.
58. H. Yoshitake, T. Yokoi and T. Tatsumi, *Chemistry of Materials*, 2002, **14**, 4603-4610.
59. A. Liu, K. Hidajat, S. Kawi and D. Zhao, *Chemical Communications*, 2000, 1145-1146.
60. C. Lei, Y. Shin, J. Liu and E. J. Ackerman, *Journal of the American Chemical Society*, 2002, **124**, 11242-11243.
61. H. Y. Huang, R. T. Yang, D. Chinn and C. L. Munson, *Industrial & Engineering Chemistry Research*, 2003, **42**, 2427-2433.
62. R. A. Khatri, S. S. Chuang, Y. Soong and M. Gray, *Industrial & Engineering Chemistry Research*, 2005, **44**, 3702-3708.
63. T. Yokoi, H. Yoshitake and T. Tatsumi, *Journal of Materials Chemistry*, 2004, **14**, 951-957.
64. F. Zheng, D. N. Tran, B. J. Busche, G. E. Fryxell, R. S. Addleman, T. S. Zemanian and C. L. Aardahl, *Industrial & Engineering Chemistry Research*, 2005, **44**, 3099-3105.
65. P. Trens, M. L. Russell, L. Spjuth, M. J. Hudson and J.-O. Liljezin, *Industrial & engineering chemistry research*, 2002, **41**, 5220-5225.
66. L. Mercier and T. J. Pinnavaia, *Environmental Science & Technology*, 1998, **32**, 2749-2754.
67. V. Antochshuk and M. Jaroniec, *Chemical Communications*, 2002, 258-259.
68. V. Antochshuk, O. Olkhovyk, M. Jaroniec, I.-S. Park and R. Ryoo, *Langmuir*, 2003, **19**, 3031-3034.
69. O. Olkhovyk, V. Antochshuk and M. Jaroniec, *Colloids and Surfaces A: Physicochemical and Engineering Aspects*, 2004, **236**, 69-72.
70. K. Venkatesan, T. Srinivasan and P. Vasudeva Rao, *Journal of radioanalytical and nuclear chemistry*, 2003, **256**, 213-218.
71. T. Kang, Y. Park, K. Choi, J. S. Lee and J. Yi, *Journal of Materials Chemistry*, 2004, **14**, 1043-1049.

72. T. Kang, Y. Park and J. Yi, *Industrial & Engineering Chemistry Research*, 2004, **43**, 1478-1484.
73. G. Armatas, C. Salmas, M. Louloudi, G. Androutsopoulos and P. Pomonis, *Langmuir*, 2003, **19**, 3128-3136.
74. G. Rodríguez-López, M. D. Marcos, R. Martínez-Máñez, F. Sancenón, J. Soto, L. A. Villaescusa, D. Beltrán and P. Amorós, *Chemical Communications*, 2004, 2198-2199.
75. M. H. Lim and A. Stein, *Chemistry of Materials*, 1999, **11**, 3285-3295.
76. S. Huh, J. W. Wiench, J.-C. Yoo, M. Pruski and V. S.-Y. Lin, *Chemistry of materials*, 2003, **15**, 4247-4256.
77. S. L. Burkett, S. D. Sims and S. Mann, *Chemical Communications*, 1996, 1367-1368.
78. L. Mercier and T. J. Pinnavaia, *Chemistry of Materials*, 2000, **12**, 188-196.
79. C. E. Fowler, S. L. Burkett and S. Mann, *Chemical Communications*, 1997, 1769-1770.
80. R. Richer, *Chemical Communications*, 1998, 1775-1777.
81. A. Walcarius and C. Delacôte, *Chemistry of materials*, 2003, **15**, 4181-4192.
82. S. Hall and C. Fowler, *Chemical Communications*, 1999, 201-202.
83. D. J. Macquarrie, *Chemical Communications*, 1996, 1961-1962.
84. A. Maria Chong and X. Zhao, *The Journal of Physical Chemistry B*, 2003, **107**, 12650-12657.
85. D. Macquarrie, D. Jackson, J. G. Mdoe and J. Clark, *New journal of chemistry*, 1999, **23**, 539-544.
86. T. Yokoi, H. Yoshitake and T. Tatsumi, *Chemistry of materials*, 2003, **15**, 4536-4538.
87. N. Liu, R. A. Assink, B. Smarsly and C. J. Brinker, *Chemical Communications*, 2003, 1146-1147.
88. F. Cagnol, D. Grosso and C. Sanchez, *Chemical Communications*, 2004, 1742-1743.
89. M. H. Lim, C. F. Blanford and A. Stein, *Journal of the American Chemical Society*, 1997, **119**, 4090-4091.
90. Y. Wang, C. Yang, B. Zibrowius, B. Spliethoff, M. Lindén and F. Schüth, *Chemistry of materials*, 2003, **15**, 5029-5035.

91. Y. Wang, B. Zibrowius, C.-M. Yang, B. Spliethoff and F. Schüth, *Chemical Communications*, 2004, 46-47.
92. R. J. Corriu, C. Hoarau, A. Mehdi and C. Reyé, *Chemical Communications*, 2000, 71-72.
93. C. M. Bambrough, R. C. Slade and R. T. Williams, *Journal of Materials Chemistry*, 1998, **8**, 569-571.
94. R. C. Slade, C. M. Bambrough and R. T. Williams, *Physical Chemistry Chemical Physics*, 2002, **4**, 5394-5399.
95. T. Asefa, M. Kruk, M. J. MacLachlan, N. Coombs, H. Grondey, M. Jaroniec and G. A. Ozin, *Advanced Functional Materials*, 2001, **11**, 447-456.
96. M. H. Lim, C. F. Blanford and A. Stein, *Chemistry of materials*, 1998, **10**, 467-470.
97. W. Van Rhijn, D. De Vos, B. Sels and W. Bossaert, *Chemical communications*, 1998, 317-318.
98. I. Díaz Carretero, C. Márquez Álvarez, F. Mohino, J. Pérez Pariente and E. Sastre, 2000.
99. V. Ganesan and A. Walcarius, *Langmuir*, 2004, **20**, 3632-3640.
100. D. Margolese, J. Melero, S. Christiansen, B. Chmelka and G. Stucky, *Chemistry of Materials*, 2000, **12**, 2448-2459.
101. C.-m. Yang, B. Zibrowius and F. Schüth, *Chemical Communications*, 2003, 1772-1773.
102. R. J. Corriu, L. Datas, Y. Guari, A. Mehdi, C. Reyé and C. Thieuleux, *Chemical Communications*, 2001, 763-764.
103. S. Inagaki, S. Guan, Y. Fukushima, T. Ohsuna and O. Terasaki, *Journal of the American Chemical Society*, 1999, **121**, 9611-9614.
104. B. J. Melde, B. T. Holland, C. F. Blanford and A. Stein, *Chemistry of Materials*, 1999, **11**, 3302-3308.
105. T. Asefa, M. J. MacLachlan, N. Coombs and G. A. Ozin, *Nature*, 1999, **402**, 867.
106. K. Landskron and G. A. Ozin, *Science*, 2004, **306**, 1529-1532.
107. W. J. Hunks and G. A. Ozin, *Advanced Functional Materials*, 2005, **15**, 259-266.
108. C. Yoshina-Ishii, T. Asefa, N. Coombs, M. J. MacLachlan and G. A. Ozin, *Chemical Communications*, 1999, 2539-2540.



109. G. Temtsin, T. Asefa, S. Bittner and G. A. Ozin, *Journal of Materials Chemistry*, 2001, **11**, 3202-3206.
110. M. P. Kapoor, Q. Yang and S. Inagaki, *Journal of the American Chemical Society*, 2002, **124**, 15176-15177.
111. A. Sayari and W. Wang, *Journal of the American Chemical Society*, 2005, **127**, 12194-12195.
112. M. P. Kapoor, Q. Yang and S. Inagaki, *Chemistry of materials*, 2004, **16**, 1209-1213.
113. W. J. Hunks and G. A. Ozin, *Chemical Communications*, 2004, 2426-2427.
114. W. J. Hunks and G. A. Ozin, *Chemistry of materials*, 2004, **16**, 5465-5472.
115. M. Kuroki, T. Asefa, W. Whitnal, M. Kruk, C. Yoshina-Ishii, M. Jaroniec and G. A. Ozin, *Journal of the American Chemical Society*, 2002, **124**, 13886-13895.
116. S. Kango, S. Kalia, A. Celli, J. Njuguna, Y. Habibi and R. Kumar, *Progress in Polymer Science*, 2013, **38**, 1232-1261.
117. V. Cauda, C. Argyo and T. Bein, *Journal of Materials Chemistry*, 2010, **20**, 8693-8699.
118. Y. Yang, X. Yan, Y. Cui, Q. He, D. Li, A. Wang, J. Fei and J. Li, *Journal of Materials Chemistry*, 2008, **18**, 5731-5737.
119. L. Yuan, Q. Tang, D. Yang, J. Z. Zhang, F. Zhang and J. Hu, *The Journal of Physical Chemistry C*, 2011, **115**, 9926-9932.
120. J. L. Paris, M. V. Cabañas, M. Manzano and M. Vallet-Regí, *ACS nano*, 2015, **9**, 11023-11033.
121. M. I. Gibson and R. K. O'Reilly, *Chemical society reviews*, 2013, **42**, 7204-7213.
122. Y. Tran and P. Auroy, *Journal of the American Chemical Society*, 2001, **123**, 3644-3654.
123. P. Mansky, Y. Liu, E. Huang, T. Russell and C. Hawker, *Science*, 1997, **275**, 1458-1460.
124. O. Prucker and J. Rühe, *Macromolecules*, 1998, **31**, 592-601.
125. G. Kickelbick, *Progress in polymer science*, 2003, **28**, 83-114.
126. N. Tsubokawa, A. Kogure and Y. Sone, *Journal of Polymer Science Part A: Polymer Chemistry*, 1990, **28**, 1923-1933.

127. T. von Werne and T. E. Patten, *Journal of the American Chemical Society*, 2001, **123**, 7497-7505.
128. Y.-H. Lien and T.-M. Wu, *Journal of colloid and interface science*, 2008, **326**, 517-521.
129. Y. Zhu, H. S. Sundaram, S. Liu, L. Zhang, X. Xu, Q. Yu, J. Xu and S. Jiang, *Biomacromolecules*, 2014, **15**, 1845-1851.
130. T. Yu, A. Malugin and H. Ghandehari, *ACS nano*, 2011, **5**, 5717-5728.
131. M. A. Maurer-Jones, Y.-S. Lin and C. L. Haynes, *ACS nano*, 2010, **4**, 3363-3373.
132. I. I. Slowing, C. W. Wu, J. L. Vivero-Escoto and V. S. Y. Lin, *Small*, 2009, **5**, 57-62.
133. Y.-S. Lin and C. L. J. J. o. t. A. C. S. Haynes, 2010, **132**, 4834-4842.
134. S. Lee, H.-S. Yun and S.-H. J. B. Kim, 2011, **32**, 9434-9443.
135. I. Slowing, B. G. Trewyn and V. S.-Y. Lin, *Journal of the American Chemical Society*, 2006, **128**, 14792-14793.
136. A. Verma and F. J. S. Stellacci, 2010, **6**, 12-21.
137. A. E. Nel, L. Mädler, D. Velegol, T. Xia, E. M. Hoek, P. Somasundaran, F. Klaessig, V. Castranova and M. J. N. m. Thompson, 2009, **8**, 543.
138. H. Nabeshi, T. Yoshikawa, K. Matsuyama, Y. Nakazato, K. Matsuo, A. Arimori, M. Isobe, S. Tochigi, S. Kondoh and T. Hirai, *Biomaterials*, 2011, **32**, 2713-2724.
139. F. Rancan, Q. Gao, C. Graf, S. Troppens, S. Hadam, S. Hackbarth, C. Kembuan, U. Blume-Peytavi, E. Rühl and J. r. Lademann, *ACS nano*, 2012, **6**, 6829-6842.
140. A. Awaad, M. Nakamura and K. Ishimura, *Nanomedicine: Nanotechnology, Biology and Medicine*, 2012, **8**, 627-636.
141. R. L. Owen and A. L. Jones, *Gastroenterology*, 1974, **66**, 189-203.
142. F. Lu, S. H. Wu, Y. Hung and C. Y. Mou, *Small*, 2009, **5**, 1408-1413.
143. B. D. Chithrani, A. A. Ghazani and W. C. J. N. I. Chan, 2006, **6**, 662-668.
144. F. Osaki, T. Kanamori, S. Sando, T. Sera and Y. Aoyama, 2004, **126**, 6520-6521.
145. X. Huang, L. Li, T. Liu, N. Hao, H. Liu, D. Chen and F. Tang, *ACS nano*, 2011, **5**, 5390-5399.

146. G. Xie, J. Sun and G. Zhong, *Journal of Nanoparticle Research*, 2012, **14**, 671.
147. X. He, H. Nie, K. Wang, W. Tan, X. Wu and P. Zhang, *Analytical chemistry*, 2008, **80**, 9597-9603.
148. T. Liu, L. Li, X. Teng, X. Huang, H. Liu, D. Chen, J. Ren, J. He and F. Tang, *Biomaterials*, 2011, **32**, 1657-1668.
149. C. Fu, T. Liu, L. Li, H. Liu, D. Chen and F. Tang, *Biomaterials*, 2013, **34**, 2565-2575.
150. K. Takeda, K.-i. Suzuki, A. Ishihara, M. Kubo-Irie, R. Fujimoto, M. Tabata, S. Oshio, Y. Nihei, T. Ihara and M. Sugamata, 2009, **55**, 95-102.
151. M. Shimizu, H. Tainaka, T. Oba, K. Mizuo, M. Umezawa and K. J. P. a. f. t. Takeda, 2009, **6**, 20.
152. F. Tian, D. Razansky, G. G. Estrada, M. Semmler-Behnke, A. Beyerle, W. Kreyling, V. Ntziachristos and T. J. I. t. Stoeger, 2009, **21**, 92-96.
153. M. Saunders, 2009, **1**, 671-684.
154. M. Chu, Q. Wu, H. Yang, R. Yuan, S. Hou, Y. Yang, Y. Zou, S. Xu, K. Xu and A. J. S. Ji, 2010, **6**, 670-678.
155. K. S. Hougaard, P. Jackson, K. A. Jensen, J. J. Sloth, K. Löschner, E. H. Larsen, R. K. Birkedal, A. Vibenholt, A.-M. Z. Boisen and H. Wallin, 2010, **7**, 16.
156. K. Yamashita, Y. Yoshioka, K. Higashisaka, K. Mimura, Y. Morishita, M. Nozaki, T. Yoshida, T. Ogura, H. Nabeshi and K. Nagano, *Nature nanotechnology*, 2011, **6**, 321.
157. A. E. J. N. Garcia-Bennett, 2011, **6**, 867-877.
158. A. Bitar, N. M. Ahmad, H. Fessi and A. Elaissari, *Drug Discovery Today*, 2012, **17**, 1147-1154.
159. F. Tang, L. Li and D. Chen, *Advanced materials*, 2012, **24**, 1504-1534.
160. P. Tallury, K. Payton and S. Santra, 2008.
161. A. Azioune, A. Ben Slimane, L. Ait Hamou, A. Pleuvy, M. M. Chehimi, C. Perruchot and S. P. J. L. Armes, 2004, **20**, 3350-3356.
162. S. H. Kim, M. Jeyakumar and J. Katzenellenbogen, 2007, **129**, 13254-13264.
163. E. Kang, J.-W. Park, S. J. McClellan, J.-M. Kim, D. P. Holland, G. U. Lee, E. I. Franses, K. Park and D. Thompson, 2007, **23**, 6281-6288.

164. T. Shiomi, M. Matsui, F. Mizukami and K. J. B. Sakaguchi, 2005, **26**, 5564-5571.
165. Y. Wang, K.-Y. Pu and B. J. L. Liu, 2010, **26**, 10025-10030.
166. L. R. Hilliard, X. Zhao and W. J. A. C. A. Tan, 2002, **470**, 51-56.
167. A. Y. Gore and G. Banker, 1979, **68**, 197-202.
168. G. Ragnarsson, A. Hölzer and J. Sjögren, 1979, **3**, 127-131.
169. S. Jonat, S. Hasenzahl, M. Drechsler, P. Albers, K. Wagner and P. Schmidt, 2004, **141**, 31-43.
170. M. Vallet-Regi, A. Ramila, R. Del Real and J. Pérez-Pariente, 2001, **13**, 308-311.
171. A. M. Chen, M. Zhang, D. Wei, D. Stueber, O. Taratula, T. Minko and H. J. S. He, 2009, **5**, 2673-2677.
172. J. Lu, M. Liong, J. I. Zink and F. J. s. Tamanoi, 2007, **3**, 1341-1346.
173. J. Gu, S. Su, Y. Li, Q. He, J. Zhong and J. Shi, 2010, **1**, 3446-3450.
174. R. Mellaerts, R. Mols, J. A. Jammaer, C. A. Aerts, P. Annaert, J. Van Humbeeck, G. Van den Mooter, P. Augustijns and J. Martens, 2008, **69**, 223-230.
175. D. Lozano, M. Manzano, J. C. Doadrio, A. J. Salinas, M. Vallet-Regí, E. Gómez-Barrena and P. Esbrit, 2010, **6**, 797-803.
176. M. Zhu, H. Wang, J. Liu, H. He, X. Hua, Q. He, L. Zhang, X. Ye and J. J. B. Shi, 2011, **32**, 1986-1995.
177. M. Vallet-Regí, 2006, **12**, 5934-5943.
178. A. Suwalski, H. Dabboue, A. Delalande, S. F. Bensamoun, F. Canon, P. Midoux, G. Saillant, D. Klatzmann, J.-P. Salvétat and C. J. B. Pichon, 2010, **31**, 5237-5245.
179. H. J. Kim, H. Matsuda, H. Zhou and I. J. A. M. Honma, 2006, **18**, 3083-3088.
180. Y. Zhao, B. G. Trewyn, I. I. Slowing and V. Lin, 2009, **131**, 8398-8400.
181. B. Moulari, D. Pertuit, Y. Pellequer and A. J. B. Lamprecht, 2008, **29**, 4554-4560.
182. S. Hudson, J. Cooney and E. J. Magner, 2008, **47**, 8582-8594.
183. T. P. B. Nguyen, J.-W. Lee, W. G. Shim and H. Moon, 2008, **110**, 560-569.
184. J. Zhang, L.-M. Postovit, D. Wang, R. B. Gardiner, R. Harris, M. Abdul and A. J. Thomas, 2009, **4**, 1297.

185. J. Cai, J. Yang and D. Jones, *Biochimica et Biophysica Acta (BBA)-Bioenergetics*, 1998, **1366**, 139-149.
186. I. I. Slowing, B. G. Trewyn and V. Lin, 2007, **129**, 8845-8849.
187. G. U. Dachs, G. J. Dougherty, I. J. Stratford and D. J. Chaplin, *Oncology Research Featuring Preclinical and Clinical Cancer Therapeutics*, 1997, **9**, 313-325.
188. D. R. Radu, C.-Y. Lai, K. Jeftinija, E. W. Rowe, S. Jeftinija and V. Lin, 2004, **126**, 13216-13217.
189. C. Hom, J. Lu, M. Liong, H. Luo, Z. Li, J. I. Zink and F. J. S. Tamanoi, 2010, **6**, 1185-1190.
190. I. Y. Park, I. Y. Kim, M. K. Yoo, Y. J. Choi, M.-H. Cho and C. Cho, 2008, **359**, 280-287.
191. T. Xia, M. Kovochich, M. Liong, H. Meng, S. Kabehie, S. George, J. I. Zink and A. Nel, 2009, **3**, 3273-3286.
192. J.-P. Behr, *CHIMIA International Journal for Chemistry*, 1997, **51**, 34-36.
193. F. Gao, P. Botella, A. Corma, J. Blesa and L. J. Dong, 2009, **113**, 1796-1804.
194. M.-H. Kim, H.-K. Na, Y.-K. Kim, S.-R. Ryoo, H. S. Cho, K. E. Lee, H. Jeon, R. Ryoo and D. Min, 2011, **5**, 3568-3576.
195. X. Li, Q. R. Xie, J. Zhang, W. Xia and H. J. B. Gu, 2011, **32**, 9546-9556.
196. X. Li, J. Zhang and H. J. L. Gu, 2011, **27**, 6099-6106.
197. C. E. Ashley, E. C. Carnes, G. K. Phillips, D. Padilla, P. N. Durfee, P. A. Brown, T. N. Hanna, J. Liu, B. Phillips and M. B. Carter, 2011, **10**, 389.
198. Y. Zhu, T. Ikoma, N. Hanagata and S. J. S. Kaskel, 2010, **6**, 471-478.
199. S. R. Bhattarai, E. Muthuswamy, A. Wani, M. Brichacek, A. L. Castañeda, S. L. Brock and D. J. Oupicky, 2010, **27**, 2556-2568.
200. Y. Matsumura and H. J. Maeda, 1986, **46**, 6387-6392.
201. R. Li, K. Zheng, C. Yuan, Z. Chen and M. Huang, *Nanotheranostics*, 2017, **1**, 346.
202. F. Danhier, *Journal of Controlled Release*, 2016, **244**, 108-121.
203. T. Lammers, F. Kiessling, W. E. Hennink and G. J. Storm, 2012, **161**, 175-187.
204. R. K. Jain and T. Stylianopoulos, 2010, **7**, 653.
205. J. W. Nichols and Y. Bae, 2012, **7**, 606-618.

206. J. I. Hare, T. Lammers, M. B. Ashford, S. Puri, G. Storm and S. T. Barry, 2017, **108**, 25-38.
207. C.-Y. Lai, B. G. Trewyn, D. M. Jeftinija, K. Jeftinija, S. Xu, S. Jeftinija and V. S.-Y. Lin, *Journal of the American Chemical Society*, 2003, **125**, 4451-4459.
208. J. L. Vivero-Escoto, I. I. Slowing, C.-W. Wu and V. Lin, 2009, **131**, 3462-3463.
209. S. Giri, B. G. Trewyn, M. P. Stellmaker and V. S. Y. Lin, *Angewandte Chemie International Edition*, 2005, **44**, 5038-5044.
210. N. K. Mal, M. Fujiwara and Y. J. N. Tanaka, 2003, **421**, 350.
211. Q. Lin, Q. Huang, C. Li, C. Bao, Z. Liu, F. Li and L. Zhu, 2010, **132**, 10645-10647.
212. S. Angelos, E. Choi, F. Vögtle, L. De Cola and J. I. Zink, 2007, **111**, 6589-6592.
213. Y. Zhu and M. J. A. C. I. E. Fujiwara, 2007, **46**, 2241-2244.
214. T. D. Nguyen, K. F. Leung, M. Liong, Y. Liu, J. F. Stoddart and J. Zink, 2007, **17**, 2101-2110.
215. C. Park, K. Oh, S. C. Lee and C. J. A. C. I. E. Kim, 2007, **46**, 1455-1457.
216. S. Angelos, N. M. Khashab, Y.-W. Yang, A. Trabolsi, H. A. Khatib, J. F. Stoddart and J. I. Zink, 2009, **131**, 12912-12914.
217. A. Schlossbauer, C. Dohmen, D. Schaffert, E. Wagner and T. J. Bein, 2011, **50**, 6828-6830.
218. F. Muhammad, M. Guo, W. Qi, F. Sun, A. Wang, Y. Guo and G. Zhu, 2011, **133**, 8778-8781.
219. X. Zhang, L. Clime, H. Roberge, F. Normandin, L. H. Yahia, E. Sacher and T. Veres, 2010, **115**, 1436-1443.
220. X. Wan, D. Wang and S. J. Liu, 2010, **26**, 15574-15579.
221. R. Liu, X. Zhao, T. Wu and P. J. Feng, 2008, **130**, 14418-14419.
222. A. M. Sauer, A. Schlossbauer, N. Ruthardt, V. Cauda, T. Bein and C. J. Bräuchle, 2010, **10**, 3684-3691.
223. S.-H. Hu, T.-Y. Liu, H.-Y. Huang, D.-M. Liu and S. Chen, 2008, **24**, 239-244.
224. Y. Zhu, H. Liu, F. Li, Q. Ruan, H. Wang, M. Fujiwara, L. Wang and G. J. Lu, 2010, **132**, 1450-1451.

225. A. Schlossbauer, J. Kecht and T. Bein, 2009, **48**, 3092-3095.
226. A. Bernardos, E. Aznar, M. D. Marcos, R. Martínez-Máñez, F. Sancenón, J. Soto, J. M. Barat and P. J. Amorós, 2009, **121**, 5998-6001.
227. A. Bernardos, L. Mondragon, E. Aznar, M. D. Marcos, R. Martínez-Máñez, F. Sancenón, J. Soto, J. M. Barat, E. Pérez-Payá and C. J. Guillem, 2010, **4**, 6353-6368.
228. Y. Itoh, M. Matsusaki, T. Kida and M. J. B. Akashi, 2006, **7**, 2715-2718.
229. K. Patel, S. Angelos, W. R. Dichtel, A. Coskun, Y.-W. Yang, J. I. Zink and J. Stoddart, 2008, **130**, 2382-2383.
230. R. Liu, Y. Zhang and P. J. J. o. t. A. C. S. Feng, 2009, **131**, 15128-15129.
231. N. M. Khashab, A. Trabolsi, Y. A. Lau, M. W. Ambrogio, D. C. Friedman, H. A. Khatib, J. I. Zink and J. F. Stoddart, 2009, **2009**, 1669-1673.
232. E. Aznar, M. D. Marcos, R. Martínez-Máñez, F. Sancenón, J. Soto, P. Amorós and C. Guillem, *Journal of the American Chemical Society*, 2009, **131**, 6833-6843.
233. H. P. Rim, K. H. Min, H. J. Lee, S. Y. Jeong and S. Lee, 2011, **50**, 8853-8857.
234. X. Huang, X. Peng, Y. Wang, Y. Wang, D. M. Shin, M. A. El-Sayed and S. J. A. n. Nie, 2010, **4**, 5887-5896.
235. J. M. Rosenholm, E. Peuhu, L. T. Bate-Eya, J. E. Eriksson, C. Sahlgren and M. J. S. Lindén, 2010, **6**, 1234-1241.
236. J. M. Rosenholm, E. Peuhu, J. E. Eriksson, C. Sahlgren and M. Lindén, 2009, **9**, 3308-3311.
237. J. M. Rosenholm, A. Meinander, E. Peuhu, R. Niemi, J. E. Eriksson, C. Sahlgren and M. J. Lindén, 2008, **3**, 197-206.
238. D. P. Ferris, J. Lu, C. Gothard, R. Yanes, C. R. Thomas, J. C. Olsen, J. F. Stoddart, F. Tamanoi and J. I. Zink, 2011, **7**, 1816-1826.
239. C.-L. Zhu, X.-Y. Song, W.-H. Zhou, H.-H. Yang, Y.-H. Wen and X. Wang, 2009, **19**, 7765-7770.
240. C.-P. Tsai, C.-Y. Chen, Y. Hung, F.-H. Chang and C. Mou, 2009, **19**, 5737-5743.
241. L. Li, Y. Guan, H. Liu, N. Hao, T. Liu, X. Meng, C. Fu, Y. Li, Q. Qu and Y. J. A. Zhang, 2011, **5**, 7462-7470.
242. I. I. Rabi, S. Millman, P. Kusch and J. R. Zacharias, 1939, **55**, 526.

243. J. Kellogg, I. Rabi, N. Ramsey Jr and J. J. Zacharias, 1939, **56**, 728.
244. F. J. Bloch, 1946, **70**, 460.
245. E. M. Purcell, H. C. Torrey and R. V. J. Pound, 1946, **69**, 37.
246. R. J. S. Damadian, 1971, **171**, 1151-1153.
247. P. C. Lauterbur, *Nature*, 1973, **242**, 190-191.
248. P. Mansfield and P. K. Grannell, 1973, **6**, L422.
249. P. Mansfield and A. J. Maudsley, 1977, **50**, 188-194.
250. P. Mansfield, I. Pykett, P. Morris and R. J. Coupland, 1978, **51**, 921-922.
251. N. Bloembergen and L. J. T. J. o. C. P. Morgan, 1961, **34**, 842-850.
252. W. Louisell, R. Pidd and H. J. P. R. Crane, 1954, **94**, 7.
253. I. Solomon and N. J. Bloembergen, 1956, **25**, 261-266.
254. M. P. Lowe, D. Parker, O. Reany, S. Aime, M. Botta, G. Castellano, E. Gianolio and R. Pagliarin, *Journal of the American Chemical Society*, 2001, **123**, 7601-7609.
255. P. Caravan, *Chemical Society Reviews*, 2006, **35**, 512-523.
256. M. H. M. Dias and P. C. Lauterbur, *Magnetic resonance in medicine*, 1986, **3**, 328-330.
257. T. J. Fraum, D. R. Ludwig, M. R. Bashir and K. J. Fowler, *Journal of Magnetic Resonance Imaging*, 2017, **46**, 338-353.
258. D. C. Kalogeromitros, M. P. Makris, X. S. Aggelides, N. Spanoudaki, S. G. Gregoriou, G. Avgerinou and D. G. Rigopoulos, *International archives of allergy and immunology*, 2007, **144**, 150-154.
259. D. W. Raisch, V. Garg, R. Arabyat, X. Shen, B. J. Edwards, F. H. Miller, J. M. McKoy, B. Nardone and D. P. West, *Expert opinion on drug safety*, 2014, **13**, 15-23.
260. J. Weber, K. Rainsford and G. Velo, Raven Press, New York, Editon edn., 1984.
261. A. F. Lalli, *Radiology*, 1980, **134**, 1-12.
262. J.-W. Jung, H.-R. Kang, M.-H. Kim, W. Lee, K.-U. Min, M.-H. Han and S.-H. Cho, *Radiology*, 2012, **264**, 414-422.
263. S. Aran, K. Shaqdan and H. Abujudeh, *Clinical radiology*, 2015, **70**, 466-475.
264. M. R. Prince, H. Zhang, Z. Zou, R. B. Staron and P. W. Brill, *American Journal of Roentgenology*, 2011, **196**, W138-W143.



265. T. Kanda, K. Ishii, H. Kawaguchi, K. Kitajima and D. Takenaka, *Radiology*, 2013, **270**, 834-841.
266. T. Kanda, T. Fukusato, M. Matsuda, K. Toyoda, H. Oba, J. i. Kotoku, T. Haruyama, K. Kitajima and S. Furui, *Radiology*, 2015, **276**, 228-232.
267. P. Robert, S. Lehericy, S. Grand, X. Violas, N. Fretellier, J.-M. Idée, S. Ballet and C. Corot, *Investigative radiology*, 2015, **50**, 473.
268. M. Tweedle, G. Gaughan, J. Hagan, P. Wedeking, P. Sibley, L. J. Wilson and D. W. Lee, *International Journal of Radiation Applications and Instrumentation. Part B. Nuclear Medicine and Biology*, 1988, **15**, 31-36.
269. S. Morcos, *European journal of radiology*, 2008, **66**, 175-179.
270. J.-C. Bousquet, S. Saini, D. Stark, P. Hahn, M. Nigam, J. Wittenberg and J. Ferrucci Jr, *Radiology*, 1988, **166**, 693-698.
271. D. Hao, T. Ai, F. Goerner, X. Hu, V. M. Runge and M. Tweedle, *Journal of Magnetic Resonance Imaging*, 2012, **36**, 1060-1071.
272. R. J. McDonald, J. S. McDonald, D. F. Kallmes, M. E. Jentoft, D. L. Murray, K. R. Thielen, E. E. Williamson and L. J. Eckel, *Radiology*, 2015, **275**, 772-782.
273. L. Mariane and P. Caravan, *Metallomics*, 2018.
274. W. A. Gibby, K. A. Gibby and W. A. Gibby, *Investigative radiology*, 2004, **39**, 138-142.
275. K. N. Christensen, C. U. Lee, M. M. Hanley, N. Leung, T. P. Moyer and M. R. Pittelkow, *Journal of the American Academy of Dermatology*, 2011, **64**, 91-96.
276. N. Maximova, M. Gregori, F. Zennaro, A. Sonzogni, R. Simeone and D. Zanon, *Radiology*, 2016, **281**, 418-426.
277. T. Grobner, *Nephrology Dialysis Transplantation*, 2006, **21**, 1745-1745.
278. P. Marckmann, L. Skov, K. Rossen, A. Dupont, M. B. Damholt, J. G. Heaf and H. S. Thomsen, *Journal of the American Society of Nephrology*, 2006, **17**, 2359-2362.
279. M. R. Prince, H. L. Zhang, G. H. Roditi, T. Leiner and W. Kucharczyk, *Journal of Magnetic Resonance Imaging: An Official Journal of the International Society for Magnetic Resonance in Medicine*, 2009, **30**, 1298-1308.

280. H. H. Abujudeh, R. Kaewlai, A. Kagan, L. B. Chibnik, R. M. Nazarian, W. A. High and J. Kay, *Radiology*, 2009, **253**, 81-89.
281. J. G. Do, Y. B. Kim, D. G. Lee and J. H. Hwang, *Annals of rehabilitation medicine*, 2012, **36**, 880-886.
282. T. A. Collidge, P. C. Thomson, P. B. Mark, J. P. Traynor, A. G. Jardine, S. T. W. Morris, K. Simpson and G. H. Roditi, *Radiology*, 2007, **245**, 168-175.
283. K. N. Larson, A. L. Gagnon, M. D. Darling, J. W. Patterson and T. G. Cropley, *JAMA dermatology*, 2015, **151**, 1117-1120.
284. Z. Zou, H. L. Zhang, G. H. Roditi, T. Leiner, W. Kucharczyk and M. R. Prince, *JACC: Cardiovascular Imaging*, 2011, **4**, 1206-1216.
285. E. Smorodinsky, D. S. Ansdell, Z. W. Foster, S. M. Mazhar, I. Cruite, T. Wolfson, S. B. Sugay, G. Iussich, M. Shieh morteza and Y. Kono, *Journal of Magnetic Resonance Imaging*, 2015, **41**, 1259-1267.
286. E. Gheuens, R. Daelemans and S. Mesens, *Investigative radiology*, 2014, **49**, 505-508.
287. M. Rogosnitzky and S. Branch, *Biometals*, 2016, **29**, 365-376.
288. J. G. Ray, M. J. Vermeulen, A. Bharatha, W. J. Montanera and A. L. Park, *Jama*, 2016, **316**, 952-961.
289. P. I. Wang, S. T. Chong, A. Z. Kielar, A. M. Kelly, U. D. Knoepp, M. B. Mazza and M. M. Goodsitt, *American Journal of Roentgenology*, 2012, **198**, 778-784.
290. I. Solomon, *Physical Review*, 1955, **99**, 559.
291. G.-L. Davies, I. Kramberger and J. J. Davis, *Chemical Communications*, 2013, **49**, 9704-9721.
292. Y.-S. Lin, Y. Hung, J.-K. Su, R. Lee, C. Chang, M.-L. Lin and C.-Y. Mou, *The Journal of Physical Chemistry B*, 2004, **108**, 15608-15611.
293. K. M. L. Taylor, J. S. Kim, W. J. Rieter, H. An, W. L. Lin and W. B. Lin, *Journal of the American Chemical Society*, 2008, **130**, 2154-+.
294. J. K. Hsiao, C. P. Tsai, T. H. Chung, Y. Hung, M. Yao, H. M. Liu, C. Y. Mou, C. S. Yang, Y. C. Chen and D. M. Huang, *Small*, 2008, **4**, 1445-1452.
295. J. C. Frias, Y. Ma, K. J. Williams, Z. A. Fayad and E. A. Fisher, *Nano letters*, 2006, **6**, 2220-2224.
296. N. Wartenberg, P. Fries, O. Raccurt, A. Guillermo, D. Imbert and M. Mazzanti, *Chemistry–A European Journal*, 2013, **19**, 6980-6983.

297. F. Carniato, L. Tei, W. Dastru, L. Marchese and M. Botta, *Chemical Communications*, 2009, 1246-1248.
298. F. Carniato, L. Tei, M. Cossi, L. Marchese and M. Botta, *Chemistry–A European Journal*, 2010, **16**, 10727-10734.
299. J. J. Davis, W.-Y. Huang and G.-L. Davies, *Journal of materials chemistry*, 2012, **22**, 22848-22850.
300. D. Ş. Karaman, D. Desai, J. Zhang, S. Tadayon, G. Unal, J. Teuho, J. Sarfraz, J.-H. Smått, H. Gu and T. Näreaja, *Journal of Materials Chemistry B*, 2016, **4**, 1720-1732.
301. B. G. Cha and J. Kim, *Wiley Interdisciplinary Reviews: Nanomedicine and Nanobiotechnology*, 2018, e1515.
302. W. Fan, B. Shen, W. Bu, F. Chen, Q. He, K. Zhao, S. Zhang, L. Zhou, W. Peng and Q. Xiao, *Biomaterials*, 2014, **35**, 8992-9002.
303. C. Li, D. Yang, P. a. Ma, Y. Chen, Y. Wu, Z. Hou, Y. Dai, J. Zhao, C. Sui and J. Lin, *Small*, 2013, **9**, 4150-4159.
304. R. Zou, S. Gong, J. Shi, J. Jiao, K.-L. Wong, H. Zhang, J. Wang and Q. Su, *Chemistry of Materials*, 2017, **29**, 3938-3946.
305. C. P. Tsai, Y. Hung, Y. H. Chou, D. M. Huang, J. K. Hsiao, C. Chang, Y. C. Chen and C. Y. Mou, *Small*, 2008, **4**, 186-191.
306. W.-Y. Huang, G.-L. Davies and J. J. Davis, *Chemical Communications*, 2013, **49**, 60-62.
307. K. M. Taylor, J. S. Kim, W. J. Rieter, H. An, W. Lin and W. Lin, *Journal of the American Chemical Society*, 2008, **130**, 2154-2155.

# Chapter 2

## 2. Experimental Methods

---

### 2.1 Materials and General procedures

#### 2.1.1 Starting Materials

Triethanol amine (TEA), triethyl amine, tetraethyl orthosilicate (TEOS), (3-aminopropyl) triethoxysilane (APTES), anhydrous *N, N*-dimethylformamide (DMF), hexadecyltrimethylammonium bromide (CTAB), myristyltrimethylammonium bromide, (MYRI), dodecyltrimethylammonium bromide (DODE),  $\alpha$ -bromoisobutyryl bromide (BIBB), copper bromide, *N*-isopropylacrylamide (NIPAM), 4,4'-azobis (4-cyanovaleric acid) (ACVA), *N*-methyl-*N*-vinyl acetamide (NVA), methacrylic acid (MAA), *N*-hydroxysuccinimide (NHS), *Arachis hypogaea* (peanut agglutinin) and anhydrous  $\text{GdCl}_3$  were all purchased from Sigma Aldrich (Haverhill, UK). Absolute ethanol and aqueous hydrochloric acid (37 v/v%) were supplied by VWR chemicals (Lutterworth, UK). 2,2',2''-(10-(2-((2,5-dioxopyrrolidin-1-yl) oxy)-2-oxoethyl)-1,4,7,10-tetraazacyclododecane-1,4,7-triyl) triacetic acid (DOTA-NHS ester) was supplied by CheMatech (Dijon, France). 1,1,4,7,7-pentamethyldiethyltriamine (PMDETA) was brought from Acros Organics (Geel, Belgium). NHS fluorescein (NHS-FITC) supplied by Thermo Scientific (Loughborough, UK). *N*-(3-dimethylaminopropyl)-*N*-ethylcarbodiimide hydrochloric acid (EDC-HCl) supplied by Apollo Scientific (Stockport, UK). All chemicals were used as provided. Ultrapure water was obtained from a Millipore Milli-Q gradient machine fitted with a 0.22  $\mu\text{m}$  filter operated at 18.2  $\text{M}\Omega$  (at 298 K).

For the cell assays the Human Caucasian colorectal adenocarcinoma cells (SW480 (ECACC 87092801)) were obtained from European Collection of Authenticated Cell Cultures (Nottingham, UK). 75  $\text{cm}^2$  Nunc cell culture flasks, 200  $\mu\text{L}$  of cell culture medium in 96-well plates, 0.25% trypsin 1 mM EDTA balanced salt solution,

Advanced Dulbecco's Modified Eagle (A-DMEM) Medium were supplied by Thermofisher (Rugby, UK). USA-origin foetal bovine serum (FBS), Dulbecco's phosphate buffered saline (PBS) and resazurin sodium salt were supplied by Sigma Aldrich (Haverhill, UK). Penicillin, streptomycin, amphotericin B (PSA) were supplied by HyClone (Utah, USA). All chemicals were used as provided.

## **2.2 Experimental Procedures**

### **2.2.1 Experimental Details for Chapter 3: Investigating the Impact of Nanoparticle Design on MRI Contrast Behaviour**

#### **2.2.1.1 Preparation of Mesoporous Silica Nanoparticles with Pore Diameter Variation**

MSNs were prepared with varying pore diameters, as described below, following previously published techniques.<sup>1-3</sup>

hexadecyltrimethylammonium bromide, CTAB, (0.64 g,  $1.78 \times 10^{-3}$  mol) was added to a solution of MilliQ water (16.02 mL, 0.89 mol) and ethanol (1.84 mL, 0.03 mol). Triethanol amine (TEA; 1.03 g,  $6.9 \times 10^{-3}$  mol) was added and the solution was stirred at 80 °C. Tetraethyl orthosilicate (TEOS; 1.454 mL,  $6.51 \times 10^{-3}$  mol) was added dropwise and the reaction was stirred for 2 hrs at 80 °C. After this time, the mixture was centrifuged (13200 rpm, 20 mins) and the supernatant removed. The nanoparticles were dispersed into an acidified ethanol solution (6 mL, 37% HCl in 40 mL ethanol) using sonication, then centrifuged and the supernatant removed. This was repeated a minimum of three times to remove the surfactant. The nanoparticles were then washed three times with ethanol using the same procedure as for the acid washes and retained in an ethanol suspension for characterisation.

An identical procedure with the same relative amounts of chemicals was used initially for MSNs prepared using Myristyltrimethylammonium bromide, MYRI, and Dodecyltrimethylammonium bromide, DODE. The temperatures of the reactions were then repeated with the reaction temperature lowered to 40 °C and 15 °C for MYRI and DODE respectively.

#### **2.2.1.2 Preparation of Mesoporous Silica Nanoparticles with Amine Location Variation**

MSNs were prepared with amine functional groups present in different loading locations, as described below, following previously published techniques.<sup>4, 5</sup>

The MSNs with amine location variation were prepared using the same protocol as the mesoporous silica nanoparticles with pore variation using CTAB and MYRI surfactants. Except Internally amine functionalised, Internal, MSNs were prepared by

10 mins after dropwise addition of TEOS (1.454 mL,  $6.51 \times 10^{-3}$  mol) at 80 °C (CTAB) or 40 °C (MYRI), APTES/TEOS solution (4.7 µL of a mixture of  $1 \times 10^{-4}$  mol APTES and  $1 \times 10^{-4}$  mol TEOS) was added and the reaction stirred at 80 °C (CTAB) or 40 °C (MYRI) for a further 1 h and 50 mins. For edge amine functionalised, Edge, MSNs the APTES/TEOS solution (4.7 µL of a mixture of  $100 \times 10^{-4}$  mol APTES and  $100 \times 10^{-4}$  mol TEOS) was added 1 hr after dropwise addition of TEOS (1.454 mL,  $6.51 \times 10^{-3}$  mol) at 80 °C (CTAB) or 40 °C (MYRI) and the reaction left at 80 °C (CTAB) or 40 °C (MYRI) for a further 1 hr. Finally, externally amine functionalised, External, MSNs were left at 80 °C (CTAB) or 40 °C (MYRI) for 2 hrs after dropwise addition of TEOS (1.454 mL,  $6.51 \times 10^{-3}$  mol). Then the mixture was centrifuged (13200 rpm, 20 mins), the supernatant removed, and the particles resuspended in a 2:1 volume ratio of ethanol to water solution (10 mL). APTES (2.35 µL,  $1.03 \times 10^{-5}$  mol) was added and this solution allowed to stir overnight at room temperature (~16 hrs). The nanoparticles were dispersed into an acidified ethanol solution (6 mL, 37% HCl in 40 mL ethanol) using sonication, then centrifuged. This was repeated a minimum of three times to remove the surfactant. The nanoparticles were then washed three times with ethanol and retained in an ethanol suspension for characterisation.

#### **2.2.1.3 Gd<sup>3+</sup>-DOTA Functionalisation**

Aminated MSNs (75 mg) were suspended in anhydrous *N, N*-dimethylformamide (DMF; 6 mL,  $7.8 \times 10^{-2}$  mol). DOTA-NHS-ester (2.1 mg,  $2.76 \times 10^{-6}$  mol) and triethylamine (150 µL,  $1.98 \times 10^{-3}$  mol) were added and the suspension was stirred at room temperature overnight (~16 hrs). The nanoparticles were washed with ethanol 3 times using centrifugation (13200 rpm, 20 mins) and re-suspended in ethanol (10 mL,  $1.6 \times 10^{-1}$  mol). Anhydrous GdCl<sub>3</sub> (2.1 mg,  $7.97 \times 10^{-6}$  mol) was added and the suspension was stirred for 24 hrs at room temperature. Purification was carried out *via* dialysis (3.5 kDa Snakeskin dialysis tubing) against MilliQ water for a minimum of 24 hrs, changing the Milli-Q water regularly. Nanoparticles were collected in aqueous suspension for characterisation.

Samples were tested for non-specific Gd<sup>3+</sup> physisorption to nanoparticle surfaces by stirring aminated nanoparticles with GdCl<sub>3</sub> (in the same ratio as used for Gd<sup>3+</sup>-DOTA loading above) overnight at room temperature. Samples were washed using dialysis.

## **2.2.2 Experimental Details for Chapter 4: Thermo-responsive MSNs as Diagnostic MRI Contrast Agents**

### **2.2.2.1 Internally Gd<sup>3+</sup>-DOTA Functionalised MSN synthesis**

CTAB (0.64 g,  $1.78 \times 10^{-3}$  mol) was added to a solution of MilliQ water (16.02 mL, 0.89 mol) and ethanol (1.84 mL, 0.03 mol). TEA (1.03 g,  $6.9 \times 10^{-3}$  mol) was added and the solution was stirred at 80 °C to mix. TEOS (1.45 mL,  $6.5 \times 10^{-3}$  mol) was added dropwise and the reaction stirred for 10 mins at 80 °C. An APTES/TEOS solution (4.7 µL of a mixture containing a 1:1 molar ratio of APTES:TEOS) was added dropwise and the reaction stirred at 80 °C for a further 1 hr and 50 mins. After this time, the mixture was centrifuged (11,000 rpm for 10 mins) and the supernatant removed. The nanoparticles were centrifuged and dispersed into an acidified ethanol solution (6 mL of 37% HCl in 40 mL ethanol) using sonication, centrifugation and removal of the supernatant to remove the surfactant. This step was repeated a minimum of 3 times. The nanoparticles were subsequently washed three times with ethanol. Nanoparticles were centrifuged and resuspended in anhydrous DMF (6 mL,  $7.8 \times 10^{-2}$  mol). DOTA-NHS-ester (2.1 mg,  $2.76 \times 10^{-6}$  mol) and triethylamine (150 µL,  $1.98 \times 10^{-3}$  mol) were added and the suspension was stirred at room temperature overnight (~16 hrs). The nanoparticles were washed with ethanol 3 times using centrifugation (11,000 rpm for 10 mins) and re-suspended in ethanol (10 mL). Anhydrous GdCl<sub>3</sub> (2.1 mg,  $7.97 \times 10^{-6}$  mol) was added and the suspension was stirred for 24 h at room temperature. Washing was carried out by dialysing (3.5 kDa Snakeskin dialysis tubing) against MilliQ water for a minimum of 24 hrs, changing the Milli-Q water regularly.

### **2.2.2.2 ‘Grafting From’ Method of pNIPAM Addition to MSNs**

Using a modified literature procedure,<sup>6</sup> the Gd<sup>3+</sup>-DOTA MSNs were suspended in a mixture of ethanol (20 mL,  $3.3 \times 10^{-1}$  mol) and water (10 mL,  $5.6 \times 10^{-1}$  mol). Varying amounts of APTES (measured in mol% with respect to moles of TEOS used in the MSN synthesis step; 3.2 µL,  $1.4 \times 10^{-5}$  mol for 0.2 mol% loading; 16 µL,  $6.8 \times 10^{-5}$  mol for 1 mol% loading; 40 µL,  $1.7 \times 10^{-4}$  mol for 2.5 mol% loading) were added and stirred at room temperature for ~16 hrs. These externally aminated Gd<sup>3+</sup>-DOTA MSNs were washed three times with ethanol and resuspended in dichloromethane (DCM; 7 mL,  $1.1 \times 10^{-1}$  mol). BIBB (1 mL,  $8.1 \times 10^{-3}$  mol) and triethylamine (20 µL,  $1.43 \times 10^{-4}$  mol) was added with. The solution was stirred at 0 °C for 2 hrs, then allowed to warm to



room temperature and stirred at room temperature for 14 hrs. The MSNs were then washed with MilliQ water three times using centrifugation (11,000 rpm for 10 mins). Finally, NIPAM was attached to the particles by re-suspending the prepared (BIBB surface modified) MSNs in a mixture of methanol (4 mL,  $9.9 \times 10^{-2}$  mol) and water (6 mL,  $3.3 \times 10^{-1}$  mol), using ultrasonication. This suspension was degassed by bubbling with N<sub>2</sub> for 30 minutes. Separately, copper bromide (6 mg,  $4.18 \times 10^{-5}$  mol), PMDETA (50  $\mu$ L,  $2.44 \times 10^{-4}$  mol), and NIPAM (0.75 g,  $6.63 \times 10^{-3}$  mol) was added to a mixture of methanol (4 mL,  $9.9 \times 10^{-2}$  mol) and water (6 mL,  $3.3 \times 10^{-1}$  mol). This solution was degassed by bubbling with N<sub>2</sub> for 30 mins. These two suspensions were combined and stirred under N<sub>2</sub> for 16 hrs and subsequently centrifuged at 13,200 rpm for 10 minutes, followed by re-suspension in acidified MilliQ water (20 mL MilliQ water and 2 mL of a 0.1 M HCl solution) and dialysed (3.5 kDa Snakeskin dialysis tubing) against MilliQ water for a minimum of 24 hrs, changing the MilliQ water regularly. Resulting polymer-grafted Gd<sup>3+</sup>-DOTA MSNs were collected in aqueous suspension for characterisation.

### 2.2.2.3 Preparation of pNIPAM

To determine the approximate length of the polymer chains grafted from the nanoparticle surfaces, pNIPAM was synthesised using the same conditions as used above, but in the absence of nanoparticles. In separate reaction vessels, amounts of BIBB equivalent to that grafted onto nanoparticles surfaces (1.69  $\mu$ L,  $1.4 \times 10^{-5}$  mol, equivalent to 0.2 mol% grafting density; 8.45  $\mu$ L,  $6.8 \times 10^{-5}$  mol, equivalent to 1 mol% grafting density; and 21.1  $\mu$ L,  $1.7 \times 10^{-4}$  mol, equivalent to 2.5 mol% grafting density) were added to a mixture of methanol (4 mL,  $9.9 \times 10^{-2}$  mol) and water (6 mL,  $3.3 \times 10^{-1}$  mol) and degassed by bubbling with N<sub>2</sub> for 30 mins. Separately, copper bromide (6 mg,  $4.18 \times 10^{-5}$  mol), PMDETA (50  $\mu$ L,  $2.44 \times 10^{-4}$  mol), and NIPAM (0.75 g,  $6.63 \times 10^{-3}$  mol) were added to a mixture of methanol (4 mL,  $9.9 \times 10^{-2}$  mol) and water (6 mL,  $3.3 \times 10^{-1}$  mol). This solution was degassed by bubbling with N<sub>2</sub> for 30 mins. These two suspensions were combined and stirred under N<sub>2</sub> for 16 hrs and subsequently dried using rotary evaporation and suspended in methanol (1 mL,  $2.5 \times 10^{-2}$  mol) and added to diethyl ether (40 mL,  $3.8 \times 10^{-1}$  mol) to precipitate the polymer. The suspension was centrifuged at 11,000 rpm for 10 minutes, the solvent removed, and the precipitate re-suspended again in methanol (1 mL,  $2.5 \times 10^{-2}$  mol) and precipitation in diethyl ether was repeated. The polymers were finally stored as dried powders.

## **2.2.3 Experimental Details for Chapter 5: The Application of MSNs as a Fluorescent Marker for Colorectal Cancer Cells**

### **2.2.3.1 Preparation of Internally Fluorescein Functionalised MSNs**

CTAB (0.64 g,  $1.78 \times 10^{-3}$  mol) was added to a solution of MilliQ water (16.02 mL, 0.89 mol) and ethanol (1.84 mL, 0.03 mol). TEA (1.03 g,  $6.9 \times 10^{-3}$  mol) was added and the solution was stirred at 80 °C to mix. TEOS (1.45 mL,  $6.5 \times 10^{-3}$  mol) was added dropwise and the reaction was stirred for 10 mins at 80 °C. An APTES/TEOS solution (4.7 µL of a mixture containing a 1:1 molar ratio of APTES:TEOS) was added dropwise and the reaction stirred at 80 °C for a further 1 hr and 50 mins. After this time, the mixture was centrifuged (11,000 rpm for 10 mins) and the supernatant removed. The nanoparticles were centrifuged and dispersed into an acidified ethanol solution (6 mL of 37% HCl in 40 mL ethanol) using sonication, centrifugation and removal of the supernatant to remove the surfactant. This step was repeated a minimum of 3 times. The nanoparticles were subsequently washed three times with ethanol. Nanoparticles were centrifuged and resuspended in anhydrous tetrahydrofuran (THF; 10 mL,  $1.2 \times 10^{-1}$  mol). FITC-NHS-ester (2.1 mg,  $2.76 \times 10^{-6}$  mol) and triethylamine (75 µL,  $9.45 \times 10^{-4}$  mol) were added and the suspension was stirred at room temperature overnight (~16 hrs). The nanoparticles were washed with ethanol 3 times using centrifugation (11,000 rpm for 10 mins) and re-suspended in ethanol (20 mL,  $3.3 \times 10^{-1}$  mol).

### **2.2.3.2 ‘Grafting From’ Method of NVA/MAA Copolymer Addition to MSNs using Free Radical Polymerisation**

the FITC-modified MSNs were suspended in a mixture of ethanol (20 mL,  $3.3 \times 10^{-1}$  mol) and water (10 mL,  $5.6 \times 10^{-1}$  mol). Varying amounts of APTES (measured in mol% with respect to moles of TEOS used in the MSN synthesis step; 3.2 µL,  $1.4 \times 10^{-5}$  mol for 0.2 mol% loading; 16 µL,  $6.8 \times 10^{-5}$  mol for 1 mol% loading). Then using a modified literature procedure,<sup>7, 8</sup> These externally aminated FITC MSNs were washed three times with ethanol and resuspended in DMF (10 mL,  $1.3 \times 10^{-1}$  mol). Separately, 4,4'-Azobis(4-cyanovaleric acid), (ACVA; 0.05 g,  $1.78 \times 10^{-4}$  Mol), *N*-Ethyl-*N'*-(3-dimethylaminopropyl)carbodiimide hydrochloride (EDC-HCl; 0.1 g,  $5.22 \times 10^{-4}$  mol), *N*-hydroxysuccinimide (NHS; 0.1 g,  $8.68 \times 10^{-4}$  mol) were dissolve into DMF (10 mL,  $1.3 \times 10^{-1}$  mol) and left stirring for 30 mins. Then this ACVA solution was added to

the MSN solution and left for overnight (~16 hrs). This solution was then washed three times using ethanol and dispersed in ethanol (25 mL,  $3.3 \times 10^{-1}$  mol). Dodecanethiol (514  $\mu$ L,  $2.15 \times 10^{-3}$  Mol) was added and the solution degassed under N<sub>2</sub> atmosphere for 30 mins. N-vinylacetamide (NVA; 5 mL, 0.048 mol) and methacrylic acid (MAA; 5 mL, 0.059 mol) were degassed for 30 mins under N<sub>2</sub> atmosphere and subsequently added to the MSNs solution. This combined solution was freeze thawed three times and heated to 60 °C and left for 16 hrs in the absence of light. Finally, the solution was dried using rotary evaporation and suspended in methanol (1 mL,  $2.5 \times 10^{-2}$  mol) and added to ethyl acetate (40 mL,  $4.1 \times 10^{-1}$  mol) to precipitate the polymer. The suspension was centrifuged at 11,000 rpm for 10 minutes, the solvent removed, and the precipitate re-suspended again in methanol (1 mL,  $2.5 \times 10^{-2}$  mol) and precipitation in ethyl acetate was repeated. The precipitated polymer surface functionalised MSNs were then stored in ethanol (~20 mL,  $3.3 \times 10^{-1}$  mol).

#### **2.2.3.3 NVA/MAA Copolymer Synthesis using Free Radical Polymerisation**

To determine the approximate length of the polymer chains grafted from the nanoparticle surfaces, NVA/MAA copolymer was synthesised using the same conditions as used above, but in the absence of nanoparticles. In separate reaction vessels, amounts of ACVA equivalent to that grafted onto nanoparticles surfaces (4 mg,  $1.4 \times 10^{-5}$  mol, equivalent to 0.2 mol% grafting density; 19 mg,  $6.8 \times 10^{-5}$  mol, equivalent to 1 mol% grafting density) was dissolved in ethanol (25 mL,  $4.1 \times 10^{-1}$  mol). to this solution dodecanethiol (514  $\mu$ L,  $2.15 \times 10^{-3}$  mol) was added and degassed under N<sub>2</sub> atmosphere for 30 mins. NVA (5 mL,  $4.8 \times 10^{-2}$  mol) and MAA (5 mL,  $5.9 \times 10^{-2}$  mol) were degassed for 30 mins under N<sub>2</sub> atmosphere and added to the ACVA solution. This combined solution was freeze thawed three times. Then the solution was heated up to 60 °C and left for 16 hrs. Finally, the solution was dried using rotary evaporation and suspended in methanol (1 mL,  $2.5 \times 10^{-2}$  mol) and added to ethyl acetate (40 mL,  $4.1 \times 10^{-1}$  mol) to precipitate the polymer. The suspension was centrifuged at 11,000 rpm for 10 minutes, the solvent removed, and the precipitate re-suspended again in methanol (1 mL,  $2.5 \times 10^{-2}$  mol) and precipitation in ethyl acetate was repeated. The polymers were stored as dried powders.

#### **2.2.3.4 ‘Grafting From’ Method of NVA/MAA Copolymer Addition to MSNs using Atom Transfer Radical Polymerisation**

Using a modified literature procedure,<sup>6</sup> the FITC-modified MSNs were suspended in a mixture of ethanol (20 mL,  $3.3 \times 10^{-1}$  mol) and water (10 mL,  $5.6 \times 10^{-1}$  mol). APTES (measured in mol% with respect to moles of TEOS used in the MSN synthesis step; 3.2  $\mu$ L,  $1.4 \times 10^{-5}$  mol for 0.2 mol% loading) were added and stirred at room temperature for 16 hrs. These externally aminated FITC modified MSNs were washed three times with ethanol and resuspended in dichloromethane (7 mL,  $1.1 \times 10^{-1}$  mol). BIBB (1 mL,  $8.1 \times 10^{-3}$  mol) and triethylamine (20  $\mu$ L,  $1.43 \times 10^{-4}$  mol) was added. The solution was stirred at 0 °C for 2 hrs, then allowed to warm to room temperature and stirred at room temperature for 16 hrs. The MSNs were then washed with MilliQ water three times using centrifugation (11,000 rpm for 10 mins). Finally, NVA/MAA copolymer was attached to the particles by re-suspending the prepared (BIBB surface modified) MSNs in a mixture of methanol (4 mL,  $9.9 \times 10^{-2}$  mol) and water (6 mL,  $3.3 \times 10^{-1}$  mol), using ultrasonication. This suspension was degassed by bubbling with N<sub>2</sub> for 30 minutes. Separately, copper bromide (6 mg,  $4.18 \times 10^{-5}$  mol), PMDETA (50  $\mu$ L,  $2.44 \times 10^{-4}$  mol), NVA (1 mL g,  $9.6 \times 10^{-3}$  mol) and MAA (1 mL,  $1.2 \times 10^{-2}$  Mol) was added to a mixture of methanol (4 mL,  $9.9 \times 10^{-2}$  mol) and water (6 mL,  $3.3 \times 10^{-1}$  mol). This solution was degassed by bubbling with N<sub>2</sub> for 30 mins. These two suspensions were combined and stirred under N<sub>2</sub> for 16 hrs and subsequently centrifuged at 11,000 rpm for 10 minutes, followed by re-suspension in acidified MilliQ water (20 mL MilliQ water and 2 mL of a 0.1 M HCl solution) and dialysed (3.5 kDa Snakeskin dialysis tubing) against MilliQ water for a minimum of 24 hrs, changing the MilliQ water regularly. Resulting polymer-grafted FITC-MSNs were collected in aqueous suspension for characterisation.

#### **2.2.3.5 PNA Functionalisation of NVA/MAA Surface Functionalised Fluorescein MSNs**

NVA/MAA copolymer surface functionalised fluorescein MSNs obtained using ATRP (50 mg) were suspended in water (10 mL,  $5.6 \times 10^{-1}$  mol). NHS (5 mg,  $4.34 \times 10^{-5}$  Mol) and EDC-HCl (5 mg,  $2.61 \times 10^{-5}$  mol) were added to the solution and the solution left stirring for 30 mins. Then peanut agglutinin (PNA, 5 mg) was added and

left overnight (~16 hrs). The MSNs were then washed with water 3 times and left in an aqueous solution.

#### **2.2.3.6 NVA/MAA Copolymer Synthesis using Atom Transfer Radical Polymerisation**

To determine the approximate length of the polymer chains grafted from the nanoparticle surfaces, NVA/MAA copolymer was synthesised using the same conditions as used above, but in the absence of nanoparticles. The amount of BIBB equivalent to that grafted onto nanoparticles surfaces (1.69  $\mu\text{L}$ ,  $1.4 \times 10^{-5}$  mol, equivalent to 0.2 mol% grafting density) was added to a mixture of methanol (4 mL,  $9.9 \times 10^{-1}$  mol) and water (6 mL,  $3.3 \times 10^{-1}$  mol) and degassed by bubbling with  $\text{N}_2$  for 30 mins. Separately, copper bromide (6 mg,  $4.18 \times 10^{-5}$  mol), PMDETA (50  $\mu\text{L}$ ,  $2.44 \times 10^{-4}$  mol), NVA (1 mL g,  $9.6 \times 10^{-3}$  mol) and MAA (1 mL,  $1.2 \times 10^{-2}$  Mol) were added to a mixture of methanol (4 mL,  $9.9 \times 10^{-1}$  mol) and water (6 mL,  $3.3 \times 10^{-1}$  mol). This solution was degassed by bubbling with  $\text{N}_2$  for 30 mins. These two suspensions were combined and stirred under  $\text{N}_2$  for 16 hrs and subsequently dried using rotary evaporation and suspended in methanol (1 mL,  $2.5 \times 10^{-2}$  mol) and added to ethyl acetate (40 mL,  $4.1 \times 10^{-1}$  mol) to precipitate the polymer. The suspension was centrifuged at 11,000 RPM for 10 minutes, the solvent removed, and the precipitate re-suspended again in methanol (1 mL,  $2.5 \times 10^{-2}$  mol) and precipitation in ethyl acetate was repeated. The polymer was finally stored as dried powders.

#### **2.2.3.7 Colon Cancer Cell Interaction Assay Performed by Trisha Bailey**

*Cell culture.* Human Caucasian colorectal adenocarcinoma cells (SW480 (ECACC 87092801)) were grown in 75  $\text{cm}^2$  Nunc cell culture flasks. Standard cell culture medium was composed of Advanced Dulbecco's Modified Eagle (A-DMEM) Medium supplemented with 10 % USA-origin fetal bovine serum (FBS), 100 units/mL penicillin, 100  $\mu\text{g/mL}$  streptomycin, and 250 ng/mL amphotericin B (PSA). SW480 cells were maintained in a humidified atmosphere of 5 %  $\text{CO}_2$  and 95 % air at 37  $^\circ\text{C}$  and the culture medium was renewed every 3–4 days. The cells were subcultured every 7 days or before reaching 90 % confluency. To subculture, cells were dissociated using 0.25 % trypsin plus 1 mM EDTA in balanced salt solution and reseeded at  $1.87 \times 10^5$  cells per 75  $\text{cm}^2$  cell culture flasks.

*Particle solutions.* Particles were suspended in ethanol and then spun down at 2g for 10 minutes. Ethanol was removed, and particles were re-suspended in A-DMEM in the indicated concentrations.

*SW480 binding assay.* SW480 cells were seeded at  $6.0 \times 10^4$  cells per well in 200  $\mu$ L of cell culture medium in 96-well plates. Cells were incubated for 2 hrs in a humidified atmosphere of 5 % CO<sub>2</sub> and 95 % air at 37 °C. Following the incubation period, cell medium was removed and replaced with the indicated concentration of particles in cell media. Cells were then incubated for 24 hrs. Cells were then washed twice with Dulbecco's phosphate buffered saline (PBS) and fluorescent readings were taken at excitation 485 nm and emission at 528 nm.

#### **2.2.3.8 Cell Toxicity Screening Performed by Trisha Bailey**

*Cell toxicity screening.* SW480 cells were seeded at  $6 \times 10^4$  cells per well in 200  $\mu$ L of complete cell culture medium in 96-well plates. Plates had an approximate growth area of 0.32 cm<sup>2</sup> and plates were used with the accompanying lid. Cells were allowed to attach to the entire free surface of the bottom of the well and formed a confluent layer not greater in height than one cell. Before experimental treatments, cells were allowed to attach for 2 hrs to the plates in a humidified atmosphere of 5 % CO<sub>2</sub> and 95 % air at 37 °C. The medium was exchanged against medium that was or was not supplemented with particles as indicated in the figures. Control cells received no additional solutes and experimental cells were incubated with concentrations of the individual particles ranging from 0.00122 to 2.5 mg mL<sup>-1</sup> for 24 hrs in a humidified atmosphere of 5% CO<sub>2</sub> and 95% air at 37 °C. Following the incubation period, resazurin sodium salt was dissolved in phosphate buffered saline and added to wells in an amount of 1/10<sup>th</sup> initial well volume. Absorbance readings were taken at 570/600 nm every 30 minutes until control cells reached ~70 % reduction.

*Statistical analyses.* Data was analyzed with a one-way analysis of variance (ANOVA) on ranks followed by comparison of experimental groups with the appropriate control group (Holm–Sidak method) followed by Tukey's post hoc test. Excel 2013 (Microsoft, Redmond, WA) and R (R Foundation for Statistical Computing, Vienna, Austria) were used for the analyses.

## **2.3 Characterisation Techniques**

### **2.3.1 Infrared Spectroscopy**

FTIR spectra ( $4000\text{--}400\text{ cm}^{-1}$ ) were acquired using a Bruker Alpha FT-IR spectrometer fitted with a ZnSe crystal on solid powder samples.

### **2.3.2 Thermogravimetric Analysis**

Thermogravimetric analysis (TGA) was carried out using a Mettler-Toledo DSC1-400 using alumina pans heated from  $30\text{--}600\text{ }^{\circ}\text{C}$  after 30 minutes equilibration at  $30\text{ }^{\circ}\text{C}$ , heating at  $10\text{ }^{\circ}\text{C}/\text{min}$  under an atmosphere of  $\text{N}_2$ .

### **2.3.3 Dynamic Light Scattering and Zeta Potential**

Hydrodynamic diameters and zeta potentials were determined by dynamic light scattering (DLS) using a Malvern Zetasizer Nano instrument. A 4 mW He-Ne 633 nm laser module was used, and scattered light was measured at  $173^{\circ}$  (back scattering). The attenuator and position were selected automatically by the instrument and the particle sizes reported as the average of five measurements. PDI indicated the polydispersity index of the suspensions. MSNs were suspended at  $1\text{ mg/mL}$  concentrations in Ultrapure MilliQ water for measurement.

### **2.3.4 Small Angle X-ray Scattering (SAXS)**

Small angle X-ray scattering (SAXS) was carried out using a PANalytical X'pert Pro MPD using a  $\text{Cu K}\alpha$  anode. Samples were analysed using 2-hour scans on solid powder samples on EasySAXS software.

### **2.3.5 Porosimetry**

Porosimetry data was acquired using a Micromeritics ASAP 2020 surface area and porosity analyser using  $\text{N}_2$  as the analytical gas. Pore size distributions were calculated from adsorption using the Barrett-Joyner-Halenda (BJH) method.<sup>9</sup>

### **2.3.6 Transmission Electron Microscopy**

Transmission electron microscope (TEM) images were obtained on a JEOL 2000FX TEM, 200 kV,  $\text{LaB}_6$  instrument operated with a beam current of  $\sim 115\text{ mA}$ . Images were captured using a Gatan Orius 11-megapixel camera. Samples were prepared by

deposition and drying of nanoparticle samples (10  $\mu$ L water suspension) onto formvar-coated 300 mesh copper TEM grids (Agar Scientific). Diameters were measured using Image J version 3.2; average values were calculated by counting a minimum of one hundred particles.

### **2.3.7 Gel Permeation Chromatography Performed by Christopher Stubbs**

Size exclusion chromatography was performed on an Agilent 390-LC MDS instrument equipped with differential refractive index (DRI), viscometry (VS), dual angle light scatter (LS) and UV detectors. The system was equipped with 2 x PLgel Mixed D columns (300 x 7.5 mm) and a PLgel 5  $\mu$ m guard column. The eluent is DMF with 5 mmol  $\text{NH}_4 \text{BF}_4$  additive. Samples were run at 1 ml/min at 50  $^\circ\text{C}$ . Poly (methyl methacrylate) standards (Agilent EasyVials) were used for calibration between 955,000–550  $\text{g mol}^{-1}$ . Analyte samples were filtered through a nylon membrane with 0.22  $\mu\text{m}$  pore size before injection. Respectively, experimental molar mass ( $M_n$ , SEC) and dispersity ( $\mathcal{D}$ ) values of synthesized polymers were determined by conventional calibration and universal calibration using Agilent GPC/SEC software.

### **2.3.8 Turbidimetry Analysis**

Turbidimetry analysis was carried out through the acquisition of UV-vis spectra using a UV-Vis Agilent Technologies Cary 60 UV/Vis at  $\lambda = 700 \text{ nm}$  every 1  $^\circ\text{C}$ , with temperature controlled by Quantum North West TC1 Temperature controller starting at 25  $^\circ\text{C}$  and ending at 50  $^\circ\text{C}$  with an equilibration time of 3 mins and the temperature increasing by 1 degree/min. Samples were prepared by diluting using MilliQ water to 2.5 mg/mL.

### **2.3.9 UV/vis Spectroscopy and Fluorometry with Cell Cultures**

The cells were incubated in 96 well plates and analysed using the Synergy HTX Multi-Mode Reader (BioTek, Swindon, UK) at 570/600 nm absorbance for the toxicity test and fluorescent readings were taken at excitation 485 nm and emission at 528 nm for the cell binding assay.



### 2.3.10 Ion Coupled Plasma Mass Spectroscopy

An Agilent 7500cx Inductively Coupled Plasma Mass Spectrometer (ICP-MS) was used to determine  $\text{Gd}^{3+}$  concentrations of aqueous suspensions of particles treated by hot nitric acid digestion and diluted in ultrapure MilliQ water.

### 2.3.11 $T_1$ relaxation Spectroscopy

#### 2.3.11.1 13.1 MHz Xigo

Relaxation measurements ( $T_1$ ) were carried out at room temperature using a XIGO Acorn instrument with a resonant frequency of 13.1 MHz. Samples were prepared by dispersing a known mass of nanoparticles or  $\text{Gd}^{3+}$ -DOTA into Ultrapure water. A minimum of 4 different concentrations were prepared and protic relaxation time measured for each sample.  $r_1$  relaxivity values were calculated from curves plotted of  $R_1$  ( $1/T_1$ ,  $\text{s}^{-1}$ ) vs.  $[\text{Gd}]$  concentration (mM, as measured by ICP-MS) and analysis of the slope of the line of best fit for each sample. Multiple batches of samples were analysed to confirm reproducibility and to provide standard deviations (a minimum of 3 separately prepared samples were measured at least 3 times). The water  $^1\text{H}$  longitudinal relaxation rates of these aqueous samples were measured at 293 K using the standard inversion-recovery method with **settings:** Rx Gain 10 dB, pre-amp tuning 310,  $90^\circ$  pulse duration 6.2  $\mu\text{s}$ ,  $180^\circ$  pulse duration 13.9  $\mu\text{s}$ .

#### 2.3.11.2 9.4 T MRI Scanner Performed by Ziedo Solomon

High field relaxation measurements were carried out on a Bruker 400 MHz (9.4 T) NMR Spectrometer fitted with a Bruker micro-imaging MicWB40 probe, funded through Birmingham Science City Translational Medicine Project. The water  $^1\text{H}$  longitudinal relaxation times of the aqueous samples (as prepared above) were measured at 293 K using the standard inversion-recovery method with settings: echo time 10 ms (1 average, 1 repetition);  $T_1$  experiments taken of 7 slices with 2 mm thickness; image size 64x64 with 12x12 mm field of view; resolution 0.188x0.188 mm. Standard deviation results from the analysis of pixels within a (circular) region of interest on at least one slice containing a minimum of 6366 pixels.

### **2.3.11.3 3 T MRI Scanner Performed by Dr Sarah Wayte**

MR images were acquired on a Siemens 3 T clinical imaging machine. T1 weighted fast spin echo images were acquired using the following parameters:  
- TR/TE<sub>eff</sub> = 600/8.9ms, field of view = 200x160mm, matrix size = 256x224, slice width = 2.5mm, slice gap = 0mm, 4 signal averages and acquisition time = 2min 27s. Samples were prepared by diluting using MilliQ water to 2.5 mg/mL.

## 2.4 References

1. K. Moller, J. Kobler and T. Bein, *Advanced Functional Materials*, 2007, **17**, 605-612.
2. J. S. Beck, J. Vartuli, W. J. Roth, M. Leonowicz, C. Kresge, K. Schmitt, C. Chu, D. H. Olson, E. Sheppard and S. McCullen, *Journal of the American Chemical Society*, 1992, **114**, 10834-10843.
3. C. Kresge, M. Leonowicz, W. J. Roth, J. Vartuli and J. Beck, *nature*, 1992, **359**, 710.
4. J. J. Davis, *J Mater Chem*, 2012, **22**, 22848.
5. V. Cauda, A. Schlossbauer, J. Kecht, A. Zurner and T. Bein, *Journal of the American Chemical Society*, 2009, **131**, 11361-11370.
6. Y. Yang, X. Yan, Y. Cui, Q. He, D. Li, A. Wang, J. Fei and J. Li, *Journal of Materials Chemistry*, 2008, **18**, 5731-5737.
7. S. Sakuma, M. Hayashi and M. Akashi, *Advanced drug delivery reviews*, 2001, **47**, 21-37.
8. S. Sakuma, N. Suzuki, R. Sudo, K.-i. Hiwatari, A. Kishida and M. Akashi, *International journal of pharmaceutics*, 2002, **239**, 185-195.
9. E. P. Barrett, L. G. Joyner and P. P. Halenda, *Journal of the American Chemical society*, 1951, **73**, 373-380.

# Chapter 3

## 3. Investigating the Impact of Nanoparticle Design on MRI Contrast Agent Behaviour

---

### 3.1 Chapter Summary

Magnetic resonance imaging, MRI, is a popular clinical analytical method due to its non-invasive nature and ability to provide a high-resolution deep tissue penetrating images. The administration of contrast agents to enhance the efficacy of MRI is common practice and an area in which nanomaterials have shown great promise. Despite their clear potential as high contrast agents, the influence of the nanostructure itself on contrast enhancement has been largely overlooked. Herein, mesoporous silica nanoparticles, MSNs, with different pore sizes were prepared by employing different surfactants during preparation. During synthesis, the surfactants control the size of templating micellar structures around which the silica network of the particles form, through their different hydrocarbon tail group lengths. The surfactants utilised were dodecyltrimethylammonium bromide, DODE, myristyltrimethylammonium bromide, MYRI, and hexadecyltrimethylammonium bromide, CTAB. The MSNs were prepared using similar protocols and analysed by transmission electron microscopy, TEM. Synthetic protocol optimisation was carried out by varying the reaction temperature to produce particles of comparable particle diameter. This is a vital consideration in ensuring that only pore size impacts MRI behaviour as particle diameter affects relaxation through  $\tau_R$ . Optimisation was only achieved reproducibly with CTAB and MYRI MSNs. Therefore, CTAB and MYRI MSNs were further characterised and the pore diameter was proven to be smaller for MYRI MSNs than for CTAB MSNs by small angle X-ray scattering, SAXS, and

porosimetry. Subsequent immobilisation of  $Gd^{3+}$ -chelates on these different pore sized MSNs was investigated to determine the effect of different pore sized nanoparticles MRI relaxation behaviour. MSNs were  $Gd^{3+}$  bound in 1,4,7,10-Tetraazacyclododecane-1,4,7,10-tetraacetic acid complex,  $Gd^{3+}$ -DOTA, functionalised in three differing locations, inside the pores, Internal, both in the pore and on the surface, Edge, or on the surface of the MSNs, External, through control of the synthesis. These variations were then analysed at 13.1 MHz to obtain their relaxivity trends. It was observed that for the CTAB MSNs, which obtained the larger pores,  $Gd^{3+}$ -DOTA location had no significant effect on relaxivity due to no significant water and  $Gd^{3+}$  interaction variation. However, for the MYRI MSNs the relaxivity was suppressed when the  $Gd^{3+}$ -DOTA was deeply internalised within the pore structures, then partially regained when the  $Gd^{3+}$ -DOTA was bound at the mouths of the pores, and fully recovered when the  $Gd^{3+}$ -DOTA was bound to the external surfaces of the MSNs. This is due to the smaller pores of the MYRI MSNs restricting the availability of the  $Gd^{3+}$ -DOTA therefore hindering water/ $Gd^{3+}$  interactions. Particles were characterised in detail using TEM, small angle x-ray scattering, SAXS, gas sorption porosimetry, Fourier transform infrared spectroscopy, FTIR, dynamic light scattering, DLS, and zeta potential, thermogravimetric analysis, TGA, and relaxometry at 13.1 MHz.

## 3.2 Introduction

In 2008, Kecht *et al.* proposed a method of selective location functionalisation of MSNs.<sup>1</sup> This was achieved by performing a co-condensation reaction to form the MSNs with the addition of the amine functionalised silanol, (3-Aminopropyl)triethoxysilane, APTES, varied by alteration in APTES administration time to the MSNs synthesis to alter subsequent location on the MSNs. The variation of functional group location was confirmed by zeta potential in acidic solution. It was found that the addition of an APTES/TEOS solution during the MSN synthesis after 5 mins produced MSNs with a lower zeta potential than addition after 10 mins and the MSNs obtained from the 10 mins addition having a lower zeta potential than after 30 minutes. This variation is due to the amine functional groups in APTES all being protonated, therefore giving the MSNs a positive charge at low pH. The MSNs obtained after APTES/TEOS addition after 30 minutes have more protonated amine groups on the surface of the MSNs and therefore contribute to the zeta potential. The MSNs with APTES/TEOS addition after 5 and 10 mins have more protonated amine groups inside the pores which do not contribute as much to the zeta potential of the MSNs, resulting in less positive zeta potential. APTES/TEOS addition after 30 mins did not increase the zeta potential significantly as the MSNs are already fully formed and surface functionalised at this point. The location was also confirmed using scanning transmission electron microscopy, STEM, where iridium was bound to the aminopropyl groups and used as a contrast agent to observe APTES location. This control of functional group location was developed further by V. Cauda *et al.* by synthesising bi-functional MSNs with controlled functional group location.<sup>2</sup> The location of the functional groups confirmed by a fluorescence quenching experiment.

J. Davis *et al.* utilised this method of functionalisation location control to investigate nanoconfinement effects of  $Gd^{3+}$ -DOTA chelates bound to various locations and MRI contrast efficacy.<sup>3</sup> Using a 2 hrs reaction protocol with the CTAB surfactant being utilised as the soft template, a 1:1 molar solution of APTES and TEOS was added to the MSN synthesis reaction either 10 minutes into the reaction, Internal, 1 hr into the reaction, Edge, and APTES post grafted onto the surface of the MSNs, External. These aminated MSNs at various locations were then  $Gd^{3+}$ -DOTA functionalised and analysed in a 7 T MRI scanner. A considerable increase in MRI

activity was observed for the Edge MSNs ( $33.57 \pm 1.29 \text{ mM}^{-1} \text{ s}^{-1}$ ) compared to the Internal ( $17.14 \pm 0.49 \text{ mM}^{-1} \text{ s}^{-1}$ ) and External ( $10.77 \pm 0.22 \text{ mM}^{-1} \text{ s}^{-1}$ ). This observed phenomenon was attributed to the porous network affecting the diffusion and the rotation mobility of pore confined water compared to bulk water. S. Aime *et al.* observed a similar enhancement encapsulating  $\text{Gd}^{3+}$ -DOTA into aptoferritin.<sup>4</sup> Atoferritin is a spherical protein shell consisting of 24 subunits and a central cavity. The spherical shell can be disassembled and reassembled by pH variation. This methodology of assembly was utilised to encapsulate  $\text{Gd}^{3+}$ -DOTA into the central cavity resulting in a massive relaxivity enhancement of >20x that of free  $\text{Gd}^{3+}$ -DOTA at 20 MHz ( $80 \pm 5 \text{ mM}^{-1} \text{ s}^{-1}$  to  $4.2 \text{ mM}^{-1} \text{ s}^{-1}$  respectively). J. S Ananta *et al.* observed  $T_1$  relaxation enhancement by confining  $\text{Gd}^{3+}$  ions into the nonporous structure of silicon nanoparticles.<sup>5</sup> Again exceptional enhancements in relaxivities were observed, the encapsulation of gadofullerenes into porous silicon nanoparticles resulted in a relaxivity of  $200 \text{ mM}^{-1} \text{ s}^{-1}$  at 20 MHz, a 50x increase compared to clinically available GBCAs. P. H. Fries *et al.* investigated this encapsulation enhancement theoretically.<sup>6</sup> The suggested factor which contributes to this observed relaxivity enhancement after encapsulation is the increased local viscosity of the aqueous solution around the  $\text{Gd}^{3+}$ -chelate increasing the amount of water molecules surrounding the  $\text{Gd}^{3+}$ -chelate, therefore increasing the amount of water which can interact with  $\text{Gd}^{3+}$ , hence increasing relaxivity.

There have been numerous investigations into how nanoconfinement effects water molecules and how variation in the pore diameter effects water mobility. S. Takahara *et al.* analysed MSNs suspended in water by neutron scattering to observe the translational diffusion of water in pores of diameter 21.4 Å and 28.4 Å.<sup>7</sup> A significant deceleration in diffusion was observed with the decreased pore size. I. Brovchenko *et al.* studied water phase transitions in nanopores theoretically and observed an increase in phase transition temperature with increased pore diameter.<sup>8</sup> A. Milischuk *et al.* investigated theoretically the structure and dynamics of water in silica nanopores.<sup>9</sup> Analysing pore diameter of 20 Å and 40 Å the mobility of the water molecules was found to modestly increase with increased pore diameter. E. Belorizky *et al.* investigated how confining water into the nanopores of Imogolite, a hydrous aluminosilicate found in soil, of outside pore diameter of 2.3 - 2.7 nm and internal

diameters of  $\sim 1$  nm.<sup>10</sup> the diffusion of the water was found to be  $\sim 4$ x slower in the pores than in the bulk water, which resulted in a significantly enhanced relaxation rate.

Since mesoporous silica nanostructures are widely used in several applications from catalysis to sorption, their structural parameters have been varied in a bid to tune their behaviour in these applications. Their overall size can be modified through small changes to the synthetic protocol, such as increasing temperature, amount of catalyst and source silicates; their pore sizes can also be varied through careful choice of reagents.<sup>11, 12</sup> One method was by changing the carbon chain length of the cationic surfactant for example varying the chain length from  $C_nH_{2n+1}(CH_3)N^+$  from  $n = 8$  to  $n = 16$  changed the pore diameter from 18 Å to 36 Å. Whilst the pore diameter was shown to increase on addition of mesitylene of various quantities to pore diameters between 85 Å and 120 Å. Therefore the ease of controlling functional group location,<sup>1</sup> the facile method of changing the pore diameter<sup>11</sup> and the simple methodology of covalently binding  $Gd^{3+}$ -DOTA to MSNs via surface amination of the MSNs and 2,2',2''-(10-(2-((2,5-dioxopyrrolidin-1-yl)oxy)-2-oxoethyl)-1,4,7,10-tetraazacyclododecane-1,4,7-triyl)triacetic acid (DOTA-NHS-ester)<sup>13</sup> makes them a perfect scaffold in which to investigate the effect of varying water accessibility to  $Gd^{3+}$ -chelate.

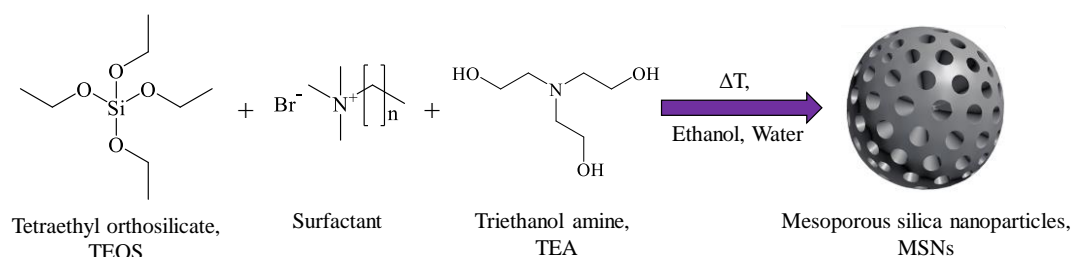
### 3.2.1 Aims

The aim of this chapter was to investigate the impact on MRI contrast enhancement behaviour (in terms of protic relaxation) of varying the pore diameter of MSNs while controlling particle diameter.



### 3.3 Preparation and Characterisation of MSNs with Controlled Variation of Pore Diameter and Gd<sup>3+</sup>-DOTA Functionalisation Location

MSNs samples were synthesised using a basic hydrolysis and condensation reaction in the presence of surfactants to produce mesoporous nanostructures (*Figure 3.1*).<sup>14</sup>

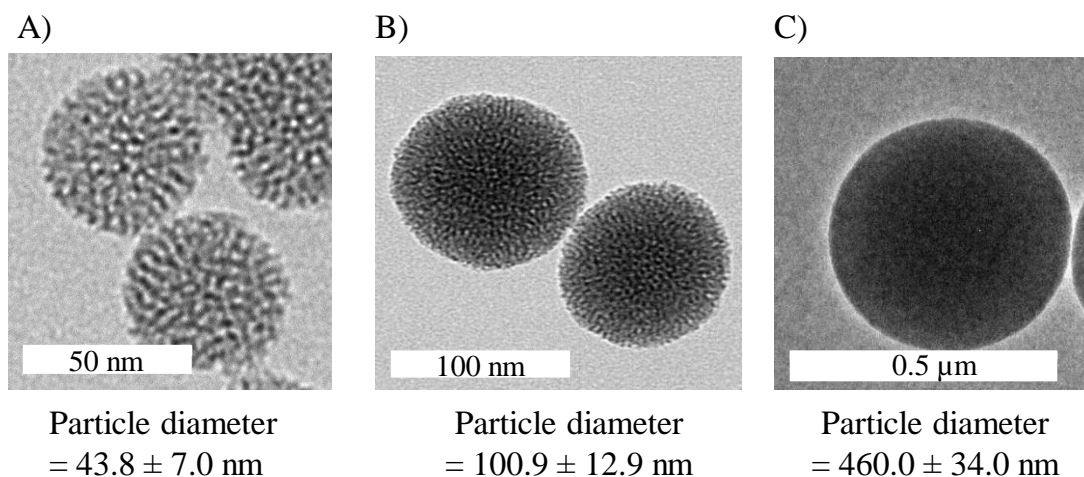


*Figure 3.1. General schematic representation of the synthesis of mesoporous silica nanoparticles.*

In this reaction the surfactant provides a surface in which the tetraethyl orthosilicate, TEOS, can react *via* hydrolysis/condensation, causing the porosity of the MSNs. Three different surfactants with varying hydrophobic carbon chain lengths were used, DODE ( $n = 11$ ), MYRI ( $n = 13$ ) and CTAB ( $n = 15$ ), to analyse what effect this would have on the properties of the MSNs produced using otherwise identical protocols.

#### 3.3.1 Transmission Electron Microscope Analysis

To observe the particle diameter of the MSNs obtained using the three separate surfactants, CTAB, MYRI and DODE, at 80 °C, the samples were investigated by transmission electron microscopy, TEM (*Figure 3.2*).



*Figure 3.2. TEM images of MSNs synthesised using three different surfactants, A) CTAB, B) MYRI and C) DODE, at 80 °C. Average particle diameter was calculated by the mean and standard deviation of at least 100 particles viewed using ImageJ.*

The particle diameters of the MSNs synthesised using the three surfactants varied considerably from  $43.8 \pm 7.0$  nm for CTAB to  $100.9 \pm 12.9$  nm for MYRI and finally  $460.0 \pm 34.0$  nm for DODE. This size deviation is due to the variation in surfactant micelle diameter affecting the kinetics of mesoporous silica formation by changing the pore template structure which the hydrolysis/condensation of tetraethyl silicates reactions occur.<sup>15, 16</sup> This variation in particle diameter needed to be controlled as the MSNs made using each surfactant were to be investigated to observe whether changing the pore diameter affected relaxation enhancement. It is already well known that changing the particle diameter of the nano-construct that the  $\text{Gd}^{3+}$  chelate is bound to lower tumbling and therefore enhance relaxation.<sup>17</sup> Therefore, the particle diameter was required to be the same to control a known variable and confirm that any variation in relaxivity was solely because of changes in the  $\text{Gd}^{3+}$ -DOTA and water interaction due to pore diameter variation.

Optimisation of the protocols was required to remove this particle diameter variable. It was found that the variation to the protocol that affected particle diameter significantly was the variation in temperature in which the MSNs were synthesised in. The CTAB diameter of  $43.8 \pm 7.0$  nm was used as the target diameter to allow direct comparison to the previous literature (*Figure 3.3*).<sup>3</sup>

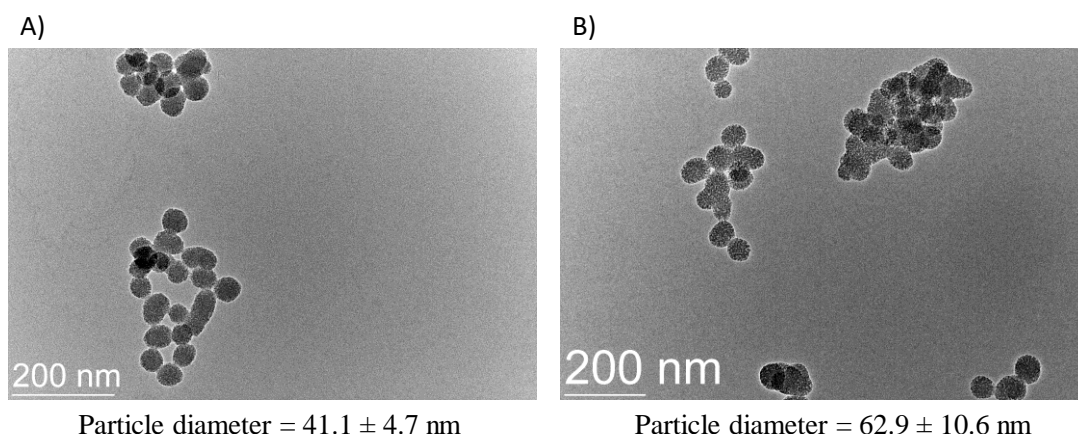
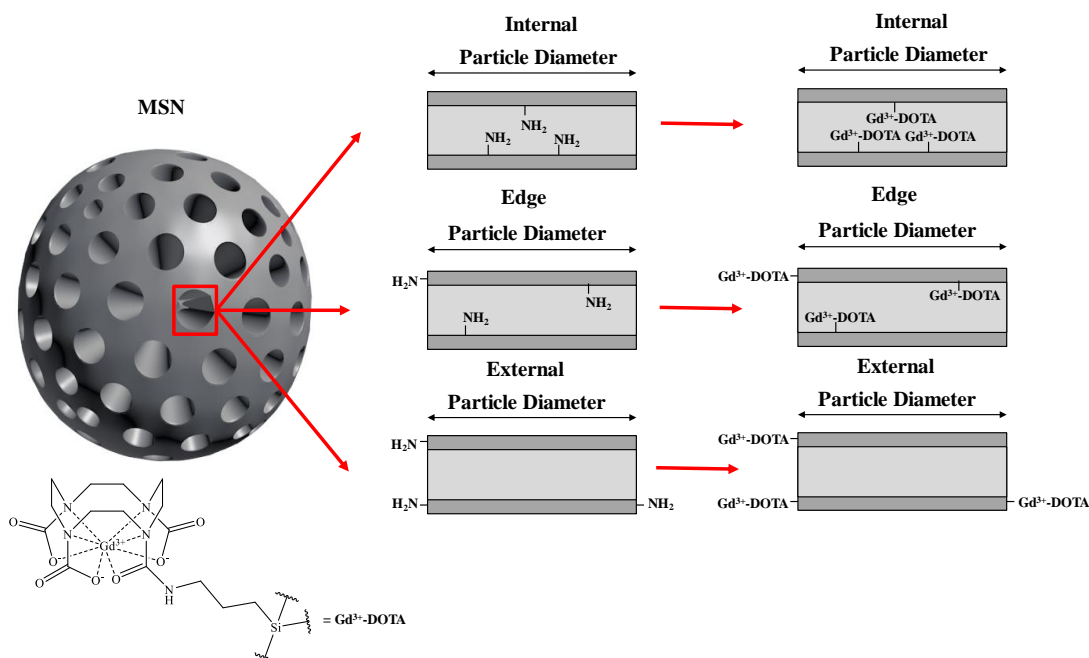


Figure 3.3. The TEM images and the particle diameter of MSNs synthesised using the surfactants A) MYRI and B) DODE at 40 °C and 15 °C respectively. The particle diameter calculated by measuring 100 MSNs.

After optimisation for the MYRI surfactant MSNs, 40 °C was observed to be the required reaction temperature to obtain equivalent particle diameters to those obtained using CTAB as 40 °C provided MSNs of particle diameters of  $41.1 \pm 4.7$  nm by TEM. 15 °C was found to be the lowest temperature in which the yield of the MSN synthesis was not significantly affected by the temperature for the DODE temperature optimisation. However, the particle diameter obtained at 15 °C was found to be significantly different at  $62.9 \pm 10.6$  nm from the particle diameters obtained using CTAB ( $43.8 \pm 7.0$  nm) and MYRI ( $41.1 \pm 4.7$  nm) for the pore diameter investigation to be progressed using the DODE surfactant protocol for MSN synthesis.

Using the selective location functionalisation observed by Kecht *et al.*, the optimised CTAB and MYRI protocols were amine functionalised through the addition of (3-aminopropyl)triethoxysilane, APTES, at three precisely tuned times in different MSN syntheses.<sup>1</sup> This reaction, termed a co-condensation, since APTES condenses alongside the TEOS in the reaction, was performed where APTES was added after three separate time intervals within the MSN synthesis. The time intervals for APTES addition were 10 minutes into the 2 hrs MSN synthesis of the MSN formation, functionalising the MSNs within the pores, Internal, 1 hr into the 2 hrs synthesis, functionalising the MSNs both in the pores and on the surface, Edge, and post grafted after the MSN synthesis had completed but the surfactant had not been removed from the pores, resulting in functionalisation on the surface of the MSNs, External (Figure 3.4). The amount of mole of APTES added to the reaction was calculated as 0.15 mol%

of the overall moles of tetraethyl orthosilicate, TEOS, added. This low concentration of APTES was used to increase the control of amine location allowing for greater clarity in the differentiation between these three methods of functionalisation and to minimise steric hindrance between  $Gd^{3+}$ -chelates.<sup>3</sup>



*Figure 3.4. A schematic of an MSN with the cross section of a pore highlighted to show the difference between the three  $Gd^{3+}$ -DOTA functionalisation locations used in investigating the effect of changing the pore diameter on relaxivity and therefore MRI contrast applicability.*

The amine functionalised MSNs using the Internal, Edge and External methodologies in combination with both CTAB and MYRI optimised protocols were analysed by TEM to confirm their particle diameters were not adversely affected by the addition of the amine functional group (*Figure 3.5*).

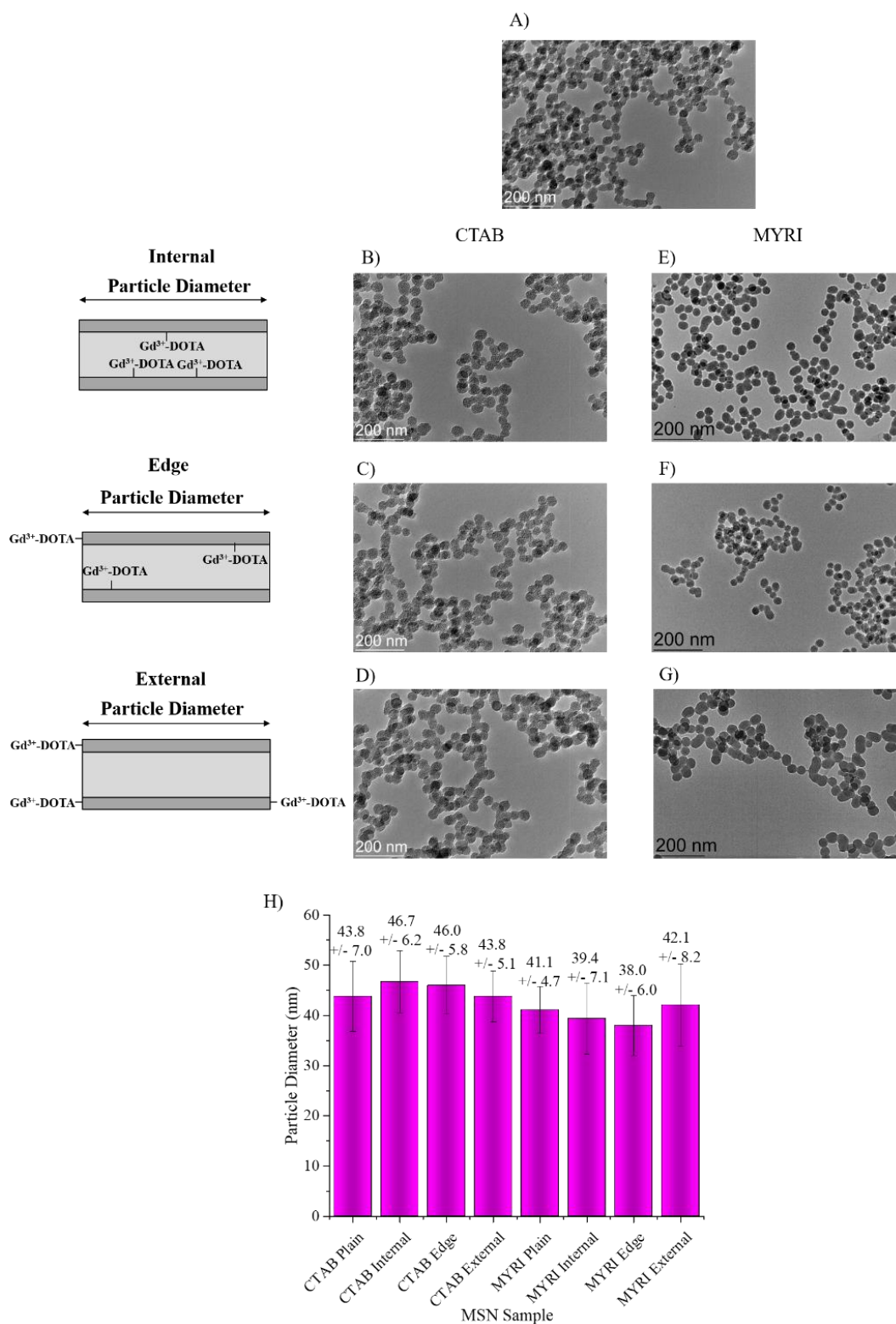


Figure 3.5. TEM images of A) Plain MSNs, B) CTAB Internal MSNs, C) CTAB Edge MSNs, D) CTAB External MSNs, E) MYRI Internal MSNs, F) MYRI Edge MSNs and G) MYRI External MSN. H) Bar chart of the particle diameter analysis by TEM of the 6 MSNs families synthesised with CTAB Plain and MYRI Plain as a comparison between aminated and non-aminated MSNs.

The particle diameter calculated for each methodology is within error of each other. Also, these particle diameters are within error of the non-amine functionalised MSNs (CTAB =  $43.8 \pm 7.0$  nm and MYRI =  $41.1 \pm 4.7$  nm) showing that amine functionalisation by the addition of APTES at various stages in the synthesis of MSNs does not affect MSN formation.

### **3.3.2 Infrared Spectroscopy**

Fourier transform infrared, FTIR, spectroscopy was used to confirm the successful formation of silica particles as well as removal of the surfactant from the pores of the MSNs (*Figure 3.6*).

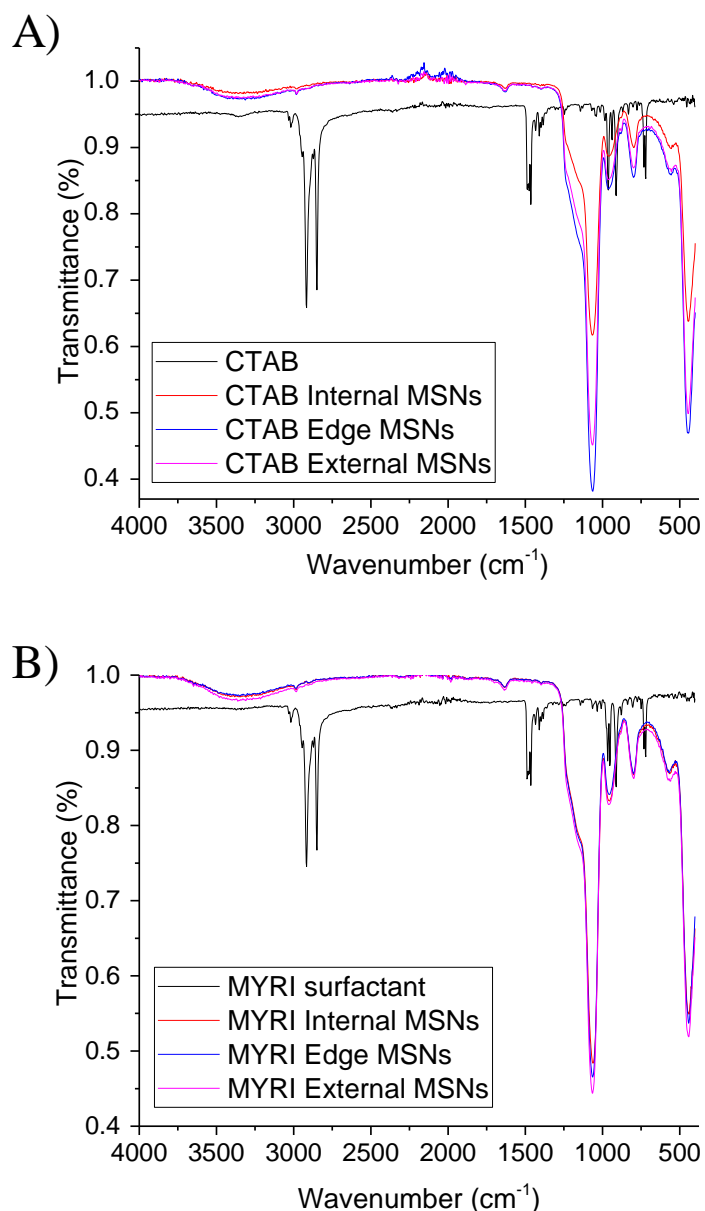


Figure 3.6. The FTIR spectra of A) CTAB Internal MSNs, CTAB Edge MSNs and CTAB External MSNs compared to CTAB surfactant and B) MYRI Internal MSNs, MYRI Edge MSNs and MYRI External MSNs compared to MYRI surfactant.

For both the CTAB and MYRI surfactants the IR spectra are very similar due to the only difference between their chemical structure being an extra ethyl group within the aliphatic hydrocarbon tail. They have stretches around  $2840\text{ cm}^{-1}$  and  $2920\text{ cm}^{-1}$  which represent C-H stretching and  $\sim 1460\text{ cm}^{-1}$  which represents C-H bending.<sup>18</sup> These are not observed in any of the MSNs synthesised proving that the removal of surfactant has been successful from the pores of the MSNs by repeated acid washes.

The stretches observed for all amine-modified MSNs are similar, with stretches between 1015-1190  $\text{cm}^{-1}$  representing Si-O-Si stretching and bending vibrations,<sup>19-21</sup> stretches around 800  $\text{cm}^{-1}$ , indicative of Si-O-Si stretches,<sup>22</sup> and those centred at ~550 and ~450  $\text{cm}^{-1}$  representing tri and tetracyclosiloxane rings of siloxanes.<sup>23</sup> There are no stretches observed in the FTIR spectra of any of the amine functionalised MSNs between 3100 - 3500  $\text{cm}^{-1}$  representing amine stretching or between 1550 and 1640  $\text{cm}^{-1}$  representing amine bending.<sup>18</sup> this is due to the very low amine functionalisation (0.15 mol%) being below the sensitivity of the machine. The broad band observed for all samples at 3400–3500  $\text{cm}^{-1}$  can be assigned to water and hydroxyl groups on the surfaces of the nanoparticles.

### 3.3.3 Thermogravimetric Analysis

To further confirm the successful removal of surfactant from the pores, thermogravimetric analysis, TGA, was performed (*Figure 3.7*).



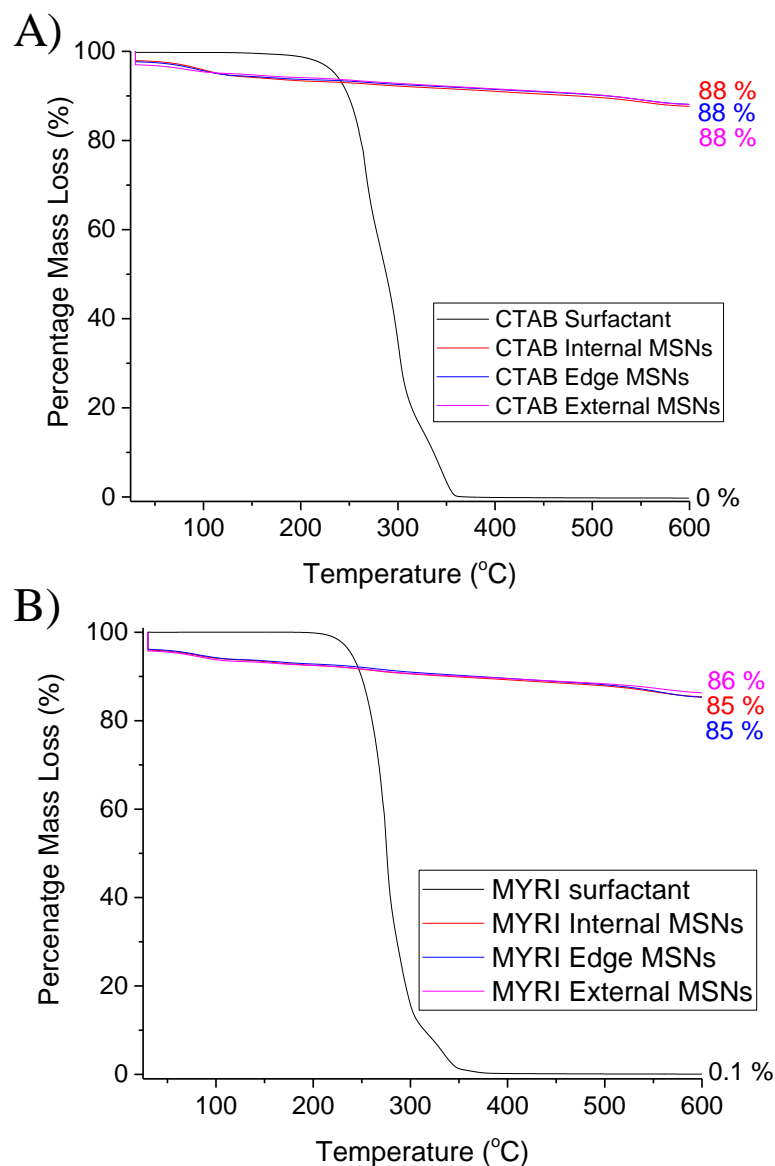


Figure 3.7. The TGA analysis between 30 - 600 °C of A) CTAB Internal MSNs, CTAB Edge MSNs and CTAB External MSNs compared to CTAB surfactant and B) MYRI Internal MSNs, MYRI Edge MSNs and MYRI External MSNs compared to MYRI surfactant.

For both MYRI and CTAB surfactants there is a distinguishable loss of mass between 215 °C and 350 °C which corresponds to the removal of the surfactant. There is no significant mass loss in this temperature range in any of the MSNs prepared further confirming the removal of surfactant from the pores of the MSNs. There is a distinctive mass loss of varying degrees between 80 °C and 120 °C for the MSNs which represents the loss of water and surface hydroxyl groups. The loss of the amino

groups from APTES surface modification cannot be observed, due to the very low grafting densities employed (0.15 mol%) being below the sensitivity threshold of the machine. The almost complete loss of mass for the surfactant and the relative low mass loss of the MSNs is due to variation in stability between these two structures between 30 °C and 600 °C.

### 3.3.4 Dynamic Light Scattering and Zeta Potential Analysis

Dynamic light scattering, DLS and zeta potential measurements were performed in aqueous suspension on all the MSNs to provide information on hydrodynamic diameter and surface charge (*Table 3.1*).

*Table 3.1. The mean hydrodynamic diameter obtained by DLS and zeta potential for all MSNs with amine functionalisation locations, Internal, Edge and External, using the CTAB and MYRI surfactants. Values are an average of 5 measurements of each sample, across 3 batches of prepared MSNs.*

<b>Sample</b>	<b>Mean hydrodynamic diameter /nm</b>	<b>Mean polydispersity index, PDI / AU</b>	<b>Zeta potential /mV</b>
<b>CTAB Internal</b>	221.7 ± 53.8	0.26 ± 0.05	-19.7 ± 4.8
<b>CTAB Edge</b>	253.9 ± 19.6	0.19 ± 0.03	-25.0 ± 7.0
<b>CTAB External</b>	224.2 ± 3.6	0.17 ± 0.08	-18.6 ± 1.7
<b>MYRI Internal</b>	169.5 ± 20.9	0.18 ± 0.02	-27.4 ± 0.7
<b>MYRI Edge</b>	209.4 ± 31.5	0.20 ± 0.06	-18.4 ± 6.2
<b>MYRI External</b>	257.6 ± 53.5	0.23 ± 0.08	-22.0 ± 3.0

The mean diameter of MSNs by DLS are larger than their diameters measured by TEM for all samples (CTAB MSNs = 43.8 ± 7.0 nm and MYRI MSNs = 41.1 ± 4.7 nm). This is due to differences between the measurement techniques. In TEM, images are taken of nanoparticles after they have dried onto a surface; DLS, on the other hand, is carried out on samples in suspension. This technique therefore considers Brownian motion effects, as well as any hydrogen bonding and Van Der Waals interactions

between the particles and surrounding solvent molecules which may contribute to the overall particle size. Due to these effects, DLS measures the hydrodynamic radius of the particles in liquid and hence show a larger value for the nanoparticles' diameter.

24-26

The hydrodynamic diameters are similar for all particles demonstrating that surface modification with amine groups does not affect the overall size of the MSNs at all ( $169.5 \pm 20.9$  to  $257.6 \pm 53.5$  nm for MYRI MSNs and  $221.7 \pm 53.8$  to  $253.9 \pm 19.6$  nm for CTAB MSNs). Their colloidal stability is confirmed by the polydispersity index, PDI, which shows all particles to be colloidally stable (PDI values  $< 1$ ). The zeta potentials ( $-19.7 \pm 4.8$  mV,  $-25.0 \pm 7.0$  mV  $-18.6 \pm 1.7$  for CTAB MSNs and  $-27.4 \pm 0.7$  mV,  $-18.4 \pm 6.2$  mV and  $-22.0 \pm 3.0$  mV for MYRI MSNs), are within range of one another showing that the MSNs obtained are similar in surface chemistry and further confirms colloidal stability in aqueous solution. The MSNs are negative due to the Si-OH functional groups being predominantly deprotonated, due the isoelectric point of Si-OH being 2,<sup>27</sup> overwhelming any positive charge obtained by the protonated amine functional groups of the APTES (which exists at very low grafting densities). The information obtained by DLS and zeta potential shows that the synthetic protocols optimised to obtain MSNs of the same size using CTAB and MYRI surfactants and amine functionalisation at various locations has had no significant effect on the overall colloidal stability of the MSNs synthesised.

### 3.3.5 Small Angle X-ray Scattering Analysis

Small angle X-ray scattering, SAXS, was performed using EasySaxs software on dried samples of all variations of amine location using MYRI and CTAB surfactant to obtain information about the effect the changing of the surfactant and location of amine functionalisation had on the pore diameter (*Figure 3.8 and Table 3.2*).<sup>28, 29</sup> The lower q values being modelled for particle diameter and the higher q values for pore diameter due to the pores being smaller than the particles and larger objects having faster oscillation time.<sup>29</sup>

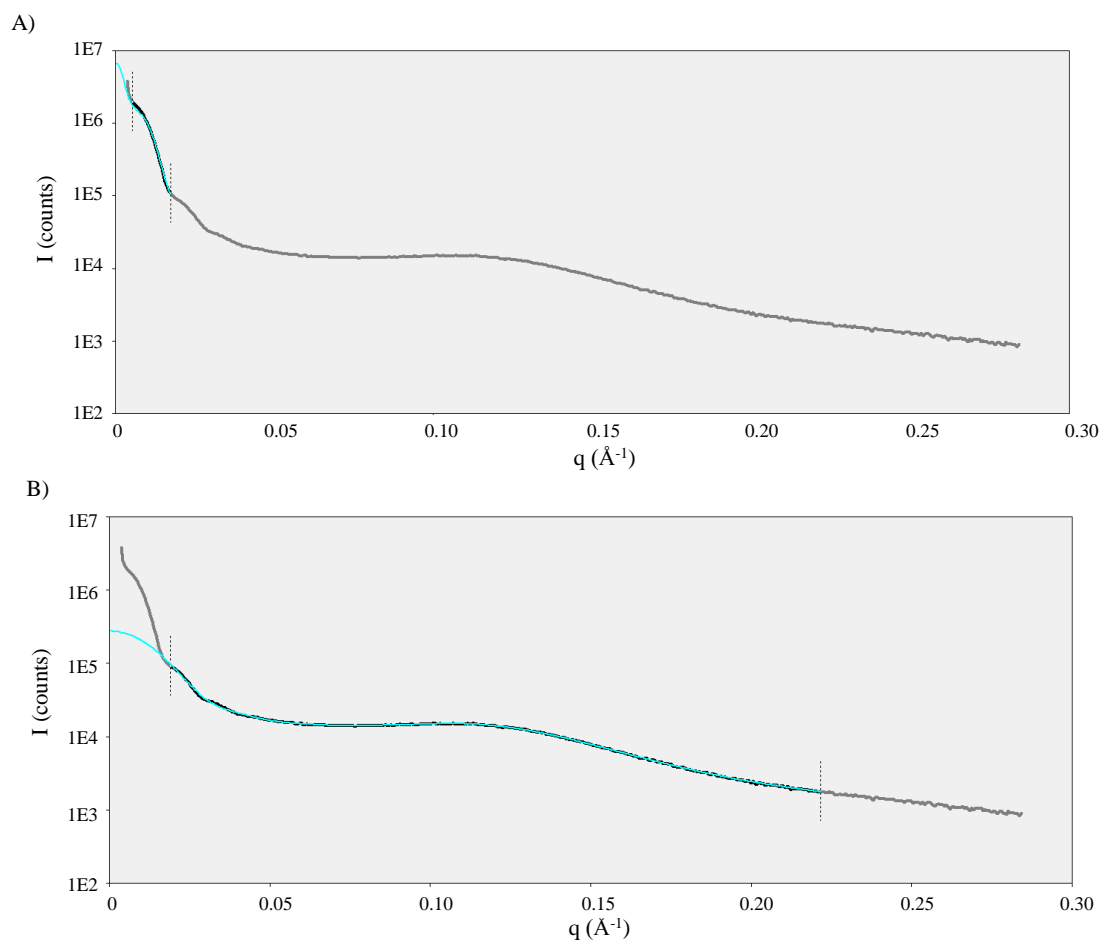


Figure 3.8. An example of the data acquired by SAXs for CTAB Internal MSNs with the area representing A) the particle diameter and B) the pore diameter of the MSNs being analysed using the EasySAXS modelling software.<sup>28</sup>  $q = [4\pi\sin(\theta)] / \lambda$  where  $\theta$  is the scattering angle and  $\lambda$  being the x-ray wavelength being used to analyse the sample.

*Table 3.2. The particle diameter and pore diameter analysed by SAXS for each of the MSNs obtained using all the variations of amine functionalisation location and CTAB and MYRI surfactants. Values are the average of the three batches of MSNs synthesised separately.*

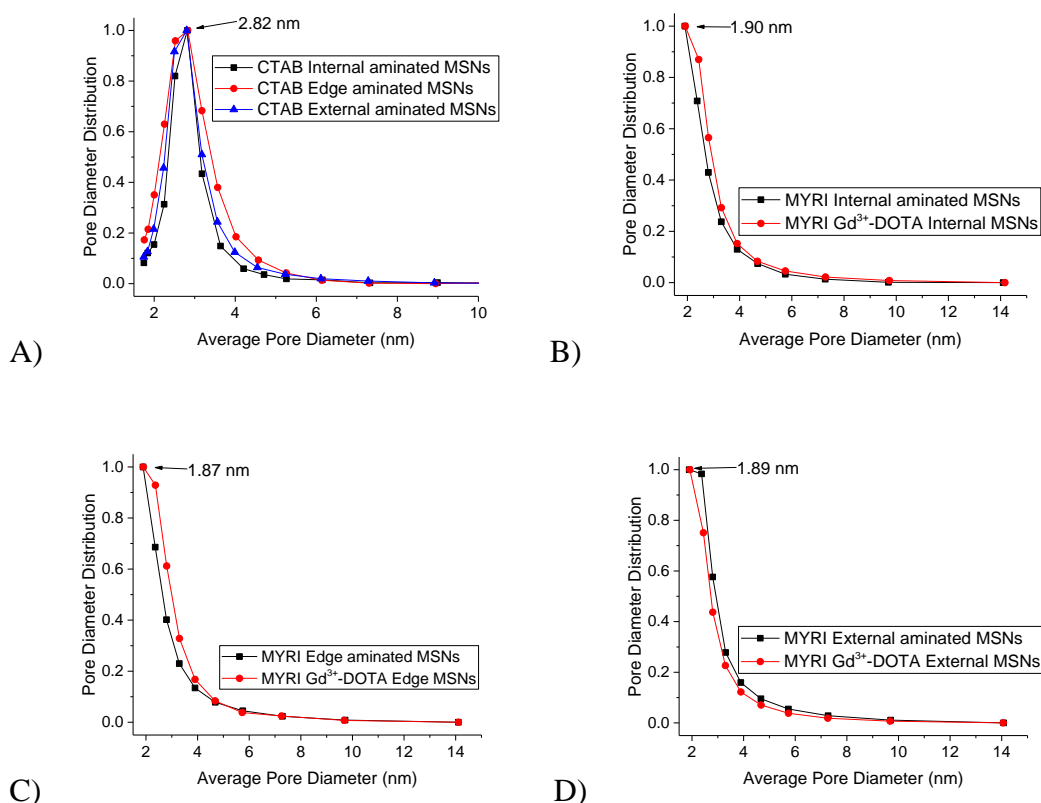
<b>Sample</b>	<b>Particle diameter/ nm</b>	<b>Pore diameter/ nm</b>
<b>CTAB Internal</b>	$47.7 \pm 7.7$	$3.55 \pm 1.15$
<b>CTAB Edge</b>	$46.7 \pm 8.1$	$3.45 \pm 1.21$
<b>CTAB External</b>	$47.2 \pm 10.3$	$3.47 \pm 1.16$
<b>MYRI Internal</b>	$49.4 \pm 9.7$	$2.40 \pm 1.03$
<b>MYRI Edge</b>	$50.8 \pm 10.8$	$2.55 \pm 1.05$
<b>MYRI External</b>	$53.3 \pm 11.3$	$2.83 \pm 0.94$

The SAXS analysis of particle diameter for all the 6 different MSNs are within standard deviation of the particle diameter results obtained by TEM (CTAB MSNs =  $43.8 \pm 7.0$  nm and MYRI MSNs =  $41.1 \pm 4.7$  nm). This demonstrates SAXS analysis of particle parameters is reasonable and comparable to TEM. The mean pore diameter obtained for the CTAB MSNs of  $3.49 \pm 1.29$  nm is the same as was found previous literature which used CTAB surfactant to provide porosity in silica molecular sieves (3.0 nm).<sup>11, 12</sup> The mean pore diameter of the MSNs obtained using MYRI is  $2.60 \pm 1.12$  nm showing that there is a lowering in pore diameter using MYRI surfactant compared to CTAB, as expected due to the smaller hydrocarbon chain length, as discussed in the introduction. However, due to the large standard deviation obtained by the analysis, it is not possible to confirm that there is a significant change in pore diameter variation.

### **3.3.6 Gas Sorption Porosimetry Analysis**

To these three variants of amine functionalisation for both MYRI and CTAB MSNs,  $Gd^{3+}$ -DOTA was bound to the MSNs by firstly amide formation with the N-hydroxysuccinimide, NHS, activated DOTA ester. The gadolinium ion,  $Gd^{3+}$ , was bound within the DOTA chelates attached to the MSNs by addition of DOTA MSNs

to a  $\text{GdCl}_3$  solution and excess  $\text{Gd}^{3+}$  removed by dialysis. To confirm that there is a statistically significant difference between the pore diameter obtained using CTAB and MYRI, and that  $\text{Gd}^{3+}$ -DOTA functionalisation had no effect on the smaller pore diameter MSNs obtained, gas sorption porosimetry was utilised using the Barrett-Joyner-Halenda (BJH) method (*Figure 3.9*).<sup>30</sup>



*Figure 3.9. Plots of the pore diameters obtained by porosimetry, A) All the pore diameters obtained for the aminated MSNs CTAB variations, Internal, Edge and External (2.82 nm). B) The pore diameters obtained before and after  $\text{Gd}^{3+}$ -DOTA functionalisation of the MYRI Internal MSNs (1.90 nm), C) The pore diameters obtained before and after  $\text{Gd}^{3+}$ -DOTA functionalisation of the MYRI Edge MSNs (1.87 nm), D) The pore diameters obtained before and after  $\text{Gd}^{3+}$ -DOTA functionalisation of the MYRI External MSNs (1.89 nm).*

The pore diameters obtained for CTAB Internal, Edge and External (A) prove again that there is no variation in pore diameter on changing the position of the amine functionalisation. The pore diameter mean value is different compared to the pore diameter obtained by SAXS ( $2.82 \pm 0.02$  nm and  $3.49 \pm 1.29$  nm for porosimeter and SAXS respectively). The reason for this restriction in pore diameter found by

porosimetry is due to the non-linear worm like structure of the pores restricting N<sub>2</sub> access and therefore lowering the calculated pore diameter.<sup>14</sup>

Comparing the pore diameter obtained for CTAB of  $2.82 \pm 0.02$  nm and MYRI (B, C, D) mean of  $1.89 \pm 0.02$  nm there is a clear variation in pore diameter between the MSN synthesised using the MYRI compared to CTAB. An issue with the MYRI analysis was that the pore diameter was right at the lower limitation of the instrument. Usually there is a bell curve set of data which allows interpretation of the pore size of the materials, which is absent for MSNs prepared using MYRI surfactant. Therefore, the SAXS pore sizes will be referred to hereafter.

Porosimetry was also used to confirm that the Gd<sup>3+</sup>-DOTA (~1.1 nm diameter chelate) binding to the MSNs had no effect on the small pore diameter ( $1.89 \pm 0.02$  nm) of the MYRI MSNs (B, C, and D). No variation was observed between pore diameter of the MSNs before and after Gd<sup>3+</sup>-DOTA functionalisation showing that the addition of the Gd<sup>3+</sup>-DOTA binding has no significant effect on the pore diameter. Further analytical experiments probing the nanostructure of the Gd<sup>3+</sup>-DOTA MSNs were not performed due to this confirmation of no variation in pore diameter and the low yields of Gd<sup>3+</sup>-DOTA MSNs acquired.

## 3.4 Investigation of MSN Pore Diameter and Gd<sup>3+</sup>-DOTA Location on Relaxivity

### 3.4.1 Relaxometry Analysis at 13.1 MHz

After having completely characterised the MSNs obtained using MYRI and CTAB surfactants and Gd<sup>3+</sup>-DOTA functionalising them, the effect of pore diameter on relaxivity was explored. This is probed by calculating the relaxivity,  $r_1$ , ( $\text{mM}^{-1} \text{s}^{-1}$ ) of the contrast agent. This was acquired by obtaining the longitudinal relaxation,  $T_1$ , (s) of the water suspension containing the contrast agent under investigation at a minimum of four differing concentrations. The  $T_1$  times acquired for each dilution are converted to  $R_{1, \text{observed}}$  and relaxivity using *Equation 3.1* and *Equation 3.2*.

$$R_1 = 1/T_1 \text{ (Equation 3.1)}$$

$$\text{Relaxivity} = r_1 = \frac{R_{1, \text{observed}} - R_{1, \text{solvent}}}{[\text{Gd}]} \text{ (Equation 3.2)}$$

The  $R_{1, \text{observed}}$  is normalised by subtracting the  $R_1$  of ultrapure water,  $R_{1, \text{solvent}}$  ( $T_1 = 2.59 \text{ s}$  or  $R_1 = 0.39 \text{ s}^{-1}$ ). This is plotted against the Gd<sup>3+</sup> concentration (mM) of each dilution of contrast agent obtained by inductively coupled plasma mass spectrometry, ICP-MS. The relaxivity of the contrast agent is calculated from the slope of the linear plot (see appendix).

Both the MYRI and CTAB MSNs without Gd<sup>3+</sup>-DOTA functionalisation were analysed at 13.1 MHz to observe if there was an inherent decrease in  $T_1$  on addition of the MSNs. The  $T_1$  of the CTAB and MYRI MSNs was found to be  $2.32 \pm 0.05 \text{ s}$  and  $2.37 \pm 0.07 \text{ s}$  respectively. This agrees with previously published research that observed a lowering in the  $T_1$  of water on addition of silica nanoparticles due to water surface association onto the nanoparticles lowering tumbling rates.<sup>31</sup> Then the six variations of Gd<sup>3+</sup>-DOTA functionalisation location on MSNs synthesised using CTAB and MYRI surfactants were analysed (*Figure 3.10*).



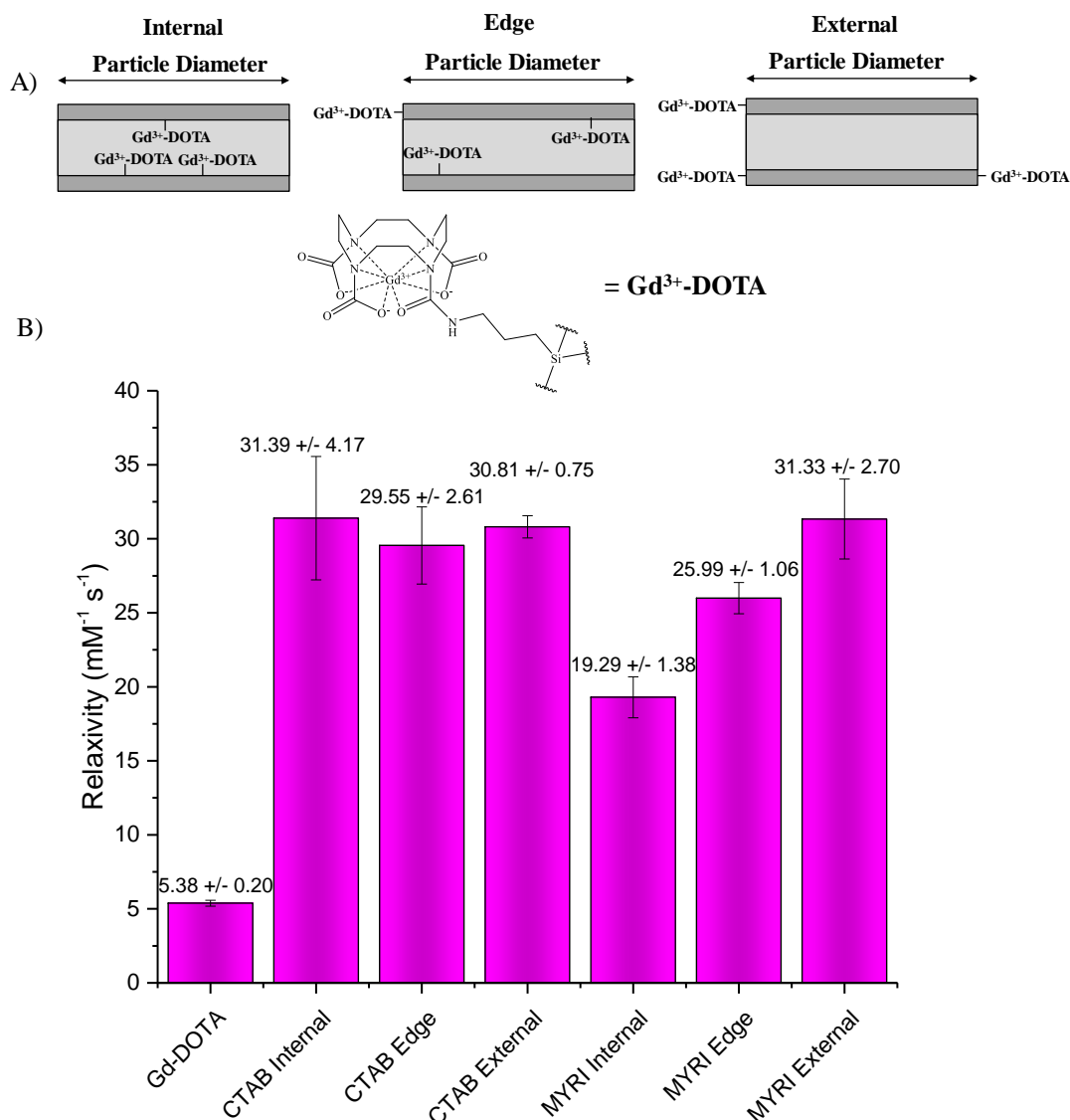


Figure 3.10. A) A schematic of the variation in location, Internal, Edge and External, of the  $Gd^{3+}$ -DOTA functionalisation on the MSNs and B) bar chart of the relaxivity at 13.1 MHz of the 6 families of MSNs synthesised using the two surfactants, MYRI and CTAB, and the three functionalisation locations, Internal, Edge and External compared to molecular  $Gd^{3+}$ -DOTA. The mean and standard deviation obtained by analysing three batches of MSNs.

All MSNs analysed gave significantly enhanced relaxivity compared to the molecular  $Gd^{3+}$ -DOTA ( $5.38 \pm 0.20 \text{ mM}^{-1} \text{ s}^{-1}$ ). This highlights the dramatic MRI contrast agent enhancement obtained by attaching a  $Gd^{3+}$  chelate to a nanostructure. This well-known behaviour is provided by the covalent linking of the chelate to the MSNs increasing  $\tau_R$  and this increasing relaxation, which is expected and documented, both experimentally and theoretically.<sup>3, 32-35</sup> For the MSNs synthesised using the

CTAB surfactant, there was no change in relaxivity with changing the location of the  $\text{Gd}^{3+}$ -DOTA from Internal ( $31.39 \pm 4.17 \text{ mM}^{-1} \text{ s}^{-1}$ ), Edge ( $29.55 \pm 2.61 \text{ mM}^{-1} \text{ s}^{-1}$ ) and External ( $30.81 \pm 0.75 \text{ mM}^{-1} \text{ s}^{-1}$ ). Therefore, for MSN synthesised using CTAB as the surfactant, the interaction with  $\text{Gd}^{3+}$  located inside the pores with water molecules, Internal functionalisation, is the same as the  $\text{Gd}^{3+}$  interacting with the bulk water on the outer surface of the MSNs, External functionalisation, or at the mouths of the pores, Edge functionalisation. The explanation is that the pore diameter of  $3.49 \pm 0.05 \text{ nm}$  facilitates excellent water exchange and mobility within the pore network, with no apparent spatial restrictions.<sup>36</sup> This results varies from previously published data where 0.15 mol%  $\text{Gd}^{3+}$ -DOTA functionalised MSNs synthesised using CTAB as a soft template.<sup>3</sup> In this research Edge localisation resulted in relaxation enhancement compared to Internal and External functionalisation ('Short delay' [ $\equiv$ Internal] =  $17.14 \pm 0.49 \text{ mM}^{-1} \text{ s}^{-1}$ , 'Long delay' ( $\equiv$ Edge) =  $33.57 \pm 1.29 \text{ mM}^{-1} \text{ s}^{-1}$  and 'Post graft' [ $\equiv$ External] =  $10.77 \pm 0.22 \text{ mM}^{-1} \text{ s}^{-1}$ ). It should be noted that in the previous study the relaxivity was analysed at 300 MHz, where the impact of  $\tau_R$  and  $\tau_M$  are different<sup>37, 38</sup> whereas here, at lower magnetic fields, dipole-dipole interactions dominate.<sup>39, 40</sup> However, MSNs prepared using MYRI as the surfactant, there is a reduction of the relaxivity to  $19.29 \pm 1.38 \text{ mM}^{-1} \text{ s}^{-1}$  when the MSNs are Internal functionalised (CTAB  $\text{Gd}^{3+}$ -DOTA Internal MSNs =  $31.39 \pm 4.17 \text{ mM}^{-1} \text{ s}^{-1}$ ). This is partially recovered to the relaxivity obtained from the CTAB MSNs analogue when the  $\text{Gd}^{3+}$  is located on the Edge of the pores (MYRI  $\text{Gd}^{3+}$ -DOTA Edge MSNs =  $25.99 \pm 1.06 \text{ mM}^{-1} \text{ s}^{-1}$  and CTAB  $\text{Gd}^{3+}$ -DOTA Edge MSNs =  $29.55 \pm 2.61 \text{ mM}^{-1} \text{ s}^{-1}$ ) and fully regained when the  $\text{Gd}^{3+}$  is located on the External of the MSNs (MYRI  $\text{Gd}^{3+}$ -DOTA External MSNs =  $31.33 \pm 2.70 \text{ mM}^{-1} \text{ s}^{-1}$  and CTAB  $\text{Gd}^{3+}$ -DOTA External MSNs =  $30.81 \pm 0.75 \text{ mM}^{-1} \text{ s}^{-1}$ ). This is due to the smaller pore diameter obtained by using MYRI ( $2.60 \pm 1.12 \text{ nm}$ ) compared to CTAB ( $3.49 \pm 1.29 \text{ nm}$ ) restricting the diffusion and mobility of water molecules to  $\text{Gd}^{3+}$  when the  $\text{Gd}^{3+}$ -DOTA is located inside the pores, Internal. This restriction lowers the interaction between  $\text{Gd}^{3+}$  and the water molecules, retarding relaxation. This restriction is partially alleviated when the  $\text{Gd}^{3+}$ -DOTA is Edge localised on the MSNs. Finally, the relaxivity is like the relaxivities obtained with the CTAB MSNs when the  $\text{Gd}^{3+}$  is fully able to interact with the bulk water when attached to the External surfaces of the MSNs. In addition, this research has shown that the optimum relaxation of MSNs synthesised in this way is  $\sim 30 \text{ mM}^{-1} \text{ s}^{-1}$  which is approximately 6 times the relaxivity obtained by molecular  $\text{Gd}^{3+}$ -DOTA ( $5.38 \pm 0.20$

mM<sup>-1</sup> s<sup>-1</sup>). The enhanced relaxivity obtained allows for the possibility of significantly reduced dosages with equal or better levels of signal. Therefore, drastically lowering the amount of Gd<sup>3+</sup> administered to a patient minimising the side effects such as nephrogenic fibrosis and Gd<sup>3+</sup> build up in the brain.<sup>41, 42</sup>

The quantity of Gd<sup>3+</sup> per mg of MSN was investigated by ICP-MS to confirm that there was no large variation in the amount of Gd<sup>3+</sup> immobilised onto the MSNs. In addition, the amount of adsorbed Gd<sup>3+</sup> per mg of MSNs was also investigated by synthesising MSNs and leaving the sample overnight in GdCl<sub>3</sub> without the NHS-DOTA functionalisation step, Gd<sup>3+</sup> Adsorption Control, (*Table 3.3*).

*Table 3.3. The mass of Gd<sup>3+</sup> per mg of MSNs for each repeat of the six families synthesised plus the Gd<sup>3+</sup> Adsorption Control. The values stated are the average of the three batches of MSN functionalised with varying surfactant and Gd<sup>3+</sup>-DOTA functionalisation location.*

<b>Sample</b>	<b>Mass of Gd per mg of MSN (ng mg<sup>-1</sup>)</b>
<b>CTAB Internal</b>	109.9 ± 61.1
<b>CTAB Edge</b>	74.4 ± 37.2
<b>CTAB External</b>	124.9 ± 35.5
<b>MYRI Internal</b>	85.8 ± 30.7
<b>MYRI Edge</b>	84.1 ± 56.1
<b>MYRI External</b>	96.1 ± 8.6
<b>Gd<sup>3+</sup> Adsorption Control</b>	0.52 ± 0.1

As can be seen in *Table 3.3* all the Gd<sup>3+</sup>-DOTA functionalised MSNs are within error of one another and the very low amount of adsorption observed means that the relaxivity of the designed MSNs was due to the chelated lanthanide species and that negligible adsorption took place throughout.

### 3.5 Conclusions

MSNs were synthesised using three surfactants of varying aliphatic chain lengths, CTAB, MYRI and DODE in order to obtain MSNs with varying pore diameters. These surfactants are well known to lead to different pore sizes due to the varying micelles into which the self-assemble and around which the silica nanostructure forms to obtain MSNs. The MSNs obtained had a large variation in particle diameter (CTAB MSNs =  $43.8 \pm 7.0$  nm, MYRI MSNs =  $100.9 \pm 12.9$  nm and DODE MSNs =  $460.0 \pm 34.0$  nm) because of variation in the kinetic rates of formation due to different micelle layer packing. The MSNs had to be the same size to minimise tumbling variation between MSN batches allowing for the variation in pore diameter and its effect on relaxivity to be examined exclusively. This was successfully achieved by changing the temperature in which MSN synthesis was performed from 80 °C with CTAB ( $43.8 \pm 7.0$  nm) to 40 °C for MYRI ( $41.1 \pm 4.7$  nm). DODE was unable to be optimised by varying the temperature as at 15 °C, the observed limit to which the yield was not drastically affected, the MSNs obtained had a particle diameter of  $62.9 \pm 10.6$  nm, which was not within error of the MSNs obtained by CTAB or MYRI.

These optimised synthetic protocols were subsequently used to synthesise families of MYRI and CTAB MSNs with surface amine functionalities in different locations by carefully controlling the addition of an aminosilane precursor to yield Internally, Edge or Externally amine-functionalised MSNs, following modified literature procedures. Various characterisation techniques (FTIR and TGA) confirmed that the surfactant had been completely removed from the pores. TEM analysis confirmed no change to the particle diameter or porosity on amine functionalisation. The hydrodynamic size and the zeta potential were analysed for each of the MSNs synthesised to confirm that there was no loss in stability of the MSNs suspended in water and that the surface charge was not affected by changing the location of the amine groups.

The pore diameters of the MSNs obtained using CTAB and MYRI were analysed by SAXS (CTAB =  $3.49 \pm 0.05$  nm, MYRI =  $2.60 \pm 0.22$  nm) and porosimetry (CTAB =  $2.82 \pm 0.02$  nm, MYRI =  $1.89 \pm 0.02$  nm). The variation in pore diameter obtained by the aliphatic carbon tail of MYRI (14 Cs) being shorter than

CTAB (16 Cs), resulting in smaller diameter micelles which provide the porosity of MSNs as a soft template.

Finally, the effect of changing the pore diameter and the location on relaxivity was monitored at 13.1 MHz. It was found that the  $\text{Gd}^{3+}$ -DOTA modified CTAB MSNs all obtained strong protic relaxation enhancement regardless of the  $\text{Gd}^{3+}$ -DOTA location on the MSNs (Internal =  $31.39 \pm 4.17 \text{ mM}^{-1} \text{ s}^{-1}$ , Edge =  $29.55 \pm 2.61 \text{ mM}^{-1} \text{ s}^{-1}$  and External  $30.81 \pm 0.75 \text{ mM}^{-1} \text{ s}^{-1}$ ). This is due to the excellent water access to the paramagnetic chelate facilitated by the unrestricted diffusion through the pores of the MSNs. However, when the MSNs were synthesised in the presence of MYRI surfactant, the smaller pore diameter obtained caused a lower relaxivity enhancement when  $\text{Gd}^{3+}$ -DOTA was located inside the pores (Internal =  $19.29 \pm 1.38 \text{ mM}^{-1} \text{ s}^{-1}$ ). This is due to the smaller pores obtained using MYRI as a soft template lowering diffusion rates of water in the pores therefore lowering water interaction with  $\text{Gd}^{3+}$ . This restriction is partially alleviated when the  $\text{Gd}^{3+}$ -DOTA is localised on the Edge ( $25.99 \pm 1.06 \text{ mM}^{-1} \text{ s}^{-1}$ ) and finally the strong protic relaxation rates are observed when  $\text{Gd}^{3+}$ -DOTA is located on the surface (External =  $31.33 \pm 2.70 \text{ mM}^{-1} \text{ s}^{-1}$ ).

### 3.6 Future Work

The first avenue would be to see whether the same trends for relaxation are found for these MSNs at varying magnetic fields. This is important as  $T_1$  relaxation is dependent on magnetic field strength.<sup>32, 33</sup> This has already been started for the MYRI Internal, MYRI Edge and MYRI External MSNs which were analysed at 9.4 Tesla (Figure 3.13).

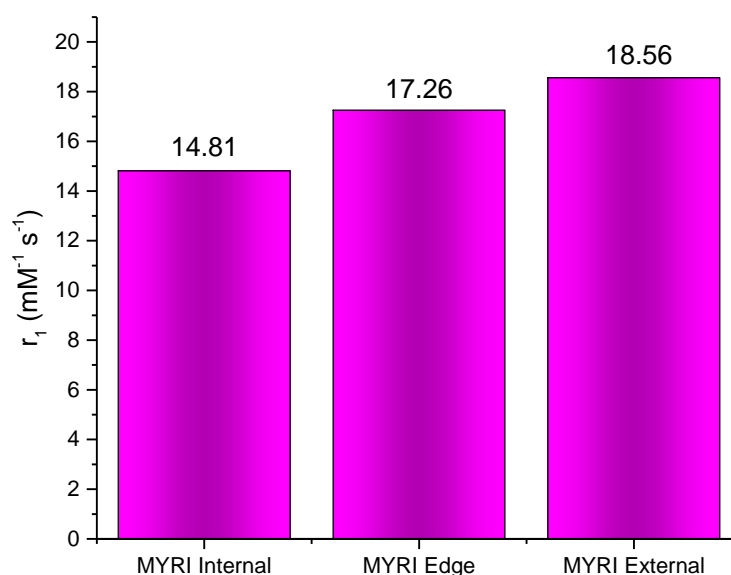


Figure 3.11. The relaxivity at 9.4 Tesla of the 3 families of MSNs synthesised using the MYRI surfactant in the three locations, Internal, Edge and External.

It is interesting to observe the significant lowering in relaxivity obtained (13.1 MHz relaxivities were MYRI Internal =  $19.29 \pm 1.38 \text{ mM}^{-1} \text{ s}^{-1}$ , MYRI Edge =  $25.99 \pm 1.06 \text{ mM}^{-1} \text{ s}^{-1}$  and MYRI External =  $31.33 \pm 2.70 \text{ mM}^{-1} \text{ s}^{-1}$  compared to 9.4 Tesla =  $14.81 \text{ mM}^{-1} \text{ s}^{-1}$ ,  $17.26 \text{ mM}^{-1} \text{ s}^{-1}$  and  $18.56 \text{ mM}^{-1} \text{ s}^{-1}$  respectively). This represents a previously observed phenomena whereby at higher fields the enhancement by increased tumbling rate is partially suppressed.<sup>37</sup> It seems the general trend observed at 13.1 MHz is observed 9.4 Tesla where the small pore diameter obtained using MYRI ( $2.60 \pm 0.22 \text{ nm}$ ) seems to lower the interaction between the water molecules and  $\text{Gd}^{3+}$  causing a decrease in the relaxivity. Further work is required to confirm reproducibility. Also,

investigation into the CTAB MSNs to observe whether their trend of no deviation between Gd location and relaxivity should be investigated, with repeats, at 9.4 T.

Another direction this could go into is optimisation of a synthetic protocol that reproducibly obtains MSNs which have pore diameters of  $> 3.49 \pm 1.29$  nm. This would provide more information into the effect of pore diameter on relaxivity. initial studies were performed by the addition of mesitylene to the CTAB protocol to cause pore swelling, replicating Kresge *et al.* findings using molecular sieves.<sup>11</sup> However, issues with reproductivity hampered further work.

### 3.7 References

1. J. Kecht, A. Schlossbauer and T. Bein, *Chemistry of Materials*, 2008, **20**, 7207-7214.
2. V. Cauda, A. Schlossbauer, J. Kecht, A. Zürner and T. Bein, *Journal of the American Chemical Society*, 2009, **131**, 11361-11370.
3. J. J. Davis, W.-Y. Huang and G.-L. Davies, *Journal of materials chemistry*, 2012, **22**, 22848-22850.
4. S. Aime, L. Frullano and S. G. Crich, *Angewandte Chemie*, 2002, **114**, 1059-1061.
5. J. S. Ananta, B. Godin, R. Sethi, L. Moriggi, X. Liu, R. E. Serda, R. Krishnamurthy, R. Muthupillai, R. D. Bolskar and L. Helm, *Nature nanotechnology*, 2010, **5**, 815.
6. P. H. Fries and E. Belorizky, *The Journal of chemical physics*, 2010, **133**, 024504.
7. S. Takahara, N. Sumiyama, S. Kittaka, T. Yamaguchi and M.-C. Bellissent-Funel, *The Journal of Physical Chemistry B*, 2005, **109**, 11231-11239.
8. I. Brovchenko, A. Geiger and A. Oleinikova, *The Journal of chemical physics*, 2004, **120**, 1958-1972.
9. A. A. Milischuk and B. M. Ladanyi, *The Journal of chemical physics*, 2011, **135**, 174709.
10. E. Belorizky, P. H. Fries, A. Guillermo and O. Poncelet, *ChemPhysChem*, 2010, **11**, 2021-2026.
11. C. Kresge, M. Leonowicz, W. J. Roth, J. Vartuli and J. Beck, *nature*, 1992, **359**, 710.
12. J. S. Beck, J. Vartuli, W. J. Roth, M. Leonowicz, C. Kresge, K. Schmitt, C. Chu, D. H. Olson, E. Sheppard and S. McCullen, *Journal of the American Chemical Society*, 1992, **114**, 10834-10843.
13. F. Carniato, L. Tei, W. Dastru, L. Marchese and M. Botta, *Chemical Communications*, 2009, 1246-1248.
14. K. Moller, J. Kobler and T. Bein, *Advanced Functional Materials*, 2007, **17**, 605-612.
15. Q. Huo, D. I. Margolese, U. Ciesla, P. Feng, T. E. Gier, P. Sieger, R. Leon, P. M. Petroff, F. Schüth and G. D. Stucky, *Nature*, 1994, **368**, 317.



16. Q. Huo, D. I. Margolese, U. Ciesla, D. G. Demuth, P. Feng, T. E. Gier, P. Sieger, A. Firouzi and B. F. Chmelka, *Chemistry of Materials*, 1994, **6**, 1176-1191.
17. N. Bloembergen, E. M. Purcell and R. V. Pound, in *Resonances*, World Scientific, Editon edn., 1990, pp. 411-444.
18. G. Socrates, *Infrared and Raman characteristic group frequencies: tables and charts*, John Wiley & Sons, 2004.
19. R. Tian, O. Seitz, M. Li, W. Hu, Y. J. Chabal and J. Gao, *Langmuir*, 2010, **26**, 4563-4566.
20. J. H. Moon, J. S. Seo, Y. Xu and S. Yang, *Journal of Materials Chemistry*, 2009, **19**, 4687-4691.
21. G.-L. Davies, J. O'Brien and Y. K. Gun'ko, *Scientific Reports*, 2017, **7**, 45862.
22. K. Nakamoto, *Handbook of Vibrational Spectroscopy*, 2006.
23. N. Maxim, A. Overweg, P. J. Kooyman, A. Nagy, R. A. van Santen and H. C. Abbenhuis, *Journal of Materials Chemistry*, 2002, **12**, 3792-3798.
24. F. Lu, S. H. Wu, Y. Hung and C. Y. Mou, *Small*, 2009, **5**, 1408-1413.
25. S. M. Egger, K. R. Hurley, A. Datt, G. Swindlehurst and C. L. Haynes, *Chemistry of Materials*, 2015, **27**, 3193-3196.
26. D. Brevet, M. Gary-Bobo, L. Raehm, S. Richeter, O. Hocine, K. Amro, B. Looock, P. Couleaud, C. Frochot and A. Morère, *Chemical Communications*, 2009, 1475-1477.
27. G. A. Parks, *Chemical Reviews*, 1965, **65**, 177-198.
28. J. Bolze, D. Beckers and B. PANalytical, *Size Distribution Determination of Nanoparticles and Nanosized Pores by Small-Angle X-Ray Scattering (SAXS) on a Multi-Purpose X-Ray Diffractometer*, tech. rep., PANalytical.
29. E. Walenta, *Acta Polymerica*, 1985, **36**, 296-296.
30. E. P. Barrett, L. G. Joyner and P. P. Halenda, *Journal of the American Chemical society*, 1951, **73**, 373-380.
31. C. L. Cooper, T. Cosgrove, J. S. van Duijneveldt, M. Murray and S. W. Prescott, *Langmuir*, 2013, **29**, 12670-12678.
32. I. Solomon and N. J. Bloembergen, 1956, **25**, 261-266.
33. N. Bloembergen and L. J. Morgan, 1961, **34**, 842-850.

34. Y.-S. Lin, Y. Hung, J.-K. Su, R. Lee, C. Chang, M.-L. Lin and C.-Y. Mou, *The Journal of Physical Chemistry B*, 2004, **108**, 15608-15611.
35. K. M. L. Taylor, J. S. Kim, W. J. Rieter, H. An, W. L. Lin and W. B. Lin, *Journal of the American Chemical Society*, 2008, **130**, 2154-+.
36. R. Guillet-Nicolas, J. L. Bridot, Y. Seo, M. A. Fortin and F. Kleitz, *Advanced Functional Materials*, 2011, **21**, 4653-4662.
37. P. Caravan, J. J. Ellison, T. J. McMurry and R. B. Lauffer, *Chemical reviews*, 1999, **99**, 2293-2352.
38. Y. Li, S. Laurent, L. Esser, L. Vander Elst, R. N. Muller, A. B. Lowe, C. Boyer and T. P. Davis, *Polymer Chemistry*, 2014, **5**, 2592-2601.
39. G. L. Davies, S. A. Corr, C. J. Meledandri, L. Briode, D. F. Brougham and Y. K. Gun'ko, *ChemPhysChem*, 2011, **12**, 772-776.
40. J. S. Ananta, *Nat Nano*, 2010, **5**, 815.
41. P. Marckmann, L. Skov, K. Rossen, A. Dupont, M. B. Damholt, J. G. Heaf and H. S. Thomsen, *Journal of the American Society of Nephrology*, 2006, **17**, 2359-2362.
42. T. Kanda, T. Fukusato, M. Matsuda, K. Toyoda, H. Oba, J. i. Kotoku, T. Haruyama, K. Kitajima and S. Furui, *Radiology*, 2015, **276**, 228-232.

# Chapter 4

## 4. Thermo-responsive MSNs as Diagnostic MRI Contrast Agents

---

### 4.1 Chapter Summary

The optimisation of MRI contrast agents is in high demand due to the constant need for better acquired images to allow for the correct diagnosis to be obtained. Nanomaterials are ideal in this field due to their high surface areas and potential for surface modification allowing for dual-functionality possibilities of both contrast and stimuli responsive properties. Therefore, an MSN based MRI contrast agent with a switchable MRI contrast in response to an external stimulus would be a highly desirable and accessible objective.

Herein MRI-active  $\text{Gd}^{3+}$ -DOTA-modified MSNs (previously tuned in Chapter 3 to present strong protic relaxation enhancement behaviour) surface functionalised with the thermoresponsive polymer poly(N-isopropylacrylamide), pNIPAM, were prepared using a ‘grafting from’ methodology using atom transfer radical polymerisation, ATRP. It was found that the synthetic protocol obtained successfully bound pNIPAM to the MSNs’ surface with minimum physisorption of unbound pNIPAM and unreacted monomer. The surface coverage and pNIPAM chain length was varied to produce a small family of polymer-grafted MRI active nanoparticles, in a bid to tune the temperature of any observed stimuli-response and hence switchable contrast behaviour. The transition temperature (indicative of a ‘stimuli-response’) was tuneable according to the grafting density and chain length of the polymer chains on the nanoparticle surfaces, from 36.4 °C to 42.3 °C. As the nanocomposite transitioned through this temperature, precipitation of the particles was observed. The MSNs produced were analysed for their applicability to the function of being MRI contrast agents by relaxometry and phantom  $T_1$  weighted images from a clinical MRI scanner.

There was found to be no suppression of the  $\text{Gd}^{3+}$ -DOTA MSNs previously confirmed enhanced contrast ability. Finally, it was investigated whether the precipitation effect provided by the pNIPAMs interaction with temperature had any qualitative effect on an MRI image. This was found to be the case with there being a stark variation between the precipitated MSNs and the surrounding water, thus proving the relevance of these MSNs as a method of observing temperature variation within a patient. This is promising result as it facilitates the possibility of tumour tissue identification by the MRI contrast agent aggregating around the hotter tumour tissue compared to the surrounding healthy tissue.

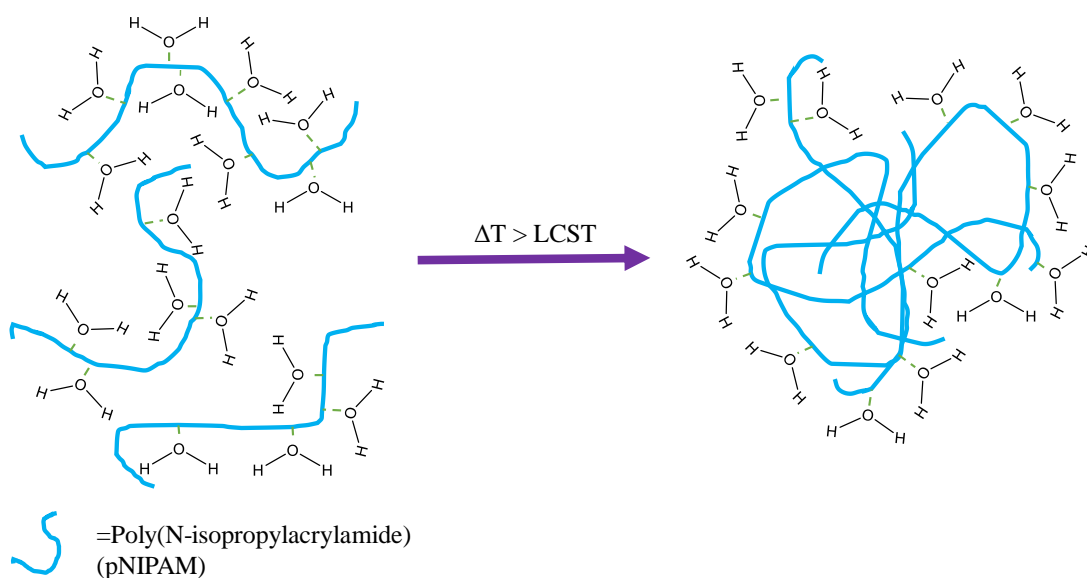
## 4.2 Introduction

Making a MRI contrast agent system that is able to respond to changes in the environment is highly desirable due to the control in location of the system that entails in the patient.<sup>1</sup> This control provides 2 major benefits, firstly the ability to localise contrast only in the tissues of interest, reducing background noise thus making correct diagnosis more likely. Secondly the control of location allows for the minimisation of GBCA administered to the patient, limiting the possibility of side effects for example  $\text{Gd}^{3+}$  deposition in tissues.<sup>2-5</sup>

Localised hyperthermia ablation is an established method of treating malignant tissues.<sup>6</sup> In this treatment the malignant tissue is heated to between 41 °C and 45 °C to initiate cancer cell death. The method of localised heating varies from the use of lasers,<sup>7</sup> microwaves,<sup>8</sup> radiofrequency<sup>9</sup> and ultrasound.<sup>10</sup> However being able to observe the shape and size of the ablation is difficult due to heterogenous temperature distribution because of differences in tissue composition, tissue anatomy and vascularisation.<sup>11, 12</sup> This results in between 30 % and 60 % malignant cells at the treated site proceeding to have tumour progression after ablation therapy.<sup>9, 13, 14</sup> Therefore the application of a contrast agent that was able to provide an intraprocedural monitoring system would aid in the reduction of local tumour progression rates after ablation and in turn benefit long-term patient survival. The multiplanar imaging capabilities and excellent soft tissue contrast makes MRI an ideal analytical method to monitor ablation.<sup>15-20</sup> The vast majority of research into thermo-responsive MRI contrast agents are based on GBCAs encapsulated in liposomes with a suitable phase transition temperature such that the GBCA is released in the desired location with the additional advantage of simultaneously being a drug delivery system.<sup>21-30</sup>

Iron oxide and silica nanoparticles have also been utilised as thermoresponsive MRI contrast agents.<sup>31-33</sup> As iron oxide and silica nanoparticles are not inherently thermoresponsive, this is provided by polymer functionalisation. The polymer commonly used to provide thermoresponsive properties is poly(N-isopropylacrylamide), pNIPAM.<sup>34</sup> pNIPAM has a lower critical solution temperature, LCST, of 32 °C whereby below the LCST pNIPAM is miscible in water whilst above the polymer separates from the water phase. This occurs due to aggregation of

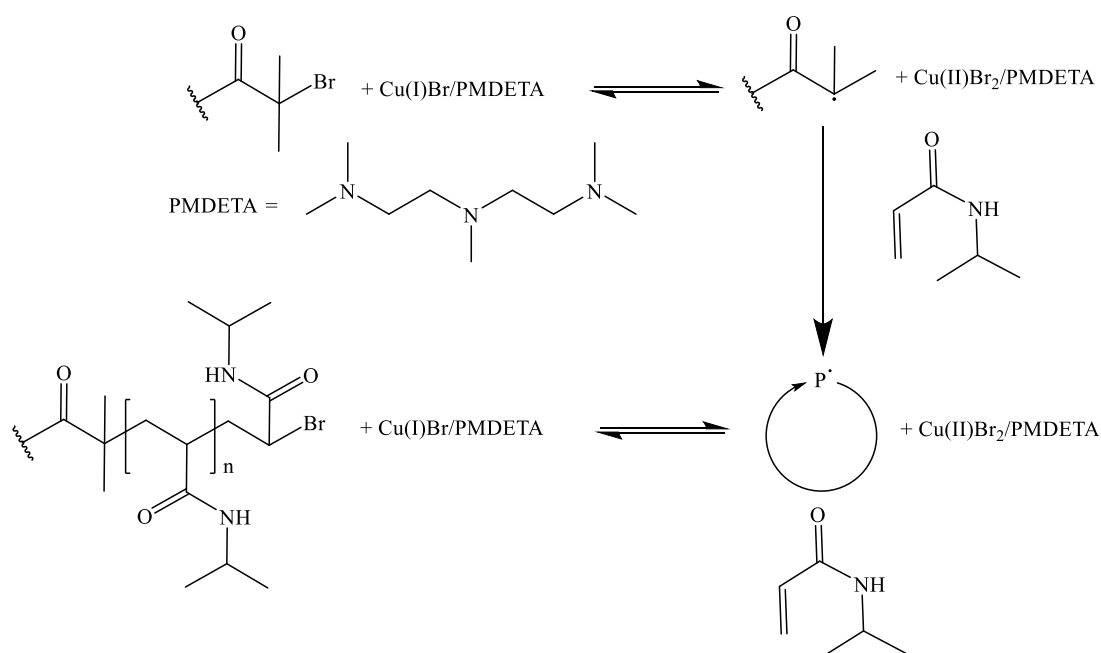
pNIPAM on formation of intermolecular hydrogen bonds between polymer chains and the weakening of the ordering effect of the water amide hydrogen bonds, a thermodynamically controlled process (*Figure 4.1*).<sup>35</sup> This transition temperature can be observed by observation of the cloud point of the system, since aggregation leads to a distinctive change in turbidity and opaqueness of the aqueous system.<sup>36</sup>



*Figure 4.1. A schematic of the change in intermolecular interactions above and below the LCST of the thermoresponsive polymer, pNIPAM. Temperature < LCST consists predominantly of intermolecular interaction with water, whilst when  $T > LCST$  most intermolecular interactions are with neighbouring polymers causing aggregation of the polymer.*

There has been a vast amount of research into pNIPAM's application to medicinal chemistry.<sup>37</sup> The desirability of pNIPAM stems from firstly its LCST of 32 °C meaning that it is soluble at room temperature and phase separates at body temperature (37 °C). This variation in property allowing pNIPAM to be utilised for drug delivery.<sup>38-40</sup> In addition the LCST is able to be tuned by binding pNIPAM on nanoparticle surfaces at different densities and chain lengths.<sup>36</sup> This enables pNIPAM to be used as a potential biomedical carrier in its linear polymer, hydrogel or copolymer form.<sup>41-45</sup> pNIPAM has also been found to have a low toxicity both in vitro<sup>46-49</sup> and in vivo.<sup>50,51</sup> Finally the versatility of pNIPAM synthesis allows for many various polymerisation methods to be performed.<sup>52-55</sup>

Atom transfer radical polymerisation, ATRP, is an applicable method of pNIPAM synthesis.<sup>56</sup> ATRP usually employs a transition metal halide with a transition metal having two stable oxidation state with a difference of one, for example  $\text{Cu}^+$  and  $\text{Cu}^{2+}$ . The rate of polymerisation and polymer chain length is controlled by the transition metal being chelated by a multidentate ligand such as *N, N, N', N'', N'''*-pentamethyldiethylenetriamine, PMDETA, to form the catalyst.<sup>57</sup> The initiator is usually an alkyl halide and the monomer is an alkene species that has substituents which are able to stabilise the propagating radical.<sup>58</sup> The objective of the transition metal halide chelate is to activate and deactivate the polymer chain by generating radicals via an one electron transfer process. This activation and deactivation of the polymer forms an equilibrium which is shifted predominantly to the deactivated polymer chains. Most of the polymer being in a deactivated state slows down the rate of propagation and minimises the amount of reactive radical species in the polymerisation, therefore minimising the amount of undesirable side reactions and polymer chain termination. This control allows for more uniform polymer chain lengths to be acquired (*Figure 4.2*).<sup>59</sup>



*Figure 4.2 The transition metal catalysed (i.e. copper bromide and PMDETA) ATRP of NIPAM to obtain pNIPAM.*

Y. Yang *et al.* utilised pNIPAM synthesised using ATRP to graft thermoresponsive polymers onto MSNs of particle diameter 200 nm.<sup>33</sup> The ATRP initiator,  $\alpha$ -

bromoisobutyryl bromide, BIBB, was bound to the surface of the MSNs and pNIPAM polymerised on the surface using a ‘Grafting From’ technique. This method was utilised due to the high grafting density of polymer brushes on the surface of the MSNs that can be obtained.<sup>60-63</sup>

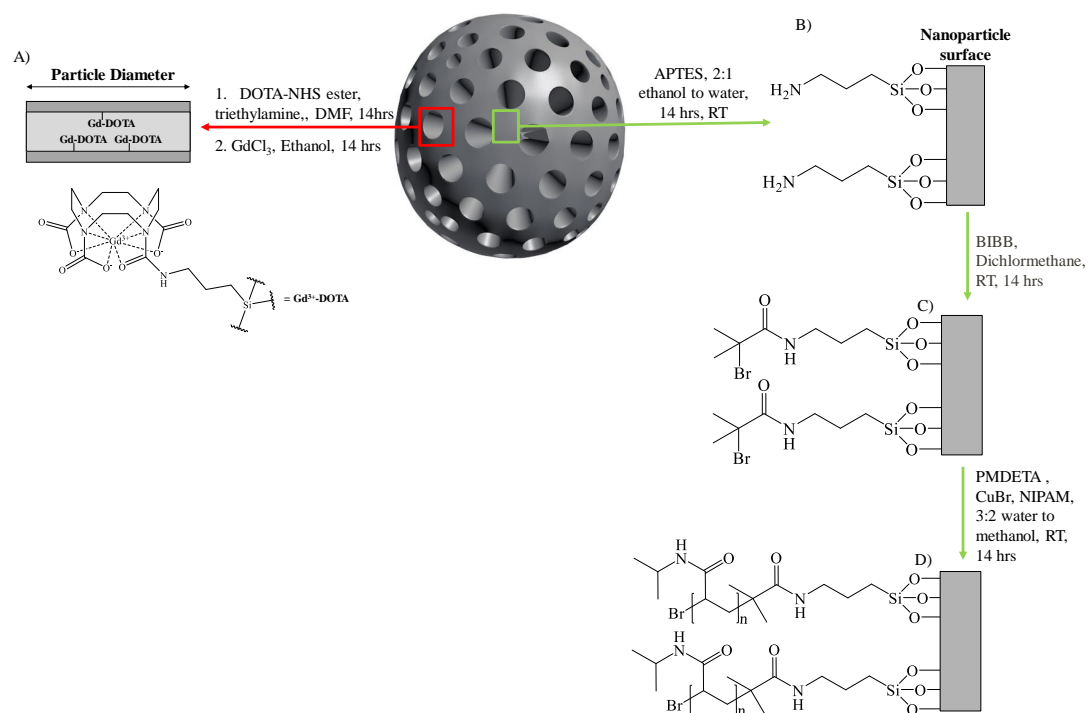
#### **4.2.1 Aims**

The aim of this work was to prepare a thermoresponsive MRI contrast agent based upon an MSN core and a polymer shell capable of demonstrating a change in MRI relaxation behaviour with changing temperature. A further aim was to tune the temperature at which this ‘response’ could be observed to provide tuneable-response composite systems through varying the grafting density of the thermoresponsive polymer on the composite surfaces.



### 4.3 Preparation and Characterisation of pNIPAM Surface Functionalised MSNs using a ‘Grafting From’ Method

CTAB internally  $\text{Gd}^{3+}$ -chelate functionalised MSNs, as prepared in chapter 3, were selected for this work, due to their high relaxivity values due to excellent water accessibility and internalised Gd-species which would not be detrimentally affected by subsequent polymer grafting. Briefly, 3.5 nm pore diameter MSNs using cetyltrimethylammonium bromide, CTAB, surfactant with amine groups located on internal surfaces by co-condensation of (3-aminopropyl)triethoxysilane had 2,2',2''-(10-(2-((2,5-dioxopyrrolidin-1-yl)oxy)-2-oxoethyl)-1,4,7,10-tetraazacyclododecane-1,4,7-triyl)triacetic acid (DOTA-NHS-ester) amide bound to the amine groups. Then these DOTA functionalised MSNs were suspended  $\text{Gd}^{3+}$  salt solution and subsequently dialysed to produce the MRI active nanoparticle systems (Figure 3.5, Section 3.4.1, Chapter 3). CTAB surfactant was used to maximise the relaxivity response of the nanoparticles, those with high relaxivity values, as found in section 3.5.1, Chapter 3. Internal functionalisation of the MR-active  $\text{Gd}^{3+}$ -DOTA probe was selected to minimise any possible interactions between the polymer and the  $\text{Gd}^{3+}$ -DOTA. As the polymer was required to be on the surface of the MSNs to increase the polymer's interaction with the surrounding water, the  $\text{Gd}^{3+}$ -DOTA was placed in the pores where they would be protected from the polymer. In order to graft the polymer onto the polymer surfaces, the ‘parent’  $\text{Gd}^{3+}$ -DOTA MSNs were firstly surface functionalised with amine groups using APTES utilising a post grafting technique. Amine surface coverage was varied between three different theoretical percentage coverages, 0.2 mol%, 1 mol% and 2.5 mol% relative to TEOS. These low loading densities were investigated in a bid to maintain good colloidal stability as well as water access to the internalised  $\text{Gd}^{3+}$  species. To these amine groups  $\alpha$ -bromoisobutyryl bromide, BIBB, was chemically bound to the MSNs via an amide bond. The final synthetic step, ATRP of NIPAM, was performed using the MSN bound BIBB as the initiator, copper bromide as the metal catalyst and *N, N, N', N'', N''*-pentamethyldiethylenetriamine, PMDETA, as the ligand (Figure 4.3).



*Figure 4.3. A Schematic of the functionalisation method to obtain thermoresponsive MRI contrast agents. A)  $\text{Gd}^{3+}$ -DOTA functionalisation inside the pores of the MSNs,  $\text{Gd}^{3+}$ -DOTA MSNs, B) external surface amine functionalisation of  $\text{Gd}^{3+}$ -DOTA MSNs, C)  $\alpha$ -Bromoisobutyryl bromide, BIBB, initiator surface functionalisation and D) N-isopropylacrylamide, NIPAM, polymerisation onto the  $\text{Gd}^{3+}$ -DOTA MSNs surface, where  $n$  represents the number of monomer repeat units.*

A control to determine the success of the polymerisation and therefore lack of surface physisorption of monomer onto nanoparticles surfaces, Adsorption Control, was performed to observe how much, if any, BIBB and therefore pNIPAM was adsorbed to the surface of the MSNs. For the adsorption control the final pNIPAM synthetic step was exactly as previously described for 0.2 mol%, 1 mol% and 2.5 mol%. However, the surface amination step (*Figure 4.3, B*) and  $\text{Gd}^{3+}$ -DOTA functionalisation step (*Figure 4.3, A*) was removed. To ensure removal of the copper catalyst, all samples were washed using dialysis after brief stirring in an aqueous acid solution.

### 4.3.1 Zeta Potential

The synthetic steps shown in *Figure 4.3* were followed by Zeta potential (*Table 4.1*). Zeta potential was found to be a more effective method of monitoring these changes than other analytical techniques, such as TGA or FTIR, in which the surface grafting

density used on MSN surfaces would be too low to detect by these techniques. Hydrodynamic diameter was not used as confirmation of synthetic steps due to most synthetic steps involved between the parent MSNs and the final composite inducing colloidal instability.

*Table 4.1. The Zeta potential obtained after key steps in the synthesis of thermoresponsive MSNs. The samples shown being the Adsorption Control, 0.2 mol%, 1 mol% and 2.5 mol%.*

Synthetic step	Sample			
	Adsorption Control / mV	0.2 mol%* / mV	1 mol%* / mV	2.5 mol%* / mV
<b>Parent MSNs</b>	-27.9 ± 1.2	-28.9 ± 5.7	-27.5 ± 2.8	-27.5 ± 2.4
<b>Gd<sup>3+</sup>-DOTA modified MSNs</b>	X**	-17.50 ± 0.4	-24.4 ± 0.6	-17.6 ± 0.3
<b>Externally aminated MSNs</b>	X*	2.5 ± 0.6	11.0 ± 1.6	22.8 ± 1.3
<b>Final composite after pNIPAM modification</b>	-11.3 ± 0.2	0.6 ± 0.1	13.9 ± 0.5	21.6 ± 0.5

\*mole percent (mol%) with respect to tetraethyl orthosilicate, TEOS for external amine modification.

\*\*Step omitted to allow accurate investigation into adsorption of pNIPAM onto the surface of the MSNs.

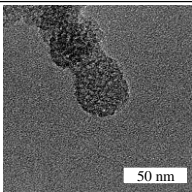
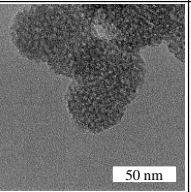
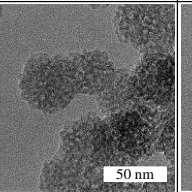
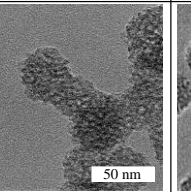
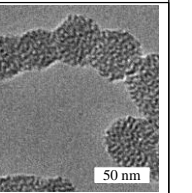
The Zeta potential of parent MSNs were all within error of each other confirming that there was no significant variation between batches of MSNs and the reproducibility of the method. The zeta potential is negative due to the abundance of Si-OH on the surface of the MSNs. The Gd<sup>3+</sup>-DOTA functionalisation of the MSNs also had no significant effect on colloidal stability as all MSNs had a strong negative zeta potential. Small changes in zeta potential after Gd<sup>3+</sup>-DOTA functionalisation indicate this modification step was successful, as some silanol groups are used to graft this

chelate onto MSN surfaces. Overall, the charge remains negative, as would be expected due to the negative silanol groups dominating. The surface amination had the most dramatic effect on Zeta potential for 0.2 mol%, 1 mol% and 2.5 mol%, all samples changing from negative Zeta potentials to positive surface charge. This is due to the amine groups added to the surface of the MSNs being basic and therefore being protonated in water. The degree of positivity clearly coincides with the percentage surface amination with 0.2 mol% =  $2.49 \pm 0.62$  mV, 1 mol% =  $11.00 \pm 1.60$  mV and 2.5 % =  $22.80 \pm 1.30$ . This shows that the increase in amine groups has changed the surface of the MSNs as expected.

The grafting of the pNIPAM had little effect on the zeta potential due to the charge neutrality of NIPAM. For the Adsorption control, on the other hand, there is a significant change in surface charge, which is likely due to some surface physisorption of NIPAM monomers on MSN surfaces causing the charge of the surface silanol groups to be less available for measurement by this technique. The physisorption of NIPAM leading to possible colloidal instability.

#### 4.3.2 Transmission Electron Microscopy

Transmission electron microscopy, TEM, was performed on all final NIPAM nanoparticle composites and the parent MSNs to confirm that the surface modification and NIPAM loading did not impact particle structure (*Figure 4.4*).

Sample	0.2 mol%	1 mol%	2.5 mol%	Adsorption Control	Parent
TEM Image					
Diameter	$43.1 \pm 5.8$ nm	$44.2 \pm 4.9$ nm	$44.2 \pm 6.3$ nm	$46.5 \pm 5.8$ nm	$47.4 \pm 4.5$ nm

*Figure 4.4. The TEM images obtained for the 0.2 mol%, 1 mol%, 2.5 mol% pNIPAM surface functionalised  $Gd^{3+}$ -DOTA MSNs, Adsorption Control  $Gd^{3+}$ -DOTA MSNs and the Parent MSNs. The particle diameters were calculated by the mean and standard deviation of 100 MSN diameters.*

All samples had similar core particle sizes ( $43.1 \pm 5.8$  to  $47.4 \pm 4.5$  nm) and their pore structure remained intact. Importantly the mean diameter does not vary from the parent MSNs, indicating that the multiple surface modification steps did not impact the

particles' morphologies and sizes. The pNIPAM surface functionalisation can't be observed in these images because of the low-density nature of the polymer (with no sample staining performed) and grafting densities were relatively low.

### 4.3.3 Infrared Spectroscopy

FTIR was used to confirm functionalisation of MSN surfaces with NIPAM. As previously stated, Section 4.3.1, FTIR could not determine the surface modification steps of amination and bromination, due to the low grafting densities employed (Figure 4.5).

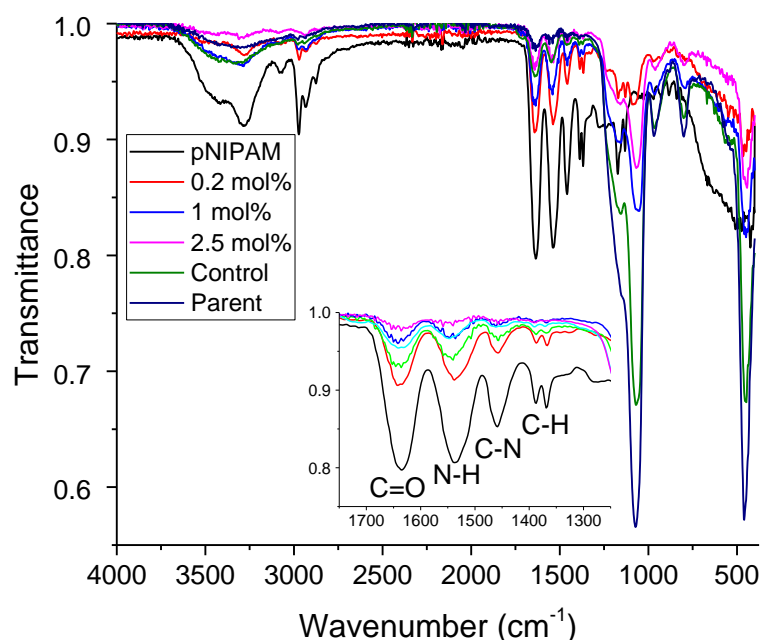


Figure 4.5. The infrared spectra of the three varying surface densities of pNIPAM, 0.2 mol%, 1 mol% and 2.5 mol% amination with respect to TEOS, the parent MSNs and the Adsorption Control compared to pNIPAM polymerised using ATRP. Inset highlights the infrared spectra between 1300  $\text{cm}^{-1}$  and 1700  $\text{cm}^{-1}$ .

The stretches observed representing the MSNs are between 1015-1190  $\text{cm}^{-1}$  representing Si-O-Si stretching and bending vibrations,<sup>64-66</sup> stretches around 800  $\text{cm}^{-1}$ , indicative of Si-O-Si stretches,<sup>67</sup> and those centred at ~550 and ~450  $\text{cm}^{-1}$  representing tri and tetracyclosiloxane rings of siloxanes.<sup>68</sup> These are coupled with the stretches representing NIPAM, C-H bending (~1400  $\text{cm}^{-1}$ ), C-N bending (~1450  $\text{cm}^{-1}$ ), N-H amide bending (~1500  $\text{cm}^{-1}$ ) and C=O stretching (~1600  $\text{cm}^{-1}$ ) appearing for

the 0.2 mol%, 1 mol%, 2.5 mol% and Adsorption Control.<sup>69</sup> The IR spectra obtained are identical to the FTIR spectra obtained by Yang *et al.* for their pNIPAM functionalised MSNs.<sup>33</sup> This shows that NIPAM is present on the MSNs obtained after the polymerisation. The presence of these stretches in the Adsorption Control strongly suggest that some NIPAM physisorption has occurred. The O-H stretch ( $\sim 3300\text{ cm}^{-1}$ ) appearing in the Adsorption Control and the 1 mol% samples appearing due to all the samples being dried from a water suspension of the MSNs.

#### 4.3.4 Dynamic Light Scattering

Measurement of the hydrodynamic diameter was performed using dynamic light scattering in aqueous suspensions on the polymer grafted samples to observe if the surface density variation from 0.2 mol%, 1 mol% and 2.5 mol% had any effect on their colloidal behaviour (*Table 4.2*).

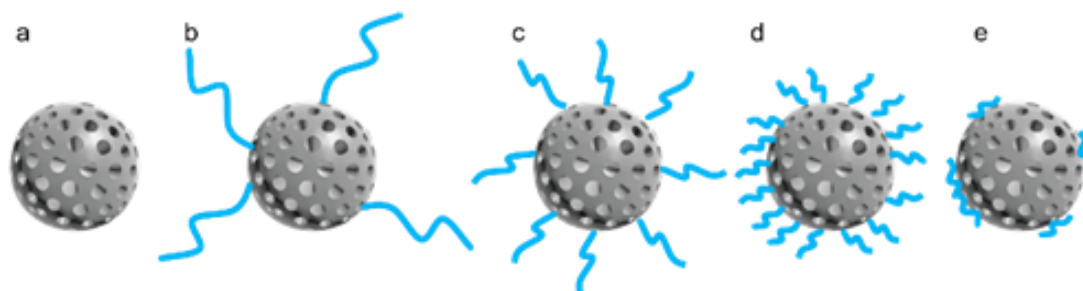
*Table 4.2. The hydrodynamic diameters and PDIs obtained from DLS of the pNIPAM functionalised  $\text{Gd}^{3+}$ -DOTA MSNs with theoretical surface densities of 0.2 mol%, 1 mol% and 2.5 mol% compared to the parent MSNs and the Adsorption Control.*

Theoretical pNIPAM grafting density on surface of $\text{Gd}^{3+}$ -DOTA MSNs / mol%*	Hydrodynamic diameter / nm	PDI
0.2	$726.3 \pm 72.1$	$0.43 \pm 0.02$
1.0	$576.4 \pm 94.2$	$0.41 \pm 0.03$
2.5	$362.1 \pm 19.3$	$0.28 \pm 0.02$
Adsorption Control	$3170 \pm 30.0$	$0.21 \pm 0.14$
Parent MSNs	$221.7 \pm 53.8$	$0.26 \pm 0.05$

\*mol% of APTES relative to TEOS.

This analysis showed that that all MSNs that were reacted with NIPAM had a significantly larger hydrodynamic diameter than the parent MSNs ( $221.7 \pm 53.8\text{ nm}$ ). This suggests that NIPAM has been bound to the surface of the MSNs. There was decreased hydrodynamic diameter on increase in percentage surface functionalisation of NIPAM from  $726.3 \pm 72.1\text{ nm}$  for 0.2 mol% to  $576.4 \pm 94.2$  for 1 mol% and finally  $362.1 \pm 19.3\text{ nm}$  for 2.5 mol%. This suggested that the polymer chain length was increasing with decreased surface grafting density, increasing the volume of water

molecules able to interact with the extended (below LCST) hydrophilic polymer chains. This is due to the consistent amount of NIPAM monomer added to the ATRP reaction. That is  $6.63 \times 10^{-3}$  mol NIPAM was added to each reaction containing 0.2 mol%, 1 mol% or 2.5 mol% surface grafted BIBB initiator; this resulted in longer polymer chains with lower grafting density of surface initiator, as the polymerisation process proceeds from less initiator groups. Conversely, shorter polymer chain lengths are formed when higher grafting densities of surface initiator was used, as the NIPAM monomer grows from each initiator group, leading to overall shorter chains (*Figure 4.6*). The large hydrodynamic diameter obtained by the Adsorption Control ( $3170 \pm 30.0$  nm) shows that the physisorbed NIPAM monomer observed has destabilised the MSNs in aqueous solution. The polydispersity indexes, PDIs, for pNIPAM functionalised MSNs for 0.2 mol% was  $0.43 \pm 0.02$ , 1 mol% was  $0.43 \pm 0.03$ , 2.5 mol% was  $0.28 \pm 0.03$  and Adsorption Control was  $0.21 \pm 0.14$ . The PDIs for 0.2 mol% and 1 mol% were significantly higher than the PDI obtained for the similarly prepared MSNs without surface grafted polymer chains, as described in Section 3.4.4, Chapter 3 ( $0.26 \pm 0.05$ ). This was expected as the addition of pNIPAM to the surface of the MSNs would have increased the polydispersity of MSNs in aqueous suspension due to greater variation in the diameter of the composite provided by the hydrophilic polymer chain on the MSN surface.



*Figure 4.6. Schematic representation of different surface grafting densities of pNIPAM (blue curves) grafted from parent  $Gd^{3+}$ -DOTA-MSNs (grey spheres, a): b) 0.2 mol%; c) 1 mol%; d) 2.5 mol%, e) Adsorption Control MSNs. Mol% as determined by the grafting density of the initiator, described in Figure 4.3.*

### 4.3.5 Gel Permeation Chromatography

Gel permeation chromatography, GPC, was used to investigate differences between polymer length chains. As GPC is not able to analyse polymers grafted onto nanostructure surfaces, the polymers had to be synthesised in the absence of MSNs. Therefore, three separate ATRP reactions were performed in the absence of MSNs, with the equivalent concentration of BIBB initiator added to the polymerisation mixture assuming 100 % conversion of surface amine groups to amide bound BIBB for each surface density investigated (*Table 4.3 and Figure 4.7*). The theoretical  $M_w$  was calculated using *Equation 4.1* and  $M_n$  calculated by *Equation 4.2* where  $N_i$  is the number of moles of each polymer species and  $M_i$  is the molar mass of that species.

$$\text{Theoretical } M_w = \frac{\text{Moles of monomer}}{\text{Moles of initiator}} \times M_{w_{\text{monomer}}} \text{ (Equation 4.1)}$$

$$M_n = \frac{\sum N_i M_i}{\sum N_i} \text{ (Equation 4.2)}$$

*Table 4.3. A table providing the calculated theoretical molecular weight,  $M_w$ , and the number averaged molar mass,  $M_n$ , with the polydispersity obtained by GPC of the calculated 0.2 mol%, 1 mol% and 2.5 mol% equivalent concentrations of BIBB.*

Sample	Theoretical $M_w$ / g mol <sup>-1</sup>	$M_n$ obtained by GPC / g mol <sup>-1</sup>	Polydispersity by GPC
<b>0.2 mol%</b>	54,800	41,900	1.62
<b>1 mol%</b>	11,000	12,400	1.29
<b>2.5 mol%</b>	4400	900	1.07



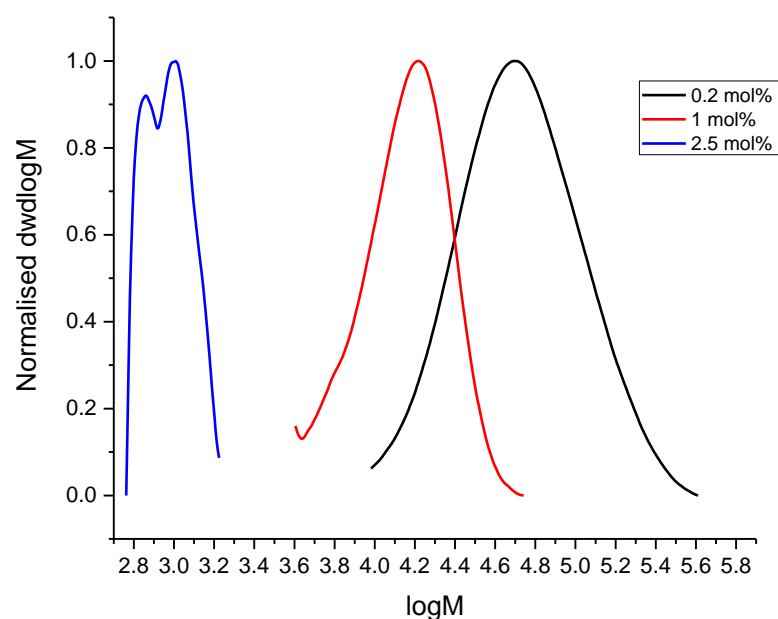


Figure 4.7. The plot of log of the molecular weight,  $\log M$ , against normalised  $dwd\log M$  for the ATRP reactions involving the theoretical BIBB concentrations calculated for the 0.2 mol%, 1 mol% and 2.5 mol% surface functionalised MSNs.

The GPC analysis showed that for 0.2 mol% the  $M_n$  of the pNIPAM was 41,900 g/mol, 1 mol% was 12,400 g/mol and 2.5 % was 900 g/mol. This supports the DLS analysis that 0.2 mol% surface functionalised MSNs have longer pNIPAM chains on the surface compared to 1 mol% which in turn has longer pNIPAM chains than 2.5 mol%. The theoretical  $M_w$  calculated for 1 mol% was comparable to the  $M_n$  obtained by GPC (Theoretical  $M_w = 11,000 \text{ g mol}^{-1}$ ,  $M_n = 12400 \text{ g mol}^{-1}$ ). The  $M_n$  obtained by GPC varied from the theoretical  $M_w$  for 0.2 mol% (Theoretical =  $54800 \text{ g mol}^{-1}$ ,  $M_n = 41,900 \text{ g mol}^{-1}$ ) and 2.5 % (Theoretical =  $4400 \text{ g mol}^{-1}$ ,  $M_n = 900 \text{ g mol}^{-1}$ ). These smaller than calculated  $M_n$  values have been obtained because the polymerisation has likely not reached completion. Therefore, every monomer has not been incorporated into the polymer.

#### 4.3.6 Thermogravimetric Analysis

Thermogravimetric analysis, TGA, was performed to obtain the mass percentage of pNIPAM on the functionalised MSNs. The samples analysed by TGA

were the three polymer grafted MSNs, 0.2 mol%, 1 mol% and 2.5 mol%, the parent  $\text{Gd}^{3+}$ -DOTA functionalised MSNs, pNIPAM and the Adsorption Control (Figure 4.8).

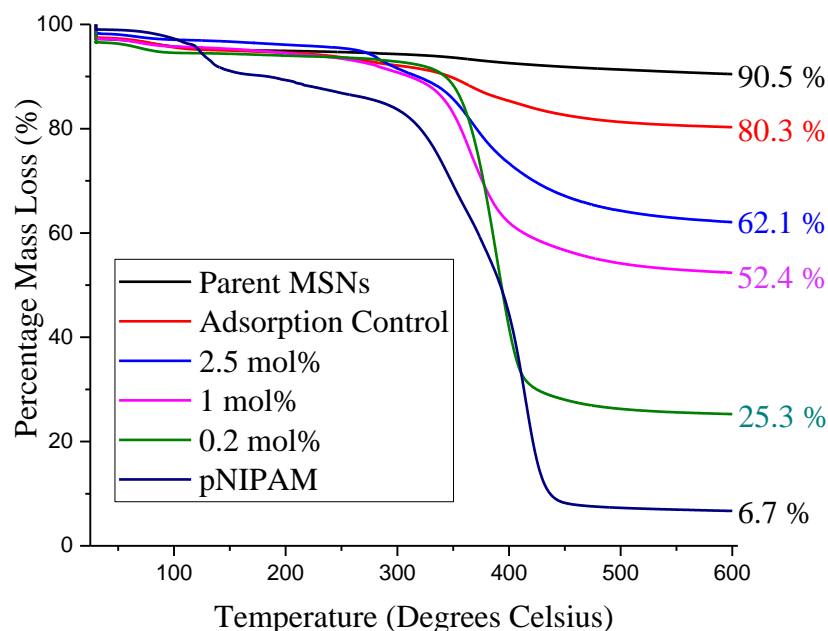


Figure 4.8. The percentage mass loss obtained by TGA of the three grafting densities, 0.2 mol%, 1 mol% and 2.5 mol%, Adsorption Control, the parent MSNs and pNIPAM versus temperature. Percentages represent the total percentage mass remaining at the end of the analysis.

The parent MSNs exhibit the same thermal stability in the 30 °C to 600 °C temperature range observed in Chapter 3 Section 3.3.3. The pNIPAM compared to the parent MSNs was used to identify the temperature at which the mass loss due to pNIPAM would be observed. The pNIPAM has a significant mass loss (4.74 wt%) between 100 °C and 135 °C which represents water in the sample. The largest mass loss for pNIPAM occurs between 325 °C and 425 °C (62.4 wt%), which represents the degradation of the polymer. For the parent MSNs, like in section 3.4.3 Chapter 3, the loss of  $\text{Gd}^{3+}$ -DOTA is not observed in the TGA analysis due to the percentage functionalisation being too low. There is mass loss for the parent MSNs between 325 °C and 425 °C (1.9 wt%), however it is negligible in comparison to the mass loss in the pNIPAM sample. Therefore, the mass lost between 325 °C and 425 °C in the pNIPAM surface functionalised MSNs would predominantly be due to the loss of pNIPAM. So, the difference in mass at 325 °C and 425 °C relative to the starting mass

was used to analyse the percentage by mass of pNIPAM of the three different surface density functionalised Gd<sup>3+</sup>-DOTA MSNs (*Table 4.4*).

*Table 4.4. The percentage by overall mass of PNIPAM on the 0.2 mol%, 1 mol%, 2.5 mol% pNIPAM surface density functionalised MSNs and Adsorption Control.*

<b>Sample</b>	<b>Percentage by overall mass of pNIPAM /wt%</b>
<b>0.2 %</b>	63.9
<b>1 %</b>	29.7
<b>2.5 %</b>	18.6
<b>Adsorption Control</b>	6.1

The percentage by overall mass of pNIPAM on the MSNs decreases with increased surface functionalisation from 63.9 % for 0.2 mol%, 29.7 % for 1 mol% and finally 18.6 % for 2.5 mol% surface density, corresponding to the shortened polymer length chains being formed on the nanoparticle surfaces. This mass percent loss in the Adsorption Control (6.1 %) being higher than the Gd<sup>3+</sup>-DOTA MSNs (1.9 %) between 325 °C and 425 °C confirmed a small amount of physisorption was occurring.

#### **4.3.7 Spectroscopic Analysis of Thermoresponsive Behaviour**

The most common measured macroscopic property analysed to prove thermoresponsive behaviour is the onset of aggregation *via* turbidimetry.<sup>36</sup> this monitors the decrease in transmitted light once the polymer has been heated above its cloud point. The cloud point is the temperature at which phase separation between the polymer and the water solvent starts, causing the solution to turn opaque. This method of analysis measures the outcome of the transition not the transition itself.<sup>70</sup> UV/vis spectroscopy at 700 nm between 25 °C and 50 °C was utilised to observe the cloud point of the MSNs of the varying surface density pNIPAM functionalisation, 0.2 mol%, 1 mol% and 2.5 mol% compared to the Adsorption Control and Gd<sup>3+</sup>-DOTA MSNs (*Figure 4.9*). The cloud point quoted was calculated as the temperature when the background normalised 1/transmittance is half the maximum 1/transmittance obtained for the sample.

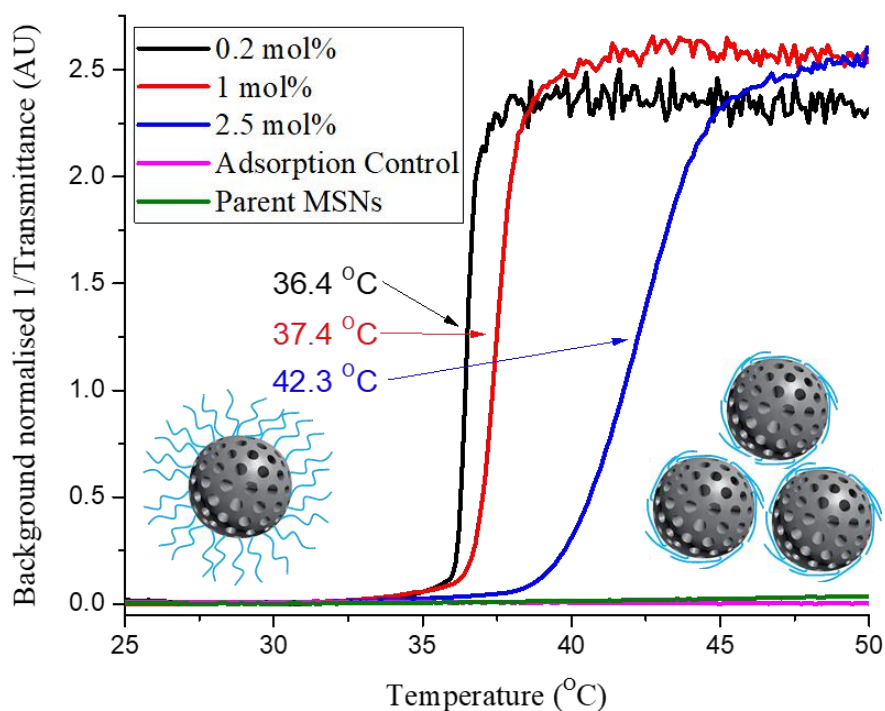
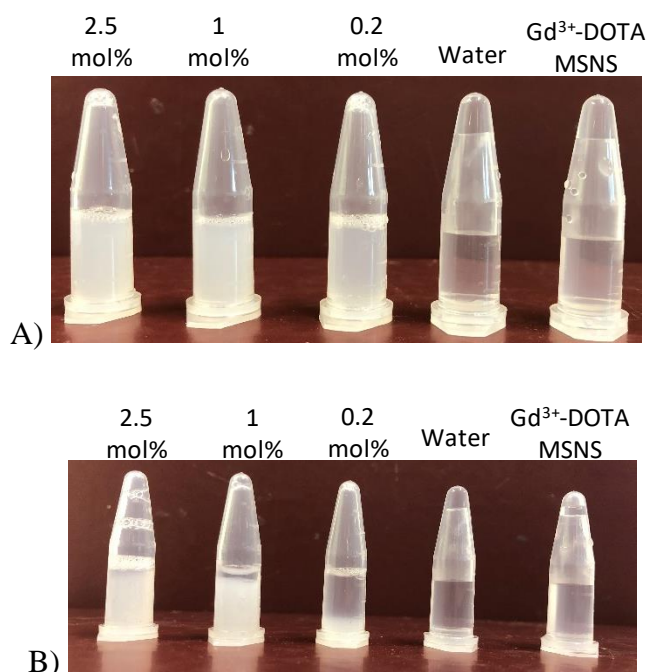


Figure 4.9. The background normalised 1/ transmittance at 700 nm between 25 °C and 50 °C of 0.2 mol%, 1 mol% and 2.5 mol% MSN surface coverage of pNIPAM, the Adsorption Control and the parent MSNs. The cloud point quoted calculated as the temperature which the background normalised 1/transmittance is half the maximum 1/transmittance obtained for the sample. The schematics represent the transition of pNIPAM from its extended formation below its LCST to the contracted formation above its LCST facilitating aggregation.

The parent MSNs have no increase in 1/transmittance with increased temperature, which would show the presence of a cloud point. This shows that the colloidal stability of the parent MSNs in aqueous suspension is independent of temperature. There is a significant increase in 1/transmittance for each of the three pNIPAM surface functionalised samples, indicating the transition through the cloud point. The cloud point varies depending on the surface density of pNIPAM on the MSNs from 36.4 °C for 0.2 mol%, 37.4 °C for 1 mol% and finally 42.3 °C for 2.5 mol%. This variation in observed cloud points between varying the surface density of pNIPAM from 0.2 mol% to 1 mol% and 2.5 mol% could be due to the lower surface densities not having enough surface coverage to ensure polymer-solvent interactions

exclusively, allowing solvent-substrate interactions to be present.<sup>71</sup> This results in the responsive behaviour of the polymer and resulting cloud point being significantly different as the contribution of the underlying substrate will vary.<sup>72</sup> T

his variation in cloud point could also be due to the larger pNIPAM surface density of 2.5 mol% inhibiting complete conversion of polymer-water interactions to polymer-polymer interactions because of steric hindrance of nearby pNIPAM chains. Thus providing colloidal stability to the MSNs up to higher temperatures. These results show that the LCST of the surface pNIPAM can be tuned and optimised to a desirable LCST which can also be observed visibly (*Figure 4.10*). There is no cloud point for the Adsorption Control. Thus, proving that the minimal physisorption of monomer observed by TGA and FTIR is not providing the MSNs with any thermoresponsive properties.



*Figure 4.10. Photographs of 2.5 mol%, 1 mol%, 0.2 mol% pNIPAM surface functionalise Gd<sup>3+</sup>-DOTA MSNs with the mol% representing the mol% of amine functionalisation relative to TEOS, water and parent MSNs at A) 35 °C and B) 40 °C. All MSNs analysed at 10 mg/mL.*

At 35 °C all the pNIPAM surface functionalised MSNs, 0.2 mol%, 1 mol% and 2.5 mol% are observed to be in suspension in the aqueous solution, as evidenced by the opaque appearance of the suspensions. However, after increasing the temperature to

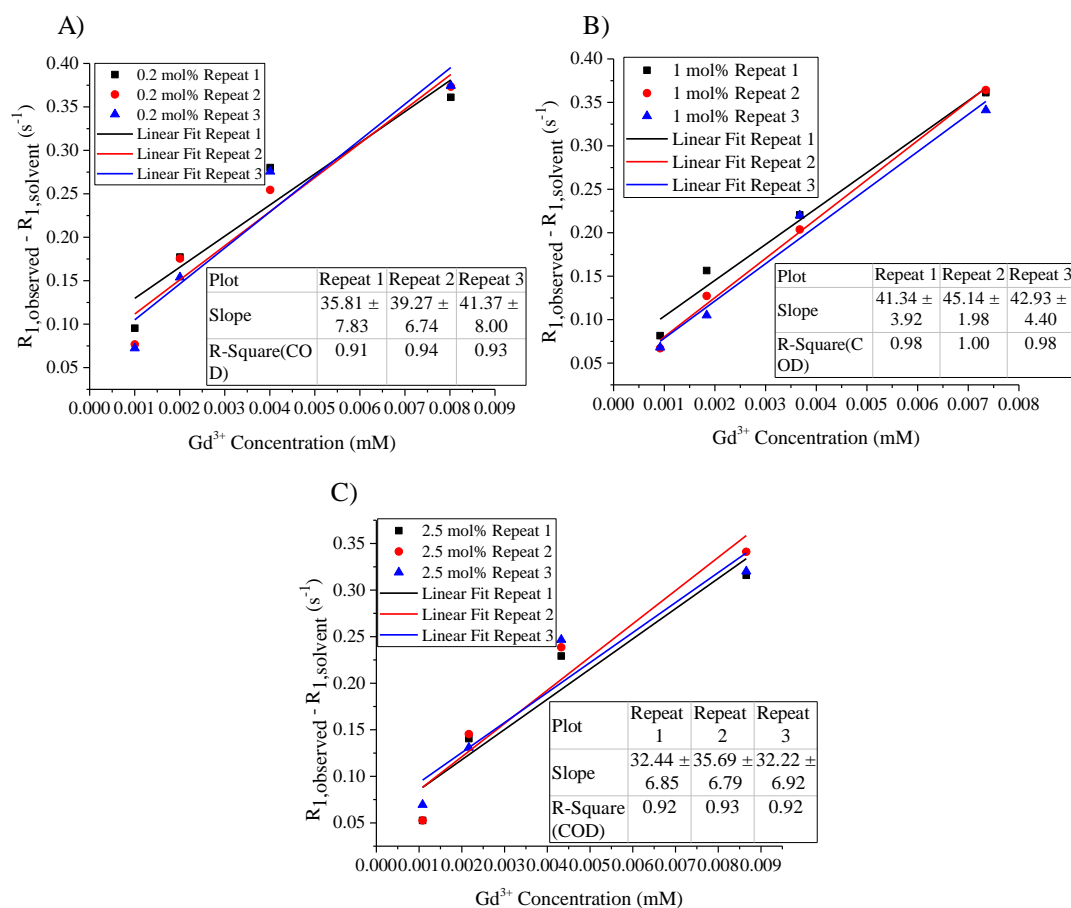
40 °C both the 0.2 mol% and 1 mol% pNIPAM surface functionalised MSNs have clearly aggregated out of suspension. The parent Gd<sup>3+</sup>-DOTA MSNs show no precipitation upon increasing temperature, demonstrating that the behaviour is because of the presence of the grafted thermoresponsive polymers. The 2.5 mol% MSNs, on the other hand, have remained suspended in the water solution, as their cloud point (42.3 °C according to *Figure 4.9*) has not yet been achieved.

Yang *et al.* was also able to acquire thermoresponsive MSNs using CTAB as a soft template and TEOS as a silica source, however used sodium hydroxide instead of TEA which was used in this investigation.<sup>33</sup> This reaction obtained MSNs of 200 nm (parent MSN = 47.4 ± 4.5 nm). The pNIPAM functionalised MSNs obtained had a cloud point in the range 30 – 34 °C, which is lower than the cloud points observed for 0.2 mol%, 1 mol% and 2.5 mol%. However, this discrepancy is due to the large variation in surface density of functionalisation between MSNs. Yang *et al.* surface functionalised the MSNs with 0.28 mL APTES to 1.265 mL TEOS to obtain a surface density of 21.4 % compared to 40 µL APTES to 1.454 mL TEOS for the highest surface density of 2.5 mol% in this research. The ratios of NIPAM monomer used in the ATRP reaction were also considerably higher (0.228 g or 0.906 g NIPAM to ~5 mg MSNs) than those used in this investigation (0.75g NIPAM to ~100 mg MSNs). Yang *et al.* performed no analysis on the grafted polymer to ascertain the  $M_n$ , however this large variation between investigations would suggest that there is a large discrepancy between polymer chain lengths obtained by Yang *et al.* and this investigation. It was also noted by TEM in the research by Yang *et al.* that the polymer chain length was effect by the monomer to initiator ratio but was not investigated further to observe its effect on thermoresponsivity.

## 4.4 Investigation into the pNIPAM Surface Functionalised $\text{Gd}^{3+}$ -DOTA MSNs' application as an MRI Contrast Agent

### 4.4.1 Relaxometry analysis

The pNIPAM functionalised MSNs were analysed at 13.1 MHz at room temperature ( $\sim 20^\circ\text{C}$ ) to obtain their relaxivity and therefore the MSNs effectiveness as MRI contrast agent. This was calculated exactly as previously described in *Equation 3.1* and 3.2, Section 3.5.1 Chapter 3 (*Figure 4.11*).



*Figure 4.11. The plots of  $\text{Gd}^{3+}$  concentration versus water normalised  $R_1$  for A) 0.2 mol%, B) 1 mol% and C) 2.5 mol% pNIPAM modified MSNs. The mol% is amine group functionalisation with respect to TEOS. Each sample has three repeats which correspond to three separate aliquots of the same batch of MSNs and  $R_1$  analysis was*

*performed at room temperature. slope is relaxivity according to Equations 3.1 and 3.2 Section 3.5.1 Chapter 3.*

As in Chapter 3 the slope of the linear plot provides the relaxivity in  $\text{mM}^{-1} \text{s}^{-1}$ . The  $R^2$  values here are lower (0.2 mol% =  $0.93 \pm 0.02$ , 1 mol% =  $0.99 \pm 0.01$  and 2.5 mol% =  $0.92 \pm 0.01$ ) than the  $>0.99$  values previously obtained for  $\text{Gd}^{3+}$ -DOTA MSNs prepared in *Figure 3.16, 3.17 and 3.18*, Appendix, Chapter 3. These slightly lower values are, however, reproducible and are therefore likely due to the Brownian motion of the thermoresponsive pNIPAM attached to the MSNs. This size fluctuation due to Brownian motion is observed in the larger PDIs obtained for the surface pNIPAM  $\text{Gd}^{3+}$ -DOTA MSNs (0.2 mol% =  $0.43 \pm 0.02$ , 1 mol% =  $0.41 \pm 0.03$  and 2.5 mol% =  $0.28 \pm 0.02$  mol%) compared to parent MSNs ( $0.26 \pm 0.05$ ). This polymer motion resulting in steric interactions that cause deviations in water accessibility to the internally  $\text{Gd}^{3+}$ -DOTA bound MSNs to such an extent that variations in the interactions occur between the thermoresponsive MSNs and the surrounding water molecules. This minor fluctuation between the amount of water molecules that can interact with the  $\text{Gd}^{3+}$ -DOTA complexes inside the pores results in differences between repeated  $T_1$  analysis of the same MSN batch and concentration. These results were used in calculating the mean and standard deviation of the relaxivity of the samples (*Figure 4.12*).



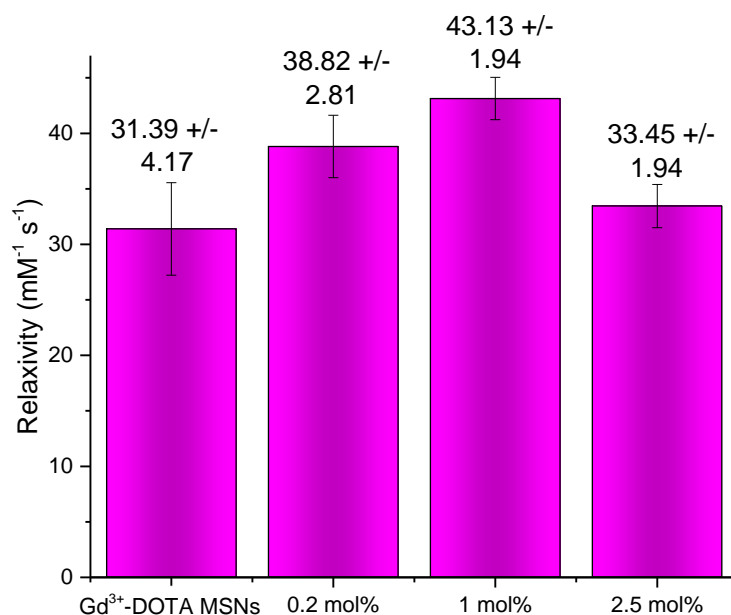


Figure 4.12. A bar chart showing the comparison in relaxivity between Gd<sup>3+</sup>-DOTA MSNs (CTAB Internal MSNs, Figure 3.11, Section 3.5.1 Chapter 3), 0.2 mol%, 1 mol% and 2.5 mol% of amine functionalisation of MSNs with respect to TEOS. at room temperature. The mean and standard deviation calculated by measurements obtained from three separate samples of the same batch of MSNs.

The relaxivities obtained, 0.2 mol% =  $38.8 \pm 2.8 \text{ mM}^{-1} \text{ s}^{-1}$ , 1 mol% =  $43.1 \pm 1.9 \text{ mM}^{-1} \text{ s}^{-1}$  and 2.5 mol%  $33.4 \pm 1.9 \text{ mM}^{-1} \text{ s}^{-1}$  are higher than the relaxivity of the Gd<sup>3+</sup>-DOTA MSNs =  $31.39 \pm 4.17 \text{ mM}^{-1} \text{ s}^{-1}$ . This shows there is no reduction in relaxivity due to the pNIPAM chains on the surface of the MSNs hindering water access to the internalised Gd<sup>3+</sup>-chelate species. This is an essential first consideration for these nanocomposites to be explored as diagnostic MRI contrast agents. The slightly heightened relaxivity values observed may be due to the pNIPAM chains slowing the tumbling of the MSNs. Slowing down the tumbling rate of the Gd<sup>3+</sup>-chelate is known to increase contrast and is represented in Solomon-Bloembergen-Morgan (SBM) Theory, specifically in *Equations 1.5 and 1.6* in Section 1.3.3, Chapter 1.<sup>73-75</sup>

As copper was used in the ATRP reaction as a catalyst and is paramagnetic and therefore could affect the relaxivity of the pNIPAM functionalised Gd<sup>3+</sup>-DOTA MSNs, ICP-MS was performed to observe the amount of copper contamination (Table 4.5).

Table 4.5. The ICP-MS analysis of copper and gadolinium in the samples 0.2 mol%, 1 mol% and 2.5 mol% pNIPAM surface functionalised MSNs, mol% of amine functionalisation with respect to TEOS.

Sample	Gd / ppb	Cu / ppb
0.2 mol%	25.22	35.63
1 mol%	23.11	63.21
2.5 mol%	27.22	42.31

The ICP-MS analysis showed that Cu impurities were present in the samples and that the concentration of Cu was consistently higher than the concentration of Gd. To investigate this further a second control, Cu Control, was made with all the synthetic steps of the 0.2 mol% pNIPAM surface coverage protocol except the Gd<sup>3+</sup>-DOTA functionalisation step (Figure 4.3, A), to investigate how much the copper impurity was affecting the relaxivity of the samples (Figure 4.13).

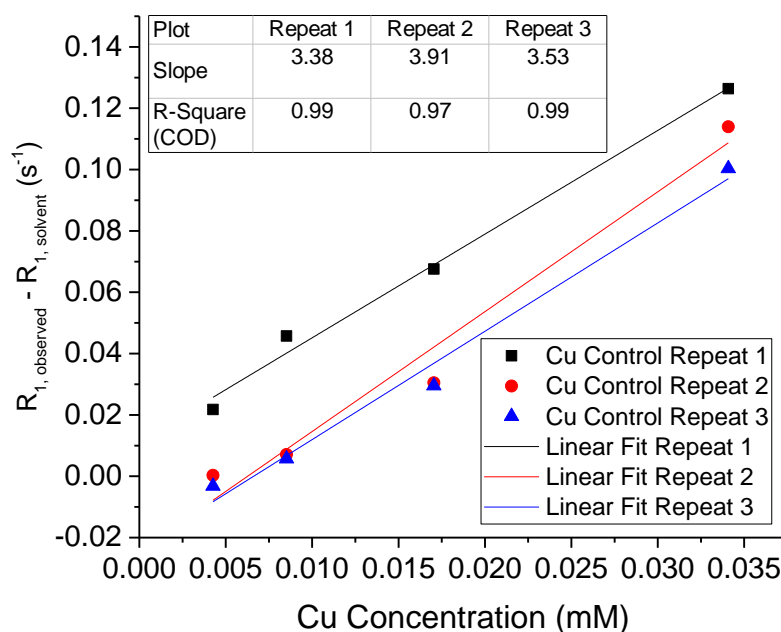


Figure 4.13. The plots of Cu concentration versus water normalised  $R_1$  for the Cu Control. The three repeats correspond to three separate aliquots of the same batch of MSNs and  $R_1$  analysis was performed at room temperature. slope is relaxivity according to Equations 3.1 and 3.2 Section 3.5.1 Chapter 3.

The Cu concentration obtained by ICP-MS for the Cu Control was 53.00 ppb which is equivalent to the concentrations of Cu obtained by the 0.2 mol% (35.63 ppb), 1 mol% (63.21 ppb) and 2.5 mol% (42.31 ppb) samples. The relaxivity obtained by the Cu Control was very low at  $3.61 \pm 0.27 \text{ mM}^{-1} \text{ s}^{-1}$  compared to the relaxivities observed for all the variations of PNIPAM surface functionalised  $\text{Gd}^{3+}$ -DOTA MSNs (0.2 mol% =  $38.8 \pm 2.8 \text{ mM}^{-1} \text{ s}^{-1}$ , 1 mol% =  $43.1 \pm 1.9 \text{ mM}^{-1} \text{ s}^{-1}$  and 2.5 mol%  $33.4 \pm 1.9 \text{ mM}^{-1} \text{ s}^{-1}$ ). This shows that the relaxivity is predominantly sourced from the water interacting with the  $\text{Gd}^{3+}$ .

#### **4.4.2 MR Imaging Analysis at Clinical Field Strengths**

The limitation of the relaxivity analysis in the 13.1 MHz Xigo machine is that it is unable to analyse precipitated MSNs effectively due to averaging the relaxation obtained across a defined area. Therefore, to analyse the MSNs after aggregation, a 3 Tesla Clinical MRI Scanner was used to collect phantom images of behaviour both below and above the cloud points of the composites (*Figure 4.13*).

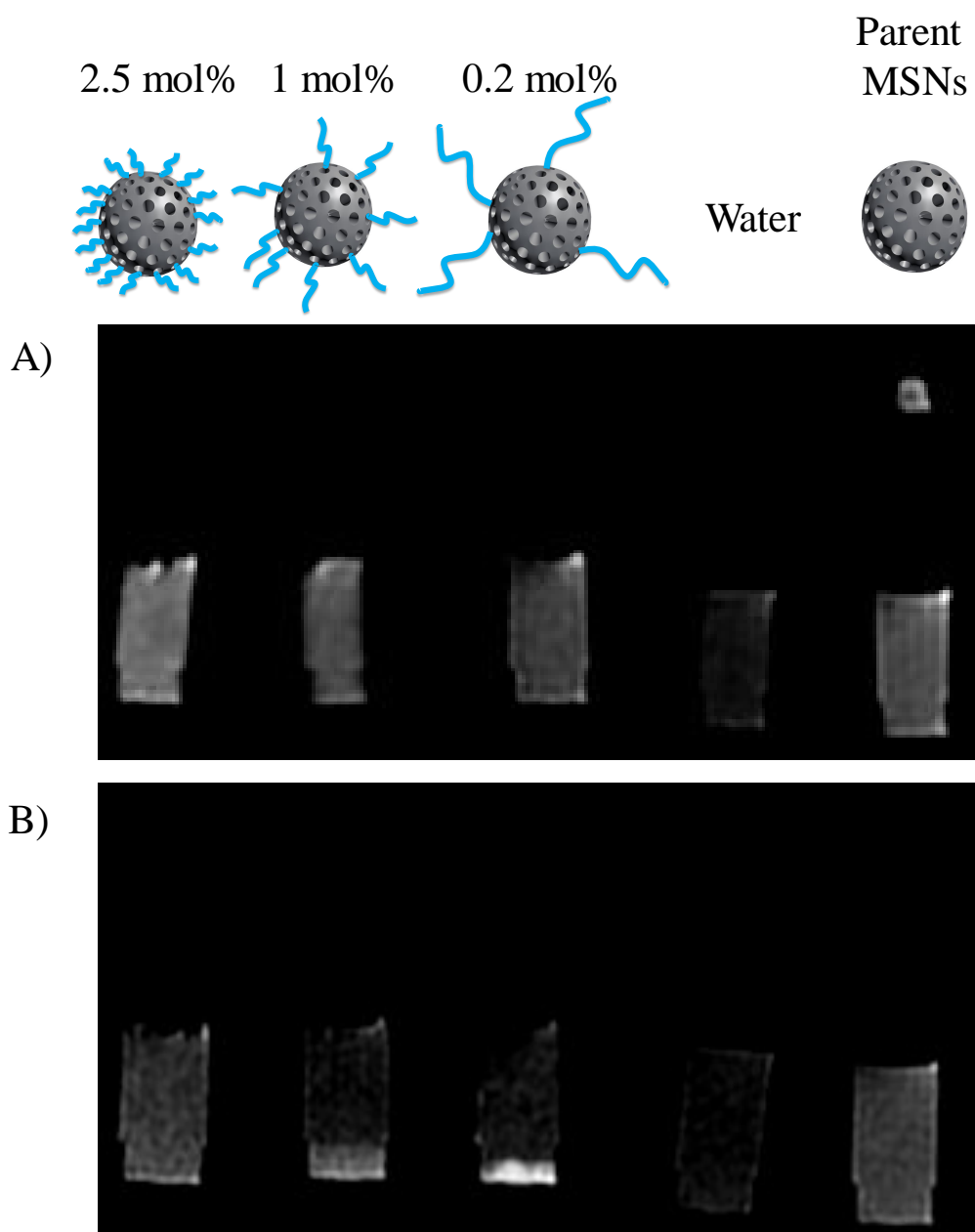


Figure 4.14. Phantom  $T_1$  weighted images obtained by a 3 Tesla MRI scanner of the pNIPAM surface density functionalised MSNs, 2.5 mol%, 1 mol% and 0.2 mol% amination with respect to TEOS compared to water and  $Gd^{3+}$ -DOTA MSNs at A) 35 °C and B) 40 °C.

The Parent MSNs and the water sample were analysed as a positive and negative control respectively. As can be observed at 35 °C all the samples, 0.2 mol%, 1 mol% and 2.5 mol% plus the Parent MSNs are all significantly brighter than the water proving that MSNs are an applicable construct for the application as a positive MRI contrast agent. At 40 °C the parent MSNs remain in suspension showing that there is

no inherent precipitation at increased temperature. The pNIPAM functionalised MSNs however are in various degrees of precipitation due to transitioning through their cloud points. This shows that the contrast ability of the MSNs does not disappear on precipitation, but rather that aggregation results in a 'concentration' of positive signal in the region of MSN aggregation. The sample with the lowest grafting density of polymer (0.2 mol%) and lowest overall cloud point of 36.4 °C (as previously described in Section 4.4.7) has precipitated to the bottom of the tube and resulted in a 'concentration' of the positive MRI signal in this area. The sample with the higher grafting density of 1 mol% shows some level of precipitation and aggregation of signal, as the nanocomposite has transitioned through its cloud point of 37.4 °C, but it still undergoing aggregation at the bottom of the tube. The highest grafting density on the other hand, 2.5 mol%, appears to remain in suspension and demonstrates no aggregation of particles and hence positive signal. This is due to the sample not yet having reached its transition temperature of 42.3 °C, and therefore remaining well dispersed in suspension.

## 4.5 Conclusions

In this chapter the aim was to develop a synthetic strategy to produce temperature responsive MSNs and observe their applicability to overcome traditional challenges in clinical diagnostic medicine by exploiting MRI. The synthetic protocol was achieved by the internal functionalisation of MSNs with  $\text{Gd}^{3+}$ -DOTA. Then post graft functionalising the surface of these  $\text{Gd}^{3+}$ -DOTA MSNs with amine groups provided by APTES. Finally, by binding BIBB initiator to the amine groups and performing an ATRP reaction with NIPAM monomer. The protocol steps involved were followed by Zeta potential and the retention of the MSN structure after the binding of pNIPAM proven by TEM. The successful pNIPAM surface functionalisation of the MSNs proved by IR, TGA and DLS. However, low levels of adsorption of pNIPAM was observed.

Three sets of MSNs with varying surface density of amine groups with respect to TEOS, 0.2 mol%, 1 mol% and 2.5 mol% were synthesised and was found to change the cloud point of the MSNs (0.2 % = 36.4 °C, 1 % = 37.4 °C and 2.5 mol% = 42.3 °C), with no observable cloud point found for the Adsorption Control. The relaxivity was analysed at 13.1 MHz to observe how the pNIPAM affected the  $\text{Gd}^{3+}$ -DOTA MSNs ability to be used as an MRI contrast agent. The relaxivities obtained (0.2 % =  $38.8 \pm 2.8 \text{ mM}^{-1} \text{ s}^{-1}$ , 1 mol% =  $43.1 \pm 1.9 \text{ mM}^{-1} \text{ s}^{-1}$  and 2.5 mol%  $33.4 \pm 1.9 \text{ mM}^{-1} \text{ s}^{-1}$ ) were all above the relaxivity obtained by plain  $\text{Gd}^{3+}$ -DOTA MSNs ( $31.39 \pm 4.17 \text{ mM}^{-1} \text{ s}^{-1}$ ) which proved that there was no negative effect of binding pNIPAM to the surface of  $\text{Gd}^{3+}$ -DOTA MSNs on their ability to be used as MRI contrast agents. Low concentrations of Cu contamination were observed, however, this contamination had only a small effect on the relaxivity observed ( $3.61 \pm 0.27 \text{ mM}^{-1} \text{ s}^{-1}$ ). Finally, the ability of all the samples (0.2 mol%, 1 mol% and 2.5 mol%) were investigated in a clinically used 3 Tesla MRI machine to observe their possible use as a thermoresponsive MRI contrast agent. This analysis obtained clear positive results that showed that the MSNs' aggregation with increased temperature could be observed by MRI.

## 4.6 Future Work

This work has the potential to be used for specific disease diagnosis, such as cancerous tumours which are well known to have slightly higher temps than healthy tissues due to the faster metabolism of cancer cells. For this application the precision and range of this temperature interaction tuneability should be investigated further by varying the surface density of pNIPAM on the MSNs and the pNIPAM polymer chain length. The Gd<sup>3+</sup>-DOTA functionalisation and the Cu contaminant removal system is another avenue of optimisation. There was significantly less Gd found in the samples ( $3.37 \pm 0.83$  ng of Gd per mg MSN) by ICP-MS than were found in the Gd<sup>3+</sup>-DOTA MSNs (~100 ng/mg). This is due to the acid method applied for the removal of Cu, protonating the DOTA chelate therefore causing dissociation of Gd<sup>3+</sup> from the DOTA chelate. Other methods were investigated before the acid method was used, such as Cuprisorb and ethylenediaminetetraacetic acid, EDTA, however none were more effective than brief stirring in acidified solution to remove the Cu from the MSNs. Another possible solution to the Gd<sup>3+</sup> loss would be to place the MSNs in the GdCl<sub>3</sub> solution after pNIPAM surface functionalisation and the subsequent acid conditions required to remove the Cu catalyst. This route however could result in an uncontrollable amount of Gd<sup>3+</sup> physisorption to the pNIPAM which would require investigation.

## 4.7 References

1. G.-L. Davies, I. Kramberger and J. J. Davis, *Chemical Communications*, 2013, **49**, 9704-9721.
2. T. Kanda, T. Fukusato, M. Matsuda, K. Toyoda, H. Oba, J. i. Kotoku, T. Haruyama, K. Kitajima and S. Furui, *Radiology*, 2015, **276**, 228-232.
3. W. A. Gibby, K. A. Gibby and W. A. Gibby, *Investigative radiology*, 2004, **39**, 138-142.
4. K. N. Christensen, C. U. Lee, M. M. Hanley, N. Leung, T. P. Moyer and M. R. Pittelkow, *Journal of the American Academy of Dermatology*, 2011, **64**, 91-96.
5. N. Maximova, M. Gregori, F. Zennaro, A. Sonzogni, R. Simeone and D. Zanon, *Radiology*, 2016, **281**, 418-426.
6. B. E. Lyons, R. H. Britt and J. W. Strohbehn, *IEEE transactions on biomedical engineering*, 1984, 53-62.
7. T. J. Vogl, R. Straub, K. Eichler, O. Söllner and M. G. Mack, *Radiology*, 2004, **230**, 450-458.
8. S. Morikawa, T. Inubushi, Y. Kurumi, S. Naka, K. Sato, T. Tani, I. Yamamoto and M. Fujimura, *Journal of Magnetic Resonance Imaging*, 2002, **16**, 576-583.
9. R. J. Bleicher, D. P. Allegra, D. T. Nora, T. F. Wood, L. J. Foshag and A. J. Bilchik, *Annals of Surgical Oncology*, 2003, **10**, 52-58.
10. K. U. Köhrmann, M. S. Michel, J. Gaa, E. Marlinghaus and P. Alken, *The Journal of urology*, 2002, **167**, 2397-2403.
11. E. J. Patterson, C. H. Scudamore, D. A. Owen, A. G. Nagy and A. K. Buczkowski, *Annals of surgery*, 1998, **227**, 559.
12. A. J. Aschoff, E. M. Merkle, V. Wong, Q. Zhang, M. M. Mendez, J. L. Duerk and J. S. Lewin, *Journal of Magnetic Resonance Imaging*, 2001, **13**, 57-63.
13. L. Solbiati, T. Livraghi, S. N. Goldberg, T. Ierace, F. Meloni, M. Dellanoce, L. Cova, E. F. Halpern and G. S. Gazelle, *Radiology*, 2001, **221**, 159-166.
14. J. Kettenbach, W. Köstler, E. Rücklinger, B. Gustorff, M. Hüpfel, F. Wolf, K. Peer, M. Weigner, J. Lammer and W. Muller, *American Journal of Roentgenology*, 2003, **180**, 1537-1545.



15. F. A. Jolesz, A. R. Bleier, P. Jakab, P. W. Ruenzel, K. Huttl and G. Jako, *Radiology*, 1988, **168**, 249-253.
16. S. Gould, N. Vaughan, W. Gedroyc, G. Lamb, R. Goldin and A. Darzi, *Lasers in Medical Science*, 1999, **14**, 250-256.
17. D. Germain, P. Chevallier, A. Laurent, M. Savart, M. Wassef and H. Saint-Jalmes, *Journal of Magnetic Resonance Imaging*, 2001, **13**, 42-49.
18. J. Palussiere, R. Salomir, B. Le Bail, R. Fawaz, B. Quesson, N. Grenier and C. T. Moonen, *Magnetic Resonance in Medicine: An Official Journal of the International Society for Magnetic Resonance in Medicine*, 2003, **49**, 89-98.
19. Q. Zhang, Y. C. Chung, J. S. Lewin and J. L. Duerk, *Journal of Magnetic Resonance Imaging*, 1998, **8**, 110-114.
20. T. Oshiro, U. Sinha, D. Lu and S. Sinha, *Journal of computer assisted tomography*, 2002, **26**, 308-316.
21. S. L. Fossheim, K. A. Il'yasov, J. Hennig and A. Bjørnerud, *Academic radiology*, 2000, **7**, 1107-1115.
22. N. McDannold, S. L. Fossheim, H. Rasmussen, H. Martin, N. Vykhodtseva and K. Hynnen, *Radiology*, 2004, **230**, 743-752.
23. L. Frich, A. Bjørnerud, S. Fossheim, T. Tillung and I. Gladhaug, *Magnetic resonance in medicine*, 2004, **52**, 1302-1309.
24. L. Lindner, H. Reinl, M. Schlemmer, R. Stahl and M. Peller, *International journal of hyperthermia*, 2005, **21**, 575-588.
25. R. Salomir, J. Palussière, S. L. Fossheim, A. Rogstad, U. N. Wiggen, N. Grenier and C. T. Moonen, *Journal of Magnetic Resonance Imaging*, 2005, **22**, 534-540.
26. M. Peller, A. Schwerdt, M. Hossann, H. M. Reinl, T. Wang, S. Sourbron, M. Ogris and L. H. Lindner, *Investigative radiology*, 2008, **43**, 877-892.
27. S. Langereis, J. Keupp, J. L. van Velthoven, I. H. de Roos, D. Burdinski, J. A. Pikkemaat and H. Grüll, *Journal of the American Chemical Society*, 2009, **131**, 1380-1381.
28. M. De Smet, S. Langereis, S. van den Bosch and H. Grüll, *Journal of Controlled Release*, 2010, **143**, 120-127.
29. H. Grüll and S. Langereis, *Journal of Controlled Release*, 2012, **161**, 317-327.

30. R. M. Staruch, M. Ganguly, I. F. Tannock, K. Hynynen and R. Chopra, *International Journal of Hyperthermia*, 2012, **28**, 776-787.
31. H. Zhu, J. Tao, W. Wang, Y. Zhou, P. Li, Z. Li, K. Yan, S. Wu, K. W. Yeung and Z. Xu, *Biomaterials*, 2013, **34**, 2296-2306.
32. Y. Yar, R. Khodadust, Y. Akkoc, M. Utkur, E. U. Saritas, D. Gozuacik and H. Y. Acar, *Journal of Materials Chemistry B*, 2018.
33. Y. Yang, X. Yan, Y. Cui, Q. He, D. Li, A. Wang, J. Fei and J. Li, *Journal of Materials Chemistry*, 2008, **18**, 5731-5737.
34. H. G. Schild, *Progress in polymer science*, 1992, **17**, 163-249.
35. M. Heskins and J. E. Guillet, *Journal of Macromolecular Science—Chemistry*, 1968, **2**, 1441-1455.
36. M. I. Gibson and R. K. O'Reilly, *Chemical society reviews*, 2013, **42**, 7204-7213.
37. M. Najafi, E. Hebel, W. E. Hennink and T. Vermonden, *Temperature-Responsive Polymers: Chemistry, Properties and Applications*, 2018, 1-34.
38. D. Schmaljohann, *Advanced drug delivery reviews*, 2006, **58**, 1655-1670.
39. T. R. Hoare and D. S. Kohane, *Polymer*, 2008, **49**, 1993-2007.
40. S. Mura, J. Nicolas and P. Couvreur, *Nature materials*, 2013, **12**, 991.
41. G. Chen and A. S. Hoffman, *Nature*, 1995, **373**, 49.
42. W. Hinrichs, N. Schuurmans-Nieuwenbroek, P. Van De Wetering and W. Hennink, *Journal of controlled release*, 1999, **60**, 249-259.
43. H. Uludag, B. Norrie, N. Kousinioris and T. Gao, *Biotechnology and bioengineering*, 2001, **73**, 510-521.
44. X.-Z. Zhang, R.-X. Zhuo, J.-Z. Cui and J.-T. Zhang, *International journal of pharmaceutics*, 2002, **235**, 43-50.
45. J. Kopeček, *European Journal of Pharmaceutical Sciences*, 2003, **20**, 1-16.
46. G.-H. Hsiue, R.-W. Chang, C.-H. Wang and S.-H. Lee, *Biomaterials*, 2003, **24**, 2423-2430.
47. G.-H. Hsiue, S.-h. Hsu, C.-C. Yang, S.-H. Lee and I.-K. Yang, *Biomaterials*, 2002, **23**, 457-462.
48. H. Vihola, A. Laukkanen, L. Valtola, H. Tenhu and J. Hirvonen, *Biomaterials*, 2005, **26**, 3055-3064.
49. D. Dubé, M. Francis, J.-C. Leroux and F. M. Winnik, *Bioconjugate chemistry*, 2002, **13**, 685-692.

50. Y. Matsumaru, A. Hyodo, T. Nose, S. Ito, T. Hirano and S. Ohashi, *Journal of Biomaterials Science, Polymer Edition*, 1996, **7**, 795-804.
51. H. Malonne, F. Eeckman, D. Fontaine, A. Otto, L. De Vos, A. Moës, J. Fontaine and K. Amighi, *European journal of pharmaceutics and biopharmaceutics*, 2005, **61**, 188-194.
52. A. J. Convertine, N. Ayres, C. W. Scales, A. B. Lowe and C. L. McCormick, *Biomacromolecules*, 2004, **5**, 1177-1180.
53. Y. Xia, X. Yin, N. A. Burke and H. D. Stöver, *Macromolecules*, 2005, **38**, 5937-5943.
54. J. O. Zoppe, Y. Habibi, O. J. Rojas, R. A. Venditti, L.-S. Johansson, K. Efimenko, M. Osterberg and J. Laine, *Biomacromolecules*, 2010, **11**, 2683-2691.
55. F. M. Winnik, H. Ringsdorf and J. Venzmer, *Macromolecules*, 1990, **23**, 2415-2416.
56. K. Matyjaszewski and J. Xia, *Chemical reviews*, 2001, **101**, 2921-2990.
57. R. M. Johnson, C. Ng, C. C. Samson and C. L. Fraser, *Macromolecules*, 2000, **33**, 8618-8628.
58. K. Matyjaszewski and N. V. Tsarevsky, *Nature chemistry*, 2009, **1**, 276.
59. J. M. G. Cowie and V. Arrighi, *Polymers: chemistry and physics of modern materials*, CRC press, 2007.
60. H. Kanazawa, K. Yamamoto, Y. Matsushima, N. Takai, A. Kikuchi, Y. Sakurai and T. Okano, *Analytical Chemistry*, 1996, **68**, 100-105.
61. Y.-Z. You, K. K. Kalebaila, S. L. Brock and D. Oupicky, *Chemistry of Materials*, 2008, **20**, 3354-3359.
62. H. Tu, C. E. Heitzman and P. V. Braun, *Langmuir*, 2004, **20**, 8313-8320.
63. S. Balamurugan, S. Mendez, S. S. Balamurugan, M. J. O'Brien and G. P. López, *Langmuir*, 2003, **19**, 2545-2549.
64. R. Tian, O. Seitz, M. Li, W. Hu, Y. J. Chabal and J. Gao, *Langmuir*, 2010, **26**, 4563-4566.
65. J. H. Moon, J. S. Seo, Y. Xu and S. Yang, *Journal of Materials Chemistry*, 2009, **19**, 4687-4691.
66. G.-L. Davies, J. O'Brien and Y. K. Gun'ko, *Scientific Reports*, 2017, **7**, 45862.
67. K. Nakamoto, *Handbook of Vibrational Spectroscopy*, 2006.

68. N. Maxim, A. Overweg, P. J. Kooyman, A. Nagy, R. A. van Santen and H. C. Abbenhuis, *Journal of Materials Chemistry*, 2002, **12**, 3792-3798.
69. G. Socrates, *Infrared and Raman characteristic group frequencies: tables and charts*, John Wiley & Sons, 2004.
70. J. Deng, Y. Shi, W. Jiang, Y. Peng, L. Lu and Y. Cai, *Macromolecules*, 2008, **41**, 3007-3014.
71. T. Wu, K. Efimenko and J. Genzer, *Journal of the American Chemical Society*, 2002, **124**, 9394-9395.
72. I. Luzinov, S. Minko and V. V. Tsukruk, *Soft Matter*, 2008, **4**, 714-725.
73. I. Solomon, *Physical Review*, 1955, **99**, 559.
74. I. Solomon and N. J. T. J. o. C. P. Bloembergen, 1956, **25**, 261-266.
75. N. Bloembergen and L. J. T. J. o. C. P. Morgan, 1961, **34**, 842-850.

# Chapter 5

## 5. Designing MSNs for Targeting of Colorectal Cancer

---

### 5.1 Chapter Summary

The ability to specifically highlight tumour tissue to allow for facile diagnosis is a highly desirable functionality. Imaging of tumour cells in a targeted manner can be facilitated by imaging active nanoparticles with a targeting moiety on their surfaces. A major challenge with the use of nanomaterials for targeting is non-specific binding, leading to the imaging species being adsorbed or taken up indiscriminately by cells within the body, which does not provide significant value clinically. Past research has discussed how the addition of a N-methyl-N-vinylacetamide (NVA) and methacrylic acid (MAA) copolymer can be utilised to minimise interactions between nanoparticles and cells by sterically blocking the nanoparticle binding with the cell whilst itself being inert. Furthermore, that the amide binding of *Arachis hypogaea* lectin (peanut agglutinin, PNA) with the MAA of the copolymer allowed for specific binding to colorectal cancer cells to be observed. Herein, we sought to investigate this; two different polymerisation approaches were employed to surface modify fluorescent MSNs at different surface grafting densities. Free radical, though successful in grafting polymer onto surfaces and in lowering non-specific binding events between the polymer-grafted nanocomposites, additionally led to a significant level of surface adsorbed monomer. Atom transfer radical polymerisation, ATRP, on the other hand, enables minimisation of surface physisorption, whilst also providing a route to controlling polymer chain length on nanoparticle surfaces. The NVA/MAA copolymer surface functionalised MSNs obtained using ATRP were found to have the same low non-specific binding with colorectal cancer cells, SW480, that was observed with the free radical polymerised NVA/MAA copolymer. Therefore, the ATRP NVA/MAA

fluorescent mesoporous silica nanoparticles, MSNs, were functionalised with PNA, PNA MSNs, in a bid to now introduce specific targeting capability. The PNA MSNs were incubated with colorectal cancer cells and found to have a high affinity to the colorectal cancer cells, SW480, suggesting that a more specific binding interaction was being observed. Finally, a toxicity test was performed to confirm the biocompatibility of the PNA MSNs, which proved the non-toxicity of the PNA MSNs up to 1.25 mg/mL.

## 5.2 Introduction

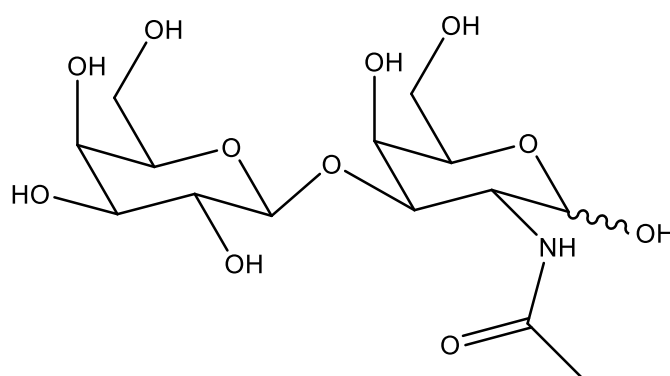
Colorectal cancer, CRC, is the third most commonly diagnosed cancer among both men and women in the United States.<sup>1</sup> In 2017 it is projected that 135,430 individuals will be diagnosed with CRC with 50,260 deaths from the disease in the U.S.A.<sup>2</sup> 39 % of patients diagnosed with CRC are in the localised stage, defined as when the cancer is limited to its origin with no sign of spread, where the 5 year survival rate is 90 %. However the 5 year survival rate drops to 71 % if diagnosed in the regional stage, defined as when the cancer has spread to nearby lymph nodes, tissues or organs, and 14 % in the distant stage of the disease, defined as when the cancer has spread to organs far from the origin.<sup>3</sup> the deterioration in survival rate highlights the essential need to diagnose and treat CRC at the initial localised stage.

If CRC is diagnosed at an early stage local treatments such as polypectomy,<sup>4</sup> local resection<sup>5</sup> and total mesorectal excision<sup>6</sup> are able to be performed. All these surgical operations involve removal of the cancerous tissue and some of the local tissue.<sup>7, 8</sup> For all these operations the elucidation of cancerous tissue is essential to minimise cancerous tissue left in the patient. Colonoscopy is the principal method of CRC tissue observation.<sup>9</sup> The major limitation of standard white-light colonoscopy is that tumour tissues are only able to be detected with a diameter ~1 cm. Tumours of this size are likely of metastasis.<sup>8, 9</sup> This limitation has been partially overcome by magnifying endoscopy.<sup>10, 11</sup> However, there is still a high demand for novel imaging strategies.<sup>10-14</sup>

Another method of improving the detection of CRC tissue is by the administration of an imaging agent.<sup>15</sup> Endoscopic imaging agents need to have four key properties. Firstly, the imaging agent needs to be non-toxic. Secondly, the agent needs to provide a distinctive signal using an imaging technique. For endoscopy this generally involves some form of fluorescence.<sup>15-20</sup> Thirdly the imaging agent requires a low affinity to healthy cells to minimise background noise. A method to minimise this non-specific binding to healthy tissue is by the functionalisation with an inert polymer, in particular polyethylene glycol, PEG.<sup>21</sup> PEG functionalisation, PEGylation, was introduced by A. Abuchowski *et al.* in 1977, who noted the superior immunogenic properties obtained by PEGylation as well as enhanced circulation lifetimes and reduced immunogenicity.<sup>22, 23</sup> PEGylation induces these properties by

providing a steric barrier against the attachment of plasma proteins such as opsonins and recognition by the cells of the mononuclear phagocyte system, resulting in a decreased rate of clearance from blood circulation.<sup>24</sup> These advantages in addition to PEG's low toxicity has led to a wide variety of small molecules and nanoparticles, including MSNs, being PEGylated, in a bid to confer these properties on the nanoparticles.<sup>25-32</sup> However it has been observed a repeat dose of pegylated liposomes after several days results in the loss of the long-circulating properties and accumulation extensively in the liver due to the accelerated blood clearance phenomenon.<sup>33-36</sup>

The final required property in the design of enhanced imaging agents for cancer detection is a high affinity to cancerous cells. This is usually acquired from a specific interaction being exploited between cancerous tissue and an external molecule which can be utilised to bind the imaging agent specifically to the CRC cells of interest. Numerous molecules have been investigated that have an observed affinity to CRC cells above healthy cells such as antibodies<sup>16, 17, 37, 38</sup> and lectins, for example helix pomatia agglutinin,<sup>39, 40</sup> soybean agglutinin,<sup>41</sup> wheat germ agglutinin,<sup>18, 42, 43</sup> galectin 3<sup>44-46</sup> and peanut (*Arachis hypogea*) agglutinin, PNA.<sup>19, 20, 47-50</sup> PNA binds to the Thomsen-Friedenreich, TF, antigen through the recognition of its terminal sugar,  $\beta$ -D-galactosyl-(1-3)-N-acetyl-D-galactosamine, Gal- $\beta$ (1-3)GalNac (*Figure 5.1*).<sup>51-58</sup>



*Figure 5.1 The chemical structure of the Gal- $\beta$ (1-3)GalNac terminal sugar on the TF antigen.*

The TF antigen is specifically expressed on the mucosal side of CRC cells in the early stages as well as breast and prostate carcinomas.<sup>51, 56, 59</sup> The role of the TF antigen is to facilitate a docking system for the cancerous cells onto endothelium by specifically interacting with the endothelium-expressed  $\beta$ -galactoside binding protein, galectin-



3.<sup>60, 61</sup> Also, the TF antigen- bearing glycoproteins are capable of mobilization of galectin-3 to the surface of endothelial cells, thus priming them for harbouring metastatic cancer cells.<sup>62</sup> TF antigen is masked by an oligosaccharide side chain extension or sialylation in healthy cells, making it an ideal selection for targetting.<sup>63</sup>

S. Sakuma *et al.* have performed a lot of research into endoscopy imaging agents.<sup>19, 47, 48, 64-69</sup> These imaging agents are based on polystyrene bound copolymers of N-vinylacetamide and methacrylic acid.<sup>70</sup> The polystyrene forming the hydrophobic core of the nanoparticles and the N-vinylacetamide and methacrylic acid copolymer forming the hydrophilic surface. Both the copolymer and polystyrene polymerisations were performed using free radical polymerisation with azobisisobutyronitrile, AIBN, as the initiator (*Figure 5.2*).

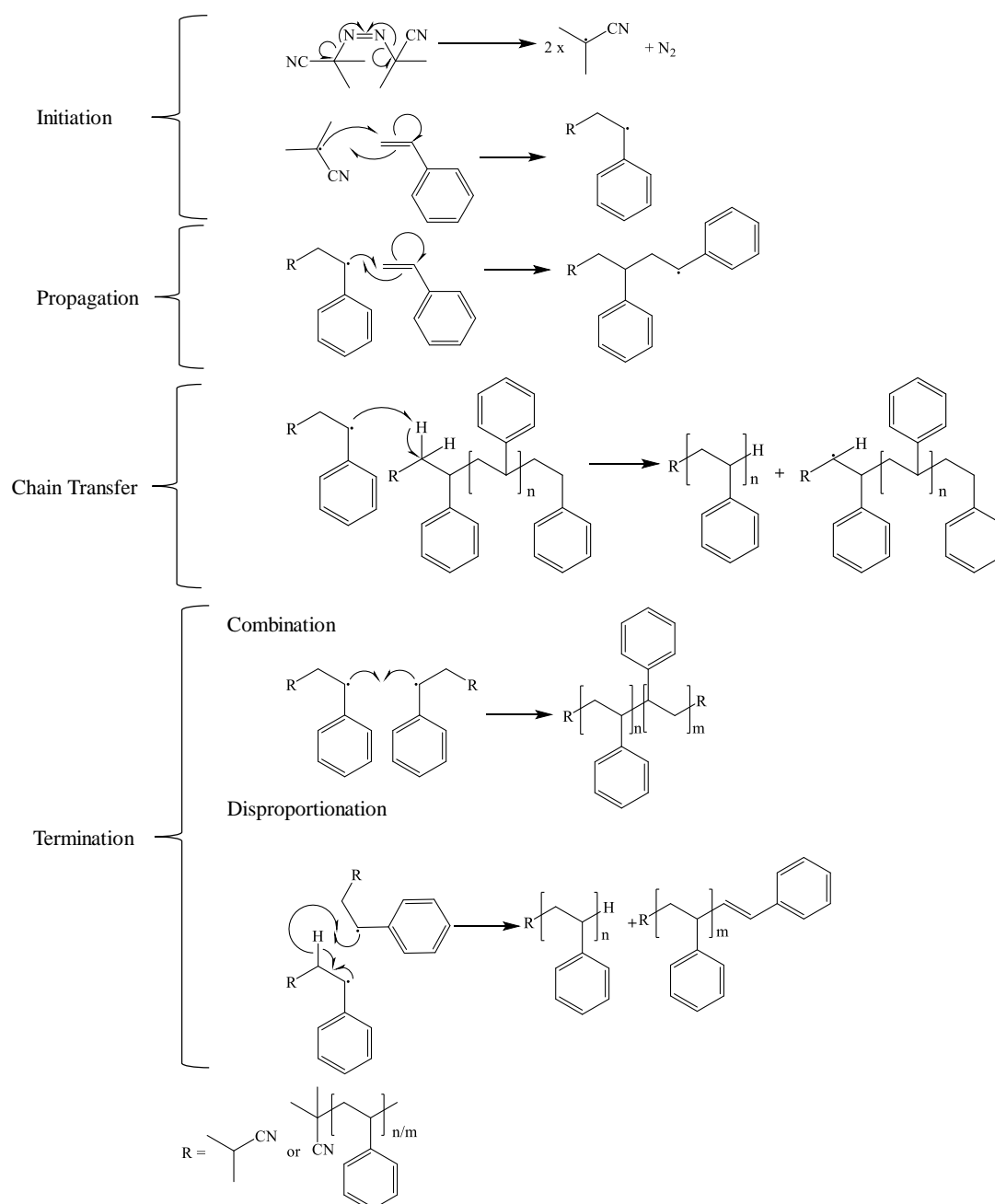
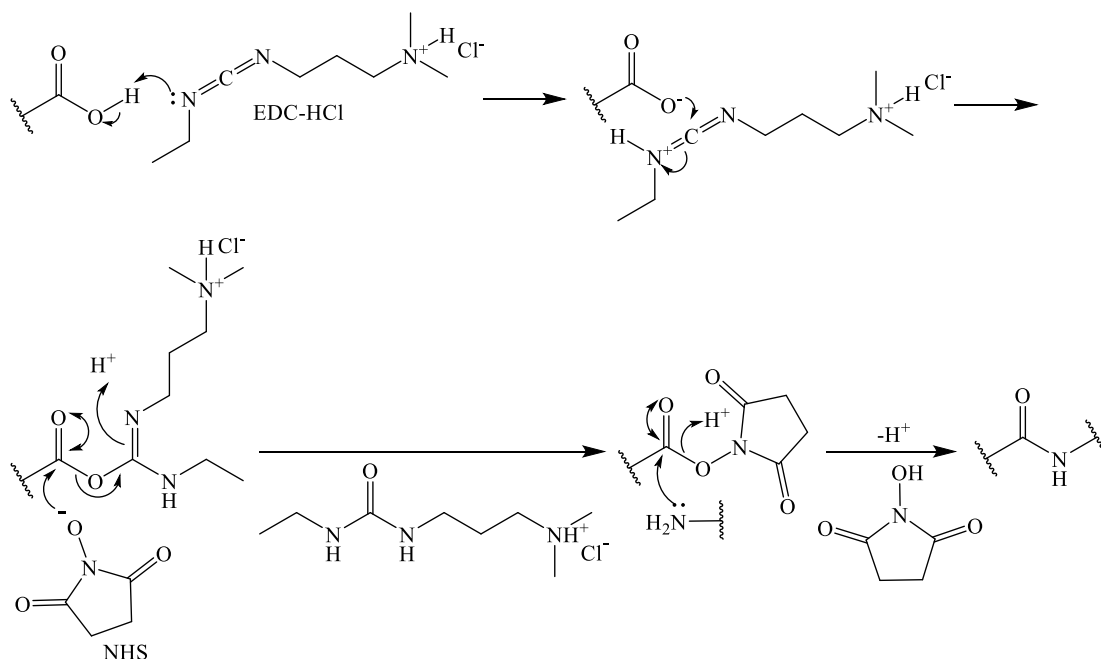


Figure 5.2. The reaction mechanism for free radical polymerisation of styrene using AIBN as initiator. Highlighting the three stages of free radical polymerisation, initiation, propagation and termination, where  $n$  and  $m$  represent the number of monomer repeat units.

S. Sakuma *et al.* performed many investigations on these polystyrene nanoparticles such as observing the non-specific binding between the nanoparticles and CRC cells<sup>64</sup> and their low toxicity both *in-vitro* and *in-vivo*.<sup>20, 69</sup> PNA was chemically bound to the MAA/ N-vinylacetamide copolymer and it was proven that specific binding was acquired with the nanoparticles and CRC cells both *in vitro* and *in vivo*.<sup>19, 47, 48, 65-68, 71</sup>

This was performed using the free amine groups in PNA and the carboxylic acid functional groups in MAA utilising the coupling agents N-(3-Dimethylaminopropyl)-N'-ethylcarbodiimide hydrochloride, EDC-HCl. This method can be optimised by the addition of N-hydroxysuccinimide, NHS, which is preferable as it increases the stability of the activated ester (*Figure 5.3*).<sup>72</sup>



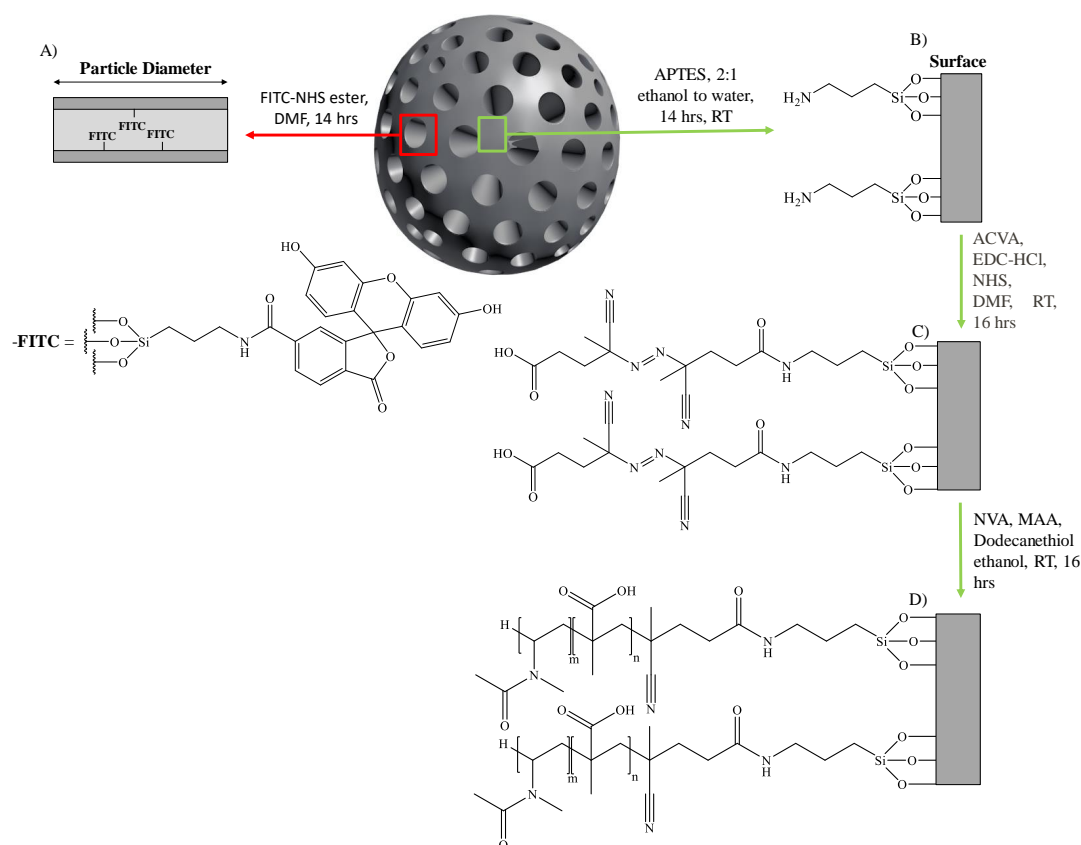
*Figure 5.3. The general reaction mechanism for amide bond formation using EDC-HCl and NHS coupling agents.*

### 5.2.1 Aims

The aim of this work was to synthesise fluorescent MSNs that specifically bind to colorectal cancer cells whilst avoiding non-specific binding that plagues traditional non-modified nanoparticles, such that they could be used in location resection or colectomy surgeries. It further aimed to develop a reliable and reproducible nanoparticle functionalisation route which is transferrable to several oxide-type nanoparticles, including MRI and imaging agents, towards highly specific targeting and evading non-specific uptake of new imaging tools

### 5.3 Free Radical Polymerisation Approach

Internally amine functionalised MSNs (0.15 mol% with respect to TEOS) were synthesised using the same protocol as Chapter 3, *Figure 3.5*. Internal functionalisation was chosen to exploit all surfaces available and prevent potential unwanted interactions with polymer reagents. Therefore, locating the fluorescein, FITC, in the pores of the MSNs would provide a physical barrier between the fluorescein and the polymer on the surface. The amine groups were then reacted with a N-hydroxysuccinimide, NHS, activated fluorescein ester to form fluorescent nanoparticles (*Figure 5.4*). External surface amination was carried out on the fluorescein functionalised MSNs at surface loadings of 0.2 mol% and 1 mol% with respect to tetraethyl silicate, TEOS. Surface density was varied to facilitate ease of varying polymer surface loading, allowing determination of the impact polymer grafting density has on controlling non-specific binding of nanoparticles to human cell lines. 4,4'-Azobis (4-cyanovaleric acid), ACVA, was used as it is a common initiator used for free radical polymerisation with two free carboxyl groups which would be available to form an amide bond with the surface amine groups on the MSNs.<sup>73</sup> ACVA, was covalently bound to the external amine groups using NHS and *N*-(3-Dimethylaminopropyl)-*N'*-ethylcarbodiimide hydrochloride, EDC-HCl, coupling to form an amide bond. Finally, a free radical polymerisation was performed using NVA and MAA as the monomers and ACVA as the initiator. Free radical polymerisation was used as this method is the most common polymerisation protocol utilised for MAA polymers (*Figure 5.4*).<sup>19, 20, 47, 48, 64-71, 74, 75</sup>



*Figure 5.4. A Schematic of the functionalisation method to obtain fluorescent MSNs with NVA/MAA copolymer surface functionalisation using free radical polymerisation. A) FITC functionalisation inside the pores of the MSNs, FITC MSNs, B) external surface amine functionalisation of FITC MSNs, C) 4,4'-Azobis (4-cyanovaleric acid), ACVA, initiator surface functionalisation and D) N-methyl-N-vinylacetamide (NVA) and methacrylic acid (MAA) copolymer surface functionalised fluorescent MSNs obtained using free radical polymerisation, where  $n$  and  $m$  represent the number of monomer repeat units.*

### 5.3.1 Dynamic Light Scattering and Zeta Potential Analysis of Nanocomposites

Dynamic light scattering, DLS, and zeta potential, *Table 5.1*, were used to monitor the stepwise surface modification as shown in *Figure 5.4*.

*Table 5.1 The Hydrodynamic diameter, polydispersity index, PDI, and zeta potential obtained after the key steps in the synthesis of NVA/MAA copolymer surface functionalised MSNs.*

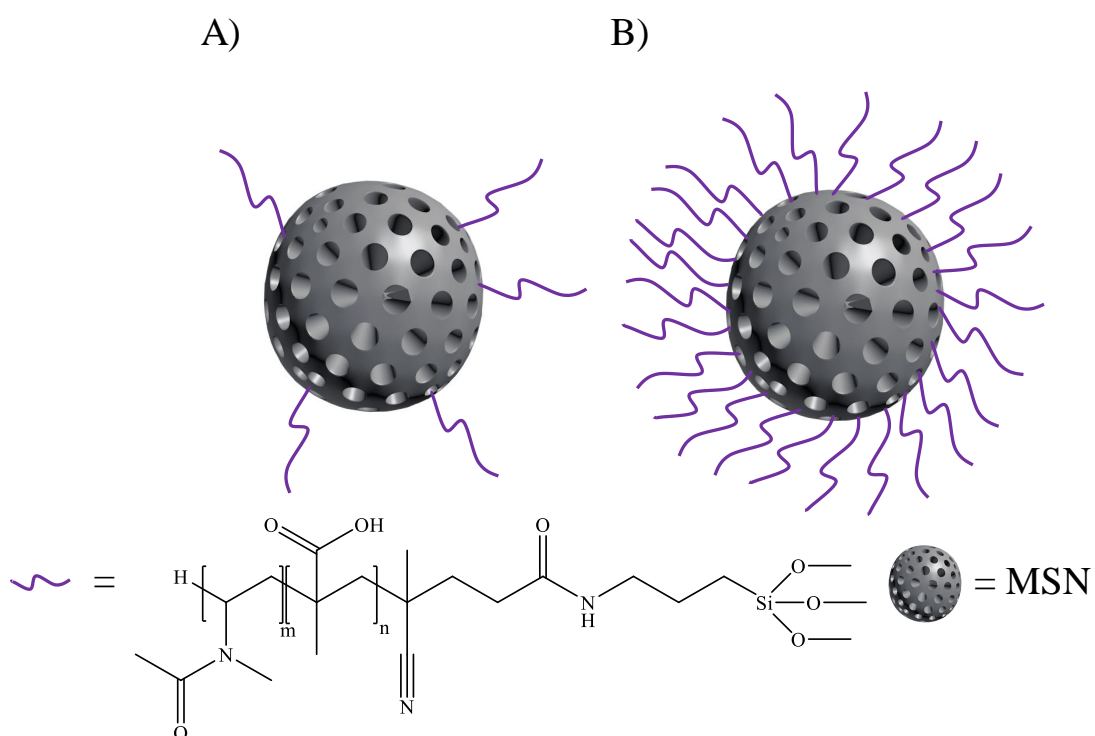
Synthetic step	Sample					
	0.2 mol%*			1 mol%*		
	Hydrodynamic diameter / nm	PDI	Zeta potential / mV	Hydrodynamic diameter / nm	PDI	Zeta potential / mV
<b>Parent MSNs</b>	266.9 ± 36.6	0.29 ± 0.02	-23.4 ± 0.6	304.7 ± 50.2	0.34 ± 0.02	-27.6 ± 2.3
<b>Fluorescein modified MSNs</b>	274.9 ± 19.8	0.23 ± 0.09	-18.4 ± 2.7	354.7 ± 27.3	0.28 ± 0.03	-29.6 ± 1.2
<b>Externally aminated MSNs</b>	1042.0 ± 144.6	0.45 ± 0.04	10.7 ± 0.8	612.3 ± 98.7	0.28 ± 0.10	20.8 ± 1.03
<b>Final composite after free radical NVA/MAA copolymer modification</b>	584.3 ± 125.2	0.36 ± 0.02	-11.0 ± 0.5	667.1 ± 132.8	0.31 ± 0.06	-18.2 ± 1.3

\*mole percent (mol%) with respect to tetraethyl orthosilicate, TEOS for external amine modification.

MSNs prepared with internal amination at 0.15 mol%, used to prepare original parent MSNs, had sizes within error of one another (0.2 mol% 266.9 ± 36.6 nm and 1 mol% = 304.7 ± 50.2 nm). The zeta potentials for the MSN batches are both in the expected range for MSNs prepared with 0.15 mol% internal amination (-23.4 ± 0.6 mV and -27.6 ± 2.3 mV respectively).<sup>76</sup> These are negative due to the abundant surface silanol groups of the MSNs. The hydrodynamic diameters obtained for each fluorescein functionalisation (0.2 mol% = 274.9 ± 19.8 nm and 1 mol% = 354.7 ± 27.3 nm) were

within error of the hydrodynamic diameters obtained after the respective MSN synthesis ( $0.2 \text{ mol\%} = 266.9 \pm 36.6 \text{ nm}$  and  $1 \text{ mol\%} = 304.7 \pm 50.2 \text{ nm}$ ). The fluorescein functionalisation also does not have a large effect on the zeta potential ( $0.2 \text{ mol\%} = -18.4 \pm 2.7 \text{ mV}$  and  $1 \text{ mol\%} = -29.6 \pm 1.2 \text{ mV}$ ). Due to the low concentration ( $0.15 \text{ mol\%}$ ) of fluorescein being bound to the MSNs this fluorescein functionalisation was expected to have little effect on hydrodynamic diameter and zeta potential. The external amination caused a significant change in the hydrodynamic diameter of the MSNs ( $0.2 \text{ mol\%} = 1042.0 \pm 144.6 \text{ nm}$  and  $1 \text{ mol\%} = 612.3 \pm 98.7 \text{ nm}$ ). This is because the surface charge has been affected by the predominantly negatively charged surface of the MSNs, due to Si-OH groups, becoming more positive due to the amine groups provided by (3-aminopropyl) triethoxysilane, APTES. This results in strong electrostatic interactions between the different surface charges on neighbouring particles, causing increased interactions between numerous particles, which are then observed by the machine as a larger particle. The explanation for the dramatic increase in hydrodynamic diameter obtained by  $0.2 \text{ mol\%}$  compared to  $1 \text{ mol\%}$  is that the  $1 \text{ mol\%}$  surface amine functionalised MSNs will be more uniformly positively charged compared to  $0.2 \text{ mol\%}$ . This greater variation in surface charge (between neighbouring positive and negative surfaces) for  $0.2 \text{ mol\%}$  creates greater electrostatic interactions between MSNs causing more aggregation and therefore resulting in a larger observed hydrodynamic diameter. This also correlates with the increased PDI values ( $0.2 \text{ mol\%} = 0.45 \pm 0.04$ ,  $1 \text{ mol\%} = 0.28 \pm 0.10$ ) and zeta potentials observed ( $0.2 \text{ mol\%} = 10.7 \pm 0.8 \text{ mV}$  and  $1 \text{ mol\%} = 20.8 \pm 1.03 \text{ mV}$ ), with a higher positive zeta potential for the more heavily loaded MSNs. Upon polymerisation the hydrodynamic diameters ( $0.2 \text{ mol\%} = 584.3 \pm 125.2 \text{ nm}$  and  $1 \text{ mol\%} = 667.1 \pm 132.8 \text{ nm}$ ) are larger than the parent MSNs, due to the polymer chains present on the surfaces increasing the hydrodynamic sizes of the particles because of increased van der Waals interactions and interchain interactions. The large sterically-induced size obtained by  $0.2 \text{ mol\%}$  external amination is no longer observed as the external surface amino groups have been used during subsequent surface modification, and polymer stabilisation aids in preventing such steric interaction. This is clearly demonstrated by the PDI of the NVA/MAA surface functionalised MSNs ( $0.2 \text{ mol\%} = 0.36 \pm 0.02$ ,  $1 \text{ mol\%} = 0.31 \pm 0.06$ ) returning to similar values to those of the parent MSNs ( $0.2 \text{ mol\%} = 0.29 \pm 0.02$ ,  $1 \text{ mol\%} = 0.34 \pm 0.02$ ). The NVA/MAA external functionalisation of the MSNs returned the zeta potential to negative ( $0.2 \text{ mol\%} = -$

$11.0 \pm 0.5$  mV and  $1\% = -18.2 \pm 1.3$  mV) due to the methacrylic acid in the copolymer. The change in zeta potential from surface amination to the NVA/MAA copolymer functionalisation of 0.2 mol% and 1 mol% varies considerably ( $\Delta 0.2$  mol% = - 21.7 mV,  $\Delta 1$  mol% = - 39 mV). This large change in zeta potential for 1 mol% compared to 0.2 mol% coupled with the similar hydrodynamic diameter obtained suggests that increasing the surface density has increased the number of polymer chains without affecting the polymer chain length (*Figure 5.5*).

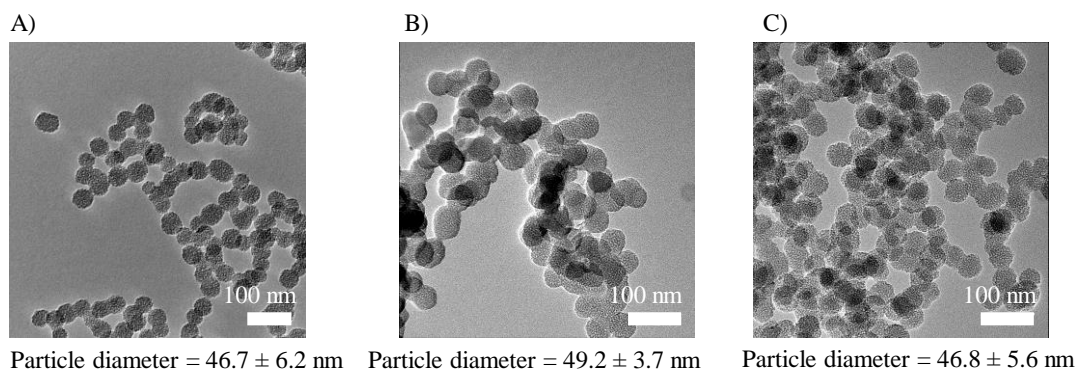


*Figure 5.5. The proposed schematic for the variation in zeta potential whilst still having equivalent hydrodynamic diameters obtained by DLS. A) 0.2 mol% surface functionalised NVA/MAA copolymer, B) 1 mol% surface functionalised NVA/MAA copolymer. Where  $n$  and  $m$  represent the number of monomer repeat units for MAA and NVA respectively.*

### 5.3.2 Transmission Electron Microscopy Analysis of Nanocomposites

Transmission electron microscopy, TEM, was utilised to observe the structural integrity and porosity of the MSNs after the NVA/MAA copolymer surface functionalisation using free radical polymerisation (*Figure 5.6*).





*Figure 5.6. The TEM images obtained for A) CTAB Internal MSNs (Chapter 3, Section 3.3.1), B) 0.2 mol% and C) 1 mol% NVA/MAA copolymer surface functionalised MSNs. The diameters of the MSNs were calculated by the mean and standard deviation of 100 MSN diameters.*

As can be observed in the images the porosity remains intact and the mean diameter (0.2 mol% =  $49.2 \pm 3.7$  nm and 1 mol% =  $46.8 \pm 5.6$  nm) is within error of the parent MSNs ( $46.7 \pm 6.2$  nm). The NVA/MAA copolymer can't be observed because no negative staining was performed due to the analysis of the MSN structure and size being the principal objective of this procedure.

### 5.3.3 Gel Permeation Chromatography Analysis of 0.2 mol% and 1 mol% NVA/ MAA Copolymer

In order to provide an estimate of the polymer chain length which has been grafted onto the MSNs surfaces, and as this technique cannot be carried out on polymer-nanoparticle composites, NVA/MAA copolymer was synthesised using the theoretical ACVA initiator concentrations for 0.2 mol% and 1 mol% surface grafting density. Here two separate free radical polymerisation reactions were performed in the absence of MSNs, with the equivalent concentration of ACVA initiator added to the polymerisation mixture assuming 100 % conversion of surface amine groups to amide bound ACVA for each surface density investigated. These copolymers were analysed by gel permeation chromatography, GPC (Table 5.2).  $M_n$  calculated by Equation 4.2 where  $N_i$  is the number of moles of each polymer species and  $M_i$  is the molar mass of that species.

$$M_n = \frac{\sum N_i M_i}{\sum N_i} \text{ (Equation 4.2)}$$

Table 5.2. The number average molecular weight,  $M_n$ , obtained by GPC with the polydispersity of the calculated 0.2 % and 1 % concentrations of ACVA.

Sample	$M_n$ / g mol <sup>-1</sup>	PDI
0.2 mol% NVA/MAA	6100	1.28
1 mol% NVA/MAA	7000	1.20

The  $M_n$  values obtained for the polymer obtained with 0.2 mol% and 1 mol% were similar with 0.2 mol% = 6100 g mol<sup>-1</sup> and 1 % = 7000 g mol<sup>-1</sup>. The PDIs are also very similar with 0.2 mol% = 1.28 and 1 mol% = 1.20. These results in addition to the similar plots obtained for  $dwd\log M$  against  $\log M$  strongly suggest that the copolymers obtained by the 0.2 mol% and 1 mol% surface densities using free radical polymerisation were very similar (Figure 5.7).

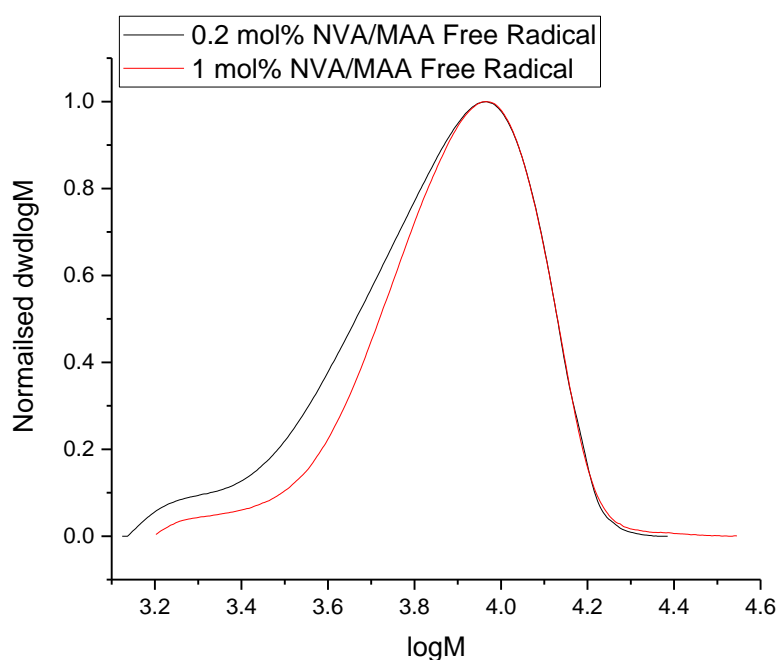


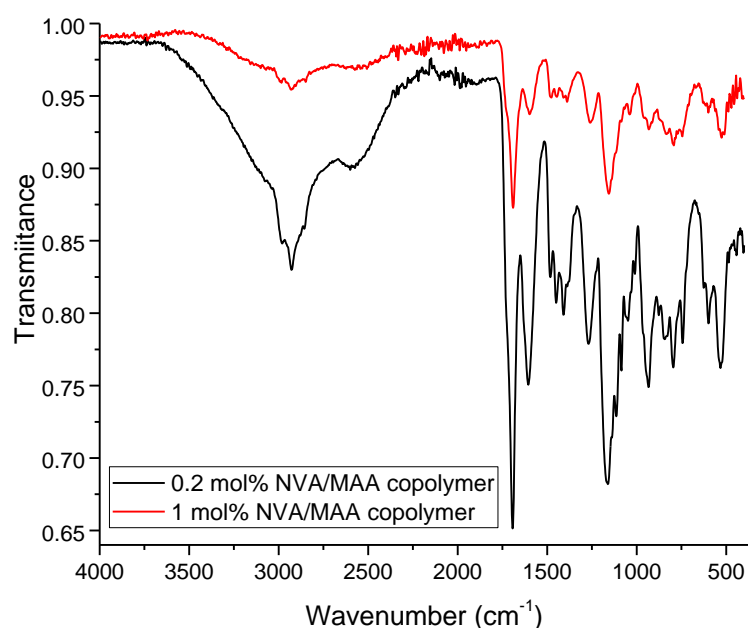
Figure 5.7. The plot of  $\log M$  against normalised  $dwd\log M$  for the free radical polymerisation reactions involving the theoretical ACVA concentrations calculated for the 0.2 mol% and 1 mol% surface functionalised MSNs.

The asymmetry of 0.2 mol% NVA/MAA and 1 mol% NVA/MAA is due to the amount of uncontrolled termination occurring using free radical polymerisation. The small

variation between 0.2 ml% NVA/MAA and 1 mol% NVA/MAA is due to the larger number of uncontrolled termination reactions occurring, shown by the increased PDI (0.2 mol% NVA/MAA = 1.28, 1 mol% NVA/MAA = 1.20). This supports the theory represented in *Figure 5.5* that the only significant difference between the copolymer bound MSNs obtained using the 0.2 mol% and 1 mol% free radical protocols is the surface density, not also the chain length, which was the behaviour previously observed when atom transfer radical polymerisation, ATRP, was employed in Chapter 4.

### 5.3.4 Infrared Spectroscopy

To confirm that there was no chemical difference between the NVA/MAA copolymers obtained by using the 0.2 mol% and 1 mol% ACVA concentrations, IR spectroscopy was performed on the samples (*Figure 5.8*).

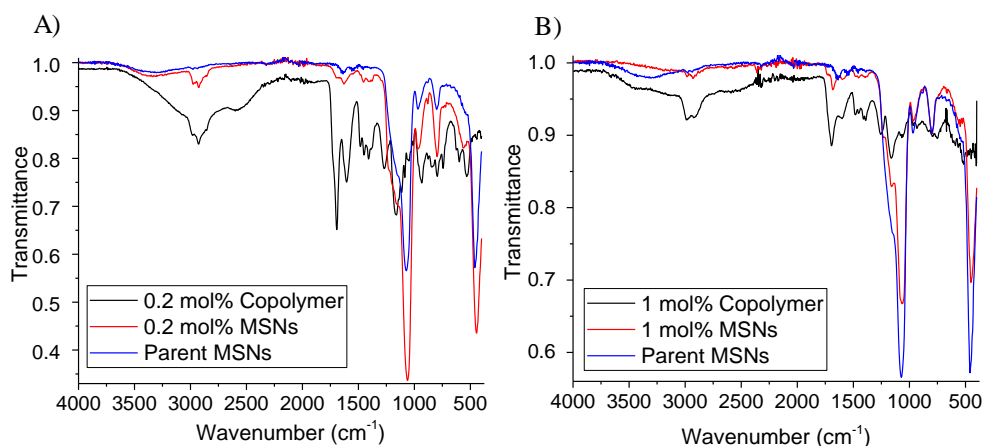


*Figure 5.8. The IR Spectra of the NVA/MAA copolymers obtained using 0.2 mol% and 1 mol% concentrations of ACVA initiator.*

The IR spectra obtained for the free radical polymerisation of NVA and MAA using 0.2 mol% and 1 mol% ACVA relative to TEOS gave the same principal transmittance peaks. The appearance of both the carboxyl stretches ( $1165\text{ cm}^{-1}$  = C-O stretch,  $1676\text{ cm}^{-1}$  = C=O stretch,  $2578\text{ cm}^{-1}$  = O-H stretch) and the amide stretches ( $1583\text{ cm}^{-1}$  =

C=O stretch) shows that both NVA and MAA are present making the polymer a copolymer of these monomers.<sup>77</sup>

After this the IR spectra of the respective copolymers were compared with the 0.2 mol% and 1 mol% surface functionalised MSNs (*Figure 5.9*).



*Figure 5.9. The comparison between the IR spectra obtained for A) 0.2 mol% and B) 1 mol% NVA/MAA copolymer surface functionalised MSN to their respective copolymers and parent MSNs.*

As can be seen in both NVA/MAA surface functionalised MSNs the stretches observed are between 1015-1190  $\text{cm}^{-1}$  representing Si-O-Si stretching and bending vibrations,<sup>78-80</sup> stretches around 800  $\text{cm}^{-1}$ , indicative of Si-O-Si stretches,<sup>81</sup> and those centred at  $\sim 550$  and  $\sim 450$   $\text{cm}^{-1}$  representing tri and tetracyclosiloxane rings of siloxanes.<sup>82</sup> However, there are minor peaks at 1672  $\text{cm}^{-1}$  and 2920  $\text{cm}^{-1}$  which are found in the copolymer (representing C=O (carboxyl) stretch and C-H stretch respectively) in the MSN spectra. The presence of these suggest that NVA/MAA copolymer surface functionalisation has occurred.

### 5.3.5 Thermogravimetric Analysis

To observe the temperature that the copolymer is thermally removed, thermogravimetric analysis, TGA, was performed on the 0.2 mol% and 1 mol% copolymers obtained in the absence of MSNs using the theoretical amount of ACVA bound to the MSNs. These were compared with the parent MSNs to confirm the variation between their degradations (*Figure 5.10*).

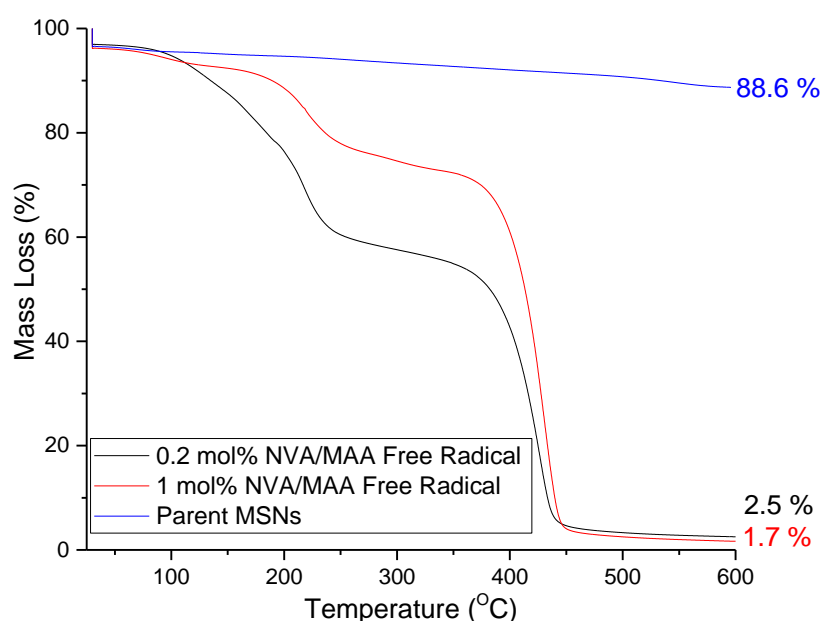
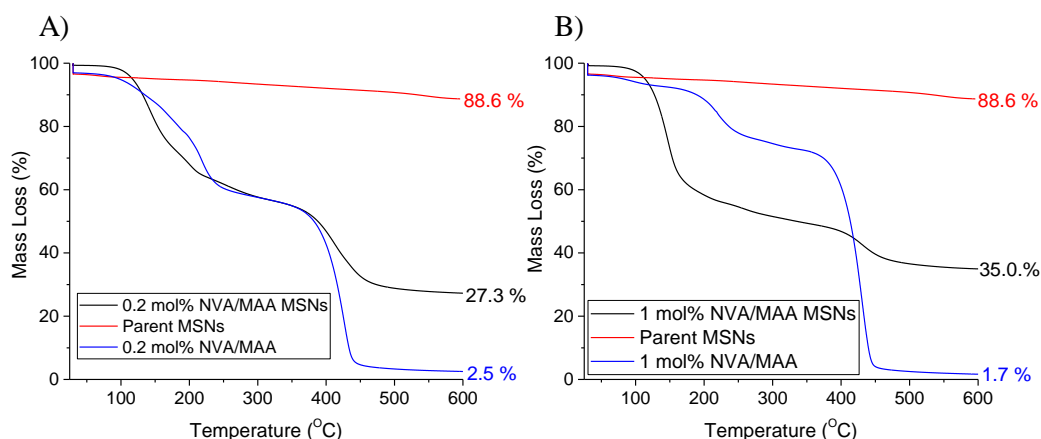


Figure 5.10. The percentage mass loss against temperature for the NVA/MAA copolymers obtained using 0.2 mol% and 1 mol% theoretical concentrations of ACVA compared to the Parent MSNs between 30 °C and 600 °C.

The small mass loss of 11.4 wt% of original mass for the parent MSNs shows the stability of the fluorescein functionalised MSNs between 30 °C and 600 °C, this loss representing the loss of adsorbed solvent and surface silanol groups. In the NVA/MAA copolymers using 0.2 mol% and 1 mol% ACVA, there is significant mass loss between 310 °C and 460 °C which represents the degradation of the copolymer (mass loss for 0.2 mol% = 53.0 wt% and 1 mol% = 70.6 wt%). Another increase in mass loss appears at 160 °C to 260 °C in both 0.2 mol% (26.0 wt%) and 1 mol% (15.1 wt%). This represents impurities in the sample, most likely MAA (boiling point = 161 °C) as all the other starting reagents have boiling points not comparable to the degradation temperatures observed (ACVA melting point = 118 – 125 °C, NVA boiling point = 70 °C and ethyl acetate = 77.1 °C, water = 100 °C). There is also significant mass loss in the 0.2 mol% NVA/MAA copolymer between 70 – 190 °C of 17.8 wt% which is most likely a mixture of NVA, ethyl acetate and water impurities evaporating off the sample. Both the NVA/MAA copolymers have almost completely degraded at 600 °C, due to the organic nature of the polymers.

With the temperature identified as between 310 °C and 460 °C for the NVA/MAA copolymer degradation obtained using free radical polymerisation, both the 0.2 mol% and 1 mol% NVA/MAA surface functionalised MSNs were analysed (*Figure 5.11*).



*Figure 5.11. The percentage mass loss versus temperature of A) 0.2 mol% NVA/MAA MSNs and B) 1 mol% NVA/MAA MSNs compared to their respective copolymers synthesised in the absence of MSNs and the Parent MSNs.*

There are significant mass losses in both samples between 70 °C and 250 °C which represents the starting reagents and water (0.2 mol% = 37.4 wt% and 1 mol% = 44.4 wt%). As it was found that the mass loss that represents NVA/MAA copolymer appeared between 310 °C and 460 °C the mass loss between these two temperatures relative to the starting mass was used as the percentage by mass of NVA/MAA copolymer in the sample. It was calculated that for 0.2 mol% NVA/MAA surface functionalised MSN the percentage by mass of copolymer was 25.9 wt% whereas for 1 mol% it was 12.5 wt%. The percentage by mass of copolymer was contrary to the proposed scheme where both 0.2 mol% and 1 mol% had same NVA/MAA copolymer chain lengths, but 1 % had more of NVA/MAA chains attached than 0.2 mol% (*Figure 5.5*). However, both 25.9 wt% and 12.5 wt% calculated for the percentage by mass lost between 310 °C and 460 °C were significantly higher than the mass lost between these two temperatures for the parent MSNs (1.9 wt%). This proves that copolymer is present on the surface of the MSNs for 0.2 mol% and 1 mol% NVA/MAA MSN samples. As such, these 2 nanocomposites were still appropriate for assessing for efficacy of NVA/MAA copolymer MSN surface functionalisation on cellular uptake and binding.

## **5.4 Investigation into the Non-Specific Binding of the Surface Functionalised NVA/MAA copolymer MSNs using Free Radical Polymerisation with the Colorectal Cancer Cells**

### **5.4.1 Colorectal Cancer Cell Binding Assay**

To assess binding between nanoparticles and cells, we chose to work with SW480 human caucasian colorectal adenocarcinoma cells line. Initially, non-polymer grafted fluorescent MSNs were incubated at a range of different concentrations (ranging 1.22  $\mu\text{g/mL}$ – 1250  $\mu\text{g/mL}$ ) with the cells for 24 hrs in standard cell conditions (See Chapter 2 Experimental for details, Section 2.2.3.7). After this time, cells were thoroughly washed, and their fluorescence signal was analysed. Remaining fluorescence was indicative of nanoparticles which had a strong binding interaction with the cells. This was confirmed through carrying out control experiments in the absence of nanoparticles and cells respectively. This procedure was then repeated with the 0.2 mol% and 1 mol% NVA/MAA MSNs (*Figure 5.12*).

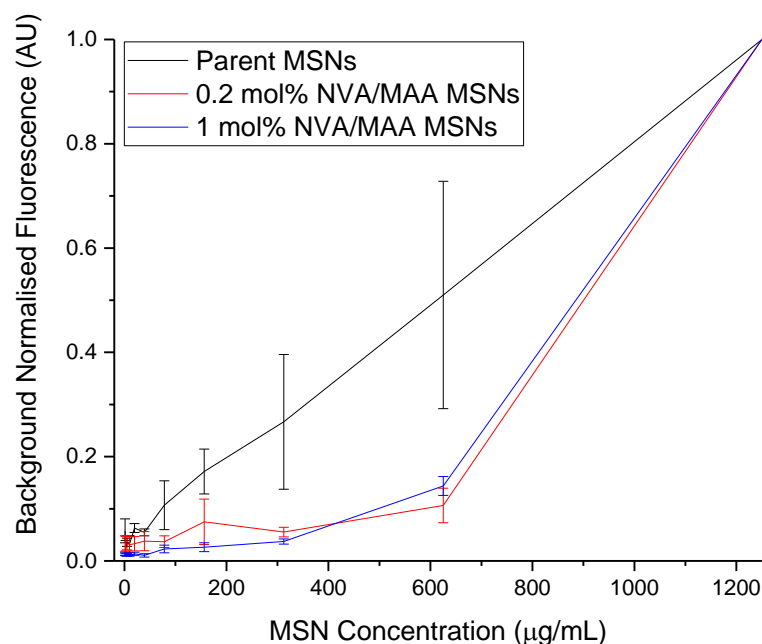


Figure 5.12. The background normalised fluorescence obtained at 528 nm after excitation at 485 nm from serial dilutions from 1250  $\mu\text{g/mL}$  to 1.22  $\mu\text{g/mL}$  after incubation with SW480 cells for 24 hrs and subsequent washes. The results shown are of the Parent Fluorescent MSNs, 0.2 mol% NVA/MAA MSNs and 1 mol% NVA/MAA MSNs.

The parent MSNs exhibit strong fluorescent emission, which increases linearly with increasing incubation concentrations, as would be expected due to strong interactions with the cells. Both 0.2 mol% and 1 mol% NVA/MAA MSNs demonstrate a similar trend to each other. Once again, increasing the number of nanoparticles applied to cells during incubation increases the fluorescent emission observed. The large fluorescence observed for 1250  $\mu\text{g/mL}$  compared to 625  $\mu\text{g/mL}$  is due to *in situ* precipitation occurring in the large dosage of 1250  $\mu\text{g/mL}$  and so uptake would be higher regardless of the particle type. However, a significant decrease in interactions between the polymer grafted MSNs occurred between 1250  $\mu\text{g/mL}$  and 625  $\mu\text{g/mL}$  (0.2% NVA/MAA  $\Delta\%$  fluorescence = 89.4 %, 1 % NVA/MAA MSNs = 85.6 %). This indicates that the polymer modified nanoparticles have a weaker binding interaction with the cells. Therefore, the presence of the polymer reduces the effect of non-specific binding. The percentage fluorescence for 0.2 % NVA/MAA MSNs and



1 % NVA/MAA MSNs were within error of each other at all incubation concentrations suggesting binding was independent of polymer grafting density.

However, there was speculation over whether the NVA/MAA copolymer was the primary factor in causing the lowering in non-specific binding due to the TGA showing a high concentration of impurities in the samples. Therefore, atom transfer polymerisation, ATRP, was utilised due to the successful application of ATRP in Chapter 4 with low monomer impurities observed in the TGA analysis. Also, because the control of chain length by variation in the BIBB initiator concentration would allow for future investigation into how polymer chain lengths affect colorectal cancer cell binding.

## **5.5 Preparation and Characterisation of Fluorescent MSNs with Surface Functionalised NVA/MAA Copolymer Synthesised using Atom Transfer Radical Polymerisation and PNA Binding**

Internally aminated MSNs were functionalised as previously stated with fluorescein NHS ester. The fluorescein MSNs were externally aminated using the same protocol as before. Only 0.2 % surface amine functionalisation was performed as this method provided equivalent binding to the 1 %, but with less contaminants (0.2 mol% = 37.4 wt% and 1 mol% = 44.4 wt%). Then  $\alpha$ -Bromoisobutryl bromide, BIBB, initiator was covalently bound to the amine groups *via* an amide bond. ATRP reaction was performed using the surface bound BIBB and a Cu ion catalyst ligated by *N,N,N',N'',N'''*-Pentamethyldiethylenetriamine, PMDETA, in the same conditions as used in Chapter 4 except with NVA and MAA monomers instead of NIPAM. Finally, the PNA was bound to the carboxyl group using EDC-HCL and NHS coupling using the same conditions used to bind the ACVA initiator to the amine groups for the free radical NVA/MAA copolymer surface functionalised MSNs (*Figure 5.13*).

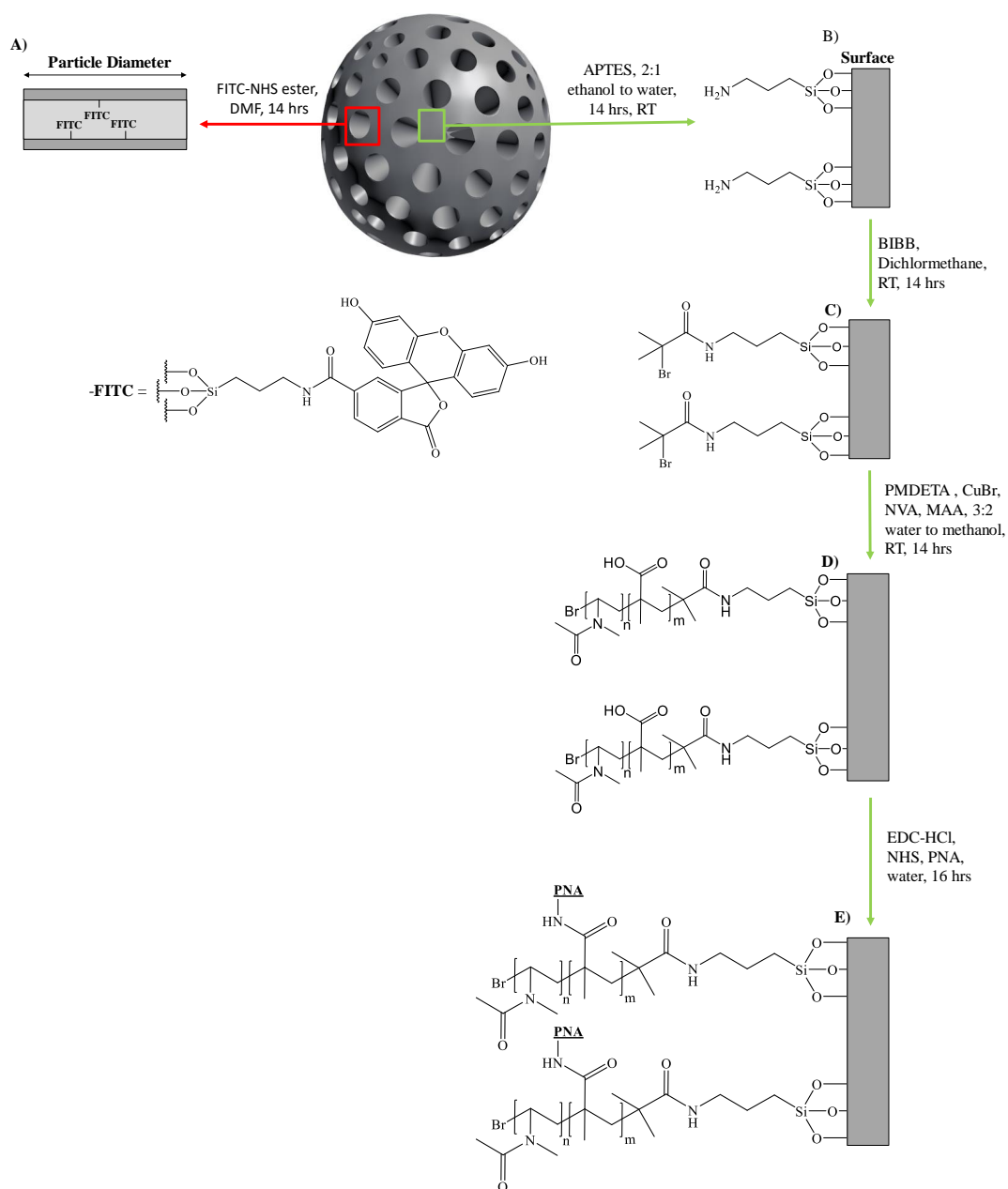


Figure 5.13. A schematic of the synthetic steps performed to obtain fluorescent MSNs with NVA/MAA copolymer surface functionalisation using ATRP. A) Internal fluorescein functionalisation of MSNs, FITC MSNs, B) external amine functionalisation of FITC MSNs, C) Surface BIBB binding via an amide bond, D) NVA/MAA copolymer surface functionalised fluorescent MSNs obtained using ATRP, E) Binding PNA to the carboxyl group of the MAA using EDC-HCl and NHS coupling.

### 5.5.1 Dynamic Light Scattering and Zeta Potential

The synthetic steps were monitored using hydrodynamic diameter and zeta potential to confirm successful functionalisation (Table 5.3).

*Table 5.3. The hydrodynamic diameters and PDIs obtained by DLS with the zeta potentials of MSNs prepare at each of the key steps required to synthesise NVA/MAA copolymer surface functionalised MSNs using ATRP with PNA amide bound to the methacrylic acid carboxyl functional group.*

<b>Synthetic step</b>	<b>Hydrodynamic diameter / nm</b>	<b>PDI</b>	<b>Zeta potential / mV</b>
<b>1. Parent MSNs</b>	$311.7 \pm 37.8$	$0.21 \pm 0.03$	$-28.5 \pm 0.6$
<b>2. Fluorescein modified MSNs</b>	$265.4 \pm 29.4$	$0.31 \pm 0.04$	$-23.8 \pm 4.5$
<b>3. Externally aminated MSNs</b>	$1461.0 \pm 348.1$	$0.36 \pm 0.14$	$5.6 \pm 2.1$
<b>4. ATRP NVA/MAA copolymer modification</b>	$1025.0 \pm 62.3$	$0.58 \pm 0.09$	$-22.5 \pm 0.6$
<b>5. Final composite after PNA functionalisation</b>	$409.0 \pm 75.2$	$0.44 \pm 0.05$	$-26.6 \pm 0.6$

The hydrodynamic diameter obtained for the parent nanoparticle ( $311.7 \pm 37.8$  nm) is within error of the two hydrodynamic diameters observed for MSN synthesis for the free radical copolymerisation (0.2 mol% =  $266.9 \pm 36.6$  nm and 1 mol% =  $304.7 \pm 50.2$  nm, *Table 5.1*). The zeta potential observed ( $-28.5 \pm 0.6$  mV) was similar to the zeta potential observed in Section 5.4.1 for the MSN synthesis for the 1 mol% free radical NVA/MAA MSNs ( $-27.6 \pm 2.3$  mV), expected due to the predominantly negative silanol surfaces. The hydrodynamic diameter of fluorescein functionalisation ( $265.4 \pm 29.4$  nm) is equivalent to the diameter obtained in Section 5.4.1 for 0.2 mol% free radical fluorescein functionalisation of MSNs ( $274.9 \pm 19.8$  nm). This is also expected as there is no deviation between the two protocols up to this point and the low concentration (0.15 mol%) of fluorescein functionalisation was expected to have little effect on hydrodynamic diameter and zeta potential. The zeta potential ( $-23.8 \pm 4.5$  mV) is also within error of the 0.2 mol% ( $-18.4 \pm 2.7$  mV). Finally, the 0.2 mol% surface amine functionalisation for the ATRP MSNs gave a hydrodynamic diameter of  $1461.0 \pm 348.1$  nm compared to the 0.2 mol% surface aminated free radical MSNs

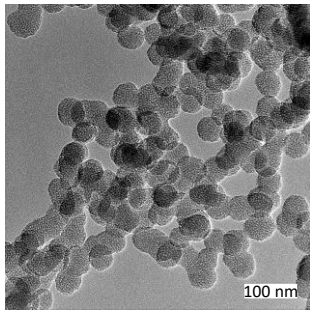
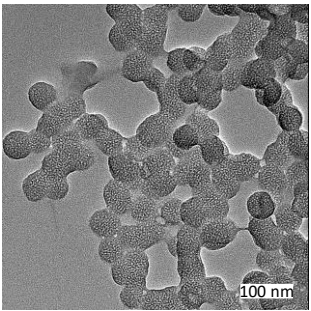
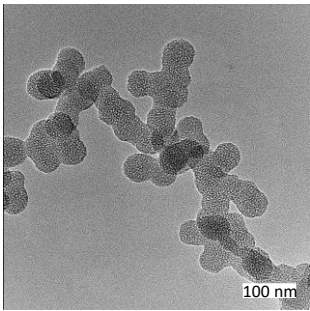
1042.0  $\pm$  144.6 nm, which are within error of each other. The dramatic increase in hydrodynamic diameter obtained by external amine functionalisation compared to the fluorescein functionalisation is due to the amine groups providing areas of positive charge on the MSNs creating greater electrostatic interactions between MSNs causing more aggregation and therefore resulting in a larger observed hydrodynamic diameter. The zeta potential obtained for 0.2 mol% amination for the ATRP MSNs is slightly lower than the zeta potential of the 0.2 % free radical MSNs (5.6  $\pm$  2.1 mV compared to 10.7  $\pm$  0.8 mV respectively). However, the change from a negative zeta potential to a positive zeta potential strongly suggests successful surface amine functionalisation and this small discrepancy may be due to a slightly different concentration of particles being measured. The PDIs up to Step 3 (1. MSN synthesis = 0.21  $\pm$  0.03, 2. Fluorescein binding = 0.31  $\pm$  0.04 and 3. 0.2 % surface amination = 0.36  $\pm$  0.14) are all below 0.40, suggesting good aqueous stability.

Upon modification of the nanoparticles with polymer using the ATRP method, ATRP NVA/MAA MSNs, the PDI increased dramatically to 0.58  $\pm$  0.09. This is indicative of unstable MSNs aggregating and the presence of polydisperse materials within the sample. This is due to the copolymers on MSNs becoming intertwined with copolymers bound on adjacent MSNs. This also explains the large hydrodynamic diameter obtained (1025.0  $\pm$  62.3 nm). The zeta potential also changed from positive to negative (5.6  $\pm$  2.1 mV to -22.5  $\pm$  0.6 mV) due to the addition of methacrylic acid to the MSNs, as expected. The differences between the hydrodynamic diameter, PDI and zeta potential obtained for the ATRP of NVA/MAA compared to the free radical polymerisation of NVA/MAA (hydrodynamic diameter = 584.3  $\pm$  125.2 nm, PDI = 0.36  $\pm$  0.02 and zeta potential = -11.0  $\pm$  0.5 respectively) suggests a difference in chain length of the copolymer obtained using the two different polymerisation protocols. The larger hydrodynamic diameter, PDI and more negative zeta potential obtained for the ATRP NVA/MAA copolymer suggests that the polymer chain length obtained is significantly larger than NVA/MAA copolymer obtained by free radical. The variation between hydrodynamic diameter, PDI and zeta potential obtained before and after ATRP proved that the MSNs had been chemically changed and that methacrylic acid was present so the PNA addition step was performed. The hydrodynamic diameter after PNA addition changed dramatically to 409.0  $\pm$  75.2 nm and the PDI lowered to 0.44  $\pm$  0.05 showing an increase in stable MSN suspension in water. The

hydrodynamic diameter decreasing shows that the bound PNA minimises the interaction and subsequent entanglement of NVA/MAA copolymers on adjacent MSNs possibly *via* steric hindrance. The zeta potential has not changed significantly from the attachment of NVA/MAA copolymer surface functionalisation and PNA binding ( $-22.5 \pm 0.6$  mV to  $-26.6 \pm 0.6$  mV), showing that the binding of PNA to the ATRP MSNs has little effect on the surface charge of the MSNs. These changes in hydrodynamic diameter, PDI and zeta potential from the starting MSNs suggested successful PNA binding to the MSNs.

### 5.5.2 Transmission Electron Microscopy

TEM images of the parent MSNs, the MSNs after NVA/MAA copolymer surface functionalisation using ATRP and the MSNs after PNA binding were obtained to allow for comparison (*Figure 5.14*).

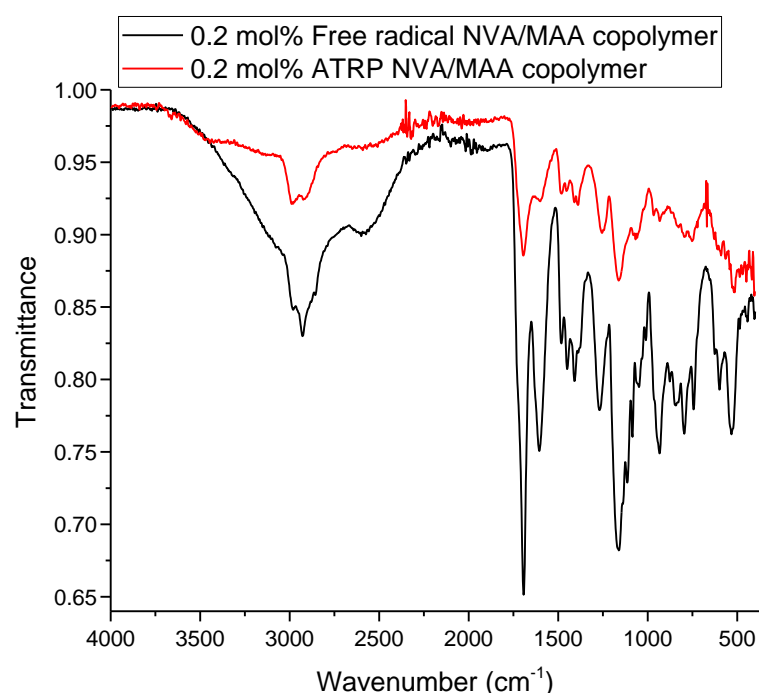
Sample	Parent MSNs	ATRP MSNs	PNA MSNs
TEM image			
Diameter	$46.7 \pm 4.6$ nm	$48.6 \pm 4.6$ nm	$49.6 \pm 4.9$ nm

*Figure 5.14. The TEM images of The Parent MSNs compared to the ATRP MSNs and the PNA MSNs. The diameter calculated as the mean and standard deviation of 100 MSNs.*

As can be seen by the MSN particle diameters obtained for each set of TEM images (ATRP MSNs =  $48.6 \pm 4.6$  nm and PNA MSNs =  $49.6 \pm 4.9$  nm), there is no significant change to the particle diameter after ATRP and PNA binding. The porosity of the MSNs does not appear to have been affected by the subsequent synthetic steps either. The NVA/MAA copolymer or PNA can't be observed because no negative staining was performed due to the analysis of the MSN structure and size being the principal objective of this procedure.

### 5.5.3 Infrared Spectroscopy

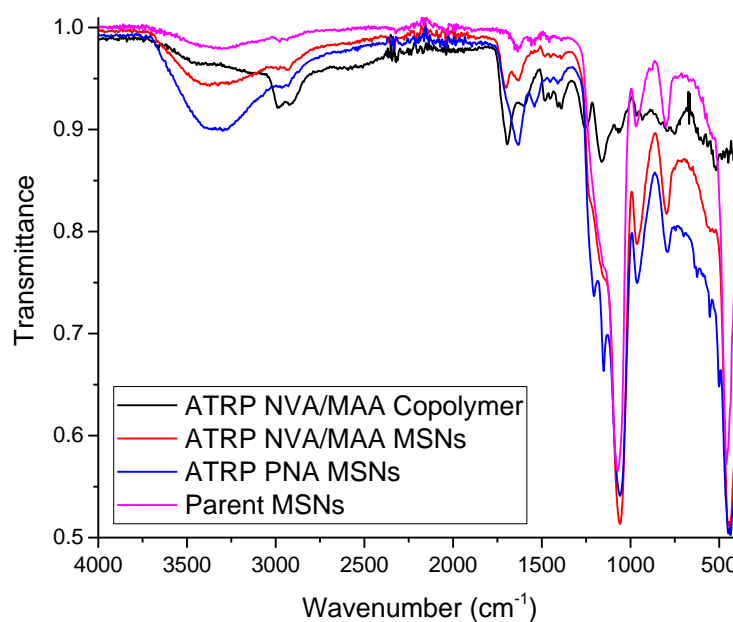
NVA/MAA copolymer synthesised by ATRP using 0.2 mol% BIBB in the absence of MSNs was analysed by IR spectroscopy to confirm that the copolymer obtained had the same structure as the copolymer obtained using free radical polymerisation (*Figure 5.15*). As before in Chapter 4 and for the NVA/MAA copolymer obtained using free radical polymerisations, the BIBB bound MSNs were replaced by the theoretical concentration of BIBB on the MSNs for 0.2 mol% surface functionalisation.



*Figure 5.15. the IR spectra of the NVA/MAA copolymer using 0.2 mol% concentration of initiator by free radical polymerisation and ATRP.*

As can be observed in the IR spectra all the same prominent absorption peaks ( $1165\text{ cm}^{-1}$  = C-O (carboxyl, stretch),  $1583\text{ cm}^{-1}$  = C=O (amide, stretch),  $1676\text{ cm}^{-1}$  = C=O (carboxyl) stretch,  $2578\text{ cm}^{-1}$  = O-H (carboxyl) stretch and  $2919\text{ cm}^{-1}$  = C-H stretch are observed corresponding to the functional groups as expected from a NVA/MAA copolymer.<sup>77</sup>

With the NVA/MAA copolymer obtained by ATRP confirmed as having a similar composition to the free radical, the NVA/MAA MSNs and the PNA MSNs were analysed by IR to observe copolymer and PNA functionalisation (*Figure 5.16*).



*Figure 5.16. The IR spectra of NVA/MAA copolymer using 0.2 mol% equivalent BIBB in the absence of MSNs, 0.2 mol% ATRP NVA/MAA surface functionalised MSNs and PNA bound 0.2 mol% NVA/MAA surface functionalised MSNs compared to Parent MSNs.*

The shifts representing the silica nanoparticle in ATRP NVA/MAA MSN samples are present at 1015-1190  $\text{cm}^{-1}$  representing Si-O-Si stretching and bending vibrations,<sup>78-80</sup> stretches around 800  $\text{cm}^{-1}$ , indicative of Si-O-Si stretches,<sup>81</sup> and those centred at ~550 and ~450  $\text{cm}^{-1}$  representing tri and tetracyclosiloxane rings of siloxanes.<sup>82</sup> There are also organic shifts such as the C=O stretches present at 1612  $\text{cm}^{-1}$  (amide), representing the NVA amide, and 1689  $\text{cm}^{-1}$  (carboxyl), representing the carboxyl group in MAA. There is a stretch at 3346  $\text{cm}^{-1}$  which represents O-H stretch from water impurity. There is a shoulder on this broad O-H stretch at 2952  $\text{cm}^{-1}$  which represents C-H stretches of the copolymer. These organic stretches observed confirmed the presence of NVA/MAA copolymer.<sup>77</sup>

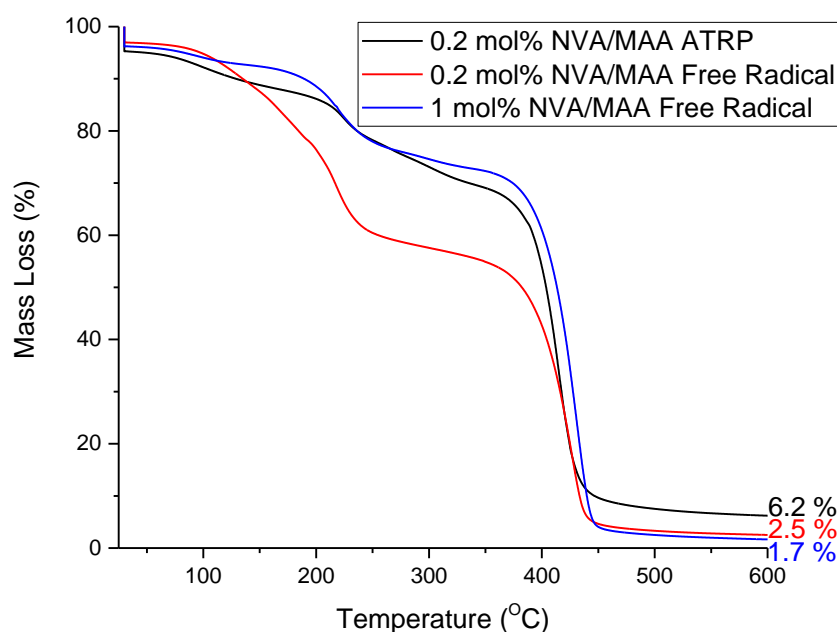
The IR spectra for the PNA MSNs had no significant variation from the ATRP NVA/MAA MSNs with stretches present for C=O (amide) at 1538  $\text{cm}^{-1}$ , C=O (carboxyl) at 1635  $\text{cm}^{-1}$  and a stretch at 2942  $\text{cm}^{-1}$  representing C-H stretches. The stretch representing O-H stretching at 3325  $\text{cm}^{-1}$  was significantly broader than for ATRP NVA/MAA MSNs, however this is more likely due to increased water



impurities than proof of PNA binding. A large variation in the IR spectra was not expected however for the binding of PNA as it is a protein that consists mainly of amide, carboxyl and C-H groups, like the NVA/MAA copolymer, but could also show a low loading density of PNA on the final composites.

#### 5.5.4 Thermogravimetric analysis

The NVA/MAA copolymer obtained using ATRP was analysed by TGA to observe if changing from free radical polymerisation to ATRP had minimised monomer impurities (*Figure 5.17*).

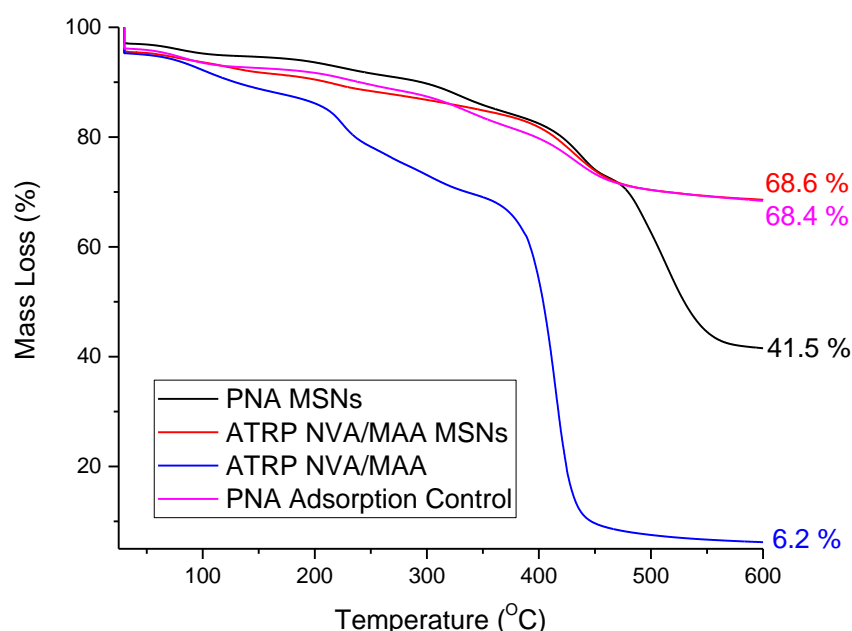


*Figure 5.17. The percentage mass loss versus temperature for the 0.2 mol% NVA/MAA copolymer obtained using ATRP in the absence of MSNs compared to the 0.2 mol% and 1 mol% NVA/MAA copolymer obtained by free radical polymerisation.*

For the 0.2 mol% NVA/MAA ATRP copolymer sample a consistent degradation is observed from 30 °C to 310 °C (23.10 wt%). This represents unreacted reagent species such as the significant acceleration in mass loss between 200 °C and 245 °C of 8.96 wt% which represents as *N, N, N', N'', N'''*-Pentamethyldiethylenetriamine (PMDETA, boiling point = 198 °C). Like the 0.2 mol% and 1 mol% NVA/MAA free radical copolymers the largest mass loss for 0.2 mol% NVA/MAA ATRP copolymer is between 310 °C and 460 °C which represents the degradation of the copolymer (mass

loss for 0.2 mol% NVA/MAA free radical = 53.0 wt%, 1 mol% NVA/MAA free radical = 70.6 wt% and 0.2 mol% NVA/MAA ATRP = 63.1 wt%).

The NVA/MAA copolymer surface functionalised MSNs obtained using ATRP were analysed in three iterations (*Figure 5.18*). The ATRP NVA/MAA MSNs (*Figure 5.13*, D) were analysed and compared to the ATRP NVA/MAA MSNs NHS/EDC-HCl coupled with PNA, PNA MSNs (*Figure 5.13*, E). Finally, the PNA MSNs were compared with ATRP NVA/MAA MSNs that were incubated with PNA without NHS/EDC-HCl, PNA Adsorption Control. This control was to confirm whether the PNA was chemically binding to the NVA/MAA copolymer and to define which peak represented PNA attached to the NVA/MAA copolymer.



*Figure 5.18. The percentage mass loss versus temperature for PNA MSNs compared to pNVA/MAA MSNs, pNVA/MAA synthesised in the absence of MSNs and the PNA Adsorption Control.*

In the NVA/MAA functionalised MSNs using ATRP the large mass loss between 70 °C and 250 °C found in the free radical NVA/MAA MSNs (ATRP NVA/MAA MSNs = 6.3 wt%, 0.2 mol% NVA/MAA free radical MSNs = 37.4 wt% and 1 mol% NVA/MAA free radical MSNs = 44.4 wt%), representing monomer and solvent impurities in the sample has been removed. The only significant mass loss

observed is the loss representing the hydrocarbon and other functional groups of NVA/MAA copolymer between 310 °C and 460 °C. The percentage by mass of copolymer was calculated to be 13.8 %. This is significantly lower than the percentage by mass of copolymer found using the same 0.2 % of initiator for free radical polymerisation (25.9 %). This could be due to less successful attachment of the BIBB initiator to the MSNs used in the ATRP reaction compared to the ACVA initiator bound MSNs for the free radical polymerisation. The small amount of mass loss observed in all MSN samples before 310 °C (ATRP NVA/MAA MSNs = 9.0 wt%, PNA Adsorption Control = 9.3 wt% and PNA MSNs = 7.9 wt%) represent physisorbed water and surface silanol groups.

A comparison of the PNA Adsorption Control and the ATRP NVA/MAA MSNs shows conclusively that no PNA is being adsorbed onto the MSNs due to the lack of variation in mass loss with increasing temperature. This is highlighted by the same percentage mass loss being obtained at the end of the analysis (ATRP NVA/MAA MSNs = 68.6 % and PNA Adsorption Control = 68.4 %). The PNA MSNs however have a significant mass loss between 470 °C and 560 °C of 28.6 % which represents the loss of bound PNA. The presence of this significant mass loss which is solely observed in the PNA MSNs confirms that the PNA is bound to the MSNs via the methacrylic acid and therefore the PNA MSNs were progressed to colorectal cancer cell binding analysis.

### **5.5.5 Gel Permeation Chromatography**

The copolymer of NVA/MAA synthesised using ATRP copolymer in the absence of MSNs, but with the equivalent theoretical moles of BIBB initiator assuming 100 % conversion of the surface amine groups on the MSNs, was analysed by GPC (*Figure 5.19*) to obtain the  $M_n$  and PDI obtained using the conditions used for the BIBB bound MSNs.

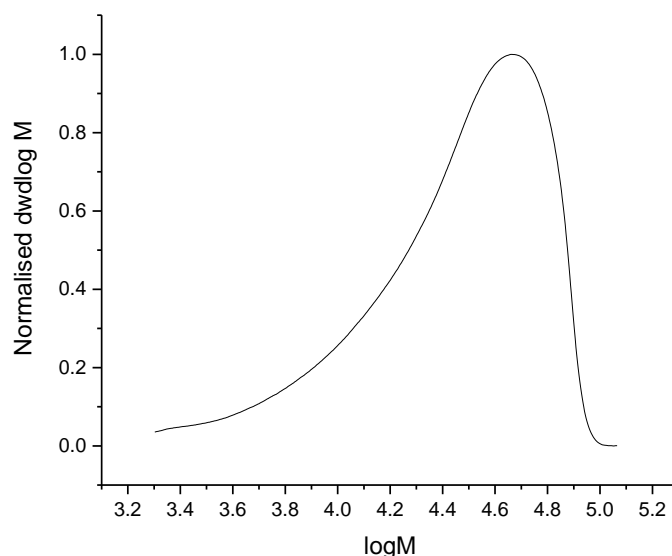


Figure 5.19. The plot of  $\log M$  against normalised  $dwd\log M$  for the ATRP reactions involving the theoretical BIBB concentration calculated for the 0.2 mol% amine surface functionalised MSNs.

The  $M_n = 19,000 \text{ g mol}^{-1}$  was significantly higher than the  $M_n$  obtained using 0.2 % and 1 % ACVA initiator free radical polymerisation (0.2 % =  $6100 \text{ g mol}^{-1}$  and 1 % =  $7000 \text{ g mol}^{-1}$ ). This is due to ATRP being a living polymerisation method, thus making the rate of growth linear and dependent on initiator and monomer concentrations.<sup>83, 84</sup> Whereas free radical polymerisation is not living and therefore the growth follows a logarithmic trend.<sup>84, 85</sup> This results in the monomer and initiator concentrations having an independent relationship with polymer chain length. The PDI obtained for the 0.2 mol% ATRP NVA/MAA copolymer was 1.81 compared to 1.28 and 1.20 for the 0.2 mol% and 1 mol% free radical NVA/MAA copolymers respectively. This is very high showing that little control of chain length is being claimed by the addition of the Cu-PMDETA chelate used in this ATRP reaction. The asymmetry of the plot for the 0.2 mol% ATRP NVA/MAA copolymer is due to uncontrolled termination occurring highlighted by the high PDI.

## **5.6 Investigation into the Specific Binding of the PNA Functionalised MSNs with the Colorectal Cancer Cells**

### **5.6.1 Colorectal Cancer Cell Binding Assay**

This was performed using the same procedure performed to investigate the non-specific binding of the MSNs with the colorectal cancer cells in Section 5.5.1 of this chapter (*Figure 5.20*). ATRP NVA/MAA grafted fluorescent MSNs were incubated at a range of different concentrations (ranging 1.22  $\mu\text{g/mL}$ – 1250  $\mu\text{g/mL}$ ) with the cells for 24 hrs in standard cell conditions (See Chapter 2 Experimental for details, Section 2.2.3.7). After this time, cells were thoroughly washed, and their fluorescence signal was analysed. As before, increased fluorescence indicates increased binding between nanoparticles and cells due to electrostatic interactions. It should be noted that control experiments carried out in the absence of nanoparticles and the absence of cells respectively showed negligible fluorescence signal, indicating that the observed fluorescent signal originates from an interaction between the particles and the cells.

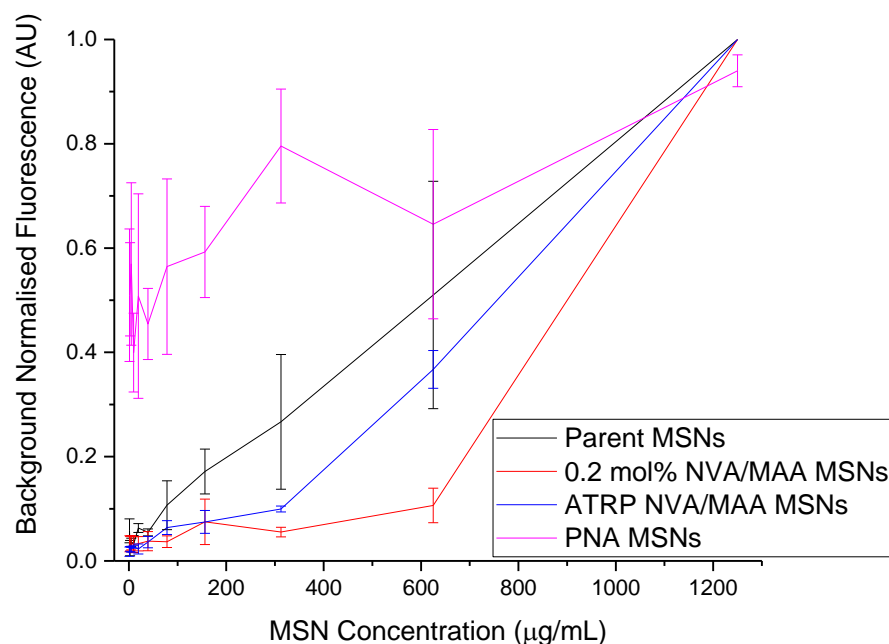


Figure 5.20. The background normalised fluorescence obtained at 528 nm after excitation at 485 nm from serial dilutions from 1250  $\mu\text{g/mL}$  to 1.22  $\mu\text{g/mL}$  after incubation with SW480 cells for 24 hrs and subsequent washes. The results shown are of ATRP NVA/MAA MSNs, free radical 0.2 mol% NVA/MAA surface functionalised MSNs (Section 5.4.1 Figure 5.12) and PNA bound ATRP NVA/MAA surface functionalised MSNs, PNA MSNs, compared to the Parent MSNs.

There is a large variation in the amount of fluorescence at 625  $\mu\text{g/mL}^{-1}$  between the ATRP 0.2 mol% NVA/MAA MSNs ( $36.73 \pm 3.63 \%$ ) and the free radical 0.2 mol% NVA/MAA MSNs ( $10.65 \pm 3.31 \%$ ). This shows that there is a larger amount of non-specific binding in the ATRP NVA/MAA MSNs than the free radical NVA/MAA MSNs at this concentration. The ATRP NVA/MAA MSNs are within error of the parent MSNs ( $51.00 \pm 21.80 \%$ ). This is due to the lower amount of polymer chains bound to the MSNs after ATRP (13.8 wt%) than free radical (25.9 wt%) and the lower amount of physisorbed starting reagents according to TGA. This has allowed for stronger interaction between the cells and the MSN surface due to the absence of polymer and physisorbed reagents preventing recognition of the nanoparticles by the cells. However, at 0.31  $\text{mg/mL}$  there is a clear deviation between the fluorescence for ATRP NVA/MAA MSNs ( $9.96 \pm 0.56 \%$ ) and the parent MSNs ( $26.67 \pm 12.92 \%$ ). This shows that the NVA/MAA copolymer synthesised using ATRP is minimising

non-specific binding between cells and the MSNs. There is more binding for the ATRP NVA/MAA MSNs than for free radical MSNs ( $5.53 \pm 0.91 \%$ ), however this difference was attributed again to the greater polymer loading and physisorbed starting reagents inhibiting MSN to cell interactions.

The chemical binding of PNA to the ATRP NVA/MAA MSNs, PNA MSNs, had a dramatic effect on cell binding. At 0.625 mg/mL the fluorescence is within error of the parent MSNs (PNA MSNs =  $68.96 \pm 20.00 \%$  compared to Parent MSNs =  $51.00 \pm 21.80 \%$ ). However, whereas the parent MSNs and both the NVA/MAA MSNs fluorescence drop at 0.31 mg/mL the PNA MSNs fluorescence remains ( $85.47 \pm 14.05 \%$ ) and is within error of the fluorescence obtained at 0.625 mg/mL down to a concentration of 1.22  $\mu\text{g/mL}$  ( $55.17 \pm 14.97 \%$ ). This clearly shows that specific strong interactions are occurring between the PNA and the SW480 cells. Sakuma *et al.* performed a very similar experiment with polystyrene nanoparticles surface functionalised with PNA bound N-vinyl acetamide/MAA copolymer.<sup>65</sup> 4 mg/mL of the functionalised nanoparticles were administered to SW480 at left to incubate for 30 mins, compared to the 24 hrs in this project. The cells were then centrifuged out to remove excess nanoparticles and analysed by fluorescence. In this research it was found that there was binding of the nanoparticles to the SW480 cells, but not as significant an amount as was found with other human carcinoma cells that were also analysed. This was explained to be due to a possible lowering in expression of the TF antigen compared to the other cells.

### 5.6.2 Cell Viability Test

A resazurin viability assay was carried out on a range of phosphate buffered saline, PBS, -suspended PNA-MSN samples (1.2  $\mu\text{g/mL}$  to 1250  $\mu\text{g/mL}$ ). Viable cells were identified through a change in absorbance of the assay due to metabolic conversion of resazurin to resofurin. (Figure 5.21).<sup>86</sup>

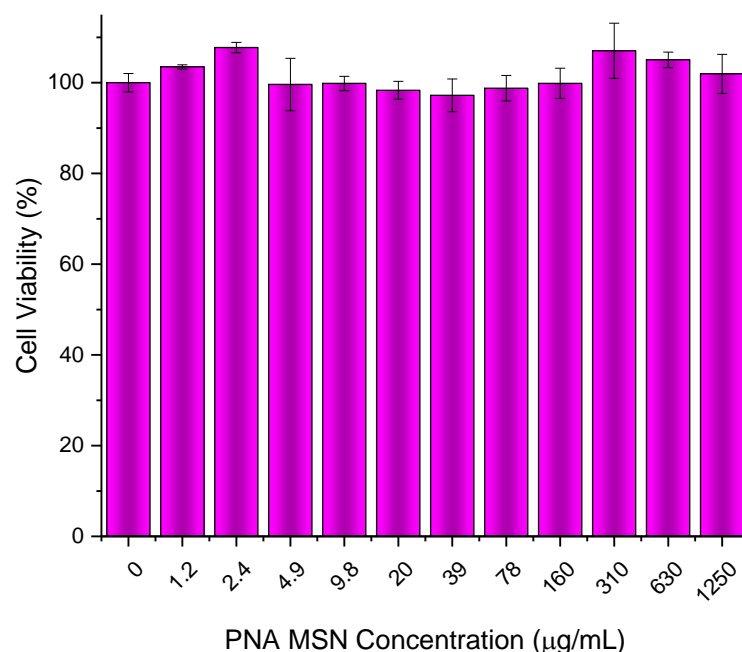


Figure 5.21. The cell viability of SW480 colorectal cancer cells incubated for 24 hrs with serial dilutions from 1250 µg/mL to 1.22 µg/mL PNA MSNs normalised to the cell viability of the control cells with no addition of PNA MSNs.

There is no decrease in cell viability compared to the control ( $100.0 \pm 2.0$  %) even up to the highest concentration of 1250 µg/mL ( $101.9 \pm 4.3$  %). This exemplifies the low toxicity of the MSNs. This result also confirms the relevance of the concentration range used in the binding assays as all concentrations analysed were non-toxic. The absence of any toxicity characteristics displayed by the SW480 up to 1250 µg/mL agrees with the research Yu et al. performed on non-small-cell lung cancer cells incubated with MSNs of particle diameter  $120 \pm 25$  nm.<sup>87</sup> In this research numerous toxicity assays were performed and it was found that MSNs did not affect the cell viability of A549 cells up to 500 µg/mL. Cancer epithelial cells were resistant to proliferation inhibition due to MSN treatment up 1000 µg/ mL post 72 hrs exposure. The plasma membrane integrity of the A549 cells was unaffected by MSNs after 24 hrs incubation with 250 µg/mL of MSNs. Also, that no haemolytic toxicity was observed for incubation with 100 µg/mL of MSNs. Sakuma *et al.* have rigorously tested the toxicity of grafted N-vinyl acetamide/MAA copolymer *in vivo*.<sup>69</sup> in this research N-vinyl acetamide/MAA copolymers surface grafted onto polystyrene beads with coumarin encapsulated were administered to rats using both oral and intrarectal



administration at 50 mg/mL, administering 20 mL per kg of body weight. The rats were observed for 7 days and no change in body weight, food consumption or water consumption was observed compared to the controls. Also, no significant difference was observed in haematological and blood biochemical parameters was observed. Necropsy revealed that there was no macroscopic nanoparticle-induced change in the rat organs. Finally, that after histopathological examination, there was no induced toxicity to the digestive organs, liver, kidneys or mesenteric, the membrane that attaches the intestine to the abdominal wall, lymph nodes.

## 5.7 Conclusions

The aim of this project was to produce fluorescent MSNs with the capability to differentiate between colorectal cancer cells and healthy cells such that they can be distinguished to facilitate earlier diagnosis and treatment. Initial investigations involved fluorescent MSNs synthesis and incubation with SW480 colorectal cancer cells. There was found to be non-specific binding present between the MSNs and the SW480 cells. So, the fluorescent MSNs were surface functionalised with NVA/MAA copolymer, synthesised using free radical polymerisation and functionalisation confirmed by TGA, DLS and IR, which had previously in literature been utilised to minimise non-specific binding with polymeric nanoparticles. Then it was investigated whether this copolymer could perform the same function on MSNs. Two surface densities were investigated 0.2 mol% and 1 mol%, to observe if this would affect non-specific binding. It was found that both 0.2 mol% ( $10.6 \pm 3.3$  % fluorescence at 0.625 mg/mL compared to 1.25 mg/mL) and 1 mol% ( $14.4 \pm 1.8$  %) had low binding with SW480 cells, however the large amount of starting reagents impurity in the MSNs (0.2 % = 37.4 wt% and 1 % = 44.4 wt%), made the efficacy of the NVA/MAA copolymer ambiguous. Therefore, ATRP was utilised to minimise starting reagent contamination and allow for polymer chain length control. ATRP was found to greatly minimise starting reagent impurity. However, the control of polymer chain length usually acquired using ATRP was not obtained ( $PDI = 1.81$ ). The ATRP MSNs then had PNA bound to them via an amide bond to the MAA in the copolymer. The PNA MSNs were incubated with SW480 colorectal cancer cells and found to strongly specifically bind. It was found that even down to concentrations as low as  $1.22 \times 10^{-3}$  mg/mL there was significant fluorescence compared to unfunctionalized NVA/MAA MSNs ( $55.2 \pm 15.0$  % of 1.25 mg/mL fluorescence obtained at  $1.22 \times 10^{-3}$  mg/mL compared to  $1.8 \pm 0.9$  % obtained for unfunctionalized NVA/MAA MSNs). Finally, the toxicity of these PNA MSNs was analysed by assessing cell viability. It was concluded from this that even with 24 hrs incubation with 1.25 mg/mL of PNA MSNs there was no effect on the metabolism of the colorectal cancer cells compared to the control cells incubated with no PNA MSNs (Cell viability for control SW480 cells =  $100.0 \pm 2.0$  %, cell viability of SW480 incubated with 1.25 mg/mL of PNA MSNs for 24 hrs =  $101.9 \pm 4.3$  %).

## 5.8 Future Work

An area of further investigation is to analyse how the PNA bound NVA/MAA copolymer surface functionalised MSNs interact with healthy colorectal cells to ascertain whether the binding is specific to cancerous colorectal cancer cells. Also, all the investigations were *in vitro* so *in vivo* studies would need to be performed to observe whether other interactions occur in a more complex system. On the synthetic side the ATRP reaction optimisation requires investigation. The PDI obtained of 1.81 is high for a controlled polymerisation. Therefore, investigating the chelate used to bind to the Cu and monomer concentrations are required. The benefit of this optimisation would be that the copolymer chain length and its relative composition could be investigated to observe their effect on binding, like in Chapter 4. Finally, synthetically, the binding of the PNA needs to be optimised. Despite the protocol's success at binding PNA, this came with a detriment to the overall fluorescence of the MSNs. This is due to the EDC-HCl or NHS compounds quenching the fluorescein.

## 5.9 References

1. R. L. Siegel, K. D. Miller, S. A. Fedewa, D. J. Ahnen, R. G. Meester, A. Barzi and A. Jemal, *CA: a cancer journal for clinicians*, 2017, **67**, 177-193.
2. R. L. Siegel, K. D. Miller and A. Jemal, *CA: a cancer journal for clinicians*, 2017, **67**, 7-30.
3. M. Horner, L. Ries, M. Krapcho, N. Neyman, R. Aminou, N. Howlader, S. Altekruse, E. Feuer, L. Huang and A. Mariotto, Editon edn., 2009.
4. B. Morson, J. Whiteway, E. Jones, F. Macrae and C. Williams, *Gut*, 1984, **25**, 437-444.
5. R. Kikuchi, M. Takano, K. Takagi, N. Fujimoto, R. Nozaki, T. Fujiyoshi and Y. Uchida, *Diseases of the colon & rectum*, 1995, **38**, 1286-1295.
6. A. M. Lacy, M. M. Tasende, S. Delgado, M. Fernandez-Hevia, M. Jimenez, B. De Lacy, A. Castells, R. Bravo, S. D. Wexner and R. J. Heald, *Journal of the American College of Surgeons*, 2015, **221**, 415-423.
7. G. C. Balch, A. De Meo and J. G. Guillem, *World journal of gastroenterology: WJG*, 2006, **12**, 3186.
8. T. Muto and M. Oya, *Diseases of the colon and rectum*, 2003, **46**, S89-93.
9. H. Kashida and S.-e. Kudo, *International journal of clinical oncology*, 2006, **11**, 1-8.
10. J. Tischendorf, H. Wasmuth, A. Koch, H. Hecker, C. Trautwein and R. Winograd, *Endoscopy*, 2007, **39**, 1092-1096.
11. R. S. DaCosta, B. C. Wilson and N. E. Marcon, *The Scientific World Journal*, 2007, **7**, 2046-2071.
12. S. Anandasabapathy, *Current opinion in gastroenterology*, 2008, **24**, 64-69.
13. F. Van Den Broek, P. Fockens and E. Dekker, *Alimentary pharmacology & therapeutics*, 2007, **26**, 91-99.
14. M. Hirata, S. Tanaka, S. Oka, I. Kaneko, S. Yoshida, M. Yoshihara and K. Chayama, *Gastrointestinal endoscopy*, 2007, **66**, 945-952.
15. K. Kelly, H. Alencar, M. Funovics, U. Mahmood and R. Weissleder, *Cancer research*, 2004, **64**, 6247-6251.
16. Y. Hiroshima, A. Maawy, C. A. Metildi, Y. Zhang, F. Uehara, S. Miwa, S. Yano, S. Sato, T. Murakami and M. Momiyama, *Journal of Laparoendoscopic & Advanced Surgical Techniques*, 2014, **24**, 241-247.

17. S. Cohen, M. Pellach, Y. Kam, I. Grinberg, E. Corem-Salkmon, A. Rubinstein and S. Margel, *Materials Science and Engineering: C*, 2013, **33**, 923-931.
18. J. C.-H. Kuo, A. E. Ibrahim, S. Dawson, D. Parashar, W. J. Howat, K. Guttula, R. Miller, N. S. Fearnhead, D. J. Winton and A. A. Neves, *Scientific reports*, 2016, **6**.
19. H. Nakase, S. Sakuma, T. Fukuchi, T. Yoshino, K. Mohri, K. Miyata, H. Kumagai, K.-I. Hiwatari, K. Tsubaki and T. Ikejima, *International Journal of Nanomedicine*, 2017, **12**, 1747.
20. S. Sakuma, M. Kataoka, H. Higashino, T. Yano, Y. Masaoka, S. Yamashita, K.-i. Hiwatari, H. Tachikawa, R. Kimura and K. Nakamura, *European Journal of Pharmaceutical Sciences*, 2011, **42**, 340-347.
21. F. M. Veronese and G. Pasut, *Drug discovery today*, 2005, **10**, 1451-1458.
22. A. Abuchowski, T. Van Es, N. Palczuk and F. Davis, *Journal of Biological Chemistry*, 1977, **252**, 3578-3581.
23. A. Abuchowski, J. R. McCoy, N. C. Palczuk, T. van Es and F. F. Davis, *Journal of Biological Chemistry*, 1977, **252**, 3582-3586.
24. V. P. Torchilin, V. G. Omelyanenko, M. I. Papisov, A. A. Bogdanov Jr, V. S. Trubetskoy, J. N. Herron and C. A. Gentry, *Biochimica et Biophysica Acta (BBA)-Biomembranes*, 1994, **1195**, 11-20.
25. S. N. Alconcel, A. S. Baas and H. D. Maynard, *Polymer Chemistry*, 2011, **2**, 1442-1448.
26. J. M. Harris and R. B. Chess, *Nature reviews Drug discovery*, 2003, **2**, 214.
27. Q. He, J. Zhang, J. Shi, Z. Zhu, L. Zhang, W. Bu, L. Guo and Y. Chen, *Biomaterials*, 2010, **31**, 1085-1092.
28. V. Cauda, C. Argyo and T. Bein, *Journal of Materials Chemistry*, 2010, **20**, 8693-8699.
29. J. V. Jokerst, T. Lobovkina, R. N. Zare and S. S. Gambhir, *Nanomedicine*, 2011, **6**, 715-728.
30. Y. H. Kim, J. Jeon, S. H. Hong, W. K. Rhim, Y. S. Lee, H. Youn, J. K. Chung, M. C. Lee, D. S. Lee and K. W. Kang, *Small*, 2011, **7**, 2052-2060.
31. S. Zhang, G. Qiu, Y. P. Ting and T.-S. Chung, *Colloids and Surfaces A: Physicochemical and Engineering Aspects*, 2013, **436**, 207-214.

32. A. S. Karakoti, S. Das, S. Thevuthasan and S. Seal, *Angewandte Chemie International Edition*, 2011, **50**, 1980-1994.
33. E. T. Dams, P. Laverman, W. J. Oyen, G. Storm, G. L. Scherphof, J. W. van der Meer, F. H. Corstens and O. C. Boerman, *Journal of Pharmacology and Experimental Therapeutics*, 2000, **292**, 1071-1079.
34. T. Ishida, K. Masuda, T. Ichikawa, M. Ichihara, K. Irimura and H. Kiwada, *International journal of pharmaceutics*, 2003, **255**, 167-174.
35. P. Laverman, M. G. Carstens, O. C. Boerman, E. T. M. Dams, W. J. Oyen, N. van Rooijen, F. H. Corstens and G. Storm, *Journal of Pharmacology and Experimental Therapeutics*, 2001, **298**, 607-612.
36. T. Ishida, S. Kashima and H. Kiwada, *Journal of Controlled Release*, 2008, **126**, 162-165.
37. C. Cortez, E. Tomaskovic-Crook, A. P. Johnston, B. Radt, S. H. Cody, A. M. Scott, E. C. Nice, J. K. Heath and F. Caruso, *Advanced Materials*, 2006, **18**, 1998-2003.
38. L. Li, D. Xiang, S. Shigdar, W. Yang, Q. Li, J. Lin, K. Liu and W. Duan, *International journal of nanomedicine*, 2014, **9**, 1083.
39. U. Schumacher, D. Higgs, M. Loizidou, R. Pickering, A. Leathem and I. Taylor, *Cancer*, 1994, **74**, 3104-3107.
40. U. Schumacher, E. Adam, D. J. Flavell, D. Boehm, S. A. Brooks and A. J. Leathem, *Clinical and Experimental Metastasis*, 1994, **12**, 398-404.
41. K. Yang, L. Cohen and M. Lipkin, *Cancer letters*, 1991, **56**, 65-69.
42. V. P. Bhavanandan and A. W. Katlic, *Journal of Biological Chemistry*, 1979, **254**, 4000-4008.
43. D. J. Desilets, K. E. Davis, P. P. Nair, K. F. Salata, C. L. Maydonovitch, R. S. Howard, J. W. Kikendall and R. K. Wong, *The American journal of gastroenterology*, 1999, **94**, 744-750.
44. R. S. Bresalier, J. C. Byrd, L. Wang and A. Raz, *Cancer research*, 1996, **56**, 4354-4357.
45. S. Kamali, E. Yilmaz, E. Sivriköz, M. Ertürk, G. Kamali, T. Sivriköz and H. Guven, *European Surgery*, 2015, **47**, 254-257.
46. L.-G. Yu, N. Andrews, Q. Zhao, D. McKean, J. F. Williams, L. J. Connor, O. V. Gerasimenko, J. Hilken, J. Hirabayashi and K. Kasai, *Journal of Biological Chemistry*, 2007, **282**, 773-781.

47. S. Sakuma, T. Yano, Y. Masaoka, M. Kataoka, K.-i. Hiwatari, H. Tachikawa, Y. Shoji, R. Kimura, H. Ma, Z. Yang, L. Tang, R. M. Hoffman and S. Yamashita, *European Journal of Pharmaceutics and Biopharmaceutics*, 2010, **74**, 451-460.
48. S. Sakuma, H. Higashino, H. Oshitani, Y. Masaoka, M. Kataoka, S. Yamashita, K.-i. Hiwatari, H. Tachikawa, R. Kimura, K. Nakamura, H. Kumagai, J. C. Gore and W. Pham, *European Journal of Pharmaceutics and Biopharmaceutics*, 2011, **79**, 537-543.
49. C. R. Boland, C. K. Montgomery and Y. S. Kim, *Proceedings of the National Academy of Sciences*, 1982, **79**, 2051-2055.
50. S. Beack, M. Cho, Y.-E. Kim, G.-O. Ahn and S. K. Hahn, *Bioconjugate Chemistry*, 2017.
51. C. Boland and J. Roberts, *Journal of Histochemistry & Cytochemistry*, 1988, **36**, 1305-1307.
52. M. A. Clark, B. H. Hirst and M. A. Jepson, *Advanced drug delivery reviews*, 2000, **43**, 207-223.
53. C. Bies, C.-M. Lehr and J. F. Woodley, *Advanced drug delivery reviews*, 2004, **56**, 425-435.
54. F. Gabor, E. Bogner, A. Weissenboeck and M. Wirth, *Advanced drug delivery reviews*, 2004, **56**, 459-480.
55. J. M. Rini, *Annual review of biophysics and biomolecular structure*, 1995, **24**, 551-577.
56. B. J. Campbell, I. A. Finnie, E. F. Hounsell and J. M. Rhodes, *Journal of Clinical Investigation*, 1995, **95**, 571-576.
57. L. David, J. Nesland, H. Clausen, F. Carneiro and M. Sobrinho-Simoes, *APMIS. Supplementum*, 1992, **27**, 162-172.
58. T. Janssen, M. Petein, R. Van Velthoven, P. Van Leer, M. Fourmarier, J.-P. Vanegas, A. Danguy, C. Schulman, J.-L. Pasteels and R. Kiss, *Human pathology*, 1996, **27**, 1341-1347.
59. R. Singh, B. Campbell, L.-G. Yu, D. Fernig, J. Milton, R. Goodlad, A. FitzGerald and J. Rhodes, *Glycobiology*, 2001, **11**, 587-592.
60. G. F. Springer, R. Cheingsong-Popov, V. Schirmacher, P. R. Desai and H. Tegtmeier, *Journal of Biological Chemistry*, 1983, **258**, 5702-5706.

61. V. V. Glinsky, M. E. Huflejt, G. V. Glinsky, S. L. Deutscher and T. P. Quinn, *Cancer research*, 2000, **60**, 2584-2588.
62. V. V. Glinsky, G. V. Glinsky, K. Rittenhouse-Olson, M. E. Huflejt, O. V. Glinskii, S. L. Deutscher and T. P. Quinn, *Cancer research*, 2001, **61**, 4851-4857.
63. E. Dabelsteen, *The Journal of pathology*, 1996, **179**, 358-369.
64. K.-i. Hiwatari, S. Sakuma, K. Iwata, Y. Masaoka, M. Kataoka, H. Tachikawa, Y. Shoji and S. Yamashita, *European Journal of Pharmaceutics and Biopharmaceutics*, 2008, **70**, 453-461.
65. S. Sakuma, T. Yano, Y. Masaoka, M. Kataoka, K.-i. Hiwatari, H. Tachikawa, Y. Shoji, R. Kimura, H. Ma and Z. Yang, *Journal of Controlled Release*, 2009, **134**, 2-10.
66. S. Sakuma, K. Hiwatari, T. Yano, K. Iwata, Y. Masaoka, M. Kataoka, H. Tachikawa, Y. Shoji, R. Kimura and K. Nakamura, The Third International Conference on the Development of Biomedical Engineering in Vietnam, 2010.
67. S. Sakuma, S. Yamashita, K.-i. Hiwatari, R. M Hoffman and W. Pham, *Current drug discovery technologies*, 2011, **8**, 367-378.
68. T. Kitamura, S. Sakuma, M. Shimosato, H. Higashino, Y. Masaoka, M. Kataoka, S. Yamashita, K. i. Hiwatari, H. Kumagai and N. Morimoto, *Contrast media & molecular imaging*, 2015, **10**, 135-143.
69. S. Sakuma, H. Kumagai, M. Shimosato, T. Kitamura, K. Mohri, T. Ikejima, K.-i. Hiwatari, S. Koike, E. Tobita and R. McClure, *Nanomedicine: Nanotechnology, Biology and Medicine*, 2015, **11**, 1227-1236.
70. S. Sakuma, N. Suzuki, H. Kikuchi, K.-i. Hiwatari, K. Arikawa, A. Kishida and M. Akashi, *International journal of pharmaceutics*, 1997, **149**, 93-106.
71. S. Sakuma, J. Y. Yu, T. Quang, K. I. Hiwatari, H. Kumagai, S. Kao, A. Holt, J. Erskind, R. McClure and M. Siuta, *International journal of cancer*, 2015, **136**, 1095-1103.
72. M. J. Fischer, in *Surface plasmon resonance*, Springer, Editon edn., 2010, pp. 55-73.
73. T. Corner, in *Initiators—Poly-Reactions—Optical Activity*, Springer, Editon edn., 1984, pp. 95-142.



74. S. Sakuma, N. Suzuki, R. Sudo, K.-i. Hiwatari, A. Kishida and M. Akashi, *International journal of pharmaceutics*, 2002, **239**, 185-195.
75. S. Sakuma, M. Hayashi and M. Akashi, *Advanced drug delivery reviews*, 2001, **47**, 21-37.
76. J. J. Davis, *J Mater Chem*, 2012, **22**, 22848.
77. G. Socrates, *Infrared and Raman characteristic group frequencies: tables and charts*, John Wiley & Sons, 2004.
78. R. Tian, O. Seitz, M. Li, W. Hu, Y. J. Chabal and J. Gao, *Langmuir*, 2010, **26**, 4563-4566.
79. J. H. Moon, J. S. Seo, Y. Xu and S. Yang, *Journal of Materials Chemistry*, 2009, **19**, 4687-4691.
80. G.-L. Davies, J. O'Brien and Y. K. Gun'ko, *Scientific Reports*, 2017, **7**, 45862.
81. K. Nakamoto, *Handbook of Vibrational Spectroscopy*, 2006.
82. N. Maxim, A. Overweg, P. J. Kooyman, A. Nagy, R. A. van Santen and H. C. Abbenhuis, *Journal of Materials Chemistry*, 2002, **12**, 3792-3798.
83. K. Matyjaszewski, T. E. Patten and J. Xia, *Journal of the American Chemical Society*, 1997, **119**, 674-680.
84. K. Matyjaszewski and T. P. Davis, *Handbook of radical polymerization*, John Wiley & Sons, 2003.
85. A. Yokoyama, R. Miyakoshi and T. Yokozawa, *Macromolecules*, 2004, **37**, 1169-1171.
86. J. O'brien, I. Wilson, T. Orton and F. Pognan, *European journal of biochemistry*, 2000, **267**, 5421-5426.
87. Y.-S. Lin and C. L. Haynes, 2010, **132**, 4834-4842.

# Chapter 6

## 6. Conclusions

---

Mesoporous silica nanoparticles, MSNs, are a highly desirable nanostructure for potential medical applications due to their high surface area, ease of functionalisation and biocompatibility. In biomedicine, a vast amount of research has been dedicated to exploiting MSNs for therapeutic delivery applications. Their high internal volumes provide large payload capacity, in addition to the possibility of stimuli-responsive capping and surface targeting, makes them an ideal structure for drug encapsulation. MSNs have additionally found use as hosts for active agents, for example, in the development of imaging agents with enhanced properties. MSNs have previously highlighted their efficacy as a diagnostic agent for magnetic resonance imaging, MRI. This is due to the considerable contrast enhancement obtained by the binding of gadolinium ion-based contrast agents, GBCAs, to the MSN surfaces, producing enhancements resulting from favourable interactions with water, as governed by Solomon- Bloembergen-Morgan (SBM) theory. This enhancement has several highly desirable outcomes for potential biomedical applications. Increased signal enhancement can effectively lower doses required, an important consideration in patient safety. This is particularly pertinent given recent evidence of the deposition of Gd in patient tissue. Additionally, the biocompatibility and ability for surface modification of these species provides the opportunity to further develop their properties to provide precise diagnostics through, for example, targeting species, or the ability to ‘switch’ their contrast signal ‘on/off’ in the presence of disease. In this work, a series of MSN systems have been designed in a bid to further develop this exciting field and produce highly tuned, targeting and diagnostic MRI agents.

The investigation into the sensitivity and optimisation of MSNs’ previously successful application as an MRI contrast agent was probed further. The importance of water access to  $\text{Gd}^{3+}$ -chelates on the mesoporous structure of MSNs was

investigated, specifically examining how even small changes in pore size can impact the resulting MRI behaviour (**Chapter 3**). This research confirmed that even with a very low concentration of GBCA bound to the surface of MSNs, a six-fold enhancement in contrast can be obtained compared to the GBCA alone. Also, that this exceptional relaxation enhancement is maintained independent of the location of the GBCA binding onto the MSNs of pore diameter  $\sim 3.5$  nm. However, with a pore diameter of  $\sim 2.6$  nm there is a reduction in the relaxation enhancement found when binding the  $\text{Gd}^{3+}$ -chelate inside the pores due to restriction of water access to the  $\text{Gd}^{3+}$ -chelate. The change in relaxation observed shows the importance in ensuring appropriate construct design. In addition, when using larger pore size materials, the absence of change in relaxation behaviour allows a range of functionalities to be incorporated onto nanoparticle structures for future multi-functional applications.

These additional desirable functionalities were pursued by the surface functionalisation of MSNs with bound GBCAs with a thermoresponsive polymer, in a bid to design contrast agents with switchable signal capable of disease diagnostics (**Chapter 4**). This would allow for the control of the contrast, by either intrinsic pathological temperature variation such as between tumour and healthy tissue or the application of a temperature gradient *via* an external source (*e.g.* hyperthermia ablation), allowing for further minimisation of the dosages required for facile successful diagnosis. This research utilised atom transfer radical polymerisation, ATRP, of a well-known thermoresponsive polymer in a ‘grafting from’ synthetic approach onto MRI-active MSNs. This resulted in the successful synthesis of a GBCA that was able to aggregate, resulting in an area of localised signal. This could potentially provide opportunities in disease diagnosis as MSNs would aggregate at the site of interest. Importantly the aggregation stimulus response was performed at physiological temperatures with the ability for further tuning of the response depending on polymer chain length and polymer surface functionalisation density. This allows the GBCA response to be tailored to its target’s thermal fingerprint. Another desirable result of this investigation is that it obtained a robust method of polymer surface functionalisation with polymer chain length control that is not restricted to MSNs but able to be transferred to several oxide-type nanoparticles. This allows for a diverse variety of surface polymer functionalisation to be achieved able

to respond to different stimuli, like pH, and various other functions through modification of the functional groups present on the polymer.

In order to further develop our systems for precise biological function, such as biological targeting, we investigated the uptake behaviour of MSNs. Non-specific binding is a common problem, so the MSNs were polymer surface functionalised to perform the function of masking the MSNs from cells (**Chapter 5**). Firstly, the type of polymerisation was varied from ATRP to free radical to allow direct comparison to previous literature. As well as successfully functionalising the MSNs, the copolymer was able to efficiently minimise the interactions between MSNs and colorectal cancer cells. This was developed further by reverting to ATRP, regaining the polymer chain length control. In order to then bestow targeting capabilities onto the MSNs, a colorectal cancer binding lectin (peanut agglutinin) was covalently bound to the polymer/MSN nanocomposite and it was observed that this successfully facilitated MSN binding interactions with colorectal cancer cells. Essentially it was also confirmed that the lectin/polymer surface functionalisation of the MSNs had no effect on the low cytotoxicity usually observed by MSNs. Finally, the MSNs throughout this investigation were fluorescent, acquiring this property using the same chemistry applied to GBCA binding to MSNs. This allows for the truly unique possibility in diagnostic agents to provide enhancement contrast properties to complimentary imaging techniques.

This research could be developed further by developing an MSN system tuned to a specific disease by for instance responding to unique stimuli the specific cell type provides or having a response due to binding to the cell. This would be beneficial as it would remove ‘false positives’ and improve diagnostics. In the future the addition of drug encapsulation into the pores of the MSNs could be incorporated. The obtained drug delivery system plus the functionalities that were probed in this thesis could achieve an all-in-one drug administration system that is capable of disease diagnosis and drug release with specific targeting.

### 3.7 Appendix Chapter 3: Investigating the Impact of Nanoparticle Design on MRI Contrast Agent Behaviour

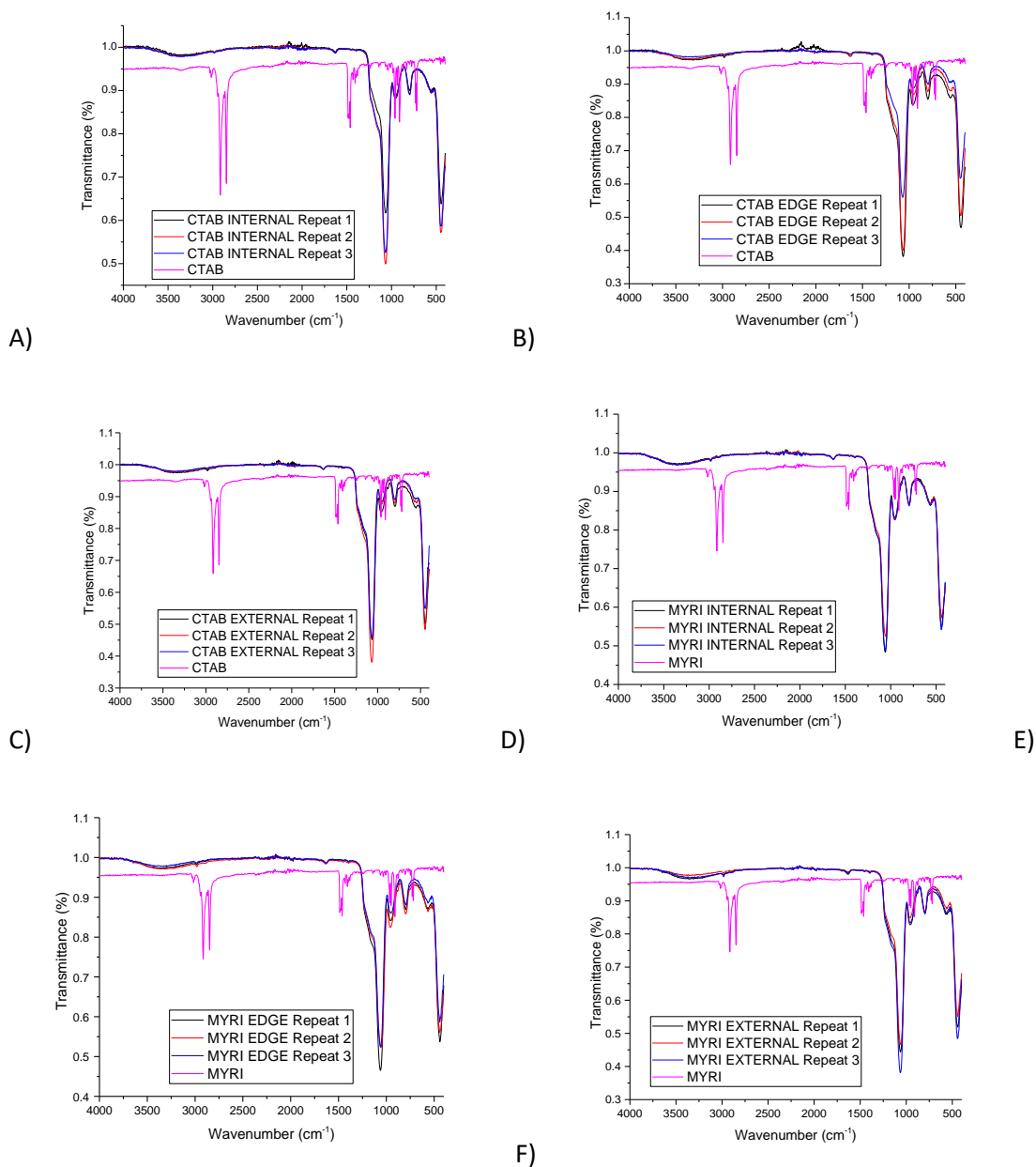


Figure 3.13. The IR spectra of the three synthetic repeats of A) CTAB Internal, B) CTAB Edge, C) CTAB External, D) MYRI Internal, E) MYRI Edge and F) MYRI External against their respective surfactant, CTAB or MYRI.

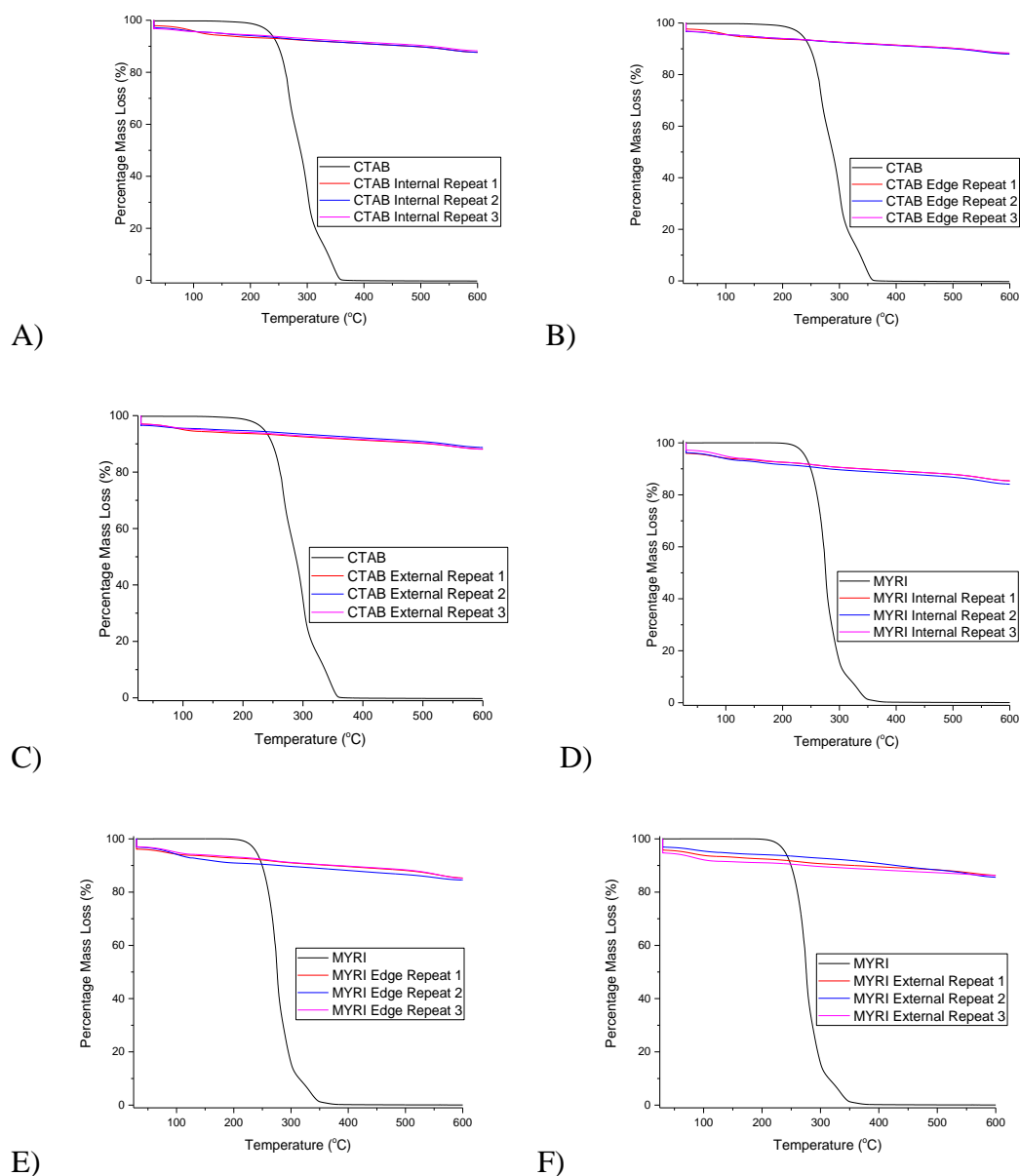
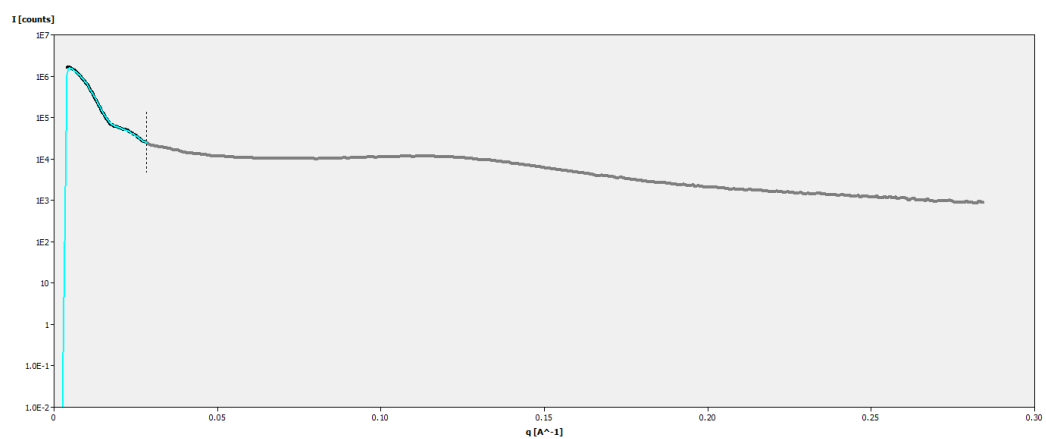


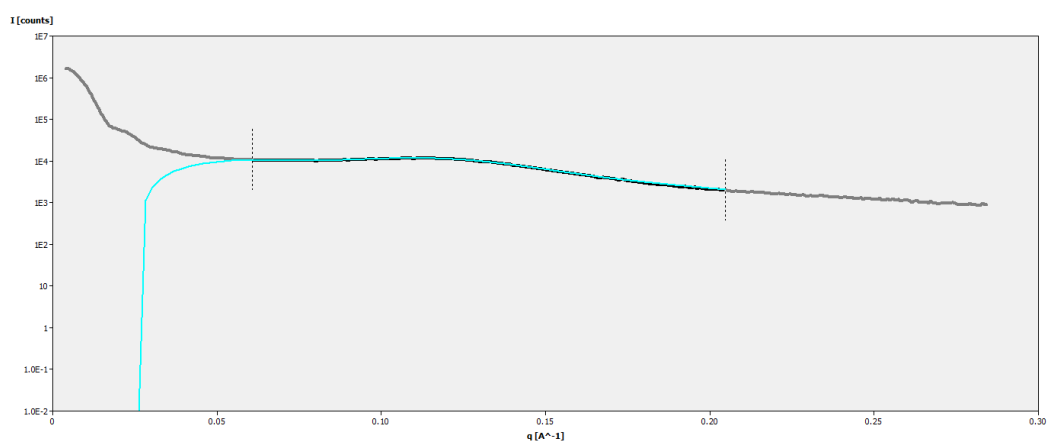
Figure 3.14. The TGA analysis of the three repeats for the synthetic protocols between 30 – 600 °C A) CTAB Internal, B) CTAB Edge, C) CTAB External, D) MYRI Internal, E) MYRI Edge and F) MYRI External compared to their respective surfactants CTAB and MYRI.

A)

I)

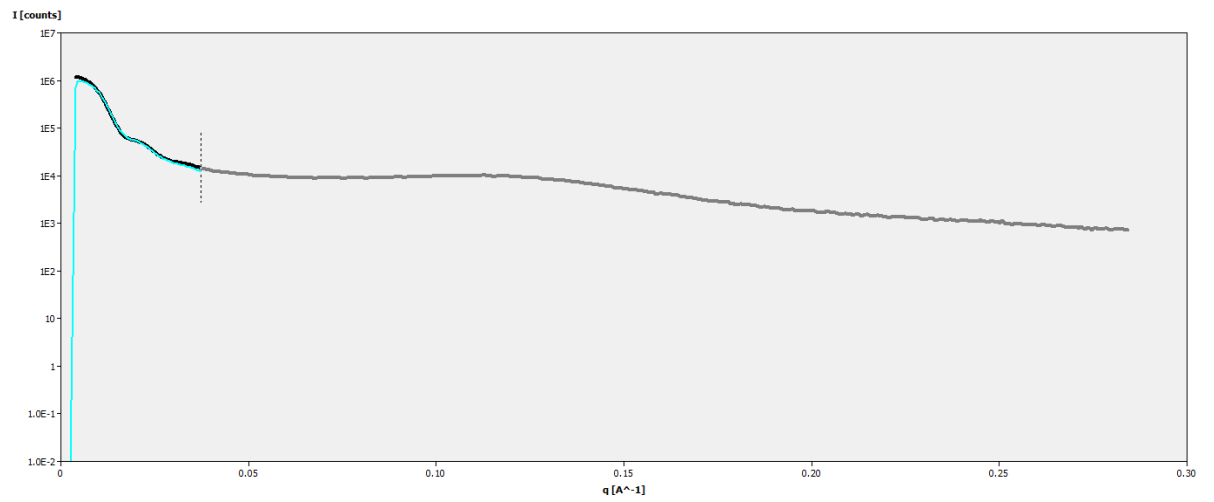


II)

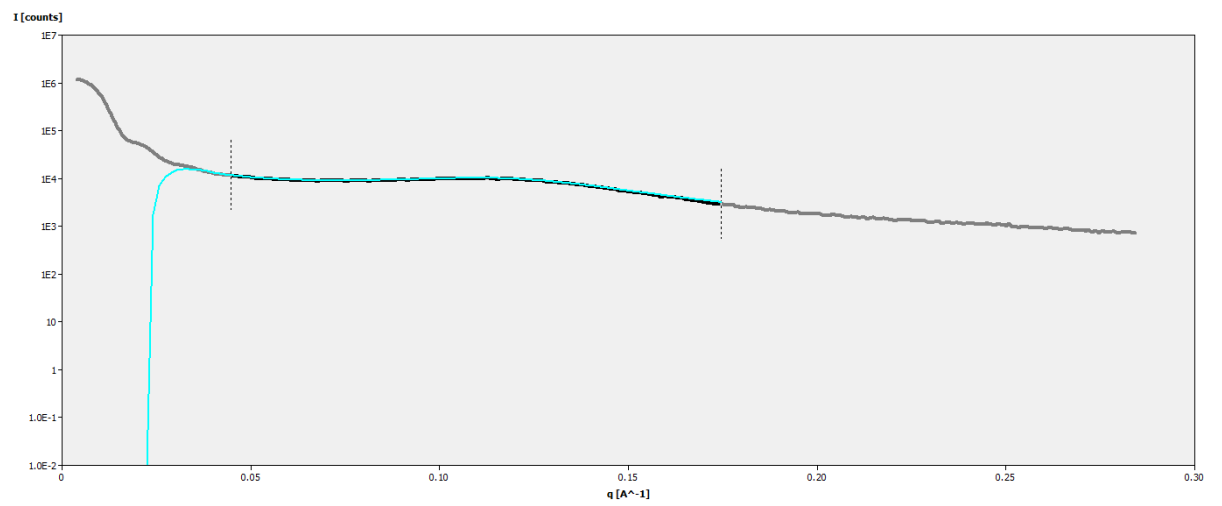


B)

D)



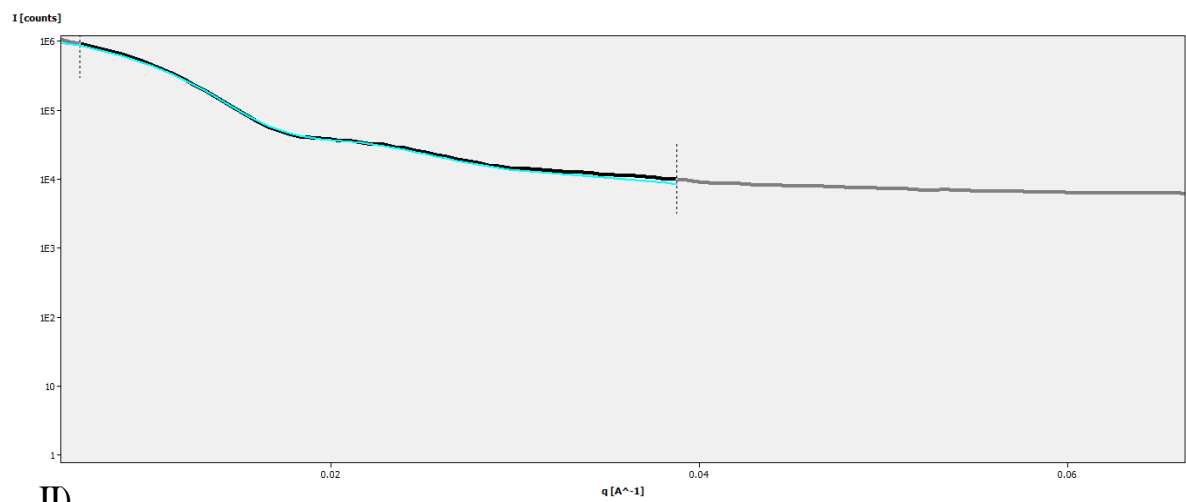
II)



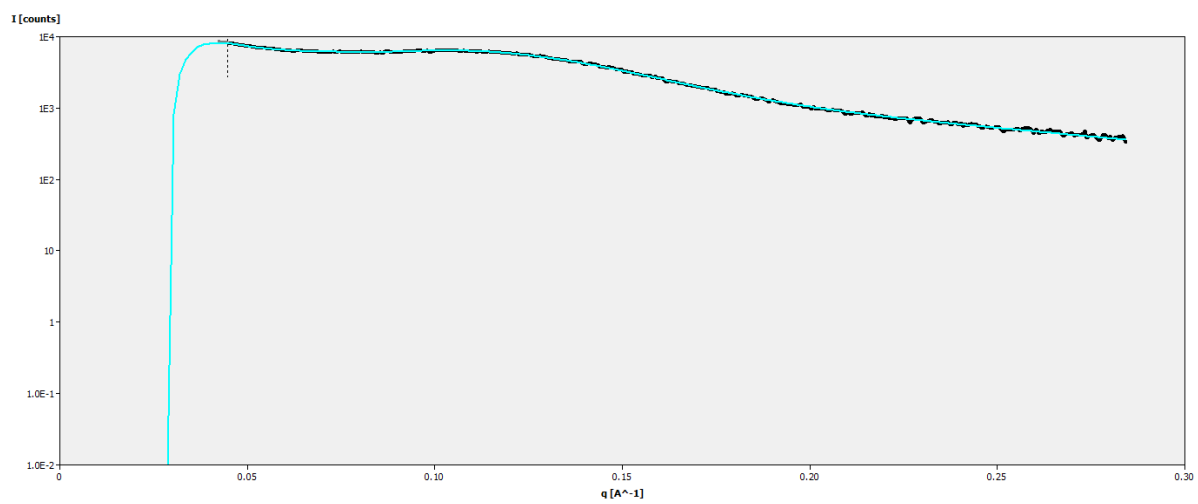


C)

D)

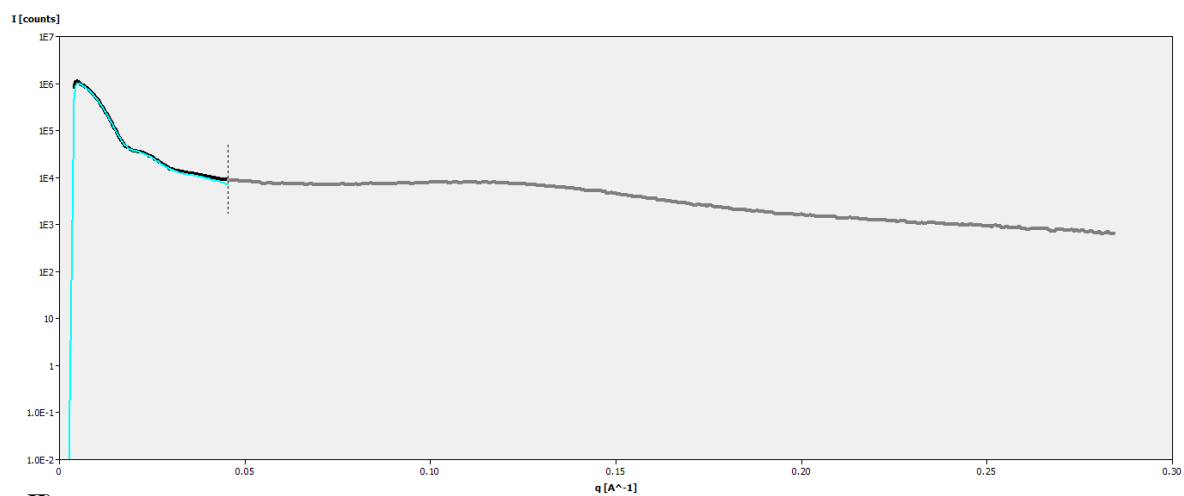


II)

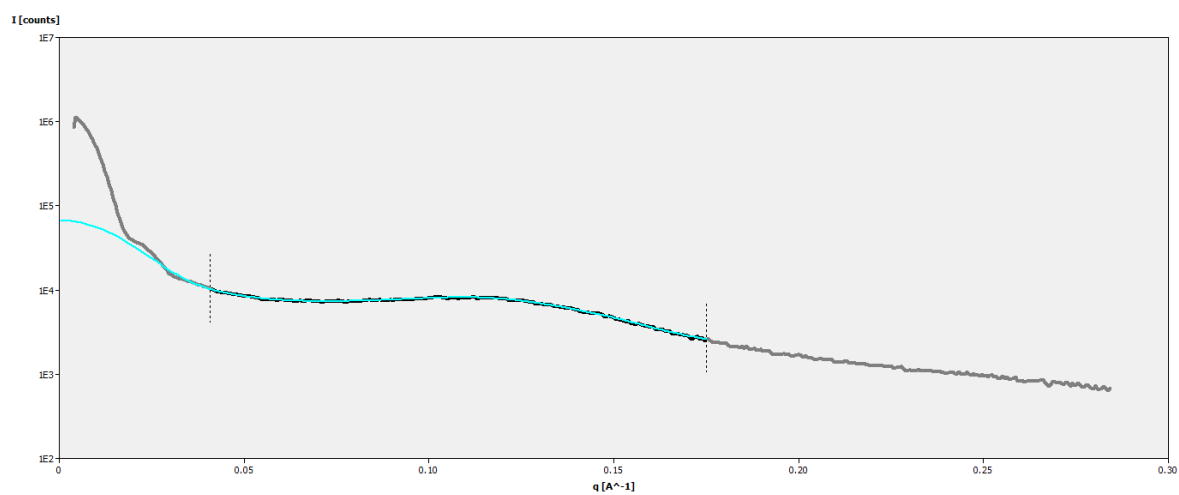


D)

I)

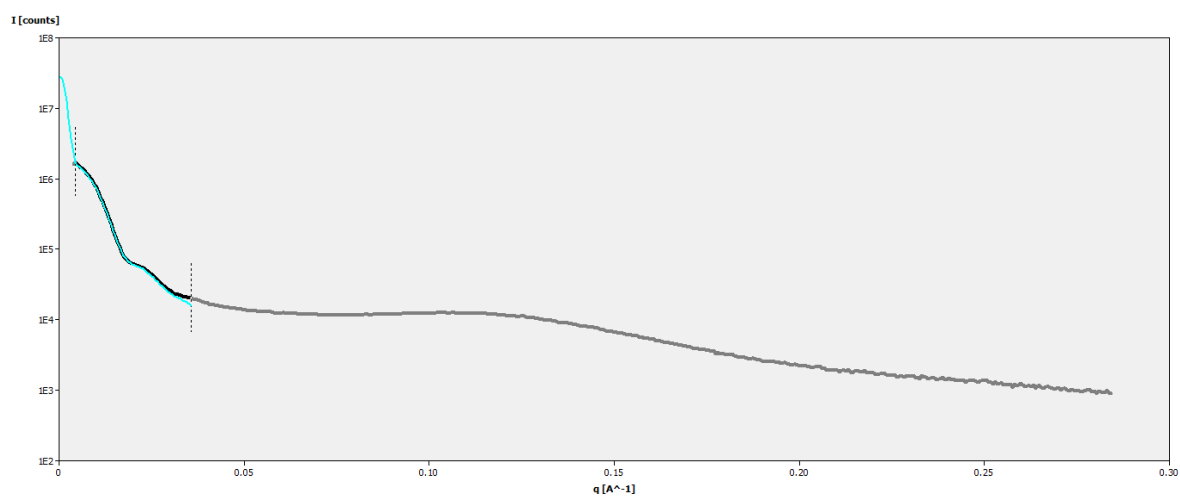


II)

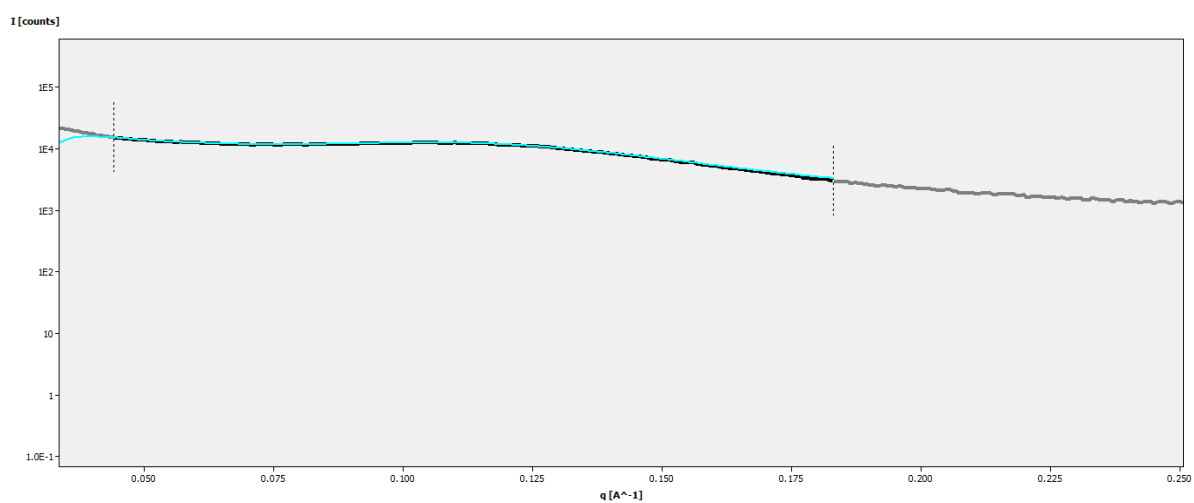


E)

D)

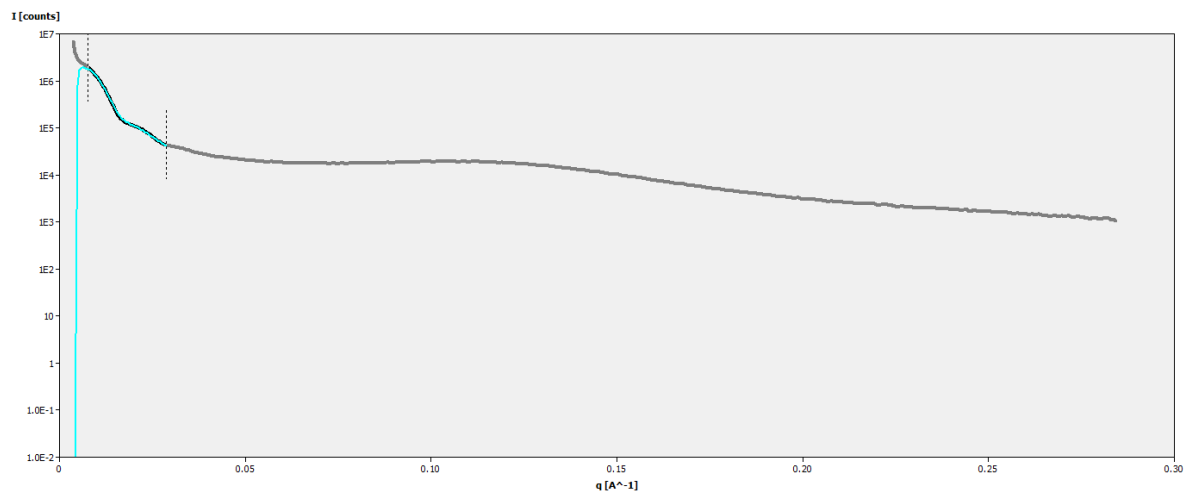


II)

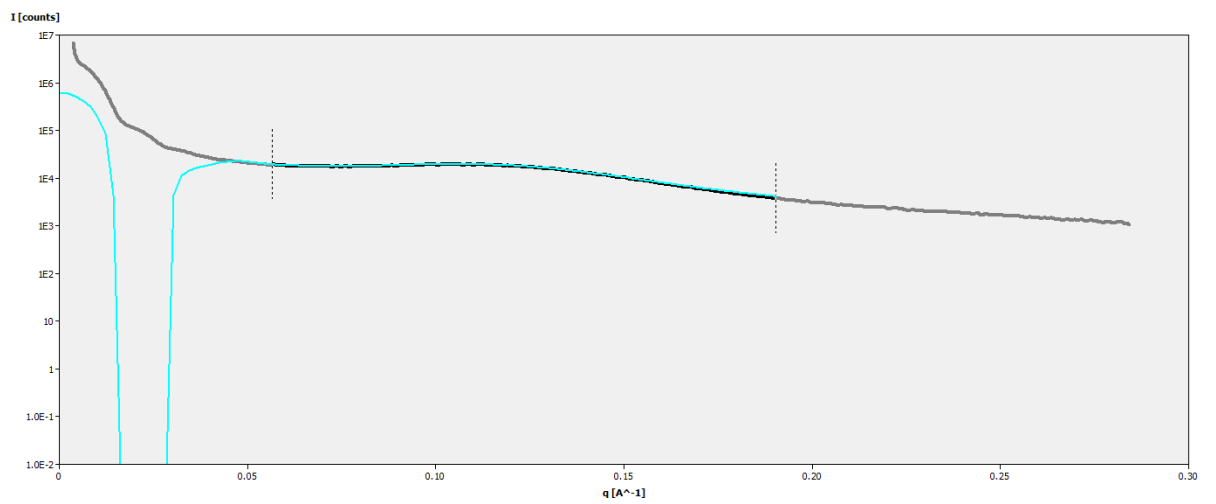


F)

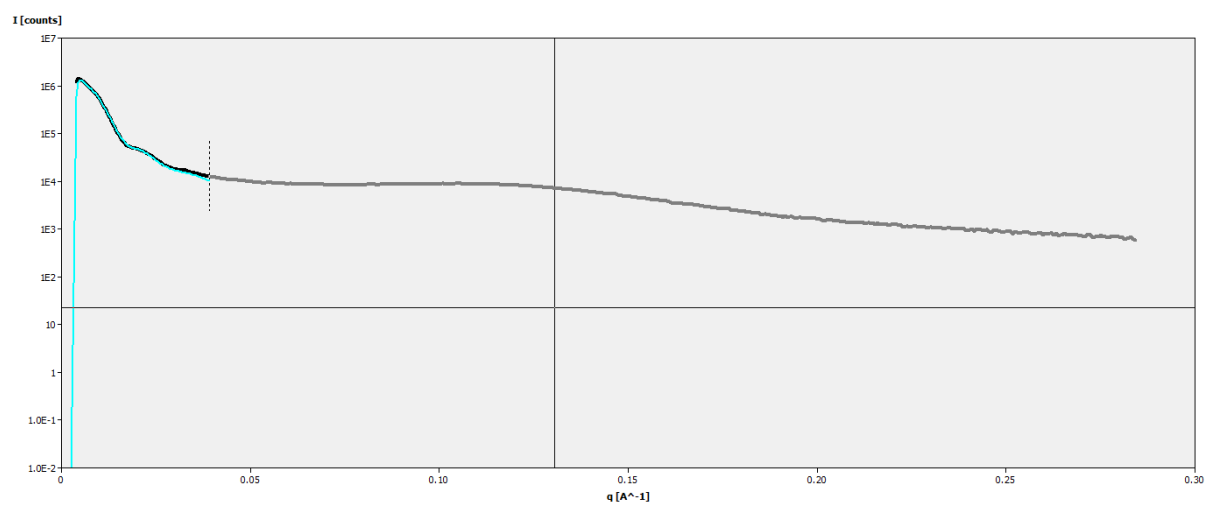
D)



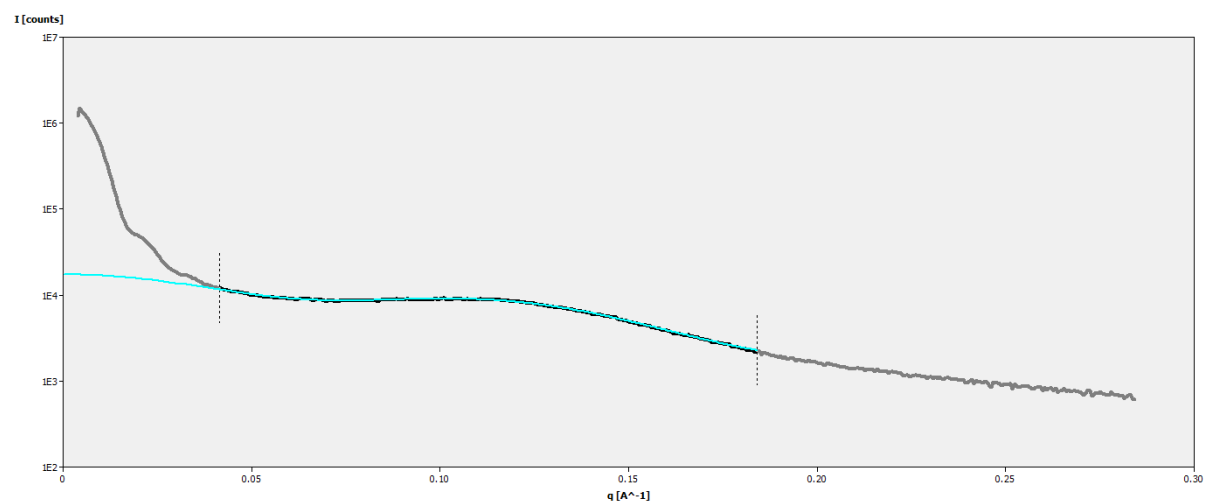
D)



G)  
D)

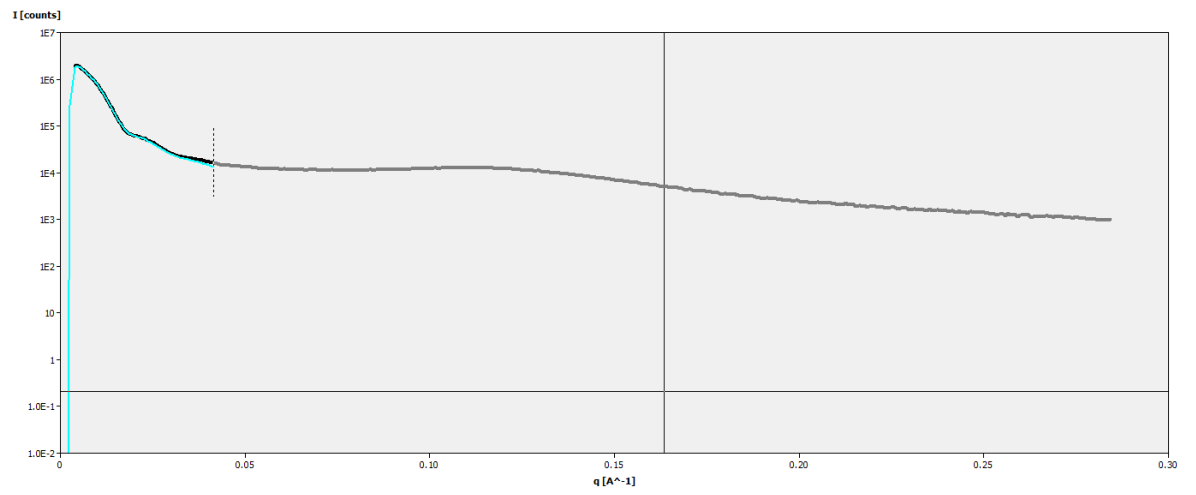


II)

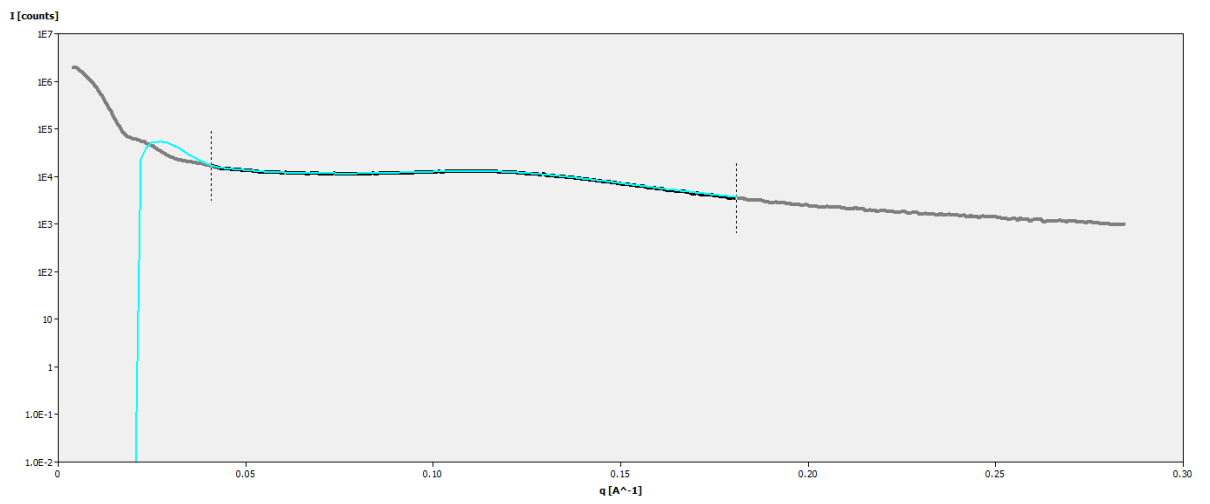


H)

I)

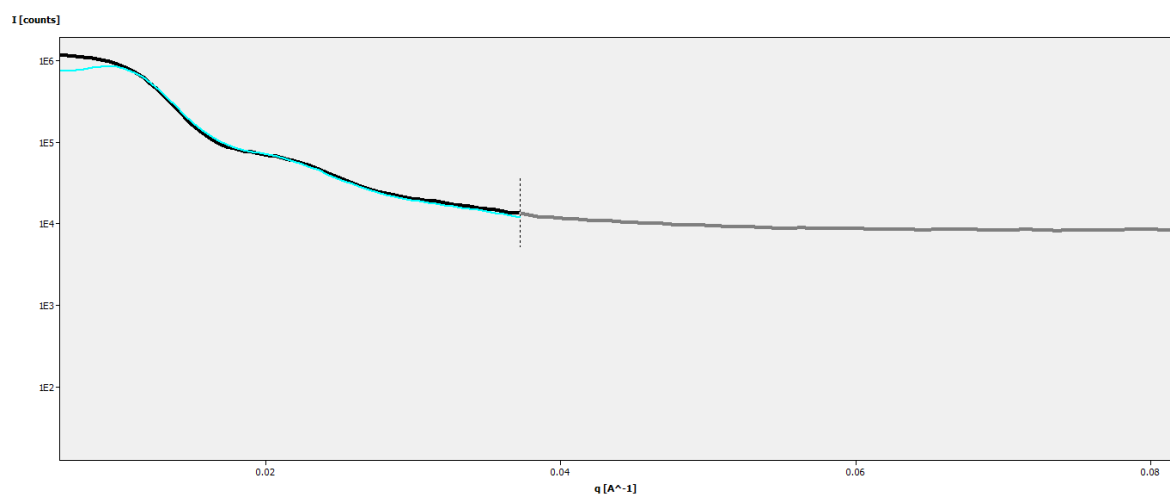


II)

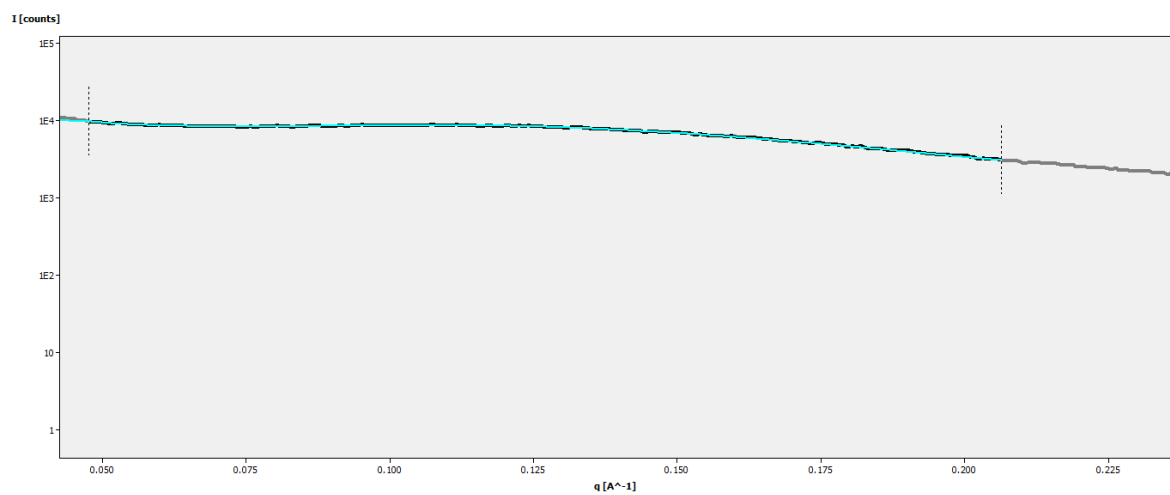


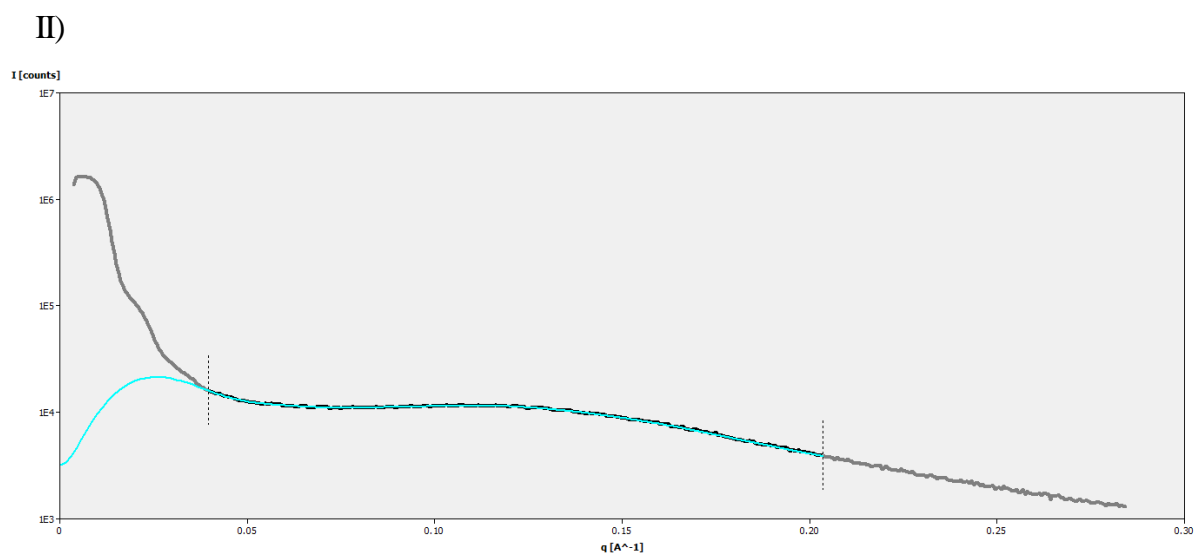
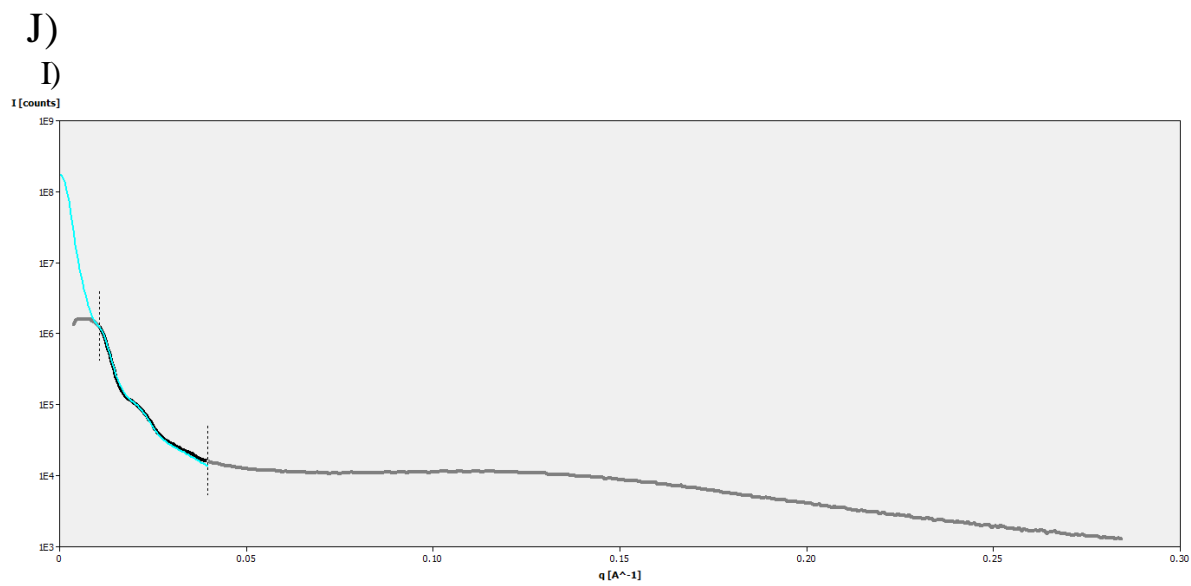
I)

I)



II)

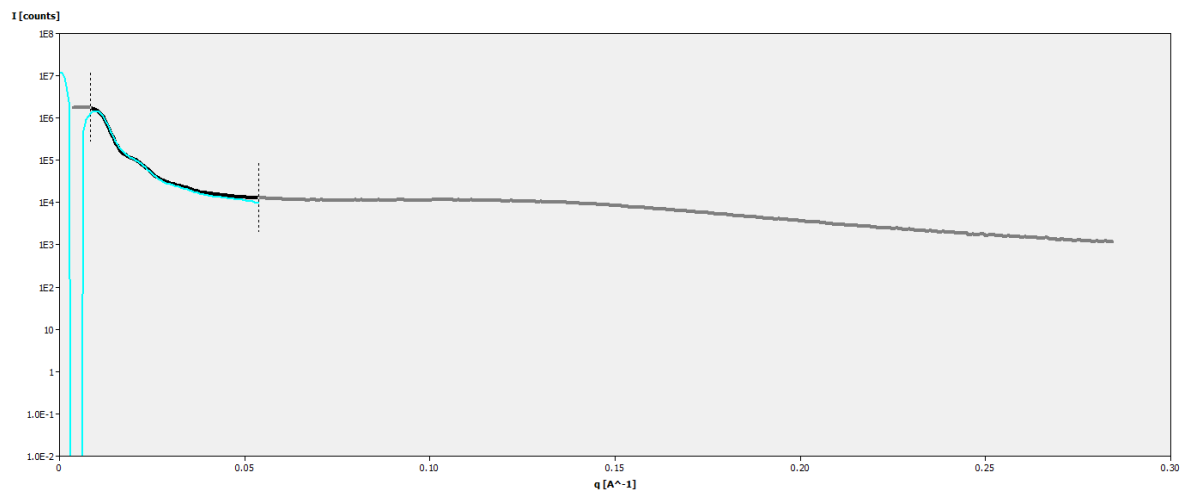




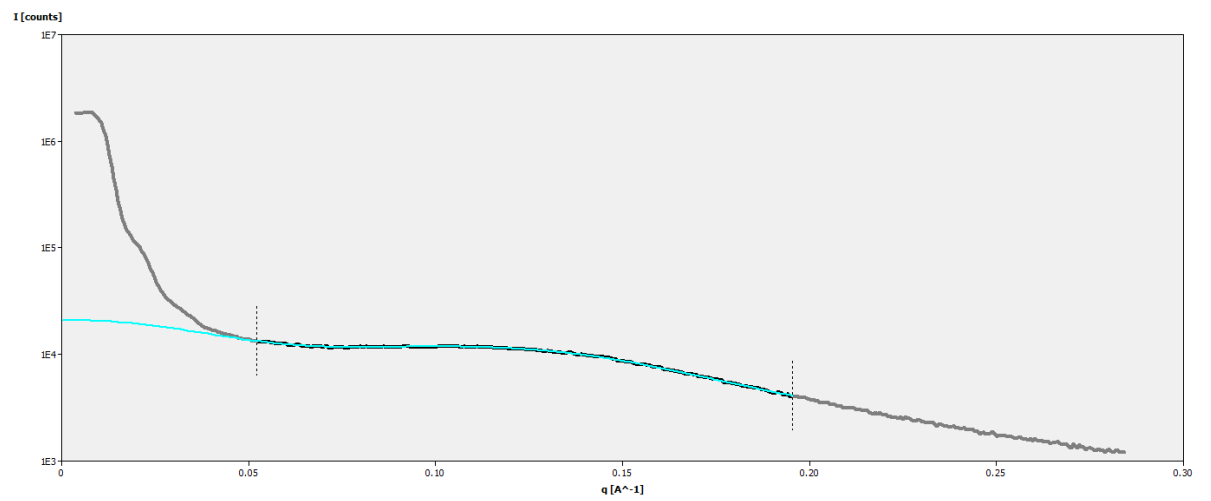


K)

D)

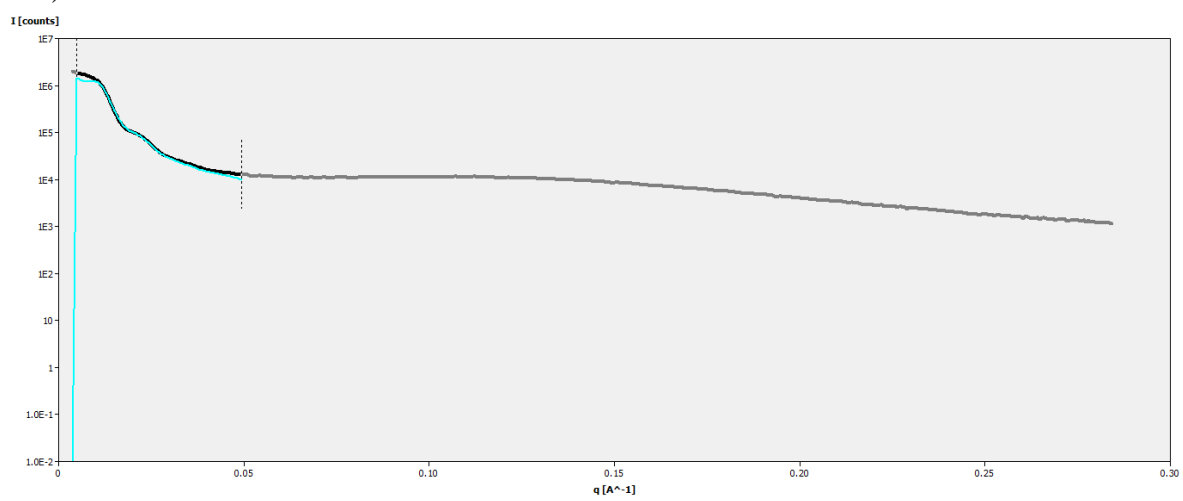


II)

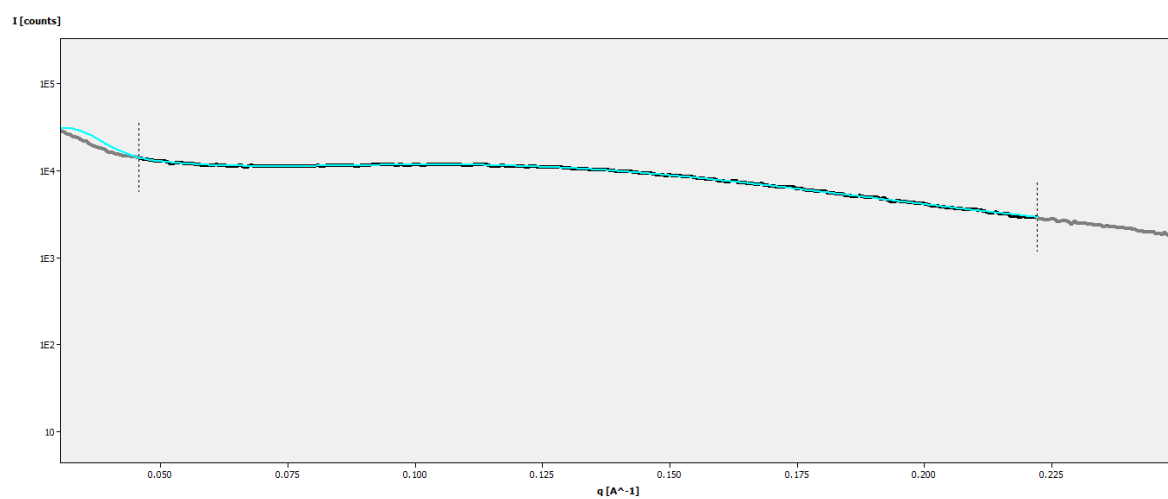


L)

D)

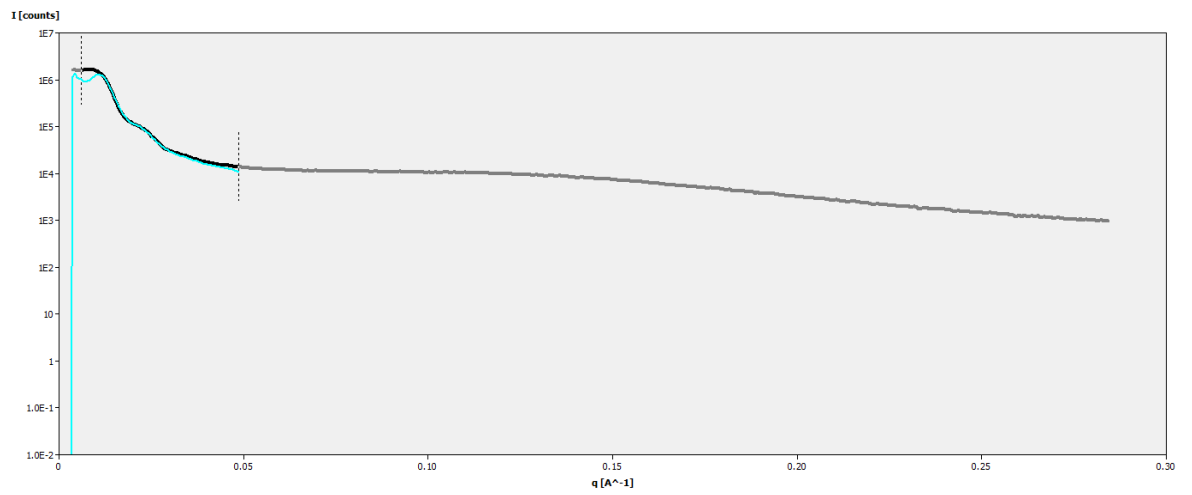


II)

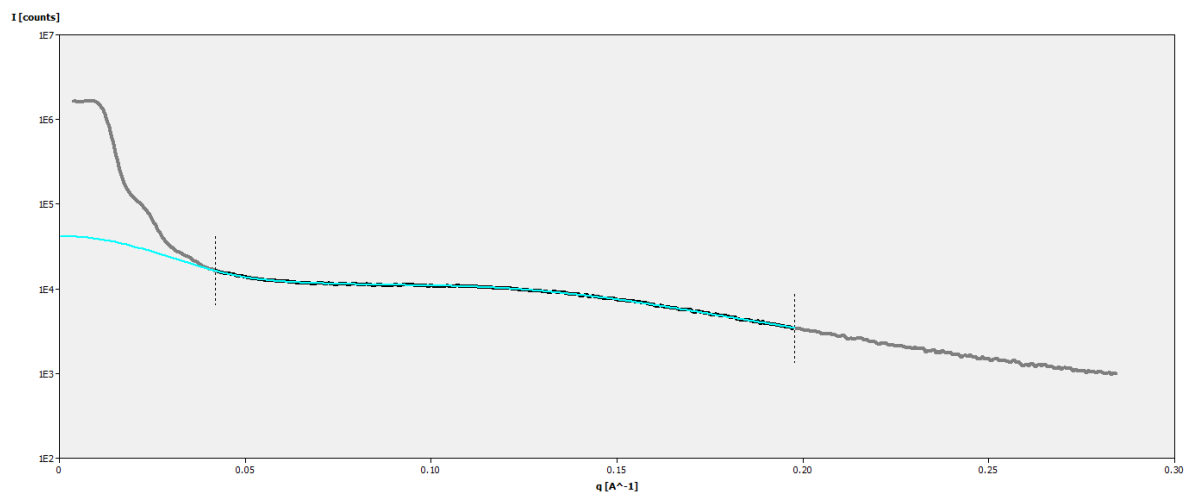


M)

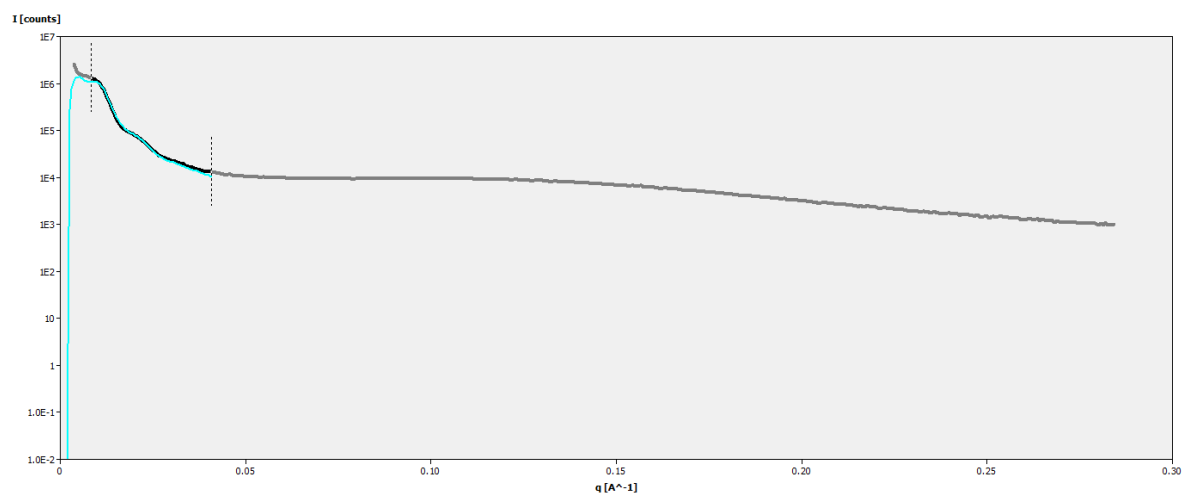
D)



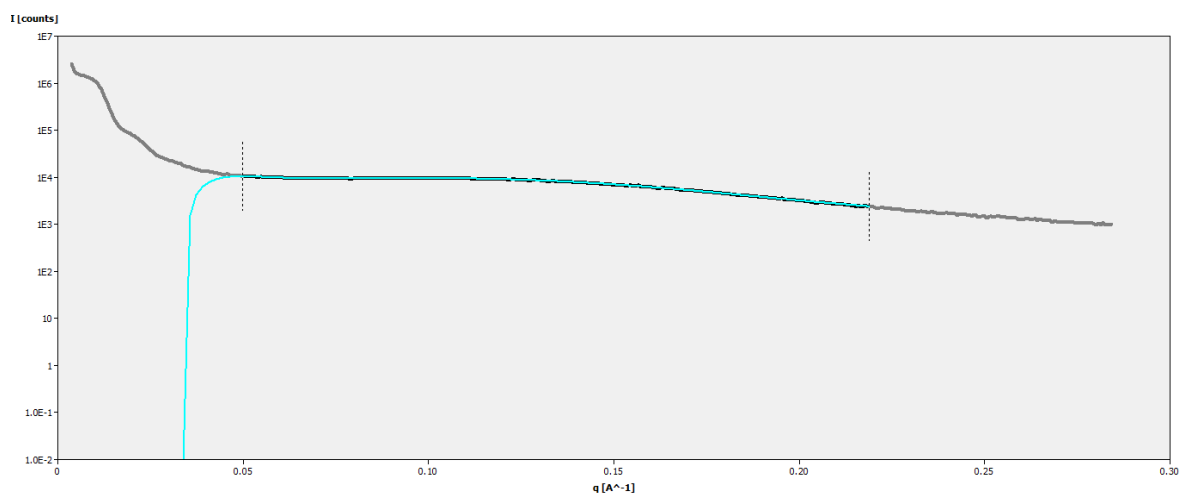
II)



N)  
D)

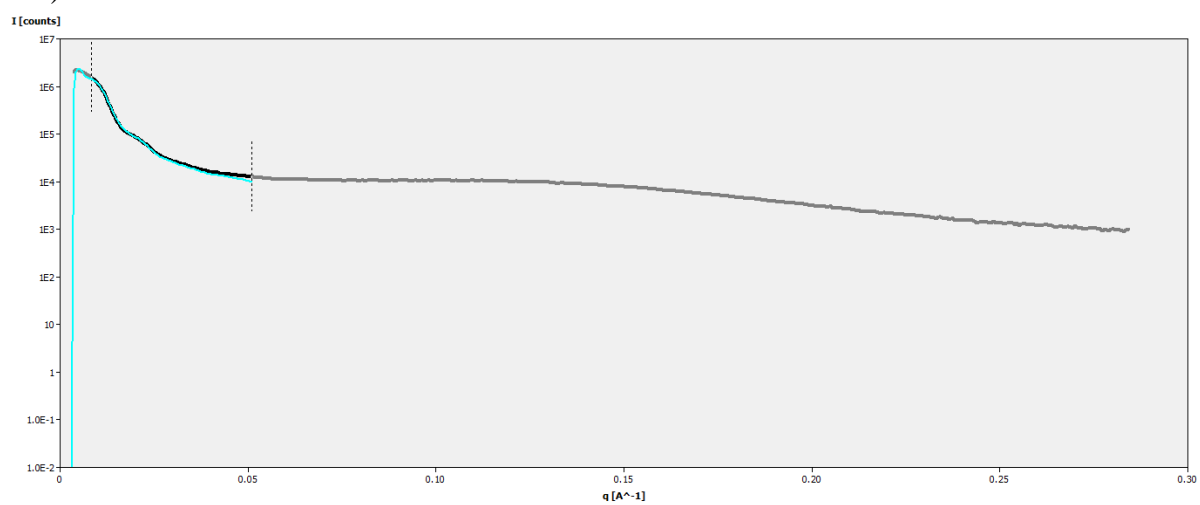


II)

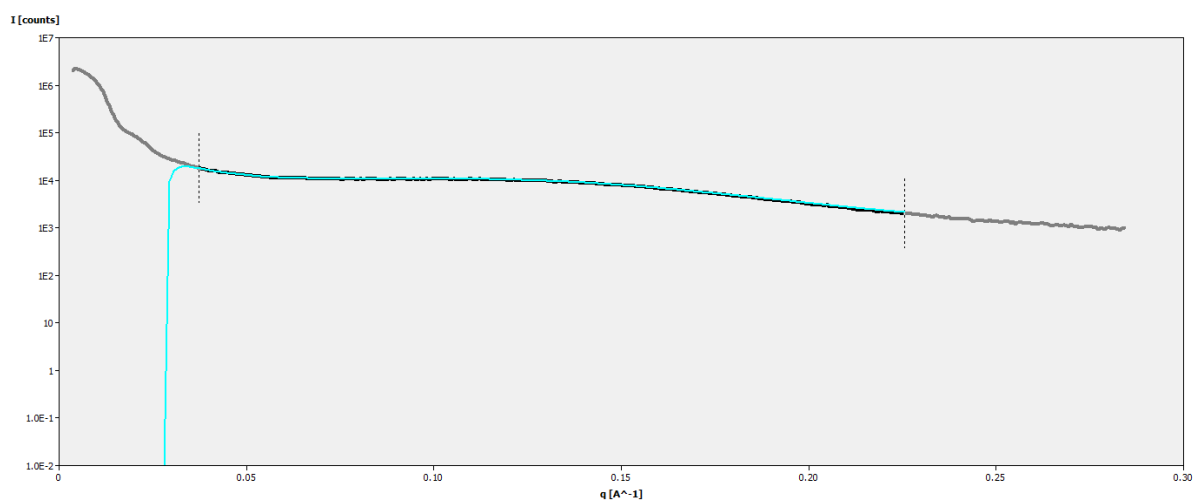


O)

D)

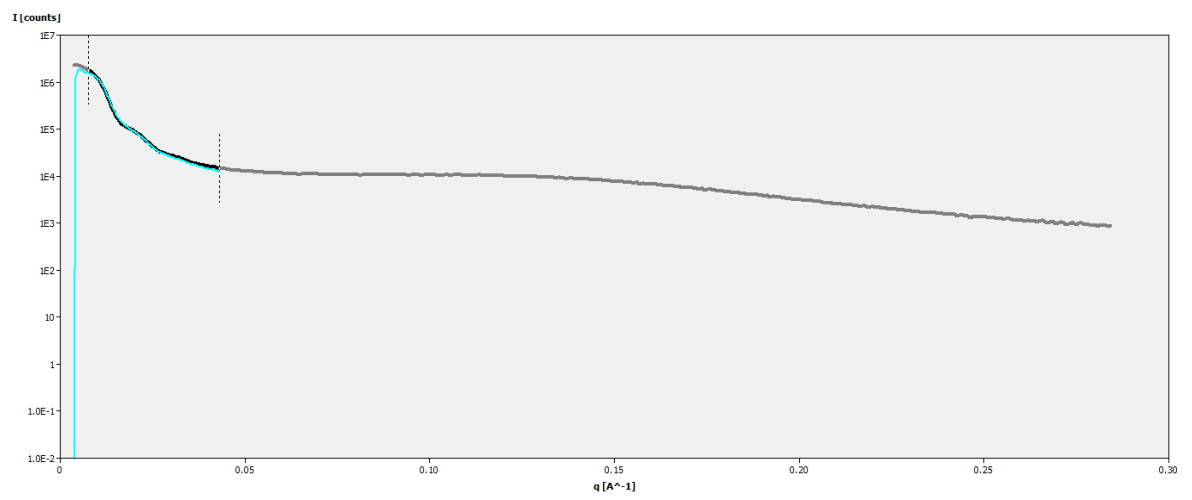


II)

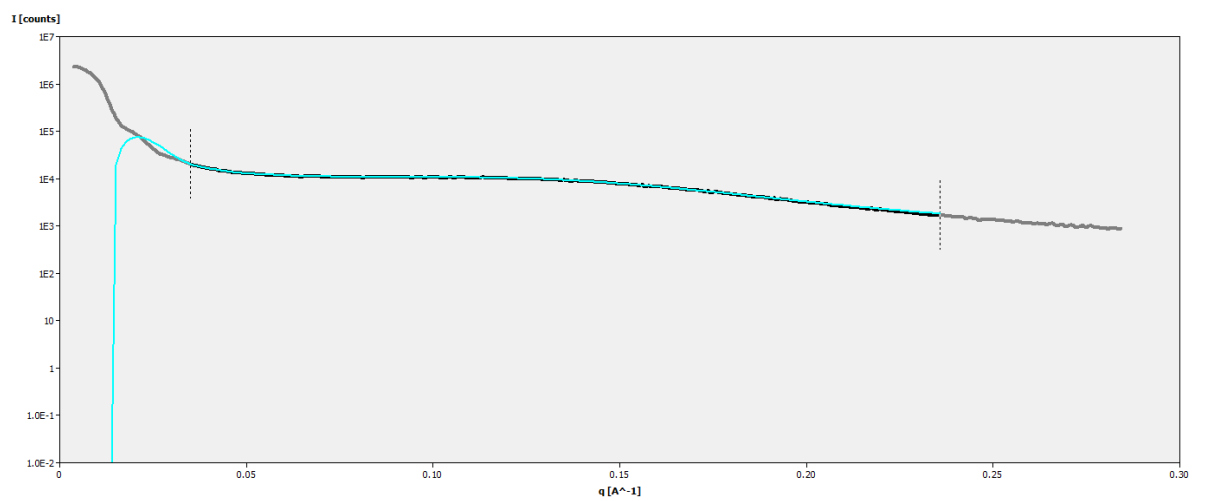


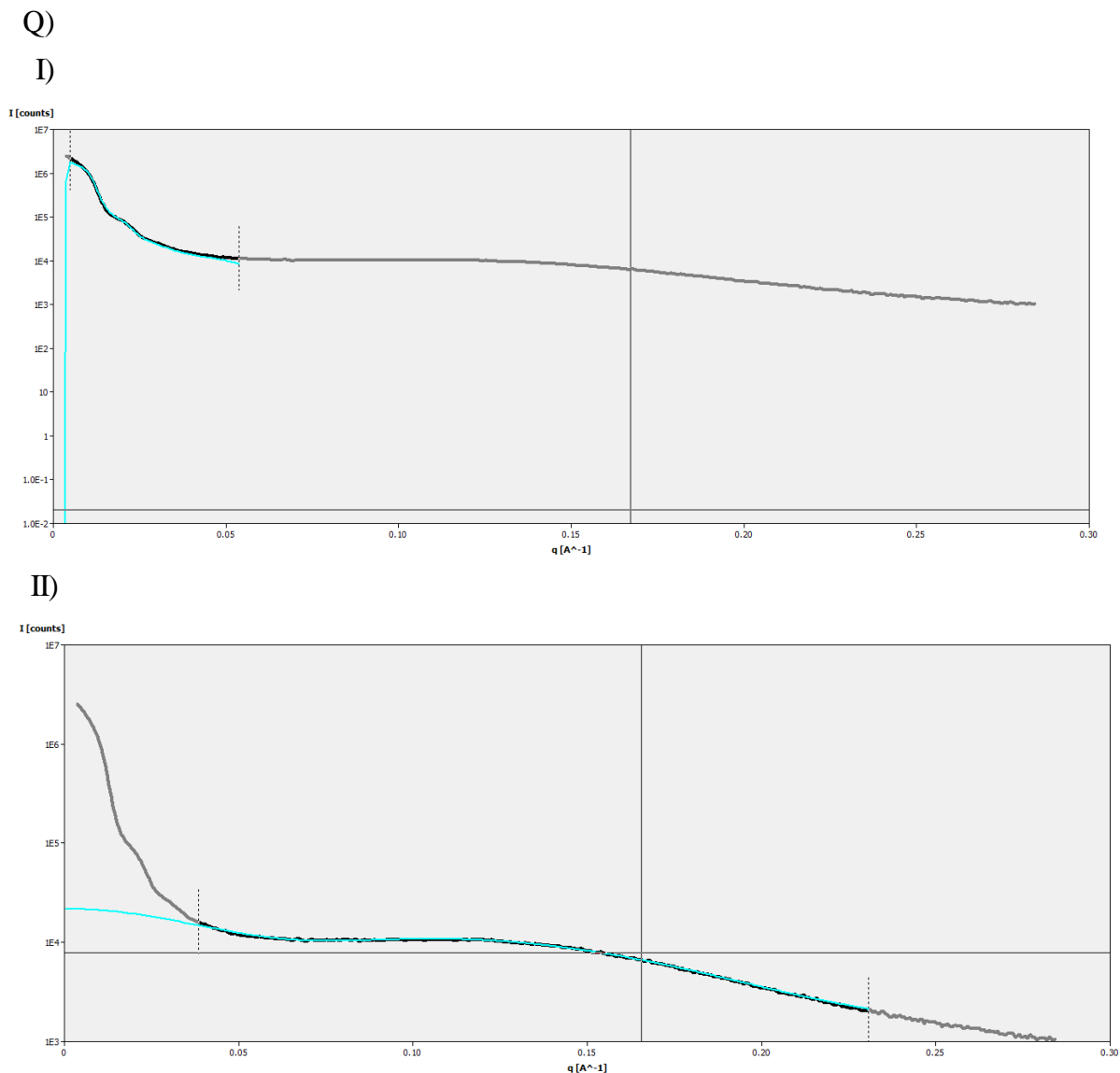
P)

I)



II)





*Figure 3.15. All the rest of the the data acquired by SAXs for A) CTAB Internal MSNs Repeat 2, B) CTAB Internal MSNs Repeat 3, C) CTAB Edge MSNs Repeat 1, D) CTAB Edge MSNs Repeat 2, E) CTAB Edge MSNs Repeat 3, F) CTAB External MSNs Repeat 1, G) CTAB External MSNs Repeat 2, H) CTAB External MSNs Repeat 3, I) MYRI Internal MSNs Repeat 1, J) MYRI Internal MSNs Repeat 2, K) MYRI Internal MSNs Repeat 3, L) MYRI Edge MSNs Repeat 1, M) MYRI Edge MSNs Repeat 2, N) MYRI Edge MSNs Repeat 3, O) MYRI External MSNs Repeat 1, P) MYRI External MSNs Repeat 2, Q) MYRI External MSNs Repeat 3, with the area representing I) the particle diameter and II) the pore diameter of the MSNs being analysed using the EasySAXS modelling software.<sup>28</sup>*

## EasySAXS general protocol

The area of the  $q$  versus intensity is highlighted that represents the property that is being analysed (Low  $q$  = particle diameter, high  $q$  = pore diameter). Then an estimated size is given to the model to make a hypothetical equation, which is plotted against the analysed area. This is repeated until a fit is obtained between the hypothetical plot and the data obtained by the sample. With this optimised plot a Fourier transform is performed. Finally, the ranges of diameters observed is calculated (Equation 3.3) where  $\Delta q$  is the distance between peak oscillations.<sup>28</sup>

$$Diameter = \frac{2\pi}{\Delta q} \text{ (Equation 3.3)}$$

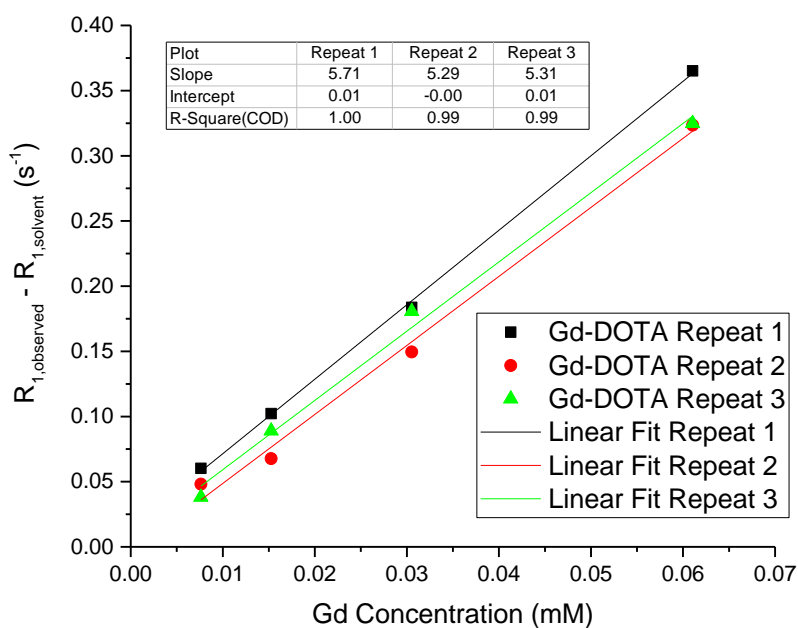


Figure 3.16. The plot of  $R_1$  against Gd concentration for the molecular  $Gd^{3+}$ -DOTA control with three repeats.



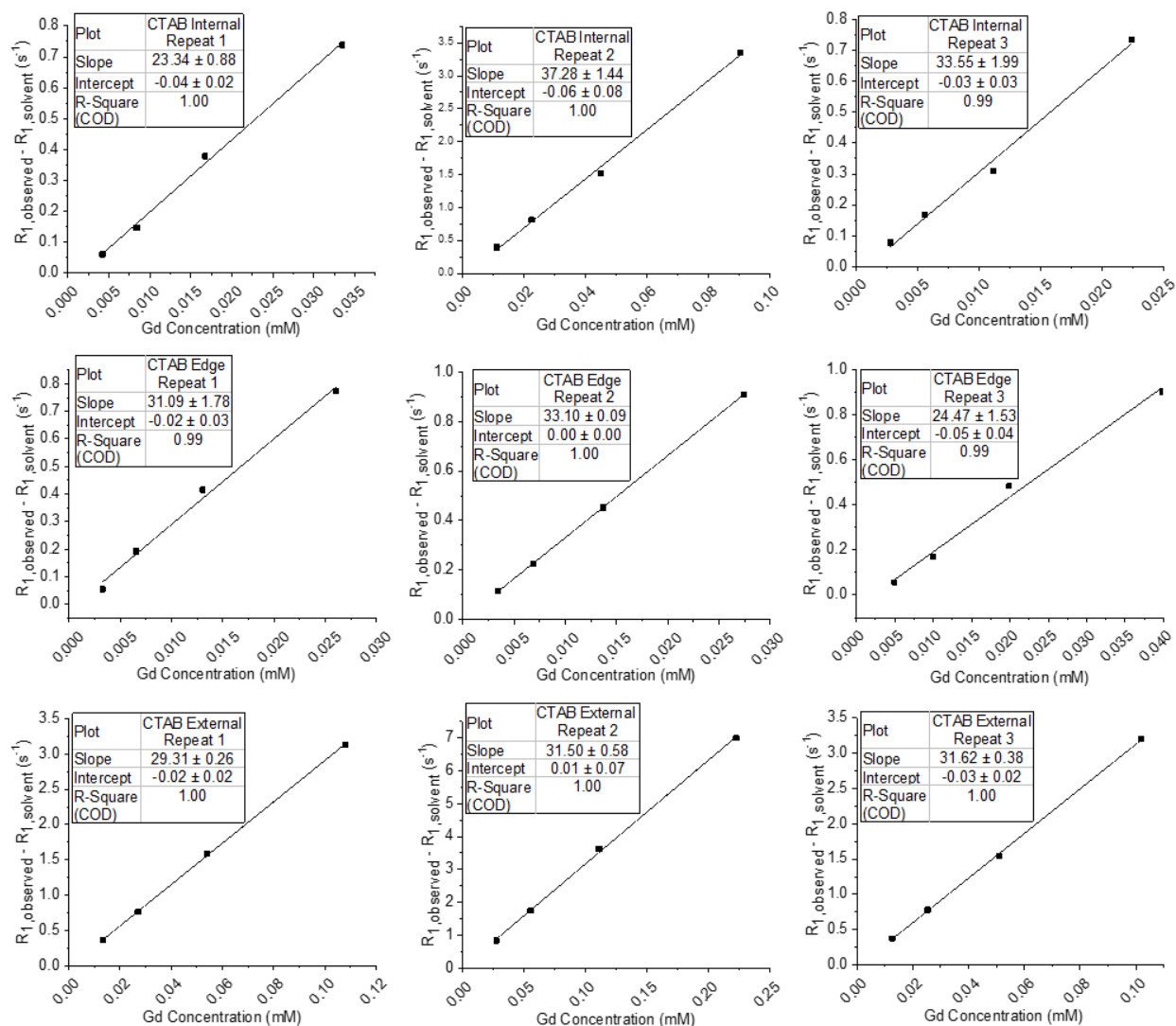


Figure 3.17. The graphs of  $R_{1,observed} - R_{1,solvent}$  against Gd concentration for all the CTAB MSNs functionalised with Gd<sup>3+</sup>-DOTA bound either in the Internal, Edge and External positions.

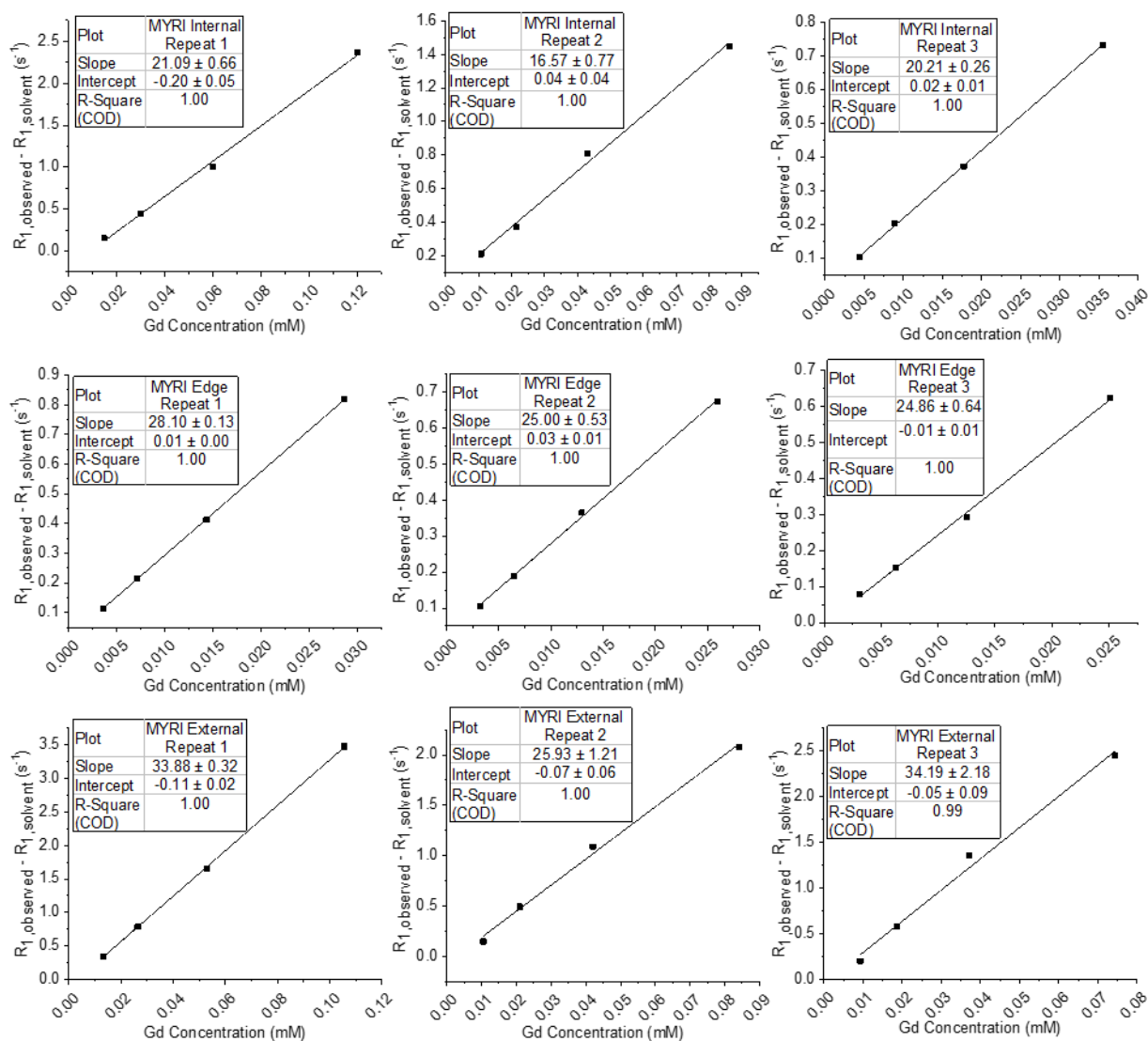


Figure 3.18. The graphs of  $R_{1, \text{observed}} - R_{1, \text{solvent}}$  against Gd concentration for all the MYRI MSNs functionalised with  $Gd^{3+}$ -DOTA bound either in the Internal, Edge and External positions.